Università degli Studi di Ferrara

DOCTORAL COURSE IN PHYSICS

CYCLE XXXV

COORDINATOR Prof. Eleonora Luppi

Charting new physics territories with cosmological observations

Scientific/Disciplinary (SDS) FIS/02

Candidate
Luca Caloni

Supervisor
Dr. Massimiliano Lattanzi

Co-advisor
Dr. Martina Gerbino

Years 2019-2022

Università degli Studi di Ferrara

DOCTORAL COURSE IN PHYSICS

CYCLE XXXV

COORDINATOR Prof. Eleonora Luppi

Charting new physics territories with cosmological observations

Scientific/Disciplinary (SDS) FIS/02

Candidate
Luca Caloni

Supervisor
Dr. Massimiliano Lattanzi

Co-advisor
Dr. Martina Gerbino

Years 2019-2022

We're all stories in the end.
Just make it a good one, eh?

(Eleventh Doctor)

Abstract

In this Thesis we exploit the latest cosmological observations to constrain fundamental physics scenarios that go beyond the standard models of cosmology and particle physics. We start by considering Macroscopic Dark Matter (MDM) candidates, which represent an appealing alternative to particle dark matter. We focus on the process of proton capture by MDM and constrain the parameter space of Macros using three cosmological probes: (*i*) the change in the baryon density between the epochs of the Big Bang Nucleosynthesis (BBN) and the Cosmic Microwave Background (CMB) decoupling; (*ii*) the production of spectral distortions in the CMB spectrum; (*iii*) the kinetic coupling between charged MDM and baryons at the time of CMB decoupling. We also show how future spectral distortions experiments, like PIXIE and SuperPIXIE, will allow us to improve these bounds. Then, we focus on thermal axion-like particles (hereafter axions), which are produced in the early Universe from scatterings between particles belonging to the primordial thermal bath. Depending on their mass, thermal axions can behave as a hot, warm or cold dark matter component. Using the latest observations of CMB anisotropies by *Planck* and of Baryon Acoustic Oscillations from galaxy surveys, we constrain the couplings of axions to photons and gluons. We compare these bounds with the constraints derived from laboratory and astrophysical probes. In the second part of the Thesis, we focus on the polarization of the CMB as a probe to test possible violations of fundamental symmetries. First, we consider models that extend Maxwell's electrodynamics by introducing renormalizable operators which break Lorentz invariance. These consist in two terms, one of which violates also CPT symmetry. Using the most recent observations of CMB polarization, we derive strong bounds on the Lorentz-violating coefficients. In particular, for the CPT-odd coefficients we obtain the strongest constraints to date, even considering non-CMB probes. Finally, we analyze the effects of chiral scalar-tensor theories of gravity during inflation, focusing on the non-Gaussianity of primordial gravitational waves. We compute the theoretical prediction for the primordial bispectrum and we discuss the prospects for detecting such parity-violating signatures with future CMB experiments.

List of papers

This Thesis is based on the results reported in the following papers:

- *Tensor non-Gaussianity in chiral scalar-tensor theories of gravity* [1],
  N. Bartolo, L. Caloni, G. Orlando, A. Ricciardone,
  Journal of Cosmology and Astroparticle Physics (JCAP) 03 (2021), 073

- *Updated cosmological constraints on Macroscopic Dark Matter* [2],
  L. Caloni, M. Gerbino, M. Lattanzi,
  Journal of Cosmology and Astroparticle Physics (JCAP) 07 (2021), 027

- *Novel cosmological bounds on thermally-produced axion-like particles* [3],
  L. Caloni, M. Gerbino, M. Lattanzi, L. Visinelli,
  Journal of Cosmology and Astroparticle Physics (JCAP) 09 (2022), 021

- *Probing Lorentz-violating electrodynamics with CMB polarization* [4],
  L. Caloni, S. Giardiello, M. Lembo, M. Gerbino, G. Gubitosi, M. Lattanzi, L. Pagano,
  Accepted for publication in Journal of Cosmology and Astroparticle Physics (JCAP),
  arXiv: 2212.04867

Contents

Part I

Introduction

We are living in the golden age of cosmology, characterized by the availability of an unprecedented amount of observational data. Several experiments aim at investigating our Universe across the different epochs of its history, from the early times, when the Cosmic Microwave Background (CMB) was produced, until the latest stage of Large-Scale Structure (LSS) formation. The standard ΛCDM cosmological model, that emerges from these observations, has been tested repeatedly over the last few years and its six parameters are now measured at percent and sub-percent level precision.

The ΛCDM model, which characterizes the dynamics of our Universe on its largest scales, is complemented by the Standard Model (SM) of particle physics, which describes all the elementary particles and their interactions at fundamental level. Since its formulation in the early 1970s, the SM has predicted the outcome of numerous experiments with astonishing accuracy.

Despite the great success of the standard models of cosmology and particle physics, many fundamental questions remain still without an answer. These include the nature of dark matter and dark energy, the quest for a consistent and experimentally-established theory of quantum gravity, the physics driving inflation and the origin of the baryon asymmetry in the Universe. Interestingly, the possible solutions to these puzzles often suggest a deep connection between cosmology and particle physics. As a result, cosmological observations are nowadays a powerful probe to test fundamental physics scenarios and they have become precise enough to start complementing, and possibly overcoming, the constraints from laboratory and collider experiments.

Most of the knowledge about our Universe comes from the observations of the CMB, an extremely isotropic radiation released when the Universe became transparent after the formation of the first neutral atoms. The CMB is linearly polarized at the 10% level due to Thomson scattering between photons and free electrons at the time of last scattering. Almost all the available information from the CMB temperature anisotropies has already been extracted by the *Planck* satellite [5, 6] at large and intermediate angular scales, and by the Atacama Cosmology Telescope (ACT) [7] at smaller scales. Nevertheless, a wealth of information is still encoded in the CMB polarization. Constraining cosmology and fundamental physics through CMB polarization is indeed the focus of the next-stage CMB surveys. One of the main goals is the detection of the so-called B-modes of polarization, that are the smoking gun of primordial gravitational waves (PGWs) sourced during inflation. Currently, the strongest bounds on B-modes come from the BICEP/Keck array [8]. The measurement of B-modes at large angular scales will be the main target of the LiteBIRD satellite [9]. The future ground-based experiments Simons Observatory (SO) [10] and CMB Stage-4 (CMB-S4) [11] will also play a fundamental role in measuring the CMB polarization at smaller angular scales and higher angular resolution. Furthermore, the increased sensitivity of future CMB surveys to primordial non-Gaussianities will provide valuable information to probe the dynamics of inflation and the associated high-energy physics [12].

The same physics that is imprinted in the CMB anisotropies also determined the initial

conditions for the clustering of matter and can thus be observed through the LSS of the Universe. In particular, Baryon Acoustic Oscillations (BAO) provide us with a cosmological standard ruler which allows us to further improve our bounds on the cosmological parameters. BAO data are extracted from galaxy surveys such as BOSS DR12 [13], 6dFGS [14] and SDSS-MGS [15].

In this Thesis we exploit the most recent cosmological observations described above to constrain various fundamental physics scenarios which go beyond the standard models of cosmology and particle physics.

As mentioned above, one of the big open questions of both cosmology and particle physics is to understand the nature of dark matter (DM). Many particle DM candidates have been proposed, including WIMPs, axions and sterile neutrinos, but no experimental evidence has been found in favour of any of them yet. An alternative possibility is that the DM is composed of macroscopic-size objects, generically dubbed Macro Dark Matter (MDM) [16]. In part II of this Thesis we analyze this possibility and use cosmological observations to constrain the parameter space of MDM. Then, we consider thermal axion-like particles (hereafter axions) produced in the early Universe from either axion-photon or axion-gluon processes. Depending on their mass, thermally-produced axions can behave as a hot, warm or cold dark matter component. We constrain the axion couplings to photons and gluons using the latest observations of the CMB from *Planck* and of BAO from galaxy surveys.

In part III of the Thesis we focus on the polarization of the CMB as a probe to test possible violations of some fundamental symmetries. The CMB polarization is particular suited to test models predicting a non-standard propagation of photons in the Universe. We consider this possibility in the context of Lorentz- and CPT-violating extensions of Maxwell's electromagnetic theory [17–19]. Two observable effects are the generation of cosmic birefringence (both isotropic and anisotropic), i.e. the rotation of the linear polarization plane of CMB photons, and the generation of circular polarization from the conversion of the primordial linear polarization components. Then, we consider the possibility that parity symmetry is violated in the gravity sector during inflation. The violation of parity symmetry induces a difference in the power spectra of left-handed and right-handed polarization states of PGWs, which is usually referred to as chirality. This can in general leave imprints in both power spectra and higher-order correlators of the CMB involving B-modes.

In more details, the Thesis is organized as follows:

- In chapter 1 we review the basics of the standard model of cosmology. We start by describing the foundations of the ΛCDM model. Then, after discussing the most important events during the thermal history of our Universe, we introduce the shortcomings of the standard cosmological model and explain how the inflationary paradigm provides compelling solutions to all of them. We also briefly recall the mechanism through which inflation can source the primordial perturbations in the Universe. Finally, we describe the main cosmological observables used in the analysis outlined in the rest of the Thesis.

- In chapter 2 we focus on MDM. Keeping a phenomenological approach, we consider a particular process that might be associated to MDM, namely the capture of baryons of the cosmological plasma by Macros. We begin by discussing the cosmological phenomenology of MDM and derive constraints on the parameter space of MDM using three cosmological probes: (*i*) the change in the baryon density between the epochs of the Big Bang Nucleosynthesis (BBN) and the CMB decoupling; (*ii*) the production of spectral distortions in the CMB spectrum; (*iii*) the kinetic coupling between charged MDM and baryons at the time of CMB decoupling. This is based on the results reported in [2].

  In chapter 3 we introduce the QCD axion and axion-like particles. We discuss the theoretical motivations behind the introduction of these new particle species and describe the main QCD axion models. Then, we focus on axions as dark matter (DM) candidates and

we conclude by summarizing the main experimental strategies to constrain the properties of axions.

In chapter 4 we focus on thermally-produced axions. We discuss the thermal production of axions in the early Universe from axion-photon or axion-gluon processes and we constrain the axion couplings to photons and gluons using the latest observations of the CMB from *Planck* and of BAO from galaxy surveys. We compare our results with the bounds derived from astrophysical and laboratory probes and we discuss the prospects for improving our limits using the next-stage CMB-S4 survey. This is based on the results of [3].

- In chapter 5 we derive new constraints on Lorentz-violating electrodynamics from the most recent measurements of the CMB polarization by *Planck* [20, 21], BICEP/Keck [8], ACT [7], CLASS [22] and SPIDER [23]. We focus on the minimal Standard Model Extension (SME) [17–19], which extends the electromagnetic Lagrangian with renormalizable operators of mass dimension $d \leq 4$. These include an operator of dimension $d = 3$ which also breaks CPT symmetry and a dimension-4 operator which instead respects the CPT symmetry. The CPT-odd operator is responsible for the cosmic birefringence effect, while the CPT-even operator instead converts linear into circular polarization. The constraints that we get on the CPT-odd parameters are roughly one and two orders of magnitude tighter than previous limits. These are the strongest bounds obtained to date on these LV coefficients. Concerning the CPT-even case, we improve previous CMB-based analysis by one order of magnitude. This chapter is based on the results reported in [4].

  In chapter 6 we study inflation within chiral scalar-tensor theories of gravity proposed in [24]. First, we show that the amount of chirality in the power spectrum of PGWs is suppressed. Motivated by this consideration and by the degeneracy between different parity-violating theories at the level of the power spectrum statistics, we make a detailed analysis of the parity-breaking signatures on the bispectrum of primordial tensor modes. We comment on the impact of these parity-violating signatures on the CMB bispectra and discuss the prospects for detecting them with future CMB experiments. This is based on [1].

- Finally, in part IV we review the main novel results derived from the analysis discussed in this Thesis. We draw our conclusions and discuss some future prospects.

Chapter 1

The ΛCDM cosmological model

1.1 Foundations of the standard cosmological model

Cosmology is the branch of physics which studies the composition and the evolution of the Universe as a whole. Started as a philosophical discipline, it is nowadays based on a solid scientific ground, being supported by a wealth of observational data. The standard cosmological model, known as the ΛCDM model, explains extraordinarily well the evolution of our Universe from its early stages (corresponding to some fraction of a second) to its current state, about 13.8 billion years later, in terms of just six parameters. The standard cosmological model is supported by three observational pillars, which have marked a revolution in our view of the Universe in the 20th century:

(i) the observation of the expansion of the Universe, made in 1929 by Hubble [25], who found that galaxies are receding away from each other with a velocity proportional to the relative distance between them;

(ii) the Big Bang Nucleosynthesis (BBN), namely the explanation of the relative abundance of light elements made by Alpher, Bethe and Gamow in 1948 [26];

(iii) the detection of the Cosmic Microwave Background (CMB) by Penzias and Wilson in 1964 [27]. This is an extremely isotropic radiation emitted when the Universe, while cooling down, reached a temperature low enough to allow the formation of neutral atoms; after that, photons decoupled from matter and started free-streaming across the Universe.

On the theoretical side, it is based on three main ingredients:

(i) the *Cosmological Principle*;

(ii) the theory of General Relativity, which provides us with a mathematical model to describe the geometry and the dynamics of the expanding Universe;

(iii) our knowledge of the content of the Universe, which is based on the Standard Model (SM) of particle physics.

We will analyze in more details these three aspects in the next subsections.

1.1.1 The cosmological principle

At the core of the ΛCDM model lies the *Cosmological Principle*, which states that:

"Each *comoving* observer sees the Universe around him, at a fixed time, as *homogeneous* and *isotropic*, on sufficiently large scales."

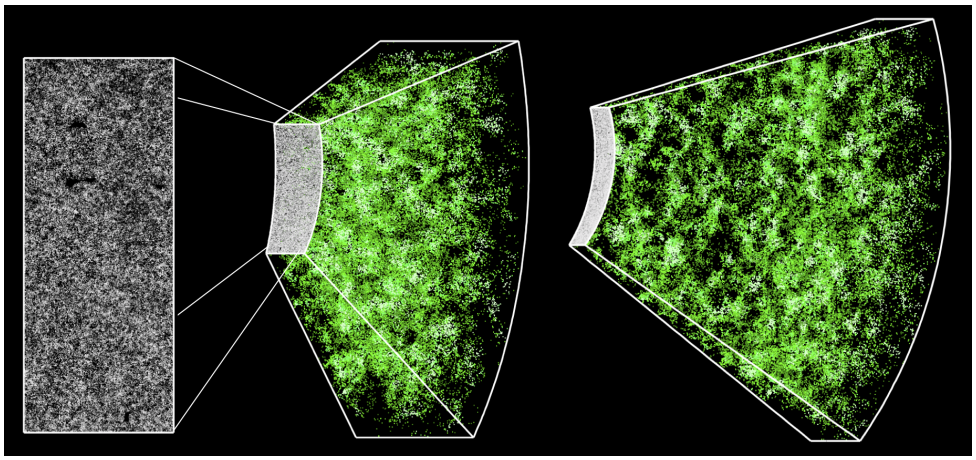

Figure 1.1: 3D map of the Universe from the Baryon Oscillation Spectroscopic Survey of the Sloan Digital Sky Survey-III collaboration [29]. The rectangle on the left shows a cutout of 1000 square degrees in the sky containing nearly 120000 galaxies, consisting of roughly 10% of the total survey.

A *comoving* observer is one which has no motion with respect to the cosmic fluid; in practice, a comoving observer sees the CMB as isotropic, apart from its tiny anisotropies. *Isotropy* means that the space looks the same no matter in what direction we look; in other words, the space has rotational invariance. *Homogeneity* means that the space looks the same at each point, with no dependence on the position; this corresponds to translational invariance. Finally, with "large scales" we refer to distances bigger than about 100 Mpc.[1]

Notice that homogeneity and isotropy are not necessarily related to each other. However, if a space is isotropic around a point and also homogeneous, then it is isotropic around any point. Since we have ample observational evidence for isotropy around us, like the isotropy of the CMB [28] and the isotropy in the statistical properties of clustering of galaxies (see Fig. 1.1), and we assume that we are not in a special place in the Universe (the so-called *Copernican principle*), then it follows that the Universe is homogeneous and isotropic around each point.

1.1.2 Geometry and dynamics of the expanding Universe

As we have already said, we know on very solid observational grounds that our Universe is expanding. Thus, we can say that the Universe is *spatially* homogeneous and isotropic, but it evolves with time. In the language of differential geometry, this translates into the statement that our Universe can be foliated into spacelike slices, such that each three-dimensional slice is a maximally symmetric space. In other words, the spacetime is a four-dimensional manifold $\mathcal{M}_4$ which can be decomposed as $\mathcal{M}_4 = \mathbb{R} \times \Sigma$, where $\mathbb{R}$ represents the time direction and Σ is a maximally symmetric three-manifold. Under this assumption, we can write the metric of the spacetime, known as the Friedmann-Lemaître-Robertson-Walker (FLRW) metric, as

$$ds^2 = -dt^2 + a^2(t)\left[\frac{dr^2}{1-kr^2} + r^2(d\theta^2 + \sin^2\theta d\phi^2)\right], \tag{1.1}$$

where (r, θ, ϕ) are comoving polar coordinates and $a(t)$ is the *scale factor*, which determines proper distances in terms of the comoving coordinates (see Fig. 1.2). Notice that we work in units with $c = 1$. By an appropriate rescaling of the coordinates, k can be set equal to $+1$, -1, or 0 for spaces of constant positive, negative, or vanishing spatial curvature, respectively. Since observations tell us that our (observable) Universe is practically indistinguishable from a Universe with vanishing spatial curvature [6], it is common practice to set $k = 0$. The

[1] We remind the reader that $1\,\text{Mpc} \simeq 3.086 \times 10^{18}\,\text{cm}$.

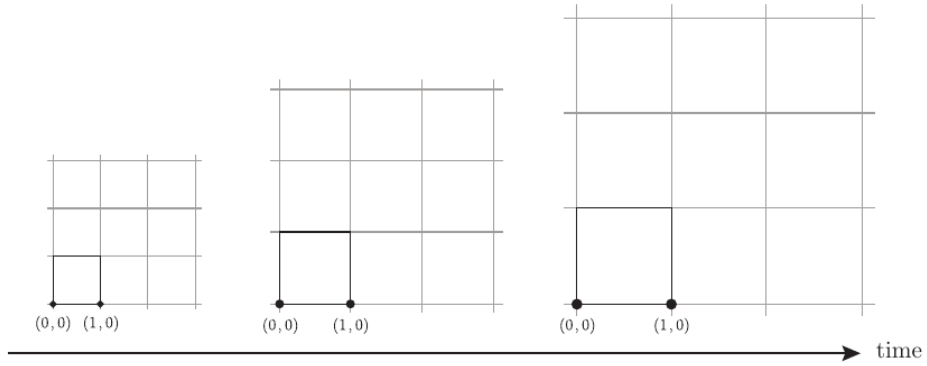

Figure 1.2: The comoving distance between points on an imaginary coordinate grid remains constant as the Universe expands. The physical distance, which is proportional to the comoving distance through the scale factor $a(t)$, gets larger as time evolves. Figure taken from [30].

time coordinate t is called *cosmic time* and represents the proper time measured by comoving observers.

It is also useful to introduce the *conformal time* τ, defined through the relation

$$d\tau = \frac{dt}{a(t)} \,. \tag{1.2}$$

With this change of time coordinate, the flat FLRW metric factorizes into a static Minkowski metric multiplied by the time-dependent conformal factor $a(\tau)$:

$$ds^2 = a^2(\tau) \left[-d\tau^2 + dr^2 + r^2(d\theta^2 + \sin^2\theta d\phi^2) \right] \,. \tag{1.3}$$

The dynamics of the expansion of the Universe is encoded in the time dependence of the scale factor $a(t)$. This can be obtained by solving the Einstein's equations

$$G_{\mu\nu} \equiv R_{\mu\nu} - \frac{1}{2} R g_{\mu\nu} = 8\pi G T_{\mu\nu} \,, \tag{1.4}$$

where G is the Newton constant. On the left hand side we have the Einstein's tensor $G_{\mu\nu}$, which is a measure of the spacetime curvature. It depends on the metric and its first and second derivatives. On the right hand side we find instead the stress-energy tensor $T_{\mu\nu}$, which describes the matter/energy content of the Universe.

To be consistent with the symmetries of the metric, the stress-energy tensor must be diagonal and the spatial components must be equal, due to isotropy. The simplest example is provided by the stress-energy tensor of a perfect fluid, which has the form

$$T^{\mu}{}_{\nu} = (\rho + p) u^{\mu} u_{\nu} + p \delta^{\mu}_{\nu} = \mathrm{diag}(-\rho, p, p, p) \,, \tag{1.5}$$

where ρ is the energy density, p is the pressure, and $u^{\mu} = (1, 0, 0, 0)$ is the four-velocity of the fluid in comoving coordinates, with respect to which the fluid is at rest.

The stress-energy tensor satisfies a continuity equation

$$\nabla_{\mu} T^{\mu\nu} = 0 \,, \tag{1.6}$$

where ∇_{μ} is the covariant derivative. In the case of a perfect fluid, the time component of Eq. (1.6) yields

$$\dot{\rho} = -3H(\rho + p) \,, \tag{1.7}$$

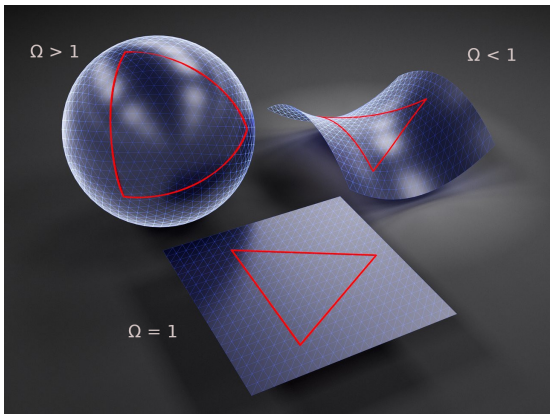

Figure 1.3: The three possible geometries of our Universe in a 2-D analogy. Figure taken from [31].

where $H = \dot{a}/a$ is the Hubble parameter. One usually refers also to Eq. (1.7) as the *continuity equation*.

By specifying the Einstein's equations to the case of a Universe described by a FLRW metric and filled with a perfect fluid, one can obtain (from the 00- and the ii-components of Eq. (1.4)) the so-called *Friedmann equations*:

$$H^2 = \frac{8\pi G}{3}\rho - \frac{k}{a^2}\,, \tag{1.8}$$

$$\frac{\ddot{a}}{a} = -\frac{4\pi G}{3}\left(\rho + 3p\right)\,, \tag{1.9}$$

which are complemented by the continuity equation. However, because of the Bianchi identities, only two among these three equations are actually independent.

As we will soon see, if we know from the continuity equation how the energy density ρ evolves with the scale factor a during a given era, we can integrate the first Friedmann equation (1.8) to obtain the dependence of the scale factor on the cosmic time t. The second Friedmann equation (1.9) then gives us the acceleration of the expansion. We will see that "ordinary components", like radiation and matter, satisfy $\rho + 3p > 0$. From Eq. (1.9) this results in a decelerated expansion of the Universe. A cosmological constant or a slowly-rolling scalar field (which is the simplest realization of an inflationary phase) obey instead $\rho + 3p < 0$, thus leading to an accelerated expansion.

It is also important to notice how the geometry of the Universe is linked to its total energy density. If we define the *critical density*

$$\rho_{\rm crit} = \frac{3H^2}{8\pi G} \tag{1.10}$$

and the dimensionless *density parameter*

$$\Omega \equiv \frac{\rho}{\rho_{\rm crit}}\,, \tag{1.11}$$

the first Friedmann equation can be rewritten as

$$\Omega - 1 = \frac{k}{a^2 H^2}\,. \tag{1.12}$$

Since $a^2H^2 > 0$, it follows that the sign of k is equal to the sign of $\Omega - 1$. In particular, we have:

$$\begin{array}{|lcllcllcl|}
\hline
\rho < \rho_{\rm crit} & \Longleftrightarrow & \Omega < 1 & \Longleftrightarrow & k < 0 & \Longleftrightarrow & \text{open Universe} \\
\rho = \rho_{\rm crit} & \Longleftrightarrow & \Omega = 1 & \Longleftrightarrow & k = 0 & \Longleftrightarrow & \text{flat Universe} \\
\rho > \rho_{\rm crit} & \Longleftrightarrow & \Omega > 1 & \Longleftrightarrow & k > 0 & \Longleftrightarrow & \text{closed Universe} \\
\hline
\end{array} \tag{1.13}$$

This means that the density parameter tells us which of the three possible geometries describes our Universe. This is sketched in Fig. 1.3.

1.1.3 Energy content of the Universe

The Friedmann equations (1.8)-(1.9) represent two independent equations in three variables, $a(t)$, $\rho(t)$ and $p(t)$. This means that we need to introduce a third equation to close the system. This can be done by specifying the equation of state of the cosmic fluid. We assume that the cosmic fluid is described by a barotropic equation of state, which means that the pressure is a function of the energy density only, $p = p(\rho)$. Moreover, we assume this relation to be linear:

$$p = w\rho\,, \tag{1.14}$$

where w is a dimensionless constant. Plugging this ansatz into the continuity equation (1.7), one can readily obtain the evolution of the energy density ρ with the scale factor:

$$\rho \propto a^{-3(1+w)}\,. \tag{1.15}$$

Depending on the value of w, we can classify different sources:

- **Non-relativistic matter**: $w = 0$. In this case $p = 0$, and consequently

  $$\rho \propto a^{-3}\,. \tag{1.16}$$

  This is a simple consequence of the expansion of the Universe, which implies that volumes scale as $V \propto a^3$. This is the case of (non-relativistic) baryonic matter and *Dark Matter*.

- **Radiaton**: $w = 1/3$. In this case $p = \rho/3$, and

  $$\rho \propto a^{-4}\,. \tag{1.17}$$

  This is the case of radiation and, more generally, relativistic particles. In addition to the a^{-3} factor due to the expansion of the Universe there is a contribution due to the redshifting of the energy, $E \propto a^{-1}$.

- **Cosmological Constant**: $w = -1$. In this case $p = -\rho$, and

  $$\rho = \text{const.} \tag{1.18}$$

  Since the energy density is constant, the energy has to increase while the Universe is expanding. More in general, *Dark Energy* has $w < -1/3$. From the second Friedmann equation (1.9), this last condition leads to an accelerated expansion of the Universe, $\ddot{a} > 0$.

Given the evolution of the energy density of these different components, it is easy to convince ourselves that our Universe underwent an early phase during which radiation was the dominant component. After some time, at the *matter-radiation equality*, the energy density of matter became equal to that of radiation and then it became the leading component. More recently in the cosmic history, the Cosmological Constant (or another form of Dark Energy with similar behavior at present time) took the stage, becoming the leading actor in driving the expansion

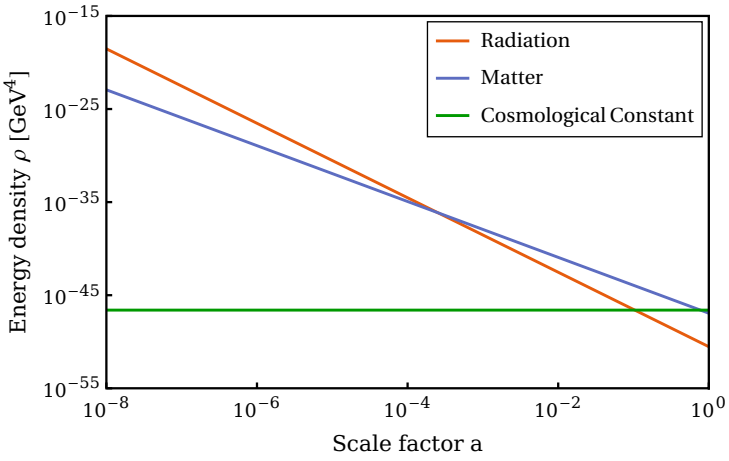

Figure 1.4: Energy density of radiation (red), matter (blue) and cosmological constant (green) as a function of the scale factor of the Universe.

of the Universe. This can be appreciated in Fig. 1.4, where we show the evolution of the energy density of radiation, matter and the cosmological constant as a function of the scale factor.

For a flat Universe, the Friedmann equation (1.8) can be easily integrated together with the continuity equation, allowing us to obtain the time evolution of the scale factor:

$$a(t) \propto \begin{cases} t^{2/3(1+w)} & w \neq -1\,, \\ e^{Ht} & w = -1\,. \end{cases} \tag{1.19}$$

It is then straightforward to determine how the scale factor evolves during the different phases of our Universe:

$$a(t) \propto \begin{cases} t^{1/2} & \text{radiation domination}\,, \\ t^{2/3} & \text{matter domination}\,, \\ e^{Ht} & \text{cosmological constant}\,. \end{cases} \tag{1.20}$$

We summarize the solutions for a flat FLRW Universe dominated by radiation, matter or a cosmological constant in Table 1.1, where we report also the evolution of the scale factor in terms of the conformal time τ.

	w	$\rho(t) \propto$	$a(t) \propto$	$a(\tau) \propto$
RD	1/3	a^{-4}	$t^{1/2}$	τ
MD	0	a^{-3}	$t^{2/3}$	τ^2
Λ	-1	constant	e^{Ht}	$-\tau^{-1}$

Table 1.1: Evolution of the energy density and scale factor for a flat Universe during the epochs dominated by radiation (RD), matter (MD) and the cosmological constant Λ.

1.2 Thermal equilibrium cosmology

Very early in the history of our Universe all the Standard Model particles were in thermal equilibrium with each other. The Universe consisted of a hot and dense plasma of relativistic particles sharing a common temperature T.

The energy density of a particle species of mass m in equilibrium at temperature T is given by

$$\rho = \frac{g}{(2\pi)^3}\int \frac{\sqrt{p^2+m^2}}{\exp\left(\sqrt{p^2+m^2}/T\right)\pm 1} d^3p\,, \tag{1.21}$$

where g is the number of internal degrees of freedom of the species and the sign $+$ $(-)$ is for fermions (bosons). In the relativistic limit $T \gg m$, this reduces to

$$\rho = \frac{\pi^2}{30} g T^4 \times \begin{cases} 1 & \text{bosons}\,, \\ 7/8 & \text{fermions}\,. \end{cases} \tag{1.22}$$

Given the previous equation, and taking into account the fact that different species can have different temperatures T_i if some of them have decoupled from the the cosmological plasma, the total energy density in relativistic species can be written as

$$\rho_{\rm rad} = \frac{\pi^2}{30} g_*(T) T^4\,, \tag{1.23}$$

where g_* is the effective number of relativistic degrees of freedom, defined as

$$g_*(T) = \sum_{i\,=\,\text{bosons}} g_i \left(\frac{T_i}{T}\right)^4 + \frac{7}{8}\sum_{i\,=\,\text{fermions}} g_i \left(\frac{T_i}{T}\right)^4\,. \tag{1.24}$$

Another quantity which is extremely useful to describe the thermal history of the Universe is the entropy S, which is conserved during the adiabatic expansion of the Universe. The total entropy for a set of different particle species is given by

$$S = \frac{2\pi^2}{45} g_{*s}(T) a^3 T^3\,, \tag{1.25}$$

where we have introduced the effective number of degrees of freedom in entropy

$$g_{*s}(T) = \sum_{i\,=\,\text{bosons}} g_i \left(\frac{T_i}{T}\right)^3 + \frac{7}{8}\sum_{i\,=\,\text{fermions}} g_i \left(\frac{T_i}{T}\right)^3\,. \tag{1.26}$$

Notice that, as long as all the particle species are in equilibrium at the same temperature T, $g_*(T) = g_{*s}(T)$. This is true at temperatures $T \gtrsim$ MeV. However, as we will discuss in Section 1.3.2, neutrinos decouple from the cosmological plasma at $T \sim$ MeV. Shortly after that, when the temperature of the Universe drops below the electron mass ($m_e = 0.511$ MeV), electron-positron annihilations take place. As a result, cosmic neutrinos have a slightly lower temperature with respect to the particles in equilibrium with the cosmological plasma, leading to $g_*(T \lesssim m_e) \neq g_{*s}(T \lesssim m_e)$. This can be seen in Fig. 1.5, where g_* and g_{*s} are shown as a function of the temperature T.

1.3 Out-of-equilibrium cosmology

Even though thermal equilibrium holds during most of the expansion history of our Universe, the most relevant events occur when departure from equilibrium takes place. These include the formation of the light elements during Big Bang Nucleosynthesis, the decoupling of neutrinos from the cosmological plasma and recombination of electrons and protons into neutral hydrogen followed by the formation of the Cosmic Microwave Background radiation.[2] In this section we describe in more details all these processes.

[2]Other important events that might be related to a departure from thermal equilibrium are the production of dark matter and the mechanism leading to the baryon asymmetry in the Universe.

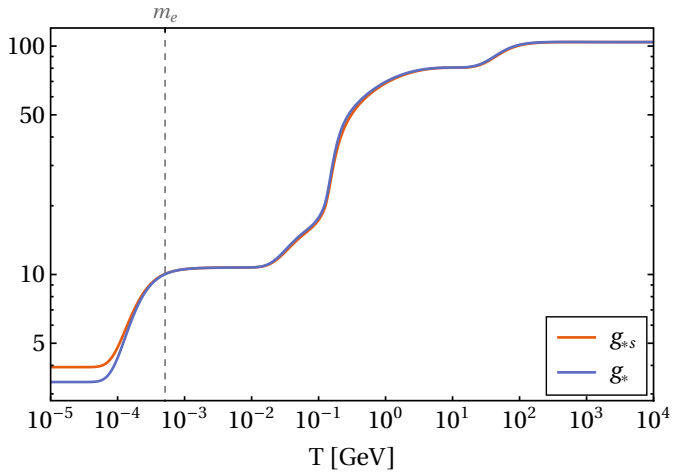

Figure 1.5: Effective number of degrees of freedom in entropy (orange line) g_{*s} and effective number of relativistic degrees of freedom (blue line) g_* in the SM as a function of the temperature of the primordial plasma. These are taken from the analysis of Ref. [32]. The difference between g_* and g_{*s} at low temperatures is due to electron-positron annihilations taking place when the temperature drops below the electron mass, $m_e = 0.511$ MeV, hence leading to $T_{\nu,0} < T_{\gamma,0}$

1.3.1 Big Bang Nucleosynthesis

Big Bang Nucleosynthesis (BBN) is the process during which the first light elements, i.e. deuterium (D), helium (^{3}He and ^{4}He), plus very small amounts of lithium (^{7}Li) and beryllium (^{7}Be), are synthesized in the early Universe. BBN proceeds first via the production of deuterium through the process

$$n + p^+ \longleftrightarrow D + \gamma\,. \tag{1.27}$$

Then, deuterium is converted into ^{3}He and ^{4}He via the reactions

$$D + p^+ \longleftrightarrow {}^3\mathrm{He} + \gamma\,, \tag{1.28}$$

$$D + {}^3\mathrm{He} \longleftrightarrow {}^4\mathrm{He} + p^+\,. \tag{1.29}$$

A key fact is that, given the small value of the *baryon-to-photon ratio*

$$\eta \equiv \frac{n_b}{n_\gamma} \simeq 5.5 \times 10^{-10} \left(\frac{\Omega_b h^2}{0.02}\right)\,, \tag{1.30}$$

production of deuterium is delayed until the temperature of the Universe drops well below the binding energy of deuterium. This is the so-called *deuterium bottleneck*. Deuterium and helium are then produced at $T \sim 0.1$ MeV, but the reaction rates are by now too low to produce any heavier elements in significant amounts. Small fractions of ^{7}Li and ^{7}Be are synthesized, while the production of heavy nuclei is blocked by the absence of stable mass-8 nuclei.

As we will also discuss in Sec. 1.3.2, weak interactions freeze-out at the temperature $T \sim$ MeV. Thus, in order to keep track of the correct neutron abundance, one must resort to a Boltzmann equation (see e.g. [33]). The theoretical predictions for the abundances of D, ^{3}He, ^{4}He and ^{7}Li are shown in Fig. 1.6, together with the observational bounds from WMAP.

Note that the abundance of light elements depends on the baryon-to-photon ratio (1.30) since, as explained above, the value of η determines the time when BBN begins. Therefore, given the measurements of the primordial abundances of light elements, one can constrain the baryon density $\Omega_b h^2$. Using the measurements of the abundances of D and ^{4}He from Refs. [34] and [35], respectively, the following bound has been obtained in [36] (see also [37] for a more recent analysis using updated expressions for nuclear rates):

$$(\Omega_b h^2)_{\mathrm{BBN}} = 0.0227 \pm 0.0005\,. \tag{1.31}$$

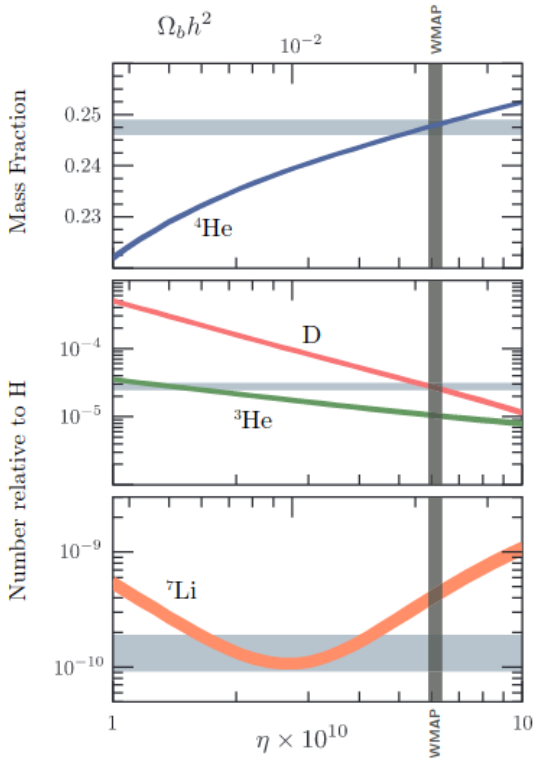

Figure 1.6: Primordial abundances of the light elements as a function of the baryon-to-photon ratio η or, equivalently, the baryon density $\Omega_b h^2$. Figure taken from [38].

Since this value is significantly lower than the total matter density, $\Omega_m h^2 = 0.1432 \pm 0.0013$ [6], the BBN provides a compelling evidence in favor of the existence of a non-baryonic matter component, which is referred to as *dark matter*.

1.3.2 Neutrino decoupling and the Cosmic Neutrino Background

At high temperatures in the early Universe, neutrinos are kept in equilibrium with the cosmological plasma through processes like

$$\begin{aligned} e^+ + e^- &\longleftrightarrow \nu_e + \bar{\nu}_e \,, \\ \nu_e + e^\pm &\longleftrightarrow \nu_e + e^\pm \,, \\ \bar{\nu}_e + e^\pm &\longleftrightarrow \bar{\nu}_e + e^\pm \,. \end{aligned} \tag{1.32}$$

As the Universe expands and cools down, the interaction rate Γ of neutrinos becomes of order of the Hubble expansion rate, H. As a consequence, processes like those in (1.32) become ineffective in keeping neutrinos in equilibrium with the cosmological plasma: this signals the decoupling of neutrinos from the primordial plasma. An estimate of the neutrino decoupling temperature T_d can thus be obtained by imposing the condition

$$\Gamma(T_d) = H(T_d) \,. \tag{1.33}$$

The interaction rate Γ can be written as

$$\Gamma = n\sigma v \,, \tag{1.34}$$

where n is the number density of particles, σ is the interaction cross-section and v is the average velocity of the particles. At temperatures $T > m_e = 0.511$ MeV, the energy density of the

Universe is dominated by the species that are ultra-relativistic (UR), like photons, electrons, positrons and neutrinos. This allows us to make two simplifications: first, the relative velocity can be well approximated with the speed of light, $v \sim 1$; secondly, in the UR limit particle masses can be ignored and, by dimensional analysis, the particle number density can be estimated as $n \sim T^3$.

The only ingredient we miss is the interaction cross-section σ. For interactions mediated by massive gauge bosons (which is the case of electroweak interactions), the cross-section can be written as[3] $\sigma \sim G_X^2 T^2$, where G_X is a (dimensional) constant related to the mass of the gauge boson. In the case of weak interactions, $G_X = G_F \simeq 1.166 \times 10^{-5}\,\mathrm{GeV}^{-2}$ is the Fermi constant. Putting all together, we are left with the following estimate of the interaction rate for weak processes:

$$\Gamma = n\sigma v \sim G_F^2 T^5 \,. \tag{1.35}$$

This has to be compared with the Hubble expansion rate, which, in a radiation-dominated Universe, is roughly given by

$$H \sim \frac{T^2}{M_{Pl}} \,, \tag{1.36}$$

where $M_{Pl} = (8\pi G)^{-1/2} = 2.44 \times 10^{18}\,\mathrm{GeV}$ is the reduced Planck mass. Using Eqs. (1.35)-(1.36) we find

$$\frac{\Gamma}{H} \sim M_{Pl} G_F^2 T^3 \sim \left(\frac{T}{\mathrm{MeV}}\right)^3 \,. \tag{1.37}$$

Therefore, imposing the condition (1.33) we obtain a decoupling temperature for neutrinos $T_d \simeq 1$ MeV.

Since neutrinos decouple while being relativistic, their distribution function maintains the form of a relativistic Fermi-Dirac distribution even at later times, with the neutrino temperature evolving as $T_\nu \propto a^{-1}$. As long as the temperature of cosmic photons evolves in the same way, the two species share the same temperature, $T_\nu = T_\gamma$. However, particle annihilations taking place after neutrino decoupling lead to an increase in T_γ relatively to T_ν, resulting in cosmic neutrinos having a slightly lower temperature today than CMB photons. In particular, shortly after neutrino decoupling ($T \simeq 1$ MeV) the temperature of the Universe drops below the mass of the electron and electron-positron annihilations start taking place:

$$e^+ + e^- \;\longrightarrow\; \gamma + \gamma \,. \tag{1.38}$$

The entropy released by these annihilations gets transferred to the cosmological plasma but not to neutrinos, which are already decoupled from the latter. As a result, the temperature of cosmic photons ($T_\gamma \propto g_{*s}^{-1/3} a^{-1}$) decreases less than the temperature of cosmic neutrinos ($T_\nu \propto a^{-1}$), which are not heated by e^+e^- annihilations. The ratio between the neutrino and photon temperature can be computed imposing the conservation of entropy across the time of electron-positron annihilation:

$$(g_{*s} T^3)|_{T>m_e} = (g_{*s} T^3)|_{T<m_e} \,. \tag{1.39}$$

At temperatures larger than the electron mass, g_{*s} receives contributions from photons, electrons and positrons, whereas at $T < m_e$ only photons are relativistic. Hence

$$g_{*s} = \begin{cases} 2 + 7/8 \times 2 \times 2 = 11/2 & T \gtrsim m_e \\ 2 & T \lesssim m_e \,. \end{cases} \tag{1.40}$$

[3] This is true only at temperatures below the mass of the gauge boson.

Therefore, from Eq. (1.39) we find that the temperatures after ($T_<$) and before ($T_>$) e^+e^- annihilations are related by

$$T_< = \left(\frac{11}{4}\right)^{1/3} T_> \,. \tag{1.41}$$

This can be used to compute the temperature of the *Cosmic Neutrino Background* (CνB) today, which is given by

$$T_{\nu,0} = \left(\frac{4}{11}\right)^{1/3} T_{\gamma,0} \simeq 1.95 \text{ K} \simeq 1.68 \times 10^{-4} \text{ eV} \,, \tag{1.42}$$

where $T_{\gamma,0} \simeq 2.73 \text{ K} \simeq 2.35 \times 10^{-4}$ eV is the current temperature of CMB photons.

The energy density of a single massive neutrino species is

$$\rho_\nu(T_\nu) = \frac{g}{(2\pi)^3} \int \frac{\sqrt{p^2+m^2}}{e^{p/T_\nu}+1} d^3p \,. \tag{1.43}$$

In analogy with Eq. (1.11), we can then define the density parameter for massive neutrinos as

$$\Omega_\nu \equiv \sum_i \frac{\rho_{\nu_i,0}}{\rho_{\text{crit},0}} \,. \tag{1.44}$$

Taking into account the effects of non-instantaneous neutrino decoupling, one finds [39]

$$\Omega_\nu h^2 = \frac{\sum_i m_{\nu,i}}{93.14 \text{ eV}} \,. \tag{1.45}$$

By requiring that neutrinos do not overclose the Universe, i.e. $\Omega_\nu < 1$, Eq. (1.45) allows us to obtain a cosmological upper bound on the sum of the neutrino masses, which reads

$$\sum_i m_{\nu,i} \lesssim 14 \text{ eV} \,. \tag{1.46}$$

This result was first derived by Gerstein and Zel'dovich [40].

To summarize, the standard cosmological model predicts that our Universe is filled with a background of relic thermal neutrinos with density of roughly 113 particles per cm^3 and temperature of 1.95 K.

1.3.3 Hydrogen recombination and the Cosmic Microwave Background radiation

A remarkable event in the thermal history of our Universe is represented by the formation of the first neutral atoms. At high temperatures, the cosmological plasma was composed of photons, free electrons and protons. Photons were interacting via Compton scattering with electrons, which in turn were coupled to protons due to Coulomb interaction. When our Universe became cold enough to allow the formation of neutral atoms (a process which is called *recombination*), the density of free electrons dropped quite abruptly. As a consequence, photons decoupled from matter and started free streaming across the Universe. These photons, which nowadays we are able to observe with both ground and spaced-based satellites, form the so-called *cosmic microwave background* radiation.

To understand when recombination takes place, we need to consider the process

$$e^- + p \longleftrightarrow H + \gamma \,. \tag{1.47}$$

Let's start by introducing the electron ionization fraction

$$X_e \equiv \frac{n_e}{n_b} \,, \tag{1.48}$$

where the baryon density n_b can be written as $n_b \approx n_p + n_H = n_e + n_H$, with the last equality holding due to charge neutrality. At high temperatures the hydrogen is fully ionized, hence $X_e = 1$. As the Universe expands and cools down, more and more electrons combine with protons to form neutral hydrogen, leading to $X_e \ll 1$. The evolution of the ionization fraction X_e can be studied in first approximation by writing down Saha equation, which reads (see e.g. [33, 41])

$$\left(\frac{1-X_e}{X_e^2}\right)_{\rm eq} = \frac{2\zeta(3)}{\pi^2}\eta\left(\frac{2\pi T}{m_e}\right)^{3/2} e^{B_H/T}\,, \tag{1.49}$$

where

$$B_H \equiv m_p + m_e - m_H \simeq 13.6 \text{ eV} \tag{1.50}$$

is the binding energy of hydrogen and η is the baryon-to-photon ratio defined in Eq. (1.30). We can then define the recombination temperature $T_{\rm rec}$ as the temperature at which 90% of the electrons have combined with protons. Imposing the condition $X_e = 0.1$ in Eq. (1.49) leads to

$$T_{\rm rec} \simeq 0.3 \text{ eV}\,. \tag{1.51}$$

Notice that this is much smaller than the hydrogen binding energy. This is due to the huge number of photons for each hydrogen atom (see Eq. (1.30)). Even at temperatures $T \lesssim B_H$, there is a large number of photons in the tail of the distribution having energy $E_\gamma > B_H$, such that any hydrogen atom which is produced is instantaneously photo-ionized. This delays recombination until the temperature of the Universe has dropped enough to make photo-dissociation not efficient anymore.

Shortly after recombination, photons decouple from baryons. Indeed, photons interact with electrons via Thomson scattering

$$e^- + \gamma \longleftrightarrow e^- + \gamma\,, \tag{1.52}$$

with an interaction rate given by

$$\Gamma_T \simeq n_e \sigma_T\,, \tag{1.53}$$

where σ_T is the Thomson cross-section. As the free electron density n_e decreases after recombination, also the interaction rate between photons and electrons drops. Decoupling takes place when the interaction rate becomes of order of the Hubble expansion rate, so that the decoupling temperature $T_{\rm dec}$ is defined by the condition

$$\Gamma_T(T_{\rm dec}) = H(T_{\rm dec})\,. \tag{1.54}$$

From this requirement one obtains

$$T_{\rm dec} \simeq 0.26 \text{ eV}\,. \tag{1.55}$$

Photon decoupling represents the last moment when photons interact with the primordial plasma. This defines the so-called *last scattering surface*.

In order to track the electron density after freeze-out, we need to resort to the Boltzmann equation, which is the key tool to describe processes involving departures from thermal equilibrium. By defining $x \equiv 1/T$, we can write a Botlzmann equation for the ionization fraction as (see e.g. [33, 42])

$$\frac{dX_e}{dx} = -\frac{\lambda}{x^2}\alpha_2 C\left[X_e^2 - (X_e^{\rm EQ})^2\right], \tag{1.56}$$

where $X_e^{\rm EQ}$ is the equilibrium ionization fraction which follows the Saha equation (1.49), α_2 is the thermally-averaged cross-section for recombination from the excited state $n = 2$, $\lambda \equiv n_b/(Hx)$ and C is a correction factor introduced by Peebles [42] (see also [33]).

In Fig. 1.7 we show the numerical solution of the Boltzmann equation (1.56) (solid orange line) together with the solution of the Saha equation (dashed blue line). Notice that the Saha equation is a good enough approximation to trace the ionization fraction around recombination, but it fails in determining the electron density after freeze-out.

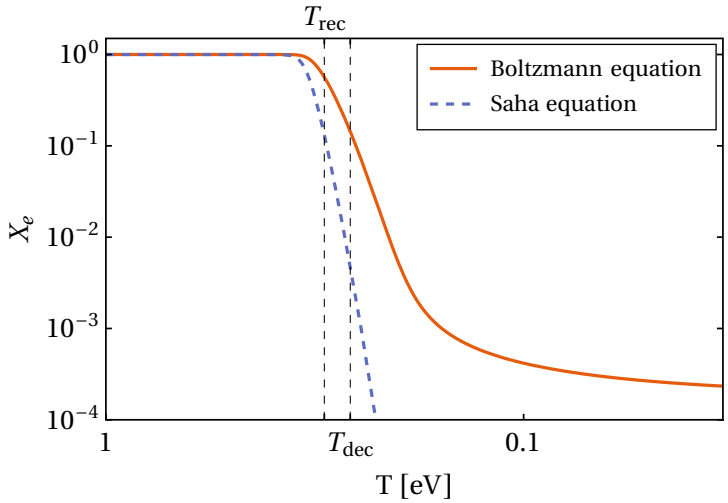

Figure 1.7: Electron ionization fraction obtained solving the Saha (dashed blue line) and Boltzmann equation (solid orange line). The recombination temperature ($T_{\rm rec} \simeq 0.3$ eV) is defined by imposing the condition $X_e = 0.1$ in the Saha equation (1.49), whereas the decoupling temperature ($T_{\rm dec} \simeq 0.26$ eV) is defined by the condition $\Gamma_\gamma(T_{\rm dec}) = H(T_{\rm dec})$, see the main text for more details.

1.4 Thermal history of the Universe

Now that we are equipped with a physical model describing the content and the dynamics of our Universe, we are ready to describe the key events of its thermal history, following the discussion of Sec. 1.3. We know that, going back in time, the Universe becomes hotter and denser. Extrapolating this argument back farther and farther in time, at some point we reach a state of infinite density and temperature, a singularity (which we commonly referred to as the *Big Bang*) that we identify as the initial time, $t = 0$. However, when we go beyond the Planck epoch, $t_{Pl} \sim 10^{-43}$ (corresponding to a temperature $T_{Pl} \sim 10^{19}$ GeV), we enter a regime in which the quantum corrections to our description of the gravitational interaction must be taken into account. Since the ΛCDM model is based on General Relativity, which is a purely classical theory, our description of these early stages of our Universe breaks down. Thus, given that we do not have any successful theory of quantum gravity yet, the first moments of life of our Universe are at the moment highly speculative. Therefore we start our description well after the Planck time.

- **Inflation and reheating**: There are many reasons to believe that our Universe underwent an early phase of accelerated expansion, called *inflation*. The existence of an inflationary phase was initially proposed as a solution to the shortcomings of the standard cosmological model, such as the horizon and the flatness problems. Soon enough it became clear that an inflationary phase can do more than that. Indeed, inflation naturally provides a mechanism to generate the primordial density perturbations, which are the seeds for the following formation of the Large-Scale Structures and which can be observed through the temperature anisotropies in the CMB. Inflation ended with the so-called *reheating* phase, after which the standard radiaton era started.

- **Baryogenesis**: we have a great number of evidence that our Universe is (almost) entirely composed of matter, with no antimatter. This fact, which might seem obvious at first sight, is instead surprising from a particle physics perspective. Indeed, the CPT theorem (valid for each local, relativistic quantum field theory) tells us that for any particle species there exists a corresponding antiparticle with the same mass, decay width and opposite charge. Thus, we would expect the Universe to be symmetric with respect to the content of

matter and antimatter. Since particles and their respective antiparticles annhilate between themselves, if the Universe was initially filled with equal amounts of matter and antimatter, these annihilations would have led to a Universe dominated by radiation. This means that we need to introduce in the early Universe some mechanism that generates dinamically a baryon asymmetry starting from an initial symmetric state. This is called *baryogenesis*. Although many models for baryogenesis exist, currently there are no experimental evidence in favor of any of them.

- **Electroweak phase transition**: at a temperature $T \sim 100$ GeV the electroweak phase transitions occured and particles obtained their masses through the Higgs mecchanism. The symmetry $SU(2)_L \otimes U(1)_Y$ of the electroweak interaction was broken to $U(1)_{EM}$ and the weak interaction became short-range, since the gauge bosons $W^{\pm}$ and Z^0 became massive ($m_W \simeq 80$ GeV, $m_Z \simeq 91$ GeV). We will describe this mechanism more in detail in the next chapter.

- **QCD phase transition**: at $T \sim 100$ MeV a second phase transition occurred, namely the QCD phase transition. After that, quarks were not "free" anymore, but formed bound states of (color singlet) quarks triplets, called *baryons*, and quark-antiquark states, called *mesons*.

- **Neutrino decoupling**: at $T \sim 1$ MeV, the interaction rate of neutrinos became of order of the expansion rate H. As a consequence, neutrinos decoupled from the primordial plasma and from there on they freely-streamed through the Universe.

- **Big Bang Nucleosynthesis**: at $T \sim 0.1$ MeV, soon after neutrino decoupling, the light elements (^{1}H, ^{4}He, with small amounts of ^{2}H and ^{3}He, and with a tiny component of ^{7}Li) were formed. This process is known as *Big Bang Nucleosynthesis* (BBN).

- **Electron-positron annihilation**: at $T \sim 511$ KeV electrons and positrons became non relativistic, hence their abundance dropped due to the annihilation process $e^+e^- \to 2\gamma$. Indeed, the energy of the thermal bath was not sufficient anymore to allow the production of e^-e^+ couples via the inverse process from photons. The energy coming from these annihlations was then transferred to the thermal plasma, but not to neutrinos, which were already decoupled. As a consequence, the temperature of the neutrino background today ($T_{\nu,0} \simeq 1.95$ K) is expected to be lower than the corresponding temperature of the photons ($T_{\gamma,0} \simeq 2.73$ K).

- **Radiation-matter equality**: at $T \sim 0.75$ eV the energy density of matter became equal to that of radiation: this epoch is usually referred to as *matter-radiation equality*. After that, the matter-dominated era started.

- **Recombination**: at $T \sim 0.3$ eV electrons and nuclei became bound to form the first neutral atoms through the process $e^- + p \to H + \gamma$. This is called *recombination* (even though they actually combined for the first time).

- **Photon decoupling**: soon after recombination ($T \sim 0.26$ eV), photons decoupled from the primordial plasma and started free-streaming across the Universe. Today we can observe them as a background radiation, the so-called *Cosmic Microwave background* (CMB) radiation, with a temperature $T_{\gamma,0} \simeq 2.73$ K. The energy density they had at the time of decoupling has indeed been red-shifted due to the expansion of the Universe.

- **Structure formation**: much later, the primordial perturbations generated during inflation grew via gravitational instability to form the structures we can observe today.

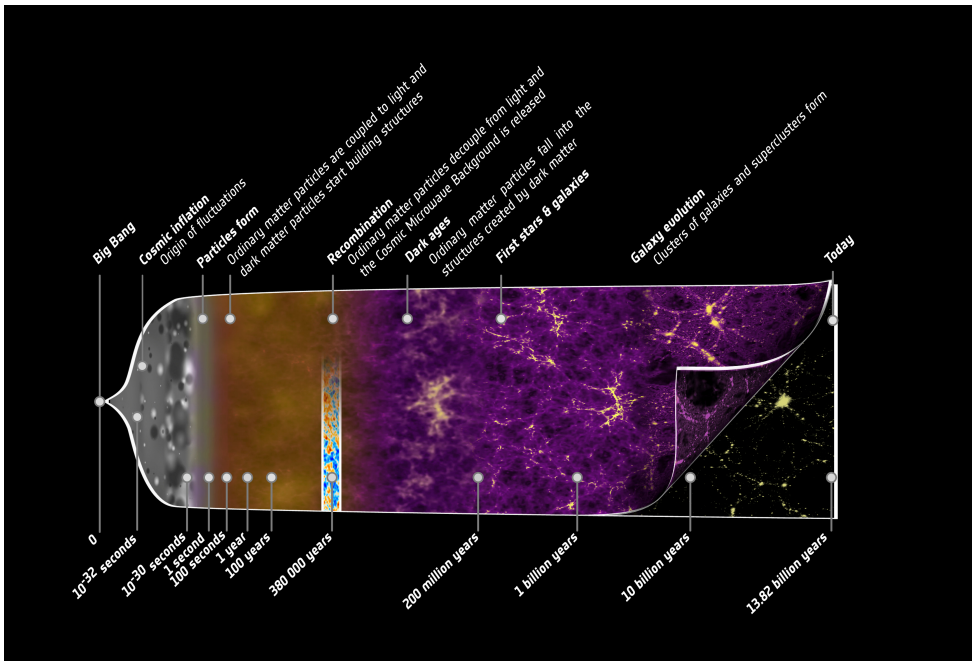

Figure 1.8: Thermal history of our Univers. Figure taken from [43].

A sketch of the thermal history just described is shown in Fig. 1.8. In the following subsections we will provide more details about three of the most important events in the history of our Universe: the BBN, the decoupling of neutrinos from the cosmological plasma, and recombination, which is followed by the decoupling of photons from matter and the formation of the CMB.

1.5 The Hot Big Bang shortcomings and the inflationary solutions

The Friedmann equations introduced in Sec. 1.1.2 allow to predict the evolution of the Universe given some initial conditions. We will now see that the standard cosmological model requires very fine-tuned initial conditions to allow the Universe to evolve to its current state: these are known as the horizon and flatness problems. This leads to the introduction of *inflation*, a phase of accelerated expansion of the Universe taking place before the standard radiation era. As we will discuss, inflation naturally solves these shortcomings of the Hot Big Bang model, providing a dynamical mechanism that brings the Universe towards these initial conditions when the standard radiation era begins.

1.5.1 The horizon problem

In order to describe the horizon problem, we first need to define some crucial quantities. Let's start introducing the *comoving particle horizon*, which is the comoving distance travelled by light from the beginning of the Universe ($t = 0$) until the time t. This is defined as

$$\tau \equiv \int_0^t \frac{dt'}{a(t')} = \int_0^{a(t)} d\ln a \left(\frac{1}{aH}\right) . \tag{1.57}$$

Thus, it is the logarithmic integral of the *comoving Hubble radius*, $r_H = (aH)^{-1}$, which quantifies the distance travelled by light in a Hubble time, H^{-1}. This means that, in order to obtain τ, we

need to integrate r_H over the past interactions. For a radiation-dominated (RD) and matter-dominated (MD) Universe, we find

$$\tau \propto r_H \propto \begin{cases} a & \text{RD}\,, \\ a^{1/2} & \text{MD}\,. \end{cases} \tag{1.58}$$

Note that the comoving horizon grows monotonically with time both in a Universe dominated by radiation and by matter. This implies that comoving scales entering the horizon today have been far outside the horizon in the past. In particular, the last scattering surface is made of several independent patches that had never been causally connected. However, the CMB sky appears extremely isotropic, implying that the Universe was extremely homogeneous at the time of last-scattering, even on scales made of many causally disconnected regions. How is this possible? This represents the so-called *horizon problem*.

A possible solution to the horizon problem is suggested by a deeper inspection to Eq. (1.57). The fact that r_H is an increasing function of time in FLRW models implies that τ is dominated by the contributions coming from late times. This means that, as we have already said, at every instant of time new regions that have never been in causal contact before come into contact for the first time. However, if τ could be much greater than r_H now, this would mean that particles which cannot communicate today were instead in causal contact in the past. This happens if the comoving Hubble radius was in the past much greater than it is now, so that τ gets most of its contributions from early times. This leads us to assume that the early Universe, before the standard FLRW phases dominated by radiation and matter, underwent a phase during which the comoving Hubble radius was a decreasing function of time. Particles separated by many Hubble radii today were instead in causal contact during this stage. The condition of decreasing comoving Hubble radius means that

$$\frac{d}{dt}\left(\frac{1}{aH}\right) = -\frac{\ddot{a}}{\dot{a}^2} < 0 \;\Leftrightarrow\; \ddot{a} > 0\,. \tag{1.59}$$

Therefore, a decreasing comoving Hubble radius requires a phase of accelerated expansion, which is called *inflation*. Using Eq. (1.9), this can be translated into a condition on the equation of state of the energy/matter giving rise to the inflationary phase:

$$p < -\frac{1}{3}\rho\,. \tag{1.60}$$

This means that we need a negative pressure to realize an inflationary phase.

1.5.2 The flatness problem

The second of the shortcomings of the Hot Big Bang model is the so-called *flatness problem*. To understand what it concerns, let's rewrite the Friedmann equation (1.8) as

$$|\Omega(t) - 1| = \frac{|k|}{a^2 H^2} = |k|\, r_H^2(t)\,. \tag{1.61}$$

Since in standard cosmology the comoving Hubble radius r_H grows with time, it follows that the departure of $\Omega(t)$ from unity also increases with time and it must eventually diverge. In other words, $\Omega = 1$ is an unstable point. A small deviation of Ω from unity in the early Universe leads to a Universe rapidly recollapsing (in the case of a close geometry), or too rapidly expanding, resulting in an empty Universe in which gravity does not succeed in forming structures (in the case of an open geometry). This requires an extreme fine-tuning of the value of Ω, which must be incredibly close to 1 in the early Universe. In particular, from the observed value of Ω today [6]

$$|\Omega(t_0) - 1| = 0.001 \pm 0.002 \quad (68\%\ \text{CL})\,, \tag{1.62}$$

it is possible to show that the deviation from $\Omega = 1$ at the Planck epoch and at the epoch of BBN must be given respectively by

$$|\Omega(t_{Pl}) - 1| \lesssim 10^{-64}\,, \tag{1.63}$$

$$|\Omega(t_{\rm BBN}) - 1| \lesssim 10^{-16}\,. \tag{1.64}$$

While this extreme fine-tuning of the value of Ω in the early Universe has no explanation and must be assumed in standard FLRW models, inflation provides a natural solution to the problem. Indeed, during the inflationary phase the comoving Hubble radius r_H decreases with time, so that

$$|\Omega(t) - 1| \propto e^{-2Ht}\,. \tag{1.65}$$

This means that, independently of the initial value of Ω, a (long enough) inflationary phase drives naturally its value towards unity before the radiation era begins, thus solving the flatness problem.

We want to stress that inflation does not change the *global* geometry of the spacetime. If the Universe is flat, closed or open, the spatial geometry stays the same with or without inflation. Inflation only increases the radius of curvature, so that *locally* (i.e. in our observable patch) the Universe looks flat with a great precision.

1.5.3 The "unwanted relics" problem

We briefly mention another problem of the standard cosmological model which is successfully solved by inflation. Historically, this is the problem that initially led to the introduction of the inflationary paradigm.

It is likely that the early Universe underwent a series of phase transitions which, depending on the broken symmetries, may have produced different topological defects like domain walls, monopoles and cosmic strings. If produced, it is easy to show that their energy density tends to become the dominant one in the Universe, leading to $\Omega_{TD} \gg 1$. This is obviously in contrast with observations, which tell us that $\Omega_{\rm tot} \simeq 1$.

Inflation naturally solves also this problem, since the accelerated expansion strongly dilutes the energy density contribution of these topological defects.

1.6 Single-field slow-roll inflation

We have seen that inflation is a phase of accelerated expansion sourced by a negative pressure, $w = p/\rho < -1/3$. The simplest way to realize such an inflationary phase is through a cosmological constant Λ, which is characterized by an equation of state with $w = -1$. As we can see from Eq. (1.20), if the energy density of the Universe is dominated by Λ, the Universe undergoes a phase during which the scale factor grows exponentially with time, $a(t) \propto e^{Ht}$. This is know as a *de Sitter phase*. The problem with this realization is that a cosmological constant does not provide any mechanism through which inflation ends, and the exponential expansion never stops. However, we know that our Universe went through a long period of decelerated expansion, when first radiation and then matter dominated its energy content. During such phases, the primordial perturbations generated during inflation re-entered the horizon to give rise, via gravitational instability, to the structures we can observe today. This can not happen in a Universe undergoing a never-ending exponential expansion. Moreover, this expansion history is supported by other important evidence, like the CMB and BBN. For these reasons we need to introduce some kind of "clock", which regulates the amount of inflation and controls its end. This can be simply realized by a slowly-rolling scalar field.

Let us consider a scalar field, which we call the *inflaton*, and slightly tilt (with respect to a constant value) the potential under which the field evolves. If the potential is sufficiently flat,

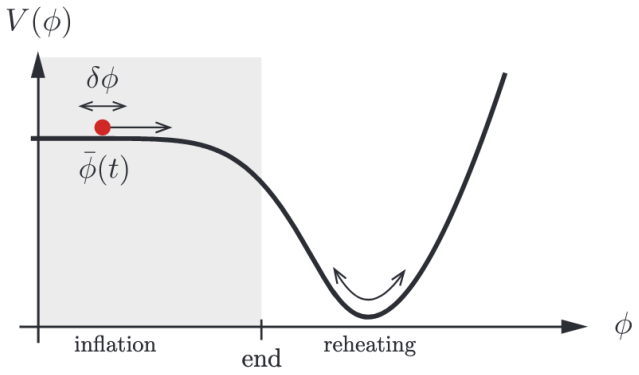

Figure 1.9: Slow-roll potential for the inflaton field. Figure taken from [30].

the scalar field can mimic an effective cosmological constant and drives inflation. Then, inflation could be ended by adding some mechanism triggered by some particular value of the field. In the case of the potential in Fig. 1.9, when the potential is no longer flat and the inflaton approaches the minimum, it begins to oscillate and then decays into ultra-relativistic particles. This phase is called *reheating*. After that, the standard radiation era begins.

The dynamics of a scalar field minimally coupled to gravity is encoded in the action

$$S = S_{EH} + S_\phi = \int d^4x\sqrt{-g}\left[\frac{M_{Pl}^2}{2}R - \frac{1}{2}g^{\mu\nu}\partial_\mu\phi\partial_\nu\phi - V(\phi)\right], \tag{1.66}$$

where $M_{Pl} \equiv (8\pi G)^{-1/2}$ is the reduced Planck mass, $g = \det(g_{\mu\nu})$ is the determinant of the metric tensor and $V(\phi)$ is the potential for the scalar field. The first term is the Einstein-Hilbert action, while the second term describes a scalar field minimally coupled to gravity through the metric $g_{\mu\nu}$. Varying this action with respect to ϕ yields the Klein-Gordon equation for the scalar field

$$\Box\phi \equiv \frac{1}{\sqrt{-g}}\partial_\nu\left(\sqrt{-g}g^{\mu\nu}\partial_\mu\phi\right) = V'(\phi)\,, \tag{1.67}$$

where $V'(\phi) = \partial V/\partial\phi$. In the case of a Universe described by a FLRW metric, this becomes

$$\ddot{\phi} + 3H\dot{\phi} - \frac{\nabla^2\phi}{a^2} + V'(\phi) = 0\,. \tag{1.68}$$

Note in particular the presence of a friction term $\propto \dot{\phi}$ which is due to the expansion of the Universe (indeed, it vanishes if $a(t) = \text{const}$). One can then compute the stress-energy tensor of the scalar field, which is given by

$$T_{\mu\nu} \equiv -\frac{2}{\sqrt{-g}}\frac{\delta S}{\delta g^{\mu\nu}} = \partial_\mu\phi\,\partial_\nu\phi + g_{\mu\nu}\left(-\frac{1}{2}g^{\alpha\beta}\partial_\alpha\phi\partial_\beta\phi - V(\phi)\right). \tag{1.69}$$

The inflaton field can be split as

$$\phi(\mathbf{x}, t) = \phi_0(t) + \delta\phi(\mathbf{x}, t)\,, \tag{1.70}$$

where $\phi_0(t)$ is the "classical" value of the field, i.e. its vacuum expectation value on the initial homogeneous and isotropic state, $\phi_0(t) = \langle\phi(\mathbf{x}, t)\rangle$, and $\delta\phi(\mathbf{x}, t)$ are the quantum fluctuations around it. For the moment we focus on the background dynamics of the classical field. In Sec. 1.7 we will discuss about the perturbations on top of this background solution. The components of the stress-energy tensor then become

$$T^0{}_0 = -\left[\frac{1}{2}\dot{\phi}_0^2 + V(\phi_0)\right], \quad T^i{}_j = \frac{1}{2}\dot{\phi}_0^2 - V(\phi_0)\,. \tag{1.71}$$

This corresponds to the stress-energy tensor of perfect fluid with energy density and pressure given by[4]

$$\rho_{\phi_0} = \frac{1}{2}\dot{\phi}_0^2 + V(\phi_0)\,, \tag{1.74}$$

$$p_{\phi_0} = \frac{1}{2}\dot{\phi}_0^2 - V(\phi_0)\,. \tag{1.75}$$

Therefore, the equation of state for the scalar field can be written as

$$w_{\phi_0} = \frac{p_{\phi_0}}{\rho_{\phi_0}} = \frac{\dot{\phi}_0^2/2 - V(\phi_0)}{\dot{\phi}_0^2/2 + V(\phi_0)}\,. \tag{1.76}$$

Now notice that, if the potential term dominates over the kinetic one, i.e.

$$\frac{1}{2}\dot{\phi}_0^2 \ll V(\phi_0)\,, \tag{1.77}$$

the equation of state reduces to $w_{\phi_0} \simeq -1$ and the Universe undergoes a *quasi-de Sitter phase*, $a(t) \simeq a_i e^{Ht}$. The condition (1.77) is known as the *slow-roll condition*.

Note also that, if before the flat plateau characterizing the slow-roll phase the Universe starts kinetic energy dominated, from Eq. (1.76) it follows that $w_{\phi_0} \simeq 1$. Then, from the continuity equation, we have that

$$\rho_{\phi_0} \propto a^{-3(1+w_{\phi_0})} \propto a^{-6}\,. \tag{1.78}$$

This means that the kinetic energy of the inflaton field gets redshifted away quickly, and the potential energy starts dominating. In this sense inflation is a dynamical attractor solution.

To formalize more precisely the slow-roll approximations, let us rewrite the equation of motion for the (homogeneous) scalar field and the first Friedmann equation as

$$\ddot{\phi}_0 + 3H\dot{\phi}_0 + V'(\phi_0) = 0\,, \tag{1.79}$$

$$3M_{Pl}^2 H^2 = \frac{1}{2}\phi_0^2 + V(\phi_0)\,. \tag{1.80}$$

The slow-roll approximation consists in requiring that the potential term dominates over the kinetic term and that the potential is sufficiently flat so that the acceleration of the field is negligible:

$$\frac{1}{2}\dot{\phi}_0^2 \ll V(\phi_0)\,, \quad |\ddot{\phi}_0| \ll |3H\dot{\phi}_0|\,. \tag{1.81}$$

The first condition leads to an inflationary phase since it implies that $w_{\phi_0} \simeq -1$, as we have already seen. The second condition requires $\dot{\phi}_0$ to change slowly such that the first condition can be satisfied for a long enough time. This corresponds to the attractor solution in which the friction force balances the external force provided by the potential, so that the acceleration of the field is nearly equal to zero.

With these two conditions, we can rewrite Eqs. (1.80) and (1.79) respectively as

$$H \simeq \sqrt{\frac{V}{3M_{Pl}^2}}\,, \tag{1.82}$$

[4]If we include also the inhomogeneities in the scalar field, we get:

$$\rho_\phi = \frac{1}{2}\dot{\phi}^2 + V(\phi) + \frac{1}{2}\frac{(\nabla\phi)^2}{a^2}\,, \tag{1.72}$$

$$p_\phi = \frac{1}{2}\dot{\phi}^2 - V(\phi) - \frac{1}{6}\frac{(\nabla\phi)^2}{a^2}\,. \tag{1.73}$$

The inflationary expansion smooths out the spatial variations, since $a^{-2} \propto e^{-2Ht}$. Thus, this term becomes quickly subdominant and the two previous expressions for ρ_ϕ and p_ϕ reduce to (1.74) and (1.75).

$$\dot{\phi}_0 \simeq -\frac{V'}{3H}\,. \tag{1.83}$$

These can be used to translate the conditions (1.81) into two conditions for the potential of the inflaton field. Let us first define the so-called *potential slow-roll parameters*:

$$\epsilon \equiv \frac{M_{Pl}^2}{2}\left(\frac{V'}{V}\right)^2 \simeq \frac{1}{2}\frac{\dot{\phi}_0^2}{H^2 M_{Pl}^2}\,, \tag{1.84}$$

$$\eta \equiv M_{Pl}^2\frac{V''}{V} \simeq -\frac{\ddot{\phi}_0}{\dot{\phi}_0 H} + \frac{1}{2}\frac{\dot{\phi}_0^2}{M_{Pl}^2 H^2}\,. \tag{1.85}$$

The slow-roll conditions can now be written as

$$\epsilon \ll 1, \quad |\eta| \ll 1\,. \tag{1.86}$$

At leading order in the slow-roll parameters, ϵ and η can be considered constant, since

$$\frac{\dot{\epsilon}}{H} = \mathcal{O}(\epsilon^2, \eta^2)\,, \quad \frac{\dot{\eta}}{H} = \mathcal{O}(\epsilon^2, \eta^2)\,. \tag{1.87}$$

We can also introduce another set of slow-roll parameters, which are not directly related to the shape of the potential, but rather to the dynamics of the scale factor:

$$\epsilon_H \equiv -\frac{\dot{H}}{H^2} = \frac{\dot{\phi}_0^2}{2H^2 M_{Pl}^2}\,, \tag{1.88}$$

$$\eta_H \equiv \frac{\dot{\epsilon}}{\epsilon H} = 2\epsilon + 2\frac{\ddot{\phi}_0}{H\dot{\phi}_0}\,. \tag{1.89}$$

These are called *Hubble slow-roll parameters*. The condition $\epsilon_H \ll 1$ requires the energy driving inflation to be dominated by the potential, exactly as the first of (1.86). The condition $|\eta_H| \ll 1$ requires that

$$\frac{\ddot{\phi}_0}{H\dot{\phi}_0} = -\epsilon_H + \frac{\eta_H}{2} \ll 1\,. \tag{1.90}$$

Analogously to the second condition in (1.86), this tells us that the (background) evolution of the inflaton is determined by the attractor solution in Eq. (1.83).

When the slow-roll conditions (1.86) are satisfied, the relations between the two sets of slow-roll parameters are

$$\epsilon_H = \epsilon + \mathcal{O}\left(\epsilon^2, \eta^2\right), \quad \eta_H = 4\epsilon - 2\eta + \mathcal{O}\left(\epsilon^2, \eta^2\right)\,. \tag{1.91}$$

The conditions defined through the Hubble slow-roll parameters ϵ_H and η_H are more general than the ones defined through ϵ and η. Indeed in some cases, while the first ones are still necessary to ensure a prolonged enough inflationary phase, the conditions on ϵ and η might not be satisfied anymore. To give some examples, the shape of the potential could be steeper, therefore not satisfying the first of (1.81), or the inflationary energy could be dominated by the kinetic energy, rather than by the potential.

Note that ϵ_H can also be regarded as a parameter that characterizes the departure from an exact de Sitter phase, in which H is constant and therefore $\epsilon_H = 0$. In particular

$$\ddot{a} = \frac{d}{dt}(aH) = a(H^2 + \dot{H}) = aH^2(1 - \epsilon_H)\,. \tag{1.92}$$

An accelerated expansion with $\ddot{a} > 0$ requires $\epsilon_H < 1$. Inflation ends when $\epsilon_H \sim 1$, namely when the inflaton starts approaching the potential well.

1.7 The primordial perturbations from inflation

In Sec. 1.5 we have seen how introducing an inflationary phase in the early Universe solves the shortcomings of the standard cosmological model. Soon enough it became clear that an inflationary phase can do more than that. Indeed, the most important feature of inflation, which makes it a *predictive* theory, is that it naturally provides a mechanism to generate the primordial density perturbations in the Universe, which are the seeds for the following formation of the Large-Scale Structures and which can be observed through the temperature and polarization anisotropies in the CMB. These are an immediate consequence of introducing quantum mechanics into the game. Indeed, the quantum fluctuations of the inflaton field are stretched outside the horizon by the exponential expansion. As a result, the amplitude of the fluctuations is "frozen" at a non-zero value, since no causal process can act anymore. These fluctuations of the scalar field induce fluctuations in the energy density and hence in the curvature, which, after the fluctuations reenter the horizon during the radiation or matter era, give rise to matter and temperature perturbations through the Poisson equation.

Moreover, inflation also leads to the production of a stochastic background of primordial gravitational waves (PGWs), i.e. transverse and traceless tensor perturbations of the metric. PGWs are the "smoking gun" of inflation. Indeed, they are a key and general prediction of all inflationary models, while alternative models to inflation typically predict an extremely small amplitude of PGWs, practically unobservable. Thus, if observed, PGWs would represent a strong evidence in support of the inflationary paradigm.

The primordial fluctuations can be characterized by a dimensionless power spectrum. For a perturbation field δ, the dimensionless power spectrum $\Delta_\delta(k)$ quantifies the contribution to the variance of δ per unit logarithmic interval in the wavenumber k. In the following we discuss the predictions for the power spectra of scalar and tensor perturbations in single-field slow-roll models of inflation.

1.7.1 Power spectrum of scalar perturbations

For scalar perturbations, it is common to introduce the so-called *curvature perturbation on uniform energy-density hypersurfaces*, ζ. At linear order, this is related to the perturbation of the inflation field $\delta\phi$ by

$$\zeta = -H\frac{\delta\phi}{\dot{\phi}_0}\,. \tag{1.93}$$

This is a gauge invariant quantity which is conserved on super-horizon scales [44].

At leading order in slow-roll parameters, the dimensionless power spectrum of scalar perturbations reads

$$\Delta_\zeta(k) = A_s(k_*)\left(\frac{k}{k_*}\right)^{n_s-1}\,, \tag{1.94}$$

where

$$A_s(k_*) = \frac{H_*^2}{8\pi^2 M_{Pl}^2\epsilon_*} \tag{1.95}$$

is the amplitude of scalar fluctuations at the pivot scale k_* and n_s is the scalar spectral index. This is given in terms of the slow-roll parameters by

$$n_s - 1 = 2\eta - 6\epsilon\,. \tag{1.96}$$

Since in slow-roll inflation ϵ and $|\eta|$ are $\ll 1$, the spectral index predicted by slow-roll inflationary models is slightly lower than unity. This corresponds to an almost scale-invariant, *red spectrum* ($n_s < 1$), where the amplitude of the fluctuations slightly decreases for decreasing cosmological scales. This feature can be understood in the following way. We know that different modes

leave the horizon at different times and after that they are frozen on super-horizon scales. The amplitude of the fluctuation of a given mode k is roughly given by the Hubble parameter H at the corresponding horizon-crossing time. Since the Hubble parameter is weakly decreasing during slow-roll infation, the longest modes, which leave the horizon before the shortest ones, have a slightly higher amplitude of fluctuations. On the other hand, in an exact de Sitter phase the Hubble parameter is constant, hence the amplitude of the fluctuations is the same for each mode. This leads to an Harrison-Zel'dovich power spectrum.

1.7.2 Power spectrum of tensor perturbations

With a similar mechanism to that just seen for scalar perturbations, inflation generates also transverse and traceless tensor perturbations of the metric, namely gravitational waves. This is a common prediction of all inflationary models. Remarkably, the amplitude of primordial gravitational waves (PGWs) in single-field slow-roll models is uniquely determined by the Hubble parameter H during inflation. This means that a measurement of the spectrum of PGWs would give direct information about the most important inflationary parameter, namely the energy scale at which inflation occurred.

Analogously to the case of scalar perturbations, the dimensionless power spectrum of primordial tensor modes can be written in terms of an amplitude $A_T(k_*)$ and a spectral index n_T as

$$\Delta_T(k) = A_T(k_*) \left(\frac{k}{k_*}\right)^{n_T} , \tag{1.97}$$

where

$$A_T(k_*) = \frac{2H_*^2}{\pi^2 M_{Pl}^2} \tag{1.98}$$

and

$$n_T = -2\epsilon \, . \tag{1.99}$$

Eq. (1.99) tells us that single-field slow-roll inflationary models predict an almost scale-invariant, red-tilted (i.e. $n_T < 0$) spectrum of PGWs, analogously to the case of scalar perturbations. Notice that the amplitude of tensor modes depends on the value of the Hubble parameter during inflation only. Thus, if measured, primordial tensor modes would give us direct information about the energy scale of inflation. Indeed, from Eqs. (1.98) and (1.82), we have that

$$A_T(k_*) \propto H_*^2 \propto V_* \, , \tag{1.100}$$

where V_* is the energy scale of inflation when the pivot scale leaves the horizon.

We can then define the *tensor-to-scalar ratio*

$$r(k_*) \equiv \frac{A_T(k_*)}{A_s(k_*)} \, , \tag{1.101}$$

which is a measure of the amplitude of tensor perturbations with respect to that of scalar perturbations at the pivot scale k_*. The tensor-to-scalar ratio can be directly related to the slow-roll parameter ϵ. Indeed, it is easy to show that

$$r = 16\epsilon \, . \tag{1.102}$$

This relation tells us that single field slow-roll inflationary models produce gravitational waves with an amplitude that is much smaller than the amplitude of scalar perturbations. Combining this result with the expression of the tensor tilt given in Eq. (1.99), one obtains the so-called *consistency relation*

$$r = -8n_T \, , \tag{1.103}$$

which relates the amplitude of tensor perturbations to the tensor spectral index.

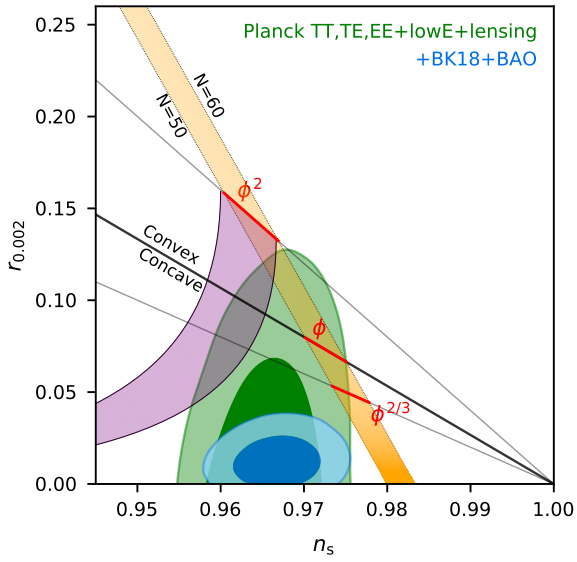

Figure 1.10: Constraints in the $r - n_s$ from *Planck* data and in combination with BICEP/Keck and BAO data [8]. In purple, it is shown the region where natural inflation models lie.

1.7.3 Observational bounds

Observations of the CMB anisotropies and Baryon Acoustic Oscillations (BAO) (see Sec. 1.8.4) allow us to put stringent constraints on inflationary models. In particular, the latest *Planck* data release bounds the scalar spectral index to [45]

$$n_s = 0.9649 \pm 0.0042 \tag{1.104}$$

at 68% CL. This rules out the possibility of having a scale-invariant (Harrison-Zel'dovich) spectrum of scalar perturbations. As we have already discussed, this is consistent with slow-roll models. The Planck 95% CL upper limit on the tensor-to-scalar ratio is [45]

$$r_{0.002} < 0.10\,. \tag{1.105}$$

This is tightened when *Planck* data are combined with those from BICEP/Keck 2018 (BK18) and BAO to obtain [8]

$$r_{0.005} < 0.036\,. \tag{1.106}$$

Figure 1.10 shows the constraints in the $r - n_s$ plane from the measurements made by the *Planck* satellite [45] and in combination with the BK18 and BAO data [8]. With the addition of BK18 data, the $\phi^{2/3}$ model now lies outside the 95% contour, as does the region of natural inflation models, shown in purple in Fig. 1.10. These observations favour the so-called *small-field* models of inflation, which have concave potentials with $V''(\phi) < 0$ (resulting in $\eta_V < 0$) and predict a small amplitude of primordial gavitational waves.

1.8 Cosmological observables

In the following subsections we will describe the main cosmological observables that will be used in this Thesis as probes to test fundamental physics scenarios.

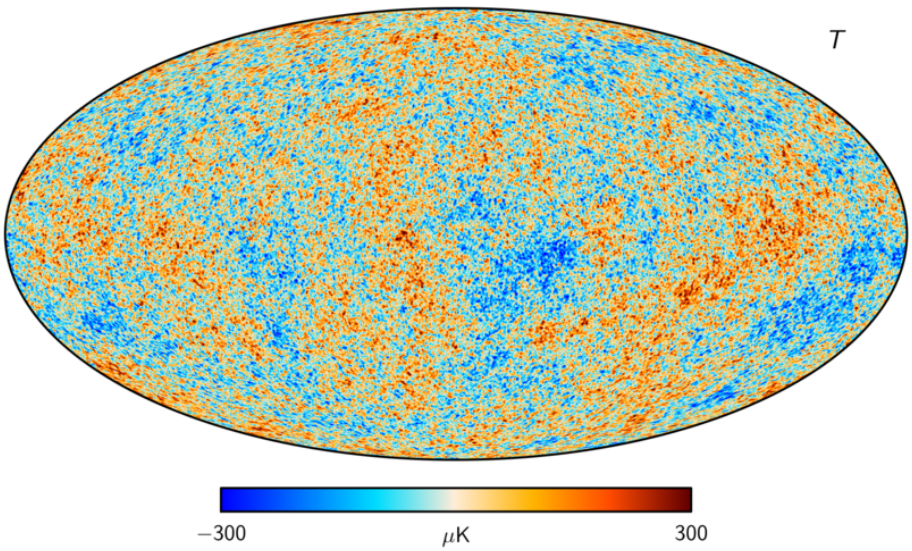

Figure 1.11: CMB temperature map from the *Planck* 2018 data release [5].

1.8.1 CMB temperature anisotropies

The CMB is an extremely isotropic radiation, with an average temperature over all directions of the sky that is given by [46]

$$T_0 = \frac{1}{4\pi}\int_{4\pi} T(\mathbf{n})d\Omega = 2.72548 \pm 0.00057\ \mathrm{K}\,, \tag{1.107}$$

where $T(\mathbf{n})$ denotes the CMB temperature measured in the direction identified by the unit vector $\mathbf{n}$. The tiny fluctuations from this mean value carry a huge amount of information about the physical processes taking place in the early stages of our Universe. The most recent map of the temperature fluctuations of the CMB obtained by the *Planck* satellite [5] is shown in Fig. 1.11. These fluctuations can be characterized by introducing the quantity

$$\delta T(\mathbf{n}) \equiv T(\mathbf{n}) - T_0\,. \tag{1.108}$$

The fluctuation field $\delta T(\mathbf{n})$ is a scalar function which is defined on a sphere, being a function of the unit vector $\mathbf{n}$ or, equivalently, of the polar angles θ and ϕ. It is useful to expand this function in spherical harmonics as

$$\delta T(\mathbf{n}) = \sum_{\ell=1}^{\infty}\sum_{m=-\ell}^{\ell} a^T_{\ell m} Y_{\ell m}(\mathbf{n})\,, \tag{1.109}$$

where $a_{\ell m}$ are the expansion coefficients, which satisfy the relation

$$a^{*T}_{\ell m} = (-1)^m a^T_{\ell,-m}\,. \tag{1.110}$$

Using the orthogonality condition of spherical harmonics, these can be computed as

$$a^T_{\ell m} = \int T(\mathbf{n}) Y^*_{\ell m} d\Omega\,. \tag{1.111}$$

Note that the sum in Eq. (1.109) starts from the multipole $\ell = 1$ rather than from $\ell = 0$. This is due to the fact that the $\ell = 0$ mode of the function $T(\mathbf{n})$ is the mean value T_0, which has already been subtracted in the definition given in Eq. (1.108).

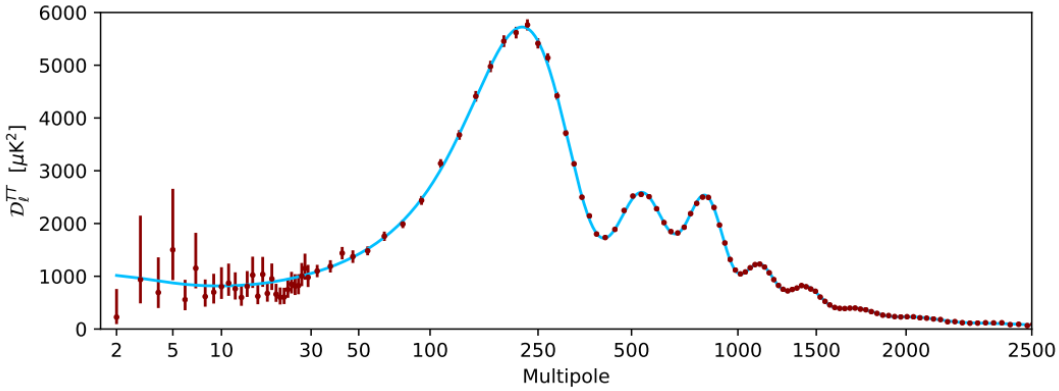

Figure 1.12: CMB temperature power spectrum, $D_\ell^{TT} = \ell(\ell+1)/(2\pi)C_\ell^{TT}$, from the Planck 2018 data release [5].

The coefficients $a_{\ell m}^T$ are stochastic variables related to the stochastic initial conditions of our Universe and can be characterized in terms of n-point correlation functions. Since the $a_{\ell m}^T$ are extracted from a distribution which is Gaussian to a a very good approximation, they can be fully described by the two-point correlation function

$$C_\ell^{TT} \equiv \langle a_{\ell m}^T a_{\ell m}^{*T} \rangle \,. \tag{1.112}$$

In the ideal case of full-sky observations, we can build an unbiased estimator for the power spectrum given by[5]

$$\hat{C}_\ell^{TT} = \frac{1}{2\ell+1} \sum_{m=-\ell}^{\ell} |a_{\ell m}^T|^2 \,. \tag{1.113}$$

The angular power spectrum is usually plotted in terms of the quantity

$$D_\ell^{TT} \equiv \frac{\ell(\ell+1)}{2\pi} C_\ell^{TT} \,. \tag{1.114}$$

In Eq. (1.113), the $|a_{\ell m}^T|$ denotes a statistical average over the ensemble. Under the assumption of ergodicity, this can be recast as an average over the $2\ell+1$ values of m for each fixed multipole ℓ. At small multipoles, there are only a few values of m over which we can take this average. This results in the so-called *cosmic variance*, which translates in a theoretical error that dominates at small multipoles (see Fig. 1.12).

After briefly reviewing the statistical treatment of the temperature fluctuations, we want to recall what is the physics that determines the final shape of the power spectrum that we can observe in Fig. 1.12. We refer the reader to [47] for a detailed treatment, while we present below the final expression for the temperature power spectrum:

$$C_\ell^{TT} = (4\pi)^2 \left(\int k^2 dk \, \left[T_\ell^{T,\zeta}(k) \right]^2 \Delta_\zeta(k) + \int k^2 dk \, \left[T_\ell^{T,h}(k) \right]^2 \Delta_h(k) \right) \,. \tag{1.115}$$

Here, $\Delta_\zeta(k)$ and $\Delta_h(k)$ are the dimensionless primordial power spectra of scalar and tensor perturbations, while $T_\ell^{T,\zeta}(k)$ and $T_\ell^{T,h}(k)$ denote the scalar and tensor transfer functions (see [47] their complete expressions). By looking at the shape of the temperature power spectrum in Fig. 1.12, we can distinguish three main regimes:

[5] In the more realistic case where the sky coverage is not complete and the observations are affected by the instrumental noise and the contamination of foregrounds, the estimator has a more complicated expression.

- At large angular scales (low multipoles) the spectrum is characterized by a flat plateau, due to the so-called *Sachs-Wolfe effect* [48]. This corresponds to fluctuations having wavelengths larger than the sound horizon at recombination. Since no causal processes can act on super-horizon scales, these fluctuations are frozen in their initial configuration, thus providing us with direct information about the primordial perturbations from inflation. When CMB photons climb out of the potential wells associated with these long-wavelength density perturbations, they lose energy. The temperature anisotropies observed today are related to the fluctuations of the gravitational potential Φ on the last scattering surface by
$$\frac{\Delta T}{T} = \frac{\Phi}{3}\,. \tag{1.116}$$

- At intermediate scales we note an oscillatory behavior corresponding to perturbations that enter the horizon, or are already sub-horizon, before recombination. These oscillations are due to the competition between gravity and the radiation pressure, which gives rise to acoustic oscillations in the pre-recombination plasma. We note in particular a series of peaks: the odd number's ones correspond to modes which are in the maximum compression phase at the time of last scattering, while the even number's peaks correspond to modes at maximum rarefaction. The first peak at $\ell \sim 200$ is particularly important. This corresponds to the mode which at recombination had just the time to experience a full compression phase. In other words, the angular scale of the first peak reflects the angular scale under which we see the sound horizon at recombination. Since we observe this characteristic scale projected on the sky, and the projection depends on the spatial geometry of our Universe, the position of the first peak allows us to constrain the curvature of our Universe. Observations are consistent with a spatially-flat Universe [6].

- At small angular scales (high multipoles) we note that the amplitude of temperature fluctuations is damped. During recombination, CMB photons execute a random walk between each collision with free electrons. If we consider perturbations with wavelengths shorter than the photon mean free path, photons can travel many wavelengths without interacting with any electron. As a result, photons mix in the plasma between hot and cold regions, thus smoothing the temperature fluctuations. This results in an exponential damping of the acoustic peaks according to $\exp[-(k/k_d)^2]$, with [49]
$$k_d^{-2} = \int_0^{a_{\rm rec}} da \frac{1}{a^3 \sigma_T n_e H} \frac{R^2 + \frac{16}{15}(1+R)}{6(1+R)^2}\,, \tag{1.117}$$
where $R = 3\rho_b/4\rho_\gamma$. This effect, which can be appreciated in Fig. 1.12, is known as *Silk damping* [50].

All the features in the CMB spectrum that we have just described strongly depend on the cosmological parameters. This means that measurements of the CMB spectrum are a powerful probe to test the standard ΛCDM cosmological model and possible extensions to it.

The six parameters of the ΛCDM model are:

- the physical baryon density $\Omega_b h^2$, where $h = H_0/(100\,\mathrm{km\,s^{-1}\,Mpc^{-1}})$ is the reduced Hubble constant;
- the physical cold dark matter density $\Omega_c h^2$;
- the amplitude of primordial curvature perturbations A_s, defined in Eq. (1.95);
- the scalar spectral index n_s, defined in Eq. (1.96);
- the optical depth τ;

Parameter	Physical meaning	Fiducial value (from [6])
ω_b	Physical baryon density ($= \Omega_b h^2$)	0.02236 ± 0.00015
ω_c	Physical cold dark matter density ($= \Omega_c h^2$)	0.1202 ± 0.0014
$100\theta_s$	$100 \times$ angular size of the sound horizon at decoupling	1.04109 ± 0.00030
τ	Reionization optical depth	$0.0544^{+0.0070}_{-0.0081}$
$\ln(10^{10} A_s)$	Log of the amplitude of scalar perturbations	3.045 ± 0.016
n_s	Scalar spectral index	0.9649 ± 0.0044

Table 1.2: Six parameters of the ΛCDM model with the corresponding fiducial values taken from the *Planck* 2018 data release [6]. The amplitude and spectral index of scalar perturbations are given at the pivot scale $k_* = 0.05\,\mathrm{Mpc}^{-1}$.

- the angular size of the sound horizon $\theta_* = r_s(z_{dec})/d_A(z_{dec})$, where $r_s(z_{dec})$ and $d_A(z_{dec})$ are respectively the comoving sound horizon and the comoving angular diameter distance at decoupling:

$$r_s(z_{dec}) = \int_{z_{dec}}^{\infty} \frac{c_s(z)}{H(z)} dz\,, \qquad d_A(z_{dec}) = \int_0^{z_{dec}} \frac{dz}{H(z)}\,, \tag{1.118}$$

  where

$$c_s(z) = \frac{1}{\sqrt{3\,[1+R(z)]}} \tag{1.119}$$

  is the sound speed in the baryon-photon fluid in units with $c = 1$.

The six cosmological parameters are listed in Table 1.2, where we also report the constraints from the 2018 *Planck* data release [6]. In the following, we briefly describe how the shape of the CMB spectrum varies with the cosmological parameters (see [33] for more details).

Since A_s sets the amplitude of the primordial power spectrum, varying its value results in an overall shift of the spectrum up or down. Varying the spectral index n_s has instead the effect of tilting the CMB spectrum, for example increasing the power at small (large) scales if $n_s > 1$ ($n_s < 1$).

As regards the baryon density, varying its value has several effects on the CMB spectrum. First of all, varying the baryon density has the effect of varying the speed of acoustic waves and thus the comoving sound horizon at decoupling. This causes a shift of the CMB spectrum. Then, if we increase the baryon density we are giving more inertia to the baryon-photon fluid. As a result, the compression peaks are increased while the rarefaction peaks are lowered. Moreover, since we are increasing the electron density, we are decreasing the mean free path of photons, which is given by $\lambda_{\mathrm{mfp}} = (n_e \sigma_T)^{-1}$. This has the effect of shifting the Silk damping scale towards larger multipoles.

Varying the abundance of cold dark matter results in varying the total matter density Ω_m. The main effect is to change the epoch of matter-radiation equality. For example, decreasing the matter density shifts the matter-radiation equality closer to recombination. This changes the forcing term which drives the oscillations in the baryon-photon fluid, resulting in an increased power at small scales.

We now discuss the impact of the optical depth τ. This is related to the reionization of the Universe, which takes place at redshift $z \sim 6$. After the Universe gets reionized, free electrons can again scatter off photons and partially damp CMB anisotropies [51–53]. At scales which are within the horizon at the epoch of reionization ($\ell \gtrsim 10$), the CMB spectrum is suppressed by a factor $e^{-2\tau}$.

Finally, varying θ_* has the effect of changing the comoving sound horizon at decoupling, thus causing an overall shift of the CMB spectrum.

As already mentioned, scenarios which extend the ΛCDM model by adding new parameters can also be constrained using CMB observations. Here, we mention a particular case which will be useful for the analysis presented in chapter 4. Let us consider a scenario in which we have additional light particle species beyond the Standard Model. The contribution to the energy of radiation given by the new light relic is parametrized by the quantity $N_{\rm eff}$, which will be defined in Sec. 4.1. Since we are increasing the energy density of radiation, the expansion rate of the Universe at early times is enhanced. As can be seen from Eq. (1.117), changing the Hubble rate H affects the damping scale k_d. However, varying H changes also the position of the first peak (see the definition of θ_* and (1.118)). Thus, it is useful to consider the ratio of the angular sizes of the damping scale and the sound horizon, $\theta_d = 1/(k_d d_A)$ and $\theta_* = r_s/d_A$, so that we can eliminate the dependence on d_A, which is also function of the Hubble rate (see [54] for more details). The ratio between these two scales is

$$\frac{\theta_d}{\theta_*} = \frac{1}{k_d r_s} \propto H_{rec}^{1/2}\,, \tag{1.120}$$

where H_{rec} is the Hubble parameter at recombination. Increasing the energy density of light relics (and hence H_{rec}), leads to a larger θ_d if we keep θ_* fixed. This implies that the damping scale is shifted to larger angular scales (smaller multipoles), so that the power at small scales is reduced. This is how observations of the CMB temperature power spectrum allow us to constrain the energy density of additional light relics.

1.8.2 CMB polarization and cross-spectra

The CMB radiation is linearly polarized due to Thomson scattering between photons and free electrons at recombination and reionization. CMB polarization spectra provide us with another fundamental tool to constrain the cosmological parameters, containing information often complementary to that encoded in the temperature spectrum. For this reason, the measurement of CMB polarization will be the main target of future experiments, like the LiteBIRD satellite [9] and the ground-based experiments Simons Observatory (SO) [10] and CMB Stage-4 (CMB-S4) [11].

The polarization of the CMB can be described in terms of the usual Stokes parameters I, U, Q and V (see e.g. [55, 56]). The I parameter describes the intensity of polarized light, U and Q carry information about the linear polarization and V is a measure of the elliptical polarization. The definition of Q and U depends on the choice of axes in the plane transverse to the direction of light propagation. Under a rotation of the axes by an angle ψ, the Q and U Stokes parameters transform as

$$Q \longrightarrow Q\cos(2\psi) - U\sin(2\psi)\,, \tag{1.121}$$
$$U \longrightarrow Q\sin(2\psi) + U\cos(2\psi)\,. \tag{1.122}$$

It is thus convenient to introduce the quantities $Q \pm iU$, which transform as spin-± 2 fields:

$$(Q \pm iU) \longrightarrow e^{\pm 2i\psi}(Q \pm iU)\,. \tag{1.123}$$

These can be expanded in terms of spin-weighted basis as

$$(Q + iU)(\hat{n}) = \sum_{\ell m} {}_2a_{\ell m}\, {}_2Y_{\ell m}(\hat{n})\,, \tag{1.124}$$
$$(Q - iU)(\hat{n}) = \sum_{\ell m} {}_{-2}a_{\ell m}\, {}_{-2}Y_{\ell m}(\hat{n})\,. \tag{1.125}$$

Then, since spin-0 quantities are easier to handle in explicit calculations, we can use the spin-lowering ($\bar{\eth}$) and spin-raising ($\eth$) operators (see Appendix A for their definitions and main properties) and act twice with them on $Q \pm iU$. The resulting quantities can then be expanded in spin-0 spherical harmonics. Acting twice with the spin operators on $Q \pm iU$, we get

$$\bar{\eth}^{\,2}(Q+iU)(\hat{n}) = \sum_{\ell m} \left[\frac{(\ell+2)!}{(\ell-2)!}\right]^{1/2} a_{2,\ell m} Y_{\ell m}(\hat{\mathbf{n}})\,, \tag{1.126}$$

$$\eth^{\,2}(Q-iU)(\hat{n}) = \sum_{\ell m} \left[\frac{(\ell+2)!}{(\ell-2)!}\right]^{1/2} a_{-2,\ell m} Y_{\ell m}(\hat{\mathbf{n}})\,. \tag{1.127}$$

The expansion coefficients $a_{\pm 2,\ell m}$ can then be obtained from Eqs. (1.126)-(1.127) using the orthogonality condition of spherical harmonics and read

$$a_{2,\ell m} = \left[\frac{(\ell+2)!}{(\ell-2)!}\right]^{-1/2} \int d\Omega\, Y^*_{\ell m}\, \bar{\eth}^{\,2}(Q+iU)(\hat{n})\,, \tag{1.128}$$

$$a_{-2,\ell m} = \left[\frac{(\ell+2)!}{(\ell-2)!}\right]^{-1/2} \int d\Omega\, Y^*_{\ell m}\, \eth^{\,2}(Q-iU)(\hat{n})\,. \tag{1.129}$$

Finally, we introduce the two quantities that are used when dealing with analysis of CMB polarization, the so-called E- and B-modes:

$$E(\hat{n}) = \sum_{\ell m} a^E_{\ell m} Y_{\ell m}(\hat{n})\,, \tag{1.130}$$

$$B(\hat{n}) = \sum_{\ell m} a^B_{\ell m} Y_{\ell m}(\hat{n})\,, \tag{1.131}$$

where we have defined

$$a^E_{\ell m} \equiv -\frac{{}_2a_{\ell m} + {}_{-2}a_{\ell m}}{2}\,, \tag{1.132}$$

$$a^B_{\ell m} \equiv -\frac{{}_2a_{\ell m} - {}_{-2}a_{\ell m}}{2i}\,. \tag{1.133}$$

The fields $E(\hat{n})$ and $B(\hat{n})$ are rotationally-invariant and transform under parity as

$$E(\hat{n}) \xrightarrow{P} E(\hat{n})\,, \tag{1.134}$$

$$B(\hat{n}) \xrightarrow{P} -B(\hat{n})\,. \tag{1.135}$$

Thus, the E field is invariant under a parity transformation, while the B field is not. The most important consequence of this fact is that the cross-correlators $\langle EB\rangle$ and $\langle TE\rangle$ are vanishing if parity symmetry is preserved. This means that, if these correlators were detected to be different from zero, they would be a clear signal of non-standard physics involving parity violation [57–59].

It is also worth stressing that circular polarization is not expected to be present at the time of last scattering. It can be generated by known physics [60–66] as CMB photons propagate across the Universe, but only in tiny amounts. A larger degree of circular polarization is predicted to be produced in several scenarios beyond the standard model of particle physics [67–73]. Therefore, observing circular polarization in the CMB would provide evidence for new physics, as will also be discussed in chapter 5.

The full derivation of the E-modes and B-modes power spectra can be found in Ref. [47]. Here, we just report the final results, which read

$$C^{EE}_\ell = (4\pi)^2 \left(\int k^2 dk \, \left[T^{E,\zeta}_\ell(k)\right]^2 \Delta_\zeta(k) + \int k^2 dk \, \left[T^{E,h}_\ell(k)\right]^2 \Delta_h(k) \right)\,, \tag{1.136}$$

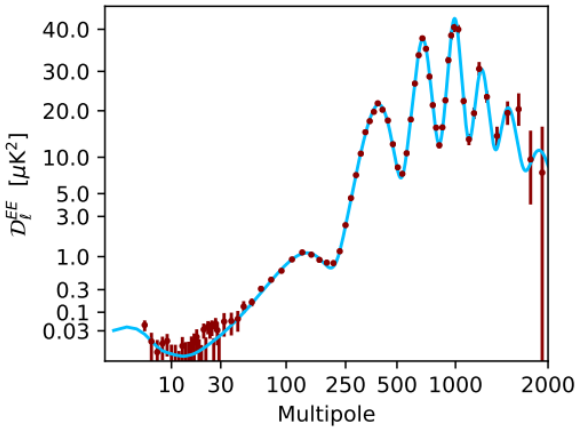

Figure 1.13: CMB E-mode polarization power spectrum from the *Planck* 2018 data release [5].

$$C_\ell^{BB} = (4\pi)^2 \int k^2 dk \left[T_\ell^{B,h}(k)\right]^2 \Delta_h(k)\,, \tag{1.137}$$

where $T_\ell^{E,\zeta/h}(k)$ and $T_\ell^{B,h}(k)$ are the transfer functions for E- and B-modes. For their full expressions we refer again the reader to [47]. Note that the E-modes spectrum receives contributions from both tensor and scalar perturbations (the last one is of course the dominant contribution, given that $A_s \gg A_T$), while the BB spectrum is sourced by primordial tensor perturbations only. For this reason, a detection of B-modes would be a strong evidence in favor of the existence of primordial gravitational waves sourced during inflation. The E-modes spectrum, as measured by *Planck* [5], is shown in Fig. 1.13. The power contained in E-modes fluctuations is roughly a factor 100 smaller than the power contained in the temperature fluctuations.

Looking at the shape of the EE spectrum in Fig. 1.13, we note the presence of acoustic oscillations as in the TT spectrum. This reflects the fact that E-modes polarization are due to velocity gradients in the photon-baryon plasma. Note also the presence of a peak at large angular scales, $\ell < 10$, which is known as the *reionization bump*. As we have discussed in Sec. 1.8.1, CMB photons scatter off electrons after reionization. Since the size of horizon at reionization is larger than at recombination, these scatterings generate a peak at large angular scales.

We can then compute the cross-correlation between E-modes and temperature fluctuations

$$C_\ell^{TE} = (4\pi)^2 \left(\int k^2 dk \left[T_\ell^{T,\zeta}(k) T_\ell^{E,\zeta}(k)\right] \Delta_\zeta(k) + \int k^2 dk \left[T_\ell^{T,h}(k) T_\ell^{E,h}(k)\right] \Delta_h(k) \right) . \tag{1.138}$$

In Fig. 1.14 we show the TE cross-spectrum as measured by *Planck* [5]. This also presents acoustic oscillations.

1.8.3 CMB spectral distortions

Another important probe to test fundamental physics is represented by spectral distortions of the CMB (see e.g. [74–76]). These are tiny departures of the CMB energy spectrum from that of a perfect blackbody. In the early Universe, a blackbody spectrum is maintained by a combination of processes such as Compton scattering, bremsstrahlung and double Compton scattering. However, due to the expansion of the Universe, these interactions become less efficient with time, such that any source of energy injection taking place at redshifts $z \lesssim 10^6$ can induce deviations from a perfect blackbody spectrum.

If energy is released in the baryon-photon plasma during the so-called μ-era, i.e. between

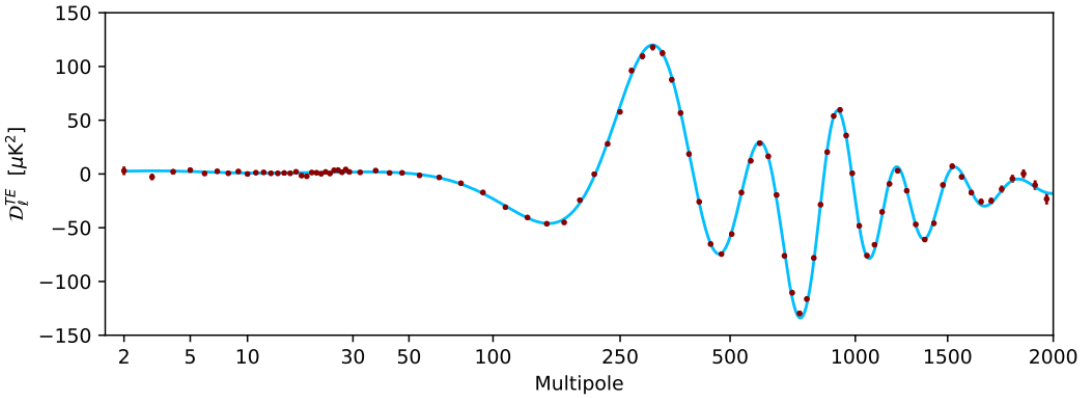

Figure 1.14: CMB TE cross-spectrum from the *Planck* 2018 data release [5].

the thermalization redshift

$$z_{\rm th} \approx 1.98 \times 10^6 \left(\frac{1 - Y_p/2}{0.8767}\right)^{-2/5} \left(\frac{\Omega_b h^2}{0.02225}\right)^{-2/5} \left(\frac{T_0}{2.726\,{\rm K}}\right)^{1/5} \tag{1.139}$$

and $z = z_{\mu y} \simeq 5 \times 10^4$, Compton scattering will still be able to drive the plasma towards kinetic equilibrium. However, the photon number-changing processes, like Bremsstrahlung and double Compton, are inefficient in this range of redshifts (see e.g. [77, 78]). Because of this, energy injection in the μ-era makes CMB photons acquire a Bose-Einstein distribution function with chemical potential $\mu \neq 0$. This deviation from a perfect blackbody spectrum is referred to as μ-distortion. At redshift $z \simeq z_{\mu y}$, instead, thermalization by Compton scattering becomes also inefficient and the transition between μ and y-distortions takes place.

The μ and y-distortions can be computed as (see e.g. [79–81])

$$\mu \simeq 1.401 \int_0^{z_{\rm in}} \mathcal{J}_\mu(z) \frac{\dot{Q}}{\rho_\gamma(z)} \frac{dz}{H(z)(1+z)}\,, \tag{1.140}$$

$$y \simeq \frac{1}{4} \int_0^{z_{\rm in}} \mathcal{J}_y(z) \frac{\dot{Q}}{\rho_\gamma(z)} \frac{dz}{H(z)(1+z)}\,, \tag{1.141}$$

where $z_{\rm in}$ is the redshift at which the energy release begins, $\rho_\gamma = (\pi^2/15)T^4$ is the energy density of background photons, $\dot{Q}$ is the heating rate and $\mathcal{J}_{\mu/y}(z)$ are the distortion visibility functions, which quantify the fraction of the energy injected into the baryon-photon plasma that contributes to μ and y-distortions, respectively. These can be analitically approximated as [80, 81]

$$\mathcal{J}_\mu(z) \approx e^{-(z/z_{\rm th})^{5/2}} \left\{1 - \exp\left[-\left(\frac{1+z}{5.8 \times 10^4}\right)^{1.88}\right]\right\}, \tag{1.142}$$

$$\mathcal{J}_y(z) \approx \begin{cases} \left[1 + \left(\frac{1+z}{6\times 10^4}\right)^{2.58}\right]^{-1} & z \geq z_{\rm rec}\,, \\ 0 & z < z_{\rm rec}\,, \end{cases} \tag{1.143}$$

where $z_{\rm rec} = 1089.95$ is the redshift at which recombination takes place. The contribution $e^{-(z/z_{\rm th})^{5/2}}$ in $\mathcal{J}_\mu(z)$ accounts for the fact that even at redshifts $z > z_{\rm th}$ a small amount of μ-distortions is produced. The other two terms in $\mathcal{J}_\mu(z)$ and $\mathcal{J}_y(z)$, instead, account for the fact that the transition between μ and y-distortions is not sudden at $z = z_{\mu y}$. Rather, around

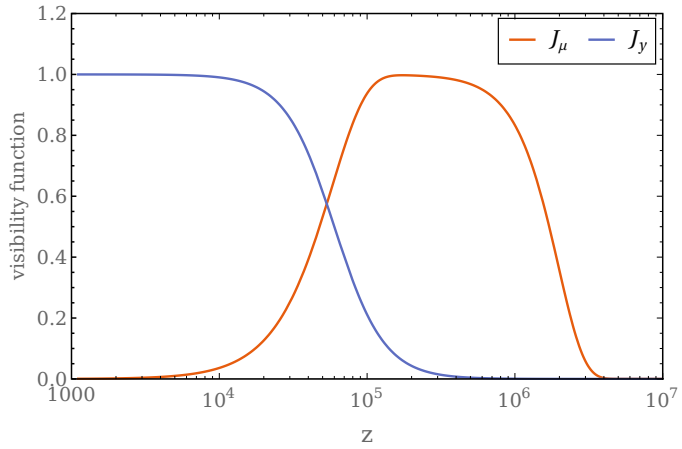

Figure 1.15: Visibility functions for μ and y-distortions as a function of the redshift z. It can be seen that energy injection taking place at redshifts $10^4 \lesssim z \lesssim 3 \times 10^5$ results in a superposition of μ and y-types.

this redshift the distortions consist of a superposition of μ and y-types. This can be seen in Figure 1.15, where the distortion visibility functions for both μ and y-types are shown as a function of the redshift.

The current upper bounds on the amount of spectral distortions are set by the FIRAS instrument aboard the COBE satellite. At 95% CL these read [82, 83]

$$|\mu| < 9 \times 10^{-5}\,, \qquad |y| < 1.5 \times 10^{-5}\,. \tag{1.144}$$

A future experiment like PIXIE, and its improved version SuperPIXIE, in case of no detection of spectral distortions would set the 1σ limits $|\mu| < 3 \times 10^{-8}$, $|y| < 3.4 \times 10^{-9}$ [75, 84] and $|\mu| < 7.7 \times 10^{-9}$, $|y| < 1.6 \times 10^{-9}$ [74, 75], respectively.

1.8.4 Baryon Acoustic Oscillations

Baryon Acoustic Oscillations (BAO) represent another signature of the acoustic oscillations in the primordial plasma, but this time left imprinted in the distribution of matter (see [85] for a review). As already discussed, the competition between the radiation pressure and gravity gives rise to acoustic oscillations in the pre-recombination plasma. Then, shortly after CMB decoupling, baryons are "released" from the drag of the photons at the redshift $z_d \simeq 1059$ [6]. From there on, photons propagate freely while the acoustic waves "freeze in" the baryons in a scale given by the size of the sound horizon at the drag epoch,

$$r_d = \int_{z_d}^{\infty} \frac{c_s(z)}{H(z)} dz \sim 150 \text{ Mpc}\,. \tag{1.145}$$

This scale is left imprinted on the distribution of baryons as a density excess. Since baryons and dark matter interact though gravity, the dark matter also preferentially clusters on this scale. Then, given that the structures form in the potential wells of dark matter, there is a higher probability that a galaxy forms somewhere in this higher density region of the baryon wave. As a result, this characteristic scale appears as a localized peak in the two-point correlation function of galaxies. A peak in the correlation function results in a damped series of oscillations in the power spectrum, given that the two quantities are Fourier conjugates. These are the so-called Baryon Acoustic Oscillations.

This characteristic scale appearing in the matter power spectrum provides us with a cosmological standard ruler which allows to improve the bounds on the cosmological parameters,

as first suggested in [86]. In particular, the goal of BAO surveys is to measure the angular diameter distance, $D_A(z)$, and the expansion rate, $H(z)$. This can be done by comparing the BAO scale in the measurements of clustering of matter with its location computed assuming a fiducial cosmological model. In practice, variations in the cosmological parameters or changes in the models, like the introduction of extra relativistic species (see Sec. 4.1), alter the value of r_d. As a result, the comparison between the BAO scales actually constrains the following two quantities:

$$\alpha_{\parallel} = \frac{(H(z)r_d)^{\rm fid}}{H(z)r_d}\,, \quad \alpha_{\perp} = \frac{(D_A r_d)^{\rm fid}}{D_A r_d}\,. \tag{1.146}$$

In this Thesis we use BAO measurements from the galaxy surveys BOSS DR12 [13], 6dFGS [14] and SDSS-MGS [15].

Part II

Probing the Dark Sector of the Universe with Cosmological Observations

Chapter 2

Cosmological constraints on Macroscopic Dark Matter

2.1 Why (Macro) Dark Matter?

One of the most astonishing results coming from cosmological observations is that only a small fraction of the total matter content of our Universe is composed of ordinary matter. Rather, the matter budget of our Universe is dominated by a yet-unknown form of matter, which we refer to as *Dark Matter* (DM), that has negligible interactions with ordinary matter and radiation, except through gravity. Observations of the Large-Scale Structure of the Universe tell us that DM had to be non-relativistic around the time of structure formation, hence the name *Cold* Dark Matter (CDM).

Nowadays, the existence of DM is supported by a large number of evidences on different scales (see e.g. [87, 88]):

- on galactic scales, the most convincing piece of evidence for dark matter comes from the observations of the rotation curves of spiral galaxies, namely the circular velocities of stars and gas as a function of their distance from the galactic center, $v_c(r)$. The departure of the circular velocity from the Keplerian behavior, $v_c(r) \propto 1/\sqrt{r}$, at large distances from the galactic center suggests that spiral galaxies are surrounded by a DM halo;

- on scales of galaxy clusters, two compelling pieces of evidence come from the *Coma Cluster* and the *Bullet Cluster*. Concerning the Coma Cluster, the presence of a DM component is signaled by the discrepancy between the observed and the predicted velocity dispersion of galaxies in the cluster. The Bullet Cluster consists instead of two colliding clusters of galaxies. The mass distribution inside the Bullet Cluster is mapped via both X-ray observations (tracing the hot gas which emits via Bremsstrahlung) and gravitational lensing. The two results do not match with each other, providing another compelling evidence of the existence of a matter component which interacts through gravity but is blind to electromagnetic interactions;

- on cosmological scales, observations of the CMB anisotropies allow us to constrain the abundances of the total matter in the Universe, $\Omega_m h^2$, and the baryonic component, $\Omega_b h^2$ (see 1.8.1 for a more detailed discussion). The fact that $\Omega_b h^2 < \Omega_m h^2$ provides another decisive proof of the existence of a DM component. The final *Planck* data release yields a CDM abundance given by [6]

$$\Omega_c h^2 = 0.1200 \pm 0.0012 \quad (\textit{Planck}\,\mathrm{TT}, \mathrm{TE}, \mathrm{EE} + \mathrm{lowE} + \mathrm{lensing})\,. \tag{2.1}$$

  As discussed in Sec. 1.3.1, BBN also allows us to constrain the baryon density. Consistently with CMB observations, measurements of the abundances of light elements tell us

that $\Omega_b h^2 < \Omega_m h^2$, supporting again the existence of a non-baryonic matter component. Furthermore, a CDM component is also necessary to boost the gravitational collapse of the primordial density perturbations, allowing the tiny fluctuations observed in the CMB to grow enough to produce the structures we observe today.

Despite the vast number of evidence in favor of the existence of dark matter, the quest for its fundamental nature is still one of the most puzzling problems of modern physics. Over the years, a plethora of models have been proposed, most of which explain the dark matter as a new particle arising in some extension of the standard model (SM) of particle physics. Among the most common particle dark matter candidates we find (see e.g. [87, 89, 90] for some reviews):

- **Weakly Interactive Massive Particles (WIMPs)**: these are particles that in the early Universe are in thermal equilibrium with the cosmological plasma. As the Universe expands and cools down, WIMPs eventually freeze-out and their comoving number density gets frozen. A remarkable fact is that, in order to end up with a relic density equal to the known dark matter density, the interaction cross-section of WIMPs must be of order of that expected for particles with electroweak-scale interactions: this is the so-called "WIMP miracle". The most common example of WIMP candidate is the neutralino, which appears in supersymmetric extensions of the SM of particle physics;

- **axions**: these are light and weakly coupled spin-0 bosons, which result from the spontaneous symmetry breaking of a new $U(1)$ symmetry. They appear as a possible solution to the strong CP problem of QCD, or in many theories that extend the SM of particle physics (e.g., string theory). Axions will be discussed extensively in Chapters 3 and 4, see in particular Sec. 3.6 for more details about axions as DM candidates;

- **sterile neutrinos**: these are particles that do not interact via any of the SM interaction, but only through gravity. For this reason, they are potentially good warm dark matter (WDM) candidates. The existence of heavy neutrinos has also been postulated since they would provide an explanation for the smallness of the neutrino masses and the observed neutrino oscillations via the seesaw mechanism.

Even though these DM candidates are well motivated from the theoretical point of view, no experimental evidence has been found in support of any of them yet. It is thus important to keep an open mind on alternative scenarios, some of which could also be realized within the SM itself.

An appealing possibility is that dark matter consists of macroscopic-size objects, generically dubbed *Macro Dark Matter* (MDM) [16]. Indeed, the interaction rate between baryons and DM goes as $n_X \sigma_X v$, where n_X is the DM number density, σ_X is the interaction cross-section and v is the relative velocity between DM and baryons. We usually assume that the DM is weakly interacting because the cross-section σ_X is intrinsically small. An alternative possibility is that this happens because the DM mass M_X is very large, resulting in a small number density, $n_X = \rho_X / M_X$. This is what happens in the case of MDM.

Many models that fall into this category have been proposed, including Strangelets [91–95], Q-balls [96–100] and Compact Composite Objects [101–105]. Primordial black holes (PBHs), that have gained much attention following the LIGO and VIRGO detection of the gravitational wave signal from black hole mergers, are also an example of MDM (see e.g. [106, 107] for a review). However, constraints on PBHs are usually the weakest that can be obtained for a given MDM mass. Indeed, a black hole is the smallest object that can exist with a given mass, and this implies it also has the smallest possible geometric cross-section.

A broad class of MDM candidates includes yet-unknown, composite states of baryonic matter. The prototype of this kind of MDM are strangelets, consisting of up, down and strange quarks

confined in a quark phase [91–95]. Interestingly enough, the existence of such a phase of quark matter might help explaining the nature of compact objects originating the gravitational wave event GW190814 observed by LIGO and VIRGO [108, 109]. Scenarios in which the DM is still a composite object, but based on physics BSM have also been envisaged, see e.g. [110–114].

In the analysis described in this chapter we derive novel cosmological bounds on MDM. We adopt a phenomenological approach, thus not making explicit reference to any specific model. Rather, we focus on a particular process that might be associated to MDM, namely the capture of protons of the cosmological plasma by Macros. In more detail, we analyze two different scenarios. In the first, proton capture results in the Macro X transitioning to a more stable state X' with energy release in the plasma. The amount of energy released is set by the binding energy of the MDM, which we treat as a free parameter. Conversely, the newly formed X' can be photodissociated by background photons. The time at which the direct and inverse processes go out of equilibrium is determined by the binding energy of Macros, which then fixes the moment in the cosmological evolution when the comoving density of baryons starts decreasing. This first scenario can be thought as representative of models of "nuclear" MDM (e.g. strangelets). In the second scenario, we consider Macros that are composed of antibaryons. In this case, proton capture results in annihilation processes, similarly to what happens with proton capture over ordinary antinuclei (see e.g. [115]). This also results in energy injection in the primordial plasma; however, differently from the first scenario, there is no inverse process by which the starting Macro population can be replenished. In both cases, we also account for the possibility that Macros carry a non-vanishing electric charge.

2.2 Baryon capture by Macro Dark Matter

In the first part of this chapter, we consider the case of Macros composed of ordinary matter. We focus on the following process, in which the dark matter X captures a baryon (a neutron or proton), emitting a photon:

$$X^N + B \longleftrightarrow X^{N+1} + \gamma\,. \tag{2.2}$$

Here, N is the baryon number of the MDM. We assume that the absorption process can continue indefinitely, i.e. that X^{N+1} can absorb another baryon to give X^{N+2}, emitting a photon of (roughly) the same energy, and so on. In principle, the inverse process is also possible: a photon with enough energy can rip a proton or neutron off the DM.

One thing to stress is that, if the emitted photon interacts with another Macro on timescales short with respect to the expansion rate, the numbers of X^N's, protons and neutrons are separately conserved on average over a Hubble time. This is a similar situation as the one with hydrogen recombination: direct recombinations to the $1s$ state of atomic hydrogen do not contribute to the recombination process, because the 13.6 eV photons emitted will soon ionize newly-formed atoms. In the case of hydrogen, $2s - 1s$ two-photon processes are instead needed in order for cosmic recombination to proceed.

We do not consider here the existence of excited states of MDM, but will instead note that the photon emitted after the capture possibly quickly interacts and thermalizes with the cosmological plasma, and is practically "lost" for the purpose of the inverse process. If such a regime is realized, the only photons that are available for the inverse process are those of the cosmic background.

We thus first proceed to check when this regime is realized, and then, armed with that information, study the evolution of the DM and baryon abundances using standard tools (e.g. the Saha equation). We will focus on redshifts before hydrogen recombination, i.e., $z > 1100$. We compare the interaction rate of the emitted photon with the primordial plasma $\Gamma_{\gamma\mathrm{Pl}}$ to the

Hubble expansion rate H, which is given by

$$H(z) = H_0 \left[\Omega_r (1+z)^4 + \Omega_m (1+z)^3 + \Omega_\Lambda\right]^{1/2} . \tag{2.3}$$

The rate $\Gamma_{\gamma \mathrm{Pl}}$ consists of the sum of different contributions

$$\Gamma_{\gamma \mathrm{Pl}} = \Gamma_{\mathrm{Comp}} + \Gamma_{\mathrm{PS}} + \Gamma_{\mathrm{PPn}} + \Gamma_{\mathrm{PP}\gamma} \,, \tag{2.4}$$

namely Compton scattering, photon scattering, pair production over nuclei (both H and ^{4}He) and pair production over photons, respectively. The interaction rate for Compton scattering with the electrons of the baryon-photon plasma can be written as [116]

$$\Gamma_{\mathrm{Comp}} = n_b \, \sigma_T \left(\frac{1+2f_{\mathrm{He}}}{1+4f_{\mathrm{He}}}\right) (1+z)^3 f(x) \,, \tag{2.5}$$

where n_b is the baryon number density, σ_T is the Thomson cross-section, $f_{\mathrm{He}} \simeq Y_P/[4(1-Y_P)]$ with Y_P denoting the primordial Helium abundance and

$$f(x) = \frac{3}{8x}\left[\left(1 - \frac{2}{x} - \frac{2}{x^2}\right)\ln(1+2x) + \frac{4}{x} + \frac{2x(1+x)}{(1+2x)^2}\right] , \tag{2.6}$$

with $x \equiv E_\gamma/m_e$.

The interaction rate for photon scattering has instead the following expression [116]

$$\Gamma_{\mathrm{PS}} = \frac{4448\pi^4}{455625}\,\alpha^4 \lambda_c^{-1} \left(\frac{T_0}{m_e}\right)^6 x^3 (1+z)^6 \,, \tag{2.7}$$

where $\lambda_c = 1/m_e$ is the Compton wavelength, $\alpha \simeq 1/137$ is the fine structure constant and $T_0 \simeq 2.35 \cdot 10^{-4}$ eV denotes the present-day CMB temperature.

Considering interactions of photons with both nuclei of H and ^{4}He, the rate for pair production over nuclei can be written as [117]

$$\Gamma_{\mathrm{PPn}} = \begin{cases} n_b \left[\sigma^{\mathrm{H}}_{x<4}(x)\left(\frac{1+2f_{\mathrm{He}}}{1+4f_{\mathrm{He}}}\right) + \sigma^{\mathrm{He}}_{x<4}(x)\left(\frac{f_{\mathrm{He}}}{1+4f_{\mathrm{He}}}\right)\right](1+z)^3 & \text{if } x < 4 \\ n_b \left[\sigma^{\mathrm{H}}_{x\geq 4}(x)\left(\frac{1+2f_{\mathrm{He}}}{1+4f_{\mathrm{He}}}\right) + \sigma^{\mathrm{He}}_{x\geq 4}(x)\left(\frac{f_{\mathrm{He}}}{1+4f_{\mathrm{He}}}\right)\right](1+z)^3 & \text{if } x \geq 4 \,, \end{cases} \tag{2.8}$$

where

$$\sigma^{\mathrm{A}}_{x<4} = \frac{2\pi}{3} Z^2 \alpha r_e^2 \left(\frac{x-2}{x}\right)^3 \left[1 + \frac{1}{2}\rho + \frac{23}{40}\rho^2 + \frac{11}{60}\rho^3 + \frac{29}{960}\rho^4 + \mathcal{O}(\rho^5)\right] , \tag{2.9}$$

$$\begin{aligned} \sigma^{\mathrm{A}}_{x\geq 4} = Z^2 \alpha r_e^2 \Bigg\{ & \frac{28}{9}\ln 2x - \frac{218}{27} + \left(\frac{2}{x}\right)^3 \left[\frac{2}{3}(\ln 2x)^3 - (\ln 2x)^2 + \left(\frac{6-\pi^2}{3}\right)\ln 2x + 2\zeta(3) + \right. \\ & \left. + \frac{\pi^2}{6} - \frac{7}{2}\right] - \left(\frac{2}{x}\right)^4 \left(\frac{3}{16}\ln x + \frac{1}{8}\right) - \left(\frac{2}{x}\right)^6 \left(\frac{29}{2304}\ln x + \frac{77}{13824}\right) + \mathcal{O}(x^{-8}) \Bigg\} , \end{aligned} \tag{2.10}$$

where Z is the charge of the A nucleus, $r_e = \alpha/m_e$ is the classical radius of the electron and we have also defined

$$\rho \equiv \frac{2x-4}{x+2+2\sqrt{2x}} \,. \tag{2.11}$$

Finally, the interaction rate for pair production over photons is given by [116]

$$\Gamma_{\mathrm{PP}\gamma} = n_b \, \sigma_T \left(\frac{1+2f_{\mathrm{He}}}{1+4f_{\mathrm{He}}}\right) \left[\frac{2\sqrt{\pi}}{\sqrt{y}e^{1/y}}\left(1 + \frac{9}{4}y\right)\right] (1+z)^3 \,, \tag{2.12}$$

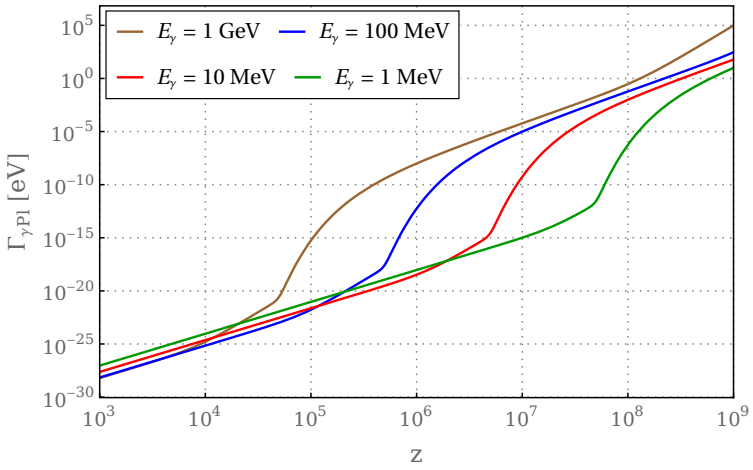

Figure 2.1: Total interaction rate for different values of the energy of the emitted photons: 1 MeV (brown), 10 MeV (red), 100 MeV (blue) and 1 GeV (green).

where we have defined

$$y \equiv x \frac{T_0}{m_e}(1+z)\,. \tag{2.13}$$

The total interaction rate $\Gamma_{\gamma\mathrm{Pl}}$ as a function of the redshift z is shown in Figure 2.1 for different values of the energy of the emitted photons: $E_\gamma = 1$ MeV, 10 MeV, 100 MeV and 1 GeV.

The other relevant quantity we need to consider is the interaction rate of emitted photons with macros, $\Gamma_{\gamma X}$:

$$\Gamma_{\gamma X} = n_X \sigma_X = \Omega_{\mathrm{DM}}\, \rho_{c,0}\, \frac{\sigma_X}{M_X}\, (1+z)^3\,, \tag{2.14}$$

where the cross-section σ_X is purely geometrical[1], i.e. $\sigma_X = \pi R_X^2$, M_X is the mass of Macros Ω_{DM} is the present DM density and $\rho_{c,0}$ is the current value of the critical density of the Universe. Notice that we are also assuming that the dark matter is entirely made up of Macros, such that $n_X \equiv n_{\mathrm{DM}}$.

In Figure 2.2 we compare the three relevant rates, $\Gamma_{\gamma\mathrm{Pl}}$, $\Gamma_{\gamma X}$ and H, as a function of the redshift z. The first two are shown for different values of the injected photon energy E_γ and of the reduced cross section σ_X/M_X, respectively. In the upper right panel, the ratio between $\Gamma_{\gamma X}$ and the Hubble parameter is shown. For values of the reduced cross-section $\sigma_X/M_X > 10^{-1}\,\mathrm{cm}^2\,\mathrm{g}^{-1}$, interactions between photons and Macros are frequent until after recombination. For values $\sigma_X/M_X < 10^{-8}\,\mathrm{cm}^2\,\mathrm{g}^{-1}$, interactions become irrelevant. The upper left panel shows that $\Gamma_{\gamma\mathrm{Pl}} > H$ for the energies and redshifts under consideration. Note that this ratio does not depend on σ_X/M_X. The bottom panel finally shows that $\Gamma_{\gamma X} < \Gamma_{\gamma\mathrm{Pl}}$ for $\sigma_X/M_X \lesssim 1\,\mathrm{cm}^2\,\mathrm{g}^{-1}$. These facts together imply that, in this region of parameter space, the injected photons thermalize efficiently with the primordial plasma before having the chance to interact with a Macro. In this regime, the chemical equilibrium of the reaction (2.2) is regulated uniquely by the cosmic background photons. In the opposite regime, $\sigma_X/M_X \gtrsim 1\,\mathrm{cm}^2\,\mathrm{g}^{-1}$, the absorption of the injected photons by Macros becomes more efficient than the absorption by the primordial plasma, since $\Gamma_{\gamma X} > \Gamma_{\gamma\mathrm{Pl}}$. When this is realized, the comoving density of baryons is again conserved. In the following, we will focus on the former case[2], namely $\sigma_X/M_X \lesssim 1\,\mathrm{cm}^2\,\mathrm{g}^{-1}$.

[1] Since we are considering macroscopic dark matter candidates, which have a radius R_X much larger than any relevant microscopic length scale, we are ignoring the quantum-mechanical aspects of the interaction of Macros with other particles (see [16]). As a result, the interaction cross-sections of Macros with both photons and baryons are purely geometrical.

[2] Strictly speaking, the comoving density is constant for $\Gamma_{\gamma X} \gg \Gamma_{\gamma\mathrm{Pl}}$. When the two rates are comparable,

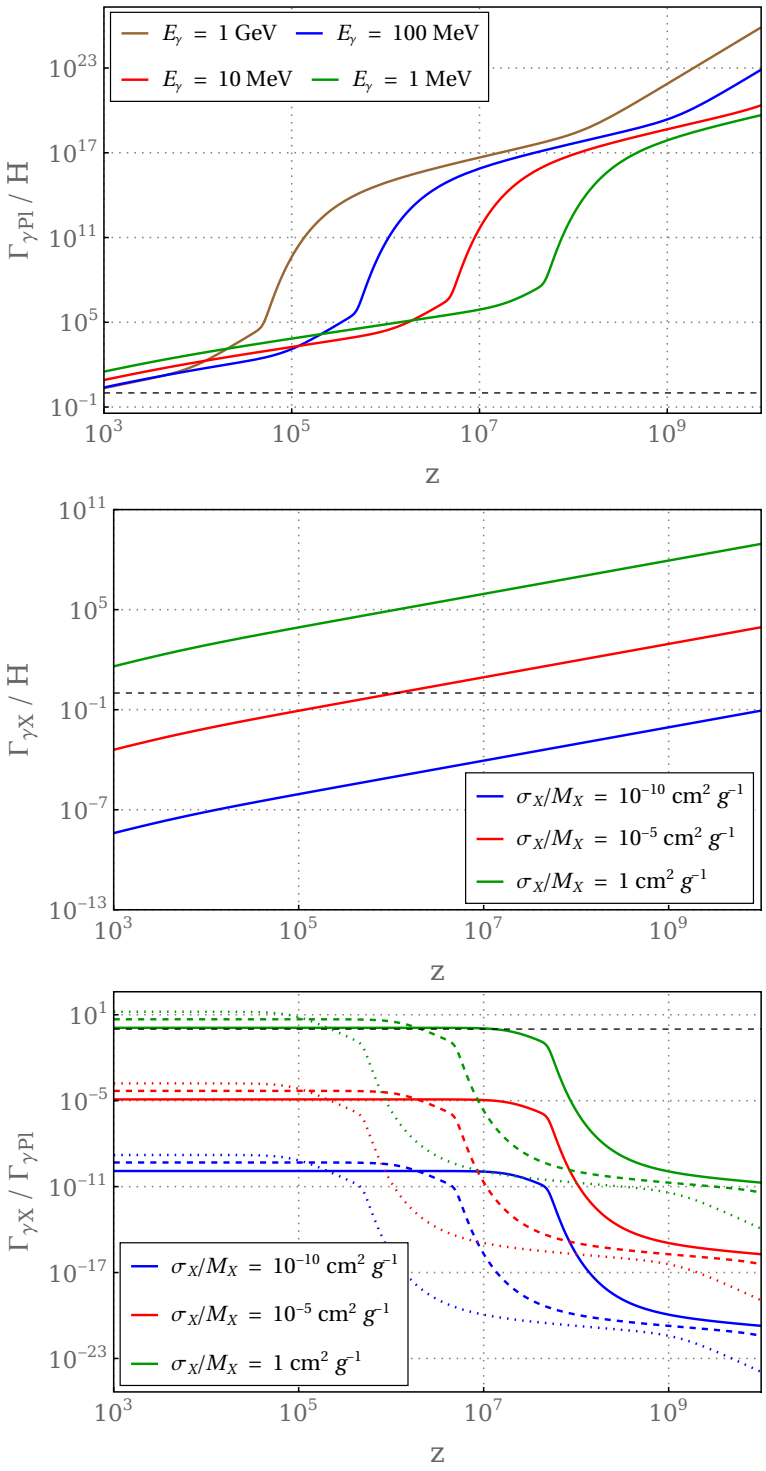

Figure 2.2: On the top we report the interaction rate of photons with the primordial plasma over the Hubble expansion rate, for different energy values: 1 MeV (green), 10 MeV (red), 100 MeV (blue) and 1 GeV (brown). On the middle panel we show the interaction rate of the emitted photon with Macros over the Hubble rate, for different values of the reduced cross-section. On the bottom panel, we report the ratio between the interaction rate of the emitted photon with Macros and with the primordial plasma, for different values of the reduced cross-section and of the energy of photons: 1 MeV (solid), 10 MeV (dashed) and 100 MeV (dotted). The black dashed lines represent the condition $\Gamma_{\gamma Pl}/H = 1$, $\Gamma_{\gamma X}/H = 1$ and $\Gamma_{\gamma X}/\Gamma_{\gamma Pl} = 1$, respectively.

Macros are kept in equilibrium with the cosmological plasma as long as the rate for baryon capture is faster than the expansion rate. The rate at which macros X^N absorb baryons is given by:

$$\Gamma_{\rm abs} = n_b \sigma_X v_{\rm rel} \simeq 21.2 \left(\frac{\Omega_b h^2}{0.022}\right) \left(\frac{\sigma_X}{10^{-15}\,{\rm cm}^2}\right) \left(\frac{T}{\rm MeV}\right)^{7/2} {\rm eV}\,, \tag{2.15}$$

where $v_{\rm rel}$ is the relative velocity between the Macro and baryon fluids, $\Omega_b h^2$ is the physical baryon density and T denotes the temperature of the baryon-photon plasma. In the last equality, we have used the fact that, when the fluids are coupled, the relative velocity is given by the thermal velocity of baryons, $v_{\rm rel} \simeq v_{\rm th} = \sqrt{3T/m_p}$.

Deep into the radiation (RD) and matter-dominated (MD) eras the Hubble rate can be written as:

$$H = \begin{cases} 2.50 \times 10^{-16} \left(\frac{T}{\rm MeV}\right)^2 {\rm eV}\,, & ({\rm RD}) \\ 2.05 \times 10^{-19} \left(\frac{\Omega_{\rm DM} h^2}{0.12}\right)^{1/2} \left(\frac{T}{\rm MeV}\right)^{3/2} {\rm eV}\,. & ({\rm MD}) \end{cases} \tag{2.16}$$

From the above expressions, it is pretty straightforward to check that Macros stay in equilibrium until after recombination ($z = 1100$) if the capture cross section $\sigma_X \gtrsim 10^{-22}\,{\rm cm}^2$.

At equilibrium, the densities of X^N's and X^{N+1}'s are related by the Saha equation (valid for $T \ll m_B$):

$$f_X \equiv \frac{n_X^{N+1}}{n_X^N} = \frac{2^{5/2}\zeta(3)}{\sqrt{\pi}}\, \epsilon_B \left(\frac{g_{N+1}}{g_N\, g_B}\right) \eta \left(\frac{T}{m_B}\right)^{3/2} e^{I/T}\,, \tag{2.17}$$

where $\epsilon_B = n_B/n_b$ is the fraction of baryons in protons or neutrons[3], I is the binding energy of macros, $\eta = n_b/n_\gamma = 5.5 \cdot 10^{-10}(\Omega_b h^2/0.02)$ is the baryon-to-photon ratio, m_B is the mass of the neutron or proton and g is the number of internal degrees of freedom. As regards the latter, $g = 2$ for neutrons and protons, while we assume that $g_{N+1}/g_N \simeq 1$ for MDM. When deriving the Saha equation, we have assumed that both protons and photons are in thermal equilibrium. The equilibrium for protons is justified by the fact that, as we shall see in the next section, observations allow for only a small fraction of protons to be absorbed by Macros. In the case of photons, we are instead using the fact that the high-energy photons released after the capture quickly thermalize with the plasma, as commented above.

From the Saha equation, it is seen that $f_X \ll 1$ for $T \gg I$, i.e., only the X^N's are populated. Hence there is no net absorption of baryons. However, as the Universe expands and cools down, the abundance of X^N's starts to be Boltzmann suppressed since there are fewer photons energetic enough to photodissociate the X^{N+1}. When this happens, macros effectively start absorbing baryons. As a benchmark, we will take the redshift $z_{\rm in}$ at which proton capture starts as the one when $f_X = 1$. In Figure 2.3 we plot $z_{\rm in}$ as a function of the Macro binding energy I. As expected, the higher is the binding energy I, the higher the redshift at which photodissociation of Macros becomes ineffective. In particular, there is a threshold value of the binding energy, $I_{\rm BBN} \simeq 3\,{\rm MeV}$, such that for $I \geq I_{\rm BBN}$ the effective absorption of baryons starts before Big Bang

$\Gamma_{\gamma X} \simeq \Gamma_{\gamma {\rm Pl}}$, a fraction of protons will still be absorbed by Macros, possibly leaving some signatures in the cosmological observables. However, we make the conservative assumption that our analysis is valid only for $\sigma_X/M_X < 1\,{\rm cm}^2\,{\rm g}^{-1}$.

[3] After the Big Bang Nucleosynthesis (BBN), i.e. at temperatures $T \lesssim 0.1$ MeV, there are no free neutrons left in the Universe and we have

$$\epsilon_p = \frac{1 + 2f_{\rm He}}{1 + 4f_{\rm He}}\,, \quad \epsilon_n = 0\,, \tag{2.18}$$

where $f_{\rm He} \simeq Y_p/[4(1 - Y_p)]$ and Y_p is the primordial Helium mass fraction. At temperatures $T \gtrsim 1$ MeV, instead, weak interactions maintain the balance between neutrons and protons and thus

$$\epsilon_p = \epsilon_n = \frac{1}{2}\,. \tag{2.19}$$

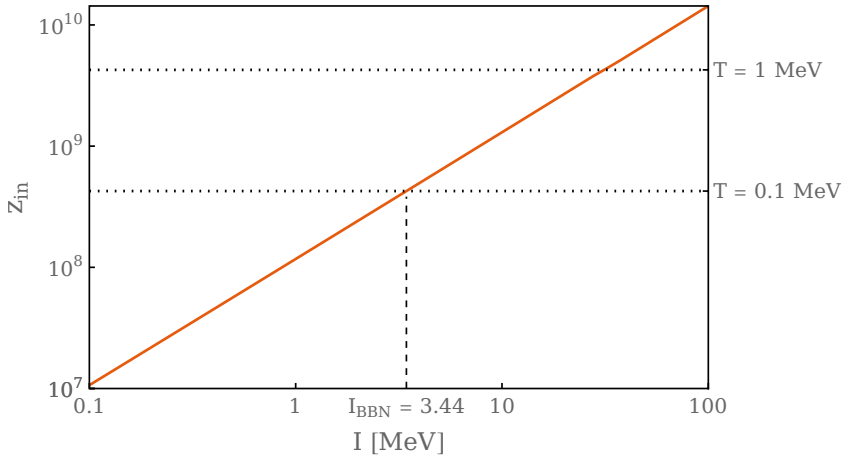

Figure 2.3: Redshift at which the reaction (2.2) goes out of equilibrium (in the case of protons) as a function of the Macro binding energy I. We define a threshold value of the binding energy, $I_{\rm BBN} \simeq 3.44$ MeV, such that for $I < I_{\rm BBN}$ the absorption of baryons starts after the BBN.

Nucleosynthesis (BBN) is complete (we take BBN to end at $T \simeq 0.1$ MeV). In this case, both protons and neutrons are absorbed by Macros and this might affect the standard BBN picture, since the interaction rates of the two particle species with Macros are in general different (as discussed in Ref. [16]). Moreover, the high-energy photons that are emitted during the process might also affect the production of light elements. In the opposite regime, i.e. when $I < I_{\rm BBN}$, the process (2.2) starts after the end of the BBN. Since there are no free neutrons left in the Universe after BBN, Macros interact only with protons. In the following, we will concentrate on the latter case.

2.3 Effects on cosmological observables

We now discuss the effects of the interaction between Macros and protons given in (2.2) on cosmological observables. We focus on the following probes of proton capture: change of baryon density between the end of BBN and the CMB decoupling; spectral distortions in the CMB; kinetic coupling between charged MDM and baryons around the time of hydrogen recombination. We also assess the impact on light element abundances, that might be changed after the end of BBN due to the energy injection associated to proton capture. These effects are then used to derive constraints on the Macro parameter space from current observations. We also discuss detection prospects from future CMB spectral distortions experiments.

2.3.1 Baryon density between BBN and CMB epochs

Cosmological observations allow to measure the baryon density at different epochs. Light element abundances depend on the baryon density at the time of BBN, while CMB anisotropies probe this quantity around the time of hydrogen recombination.[4] For the BBN we take the value of $\Omega_b h^2$ reported in Eq. (1.31). This has been derived in [36] using the measurements of the abundances of deuterium and ^{4}He from Refs. [34] and [35], respectively.[5] For the CMB, instead,

[4] More correctly, light element abundances allow to probe the baryon-to-photon ratio at the time of BBN. Things are more complicated for the CMB, since the anisotropy pattern depends on both η and n_b around the time of recombination. However, since we are neglecting the effect of photons injected between BBN and recombination, we can drop the distinction.

[5] As mentioned in Sec. 1.3.1, a new analysis has been performed in [37] using updated expressions for nuclear rates. The inclusion of these new results does not alter significantly our conclusions.

we use the constraint from the 2018 Planck data release [118]:

$$(\Omega_b h^2)_{\rm BBN} = 0.0227 \pm 0.0005\,, \quad (\Omega_b h^2)_{\rm CMB} = 0.02236 \pm 0.00015\,. \tag{2.20}$$

These values are consistent within the respective uncertainties. This fact can be used to constrain the amount of protons captured by Macros between BBN and recombination, and from that the capture cross-section.

Let us define the comoving number density of protons as[6] $\mathcal{N}_p \equiv a(t)^3\, n_p$. Following the discussion in the previous section, we can take $\mathcal{N}_p = $ const for $z > z_{\rm in}$. At lower redshifts, we can neglect the photodissociation of Macros and the comoving density evolves according to

$$\dot{\mathcal{N}}_p = -\Gamma_{pX}\, \mathcal{N}_p \qquad (z < z_{\rm in})\,, \tag{2.21}$$

where Γ_{pX} is the rate at which protons are captured by Macros. For Macros with surface potential V_X, the capture rate can be written as [16]

$$\Gamma_{pX} = n_X \sigma_X v_{\rm rel} \times \begin{cases} e^{-V_X/T} & V_X \geq 0\,, \\ 1 - V_X/T & V_X < 0\,, \end{cases} \tag{2.22}$$

where we approximate the relative velocity between Macros and protons $v_{\rm rel}$ with the thermal velocity $v_{\rm th}$ of the latter (see discussion in Sec. 2.3.3). If Macros have a positive surface potential, protons have to face a potential barrier which tends to suppress their absorption rate, as encoded in the exponential factor present in Eq. (2.22). For negative surface potentials, the proton absorption rate is instead enhanced. We will mainly consider values of the surface potential $|V_X| \simeq \mathcal{O}(\text{MeV})$, as expected for strangelets and nuclear-type MDM [93]. However, to keep our discussion more general, we will also analyze cases with smaller values of V_X. If we think of nuclear-like Macros, we expect them to have a positive electric charge. In this case, as discussed e.g. in [93] for strange matter, an external shell of electrons is formed around the Macro such that the global charge vanishes, while protons of the cosmological plasma feel an effective negative charge when they are close to the external electronic shell.

The temperature of the baryon-photon plasma evolves as $T \simeq T_0(1+z)$, where T_0 denotes the present-day CMB temperature. As above, we use the fact that

$$n_X \sigma_X = \Omega_{\rm DM}\, \rho_{c,0}\, \frac{\sigma_X}{M_X}\, (1+z)^3\,, \tag{2.23}$$

when evaluating the interaction rate.

The formal solution to Eq. (2.21) reads, for $t > t_{\rm in}$,

$$\mathcal{N}_p(t) = \mathcal{N}_{p,\rm in}\, \exp\left[-\int_{t_{\rm in}}^{t} \Gamma_{pX}\, dt \right]\,, \tag{2.24}$$

where $t_{\rm in}$ represents the time at which the absorption of protons by Macros starts, and $\mathcal{N}_{p,\rm in} = \mathcal{N}_p(t_{\rm in})$. The logarithmic ratio of the comoving number densities at BBN and recombination is then:

$$\Delta \log \mathcal{N}_p \equiv \log\left(\frac{\mathcal{N}_p(t_{\rm BBN})}{\mathcal{N}_p(t_{\rm CMB})} \right) = \int_{\max(t_{\rm in}, t_{\rm BBN})}^{t_{\rm CMB}} \Gamma_{pX}\, dt\,. \tag{2.25}$$

This expression can be used to evaluate $\Delta \log \mathcal{N}_p$ for given values of σ_X/M_X, V_X and I (since the latter determines $z_{\rm in}$).

Using the measured values in Eq. (2.20), we find the following observational constraint:

$$(\Delta \log \mathcal{N}_p)_{\rm obs} = 0.015 \pm 0.029\,. \tag{2.26}$$

Enforcing this constraint produces the exclusion plot shown in Figure 2.4.

[6] In our analysis we are assuming that only free protons of the cosmological plasma are captured by Macros, neglecting instead the possibility that He nuclei are also absorbed.

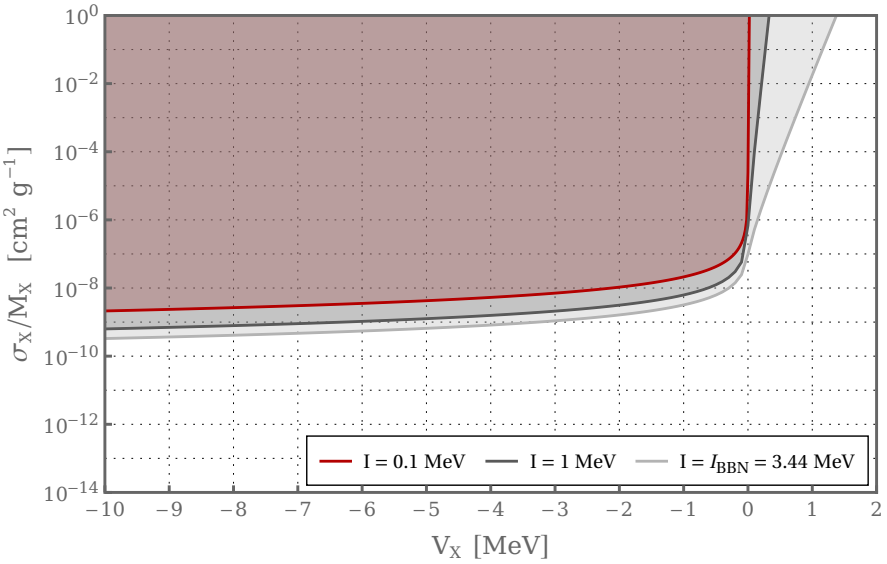

Figure 2.4: Constraints on the reduced cross-section as a function of the Macro surface potential, for different values of the binding energy I. The shaded regions are excluded by the BBN and CMB measurements of the baryon density. As discussed in Section 2.2, these constraints are valid for $\sigma_X/M_X \lesssim 1\,\mathrm{cm}^2\,\mathrm{g}^{-1}$, since for higher values of the reduced cross-section the injected photons are not absorbed efficiently by the cosmological plasma.

2.3.2 CMB spectral distortions

The capture of protons by Macros leads also to the injection of high-energy photons in the primordial plasma, see Eq. (2.2). As discussed in Section 1.8.3, a possible observational effect of any source of energy release in the early Universe is the production of spectral distortions in the CMB. The amount of μ and y-distortions can be computed using Eqs. (1.140)-(1.141). The heating rate $\dot{Q}$ is in our case given by

$$\dot{Q} = n_p(z)\Gamma_{pX}(z)I\,, \tag{2.27}$$

where the time evolution of the proton density is computed using Eq. (2.21) and hence taking into account the capture by Macros. Notice that we are assuming that all the energy released goes into heating. This is justified because, as we have shown in Section 2.2, the interaction rate of the emitted photons with the primordial plasma is always much greater than the Hubble expansion rate.

In Figure 2.5 we show the amount of μ and y-distortions that are produced as a function of the parameters of the model. Both types of spectral distortions are always below the current upper bounds set by FIRAS, $|\mu| < 9 \times 10^{-5}$ and $|y| < 1.5 \times 10^{-5}$ (95% CL) [82, 83]. However, they are within the reach of the proposed PIXIE and SuperPIXIE experiments which, in case of no detection, would set the 1σ limits $|\mu| < 3\times10^{-8}$, $|y| < 3.4\times10^{-9}$ [75,84] and $|\mu| < 7.7\times10^{-9}$, $|y| < 1.6\times10^{-9}$ [74,75], respectively. The region of the parameter space that would be accessible to PIXIE (SuperPIXIE) are those within the solid (dashed) lines.

Notice that the amount of spectral distortions is maximized for values of the reduced cross-section $\sigma_X/M_X \sim 10^{-6}$ and 10^{-7} for $V_X = -1$ MeV and $V_X = -10$ MeV, respectively. As one might naively expect, spectral distortions decrease for smaller values of the reduced cross-section since fewer protons are absorbed, resulting in less photons being released in the baryon-photon plasma. However, the amount of spectral distortions decreases also for higher values of the reduced cross-section: this happens because a large number of protons is absorbed at redshifts close to $z_{\rm in}$. This means that for high values of I (and hence of $z_{\rm in}$) most of the energy release takes place before the μ and y-eras, thus not giving rise to any detectable spectral distortion.

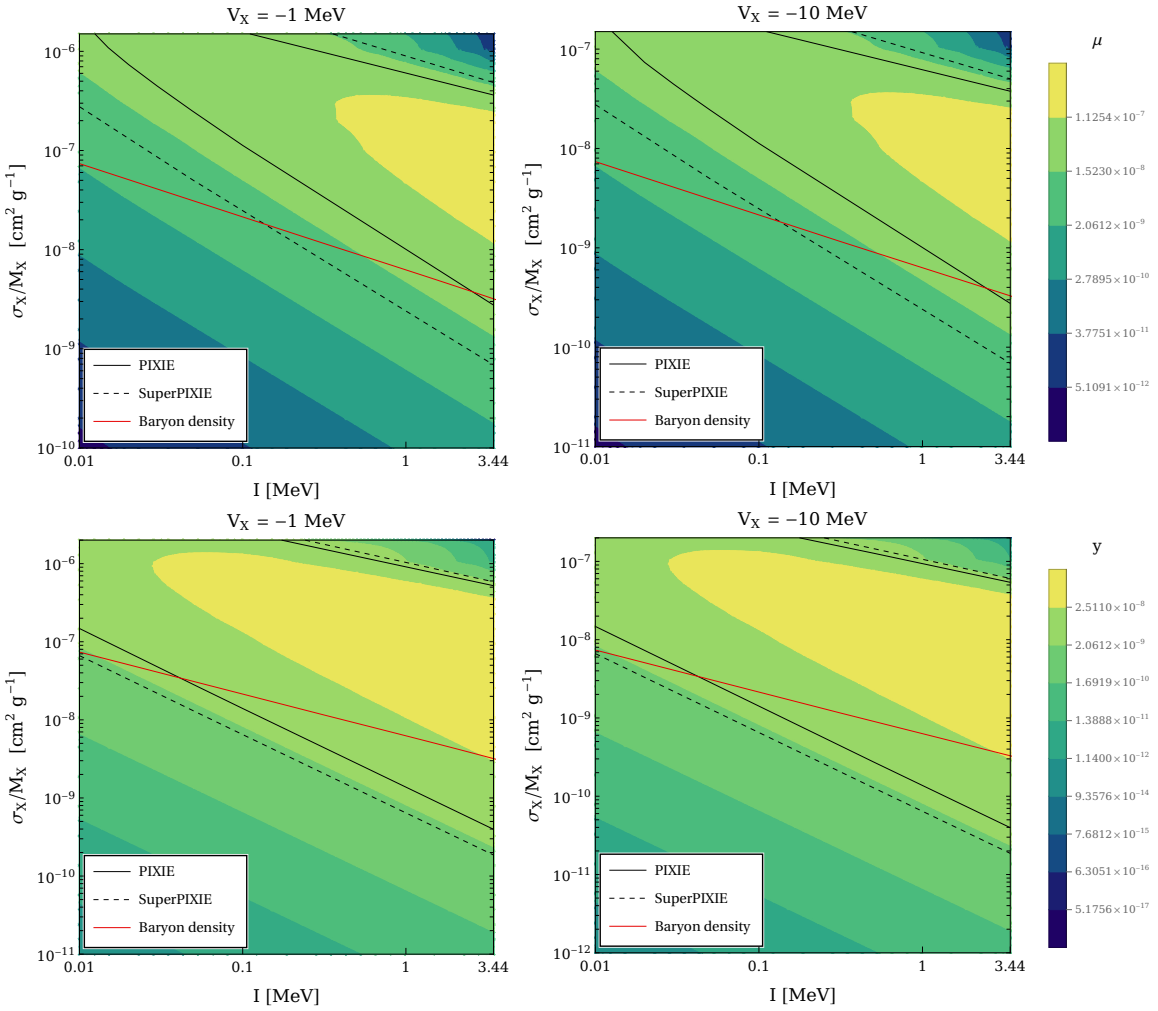

Figure 2.5: Contour plots of μ and y-distortions as a function of the reduced cross-section σ_X/M_X and the Macro binding energy I, for two different values of the surface potential V_X: -1 MeV (left panel) and -10 MeV (right panel). The regions of parameter space within the black solid and dashed lines are excluded assuming a null detection of spectral distortions from PIXIE ($|\mu| < 3 \times 10^{-8}$, $|y| < 3.4 \times 10^{-9}$) and SuperPIXIE ($|\mu| < 7.7 \times 10^{-9}$, $|y| < 1.6 \times 10^{-9}$), respectively. The regions above the red lines are excluded by the constraints from the baryon density, as discussed in the previous section.

Finally, let us remark that no sizeable spectral distortions are produced if $V_X \geq 0$. Indeed, as we can see from Figure 2.4, only in the case with $I \sim I_{\rm BBN}$ a non-negligible amount of protons is absorbed if these have to face a potential barrier. However, also in this case most of the absorptions take place at high redshifts, when the thermal energy of protons is large enough to overcome the potential barrier.

2.3.3 Tight coupling between baryons and charged Macro DM at recombination

If the dark matter is electrically charged, it can scatter off electrons and protons with the possibility of getting coupled to the baryon-photon plasma. If this condition were realized at recombination, MDM would effectively behave like baryons as regards its effects on the CMB anisotropies. Since we are assuming that Macros form the entirety of the DM, this can not be

the case and hence we must require that the two fluids are not coupled at recombination[7].

Following [120], the momentum transfer rate due to DM-baryon scattering can be written as

$$\Gamma_{\rm c} = \sum_{i=p,e} \frac{8\sqrt{2\pi}\alpha^2 q_X^2 n_i \mu_i^{1/2}}{3 M_X T^{3/2}} \ln\left(\frac{3T\lambda_D}{|q_X|\alpha}\right) , \tag{2.29}$$

where

$$\mu_i = \frac{M_X m_i}{M_X + m_i} \tag{2.30}$$

is the DM-baryon reduced mass (which in the case of Macros reduces to the mass of protons/-electrons, since $M_X \gg m_p \gg m_e$), q_X is the charge of DM in units of the elementary charge, $\alpha \simeq 1/137$ is the fine structure constant and

$$\lambda_D = \sqrt{\frac{T}{4\pi\alpha n_e}} \tag{2.31}$$

is the Debye length of the cosmological plasma.

The condition for the tight coupling between baryons and DM is that the momentum transfer rate is much larger than the Hubble expansion rate, $\Gamma_{\rm c} \gg H$. The tight coupling between baryons and charged DM has been largely studied in the context of millicharged DM, where the DM is made up of particles carrying an electric charge much smaller than the elementary charge (see e.g. [120–124]). In these scenarios, from Eq. (2.29) one can easily see that $\Gamma_{\rm c}/H \propto T^{-1/2}$ during the radiation era (neglecting the logarithmic dependence in the screening term). This means that the DM and baryons are not coupled at high redshifts and then eventually get coupled when $\Gamma_{\rm c}/H$ becomes of order unity.

The scenario considered in the present analysis differs in one aspect: protons are being absorbed by Macros, thus their number density has a different scaling than the usual one (i.e. $n_b \propto T^3$). Hence, the number of target protons that enters in the momentum transfer rate (2.29) is a function of the Macro parameters and is obtained again by numerically integrating Eq. (2.24).

The electric charge of Macros is instead fixed by the Macro surface potential and cross-section. For Macros with surface potential V_X and cross-section σ_X expressed in units of eV and eV^{-2} respectively, the charge is given by

$$q_X = \frac{V_X (\sigma_X/\pi)^{1/2}}{\alpha} . \tag{2.32}$$

Now we have everything required to compute the momentum transfer rate given in Eq. (2.29). CMB observations do not allow for a coupling between the two components at recombination, so we require $\Gamma_c/H < 1$ at that time. By imposing this condition, we derive the constraints shown in Figure 2.6. Note that these limits are likely conservative, because we expect that even relatively small momentum transfers between DM and baryons at the recombination epoch would leave a detectable imprint on CMB anisotropies. However, quantifying this effect would require a dedicated analysis, so for the time being we use the conservative condition $\Gamma_c/H < 1$.

[7] In this discussion we are assuming that the dark matter fluid approximation is still valid, in spite of the low number density of Macros. This is true provided that the diffusion time for a photon to cross the average separation between two Macros is small compared to the Hubble time, H^{-1}. In terms of the mass of Macros, this condition can be written as [119]

$$\left(\frac{M_X}{\rm g}\right)^{2/3} (1+z)^3 \ll 10^{39} . \tag{2.28}$$

Even for very massive MDM candidates (e.g. $M_X \sim 10^{20}$ g), this condition is satisfied up to high redshift values ($z \sim 10^8$). Thus, we can safely assume that the dark matter fluid approximation is valid when dealing with DM-baryon interactions at the CMB epoch.

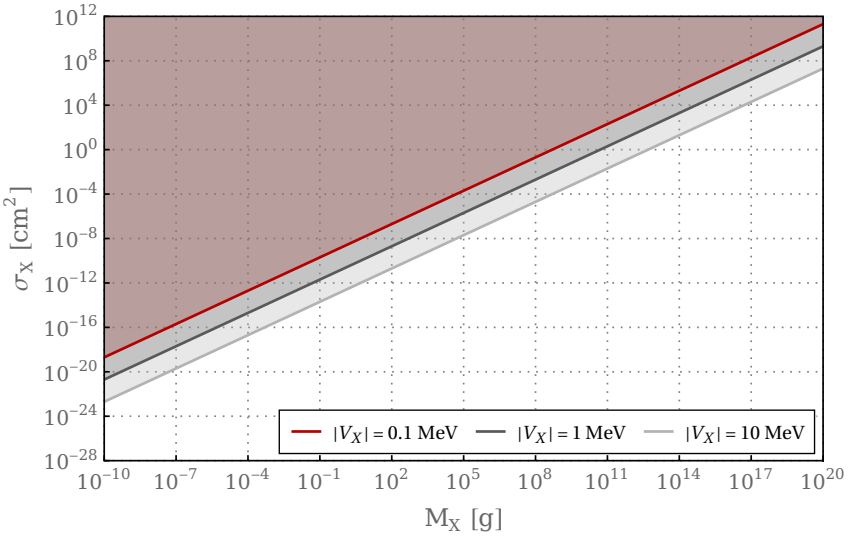

Figure 2.6: Constraints on the Macro cross-section and mass for different values of the surface potential V_X. These comes from the requirement that Macros and baryons are not tightly coupled due to Coulomb scattering at the recombination epoch.

Notice that the curves in Figure 2.6 correspond to constant values of σ_X/M_X. Indeed, the momentum transfer rate Γ_c depends on the ratio $q_X^2/M_X \propto \sigma_X/M_X$ and the proton number density also depends on σ_X/M_X (see Eqs. (2.22)-(2.24)). There is then the logarithmic dependence on $q_X \propto \sigma_X^{1/2}$, which is however very weak and gives negligible contributions. We can write the resulting constraints on the reduced cross-section as

$$\frac{\sigma_X}{M_X} \lesssim 2 \times 10^{-11} \left(\frac{|V_X|}{\text{MeV}}\right)^{-2} \text{cm}^2\,\text{g}^{-1}\,. \tag{2.33}$$

Before closing this section some comments are in order regarding our treatment of the charge of Macros and the relative velocity between MDM and baryons. Concerning the first aspect, we have assumed that the charge of Macros remains constant, despite the fact the protons are being captured. Since we are thinking of Macros as macroscopic nuclei, we might imagine that, as protons are absorbed, Macros get rid of the excess charge by converting protons to neutrons through weak processes.

As regards the relative velocity between baryons and Macros, this is in principle given by $v_{\rm rel} = (v_{\rm th}^2 + v_{\rm bulk}^2)^{1/2}$, where $v_{\rm th}$ is the thermal velocity of baryons and $v_{\rm bulk}$ is the relative bulk velocity between the DM and baryon fluids. The latter is non-vanishing only if the two matter components are not coupled. If this is not the case, DM and baryons behave as a single fluid and the relative velocity is simply given by the thermal speed of baryons. A detailed treatment of the relative motion between the DM and baryon fluids can be found in [125, 126]. For the purposes of our discussion we can approximate the relative bulk velocity as

$$v_{\rm bulk}(z) \simeq \min\left[1, \frac{1+z}{10^3}\right] \times 10^{-4}\,. \tag{2.34}$$

This is constant at redshifts $z \gtrsim 10^3$ and then decreases as $(1+z)$. In Figure 2.7 we show how the bulk, thermal and relative velocities evolve with redshift in the case in which DM and baryons are not coupled (i.e. $v_{\rm bulk} \neq 0$). It can be seen that at redshifts $z \gtrsim 10^4$ the thermal component is the dominant one and the approximation $v_{\rm rel} \simeq v_{\rm th}$ is then justified in this range of redshifts. Let us now discuss what happens at redshifts $z \lesssim 10^4$. First of all, notice that in this regime the bulk motion gives the largest contribution to $v_{\rm rel}$. It is then useful to recall that

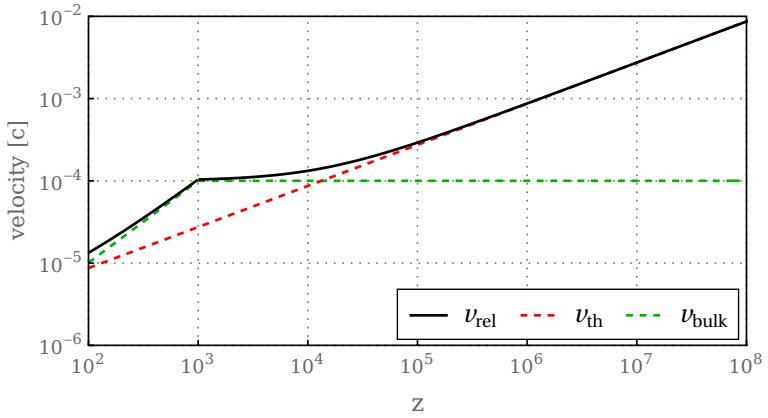

Figure 2.7: Relative bulk velocity between the baryon and DM fluids (red dashed line), thermal velocity of protons (blue dashed line) and relative velocity (black solid line) defined as $v_{\rm rel} = (v_{\rm th}^2 + v_{\rm bulk}^2)^{1/2}$.

baryons and Macros are decoupled at high redshifts and get coupled only when $\Gamma_{\rm c}/H$ becomes of order unity. If this condition is realized at redshifts $z \gtrsim 10^4$, then approximating the relative velocity with the thermal one is well justified throughout all the expansion history, since at $z \lesssim 10^4$ (i.e. when baryons and the DM are coupled) there is no relative bulk motion between the two components. If instead Macros and baryons become coupled at $z < 10^4$ but before CMB decoupling, by assuming that $v_{\rm rel} \simeq v_{\rm th}$ in this range of redshifts we are underestimating the capture rate (2.22), since $v_{\rm th} < v_{\rm rel}$. We have however verified that always approximating $v_{\rm rel} \simeq v_{\rm th}$ has a negligible impact on our results.

2.3.4 Light element abundances

Another possible effect due to photon injection is to alter the light element abundances after BBN [127–131]. For the energies under consideration (i.e., $E_\gamma \lesssim 3.44$ MeV), two relevant processes to consider are the photodissociation of the deuterium and the ^{7}Be, whose energy thresholds are given by $E_{\rm th} = 2.2246$ MeV and $E_{\rm th} = 1.5866$ MeV, respectively [127, 128]. The equation which regulates nuclear abundances ($Y_A \equiv n_A/n_b$, with $A = d$, ^{7}Be) in redshift space is given by (see e.g. [129, 130])

$$\frac{dY_A}{dz} = -\frac{1}{H(z)(1+z)}\left[\sum_T Y_T \int_0^\infty dE_\gamma f_\gamma(E_\gamma, z)\sigma_{\gamma+T\to A}(E_\gamma) + \right. \\ \left. -Y_A \sum_P \int_0^\infty dE_\gamma f_\gamma(E_\gamma, z)\sigma_{\gamma+A\to P}(E_\gamma)\right], \tag{2.35}$$

where $\sigma_{\gamma+T\to A}$ is the cross-section for the production of A via the photodissociation of nuclei T, $\sigma_{\gamma+A\to P}$ is the cross-section for the analogous destruction channel and f_γ is the nonthermal photon distribution function. The latter can be computed by solving the usual Boltzmann equation with the source term

$$S_\gamma = n_p(z)\Gamma_{pX}(z)p_\gamma\,, \tag{2.36}$$

where p_γ is the injection spectrum. In the case of Macros composed of ordinary matter, the energy of the injected photons is given by the Macro binding energy, hence $p_\gamma = \delta(E_\gamma - I)$. As discussed in Section 2.2, the interaction rate of photons with the cosmological plasma, $\Gamma_{\gamma\rm Pl}$, is much faster than the expansion rate H. As a result, f_γ is driven to a quasi-static equilibrium (i.e. $\partial f_\gamma/\partial t = 0$), such that $f_\gamma = S_\gamma/\Gamma_{\gamma\rm Pl}$ [129–131].

For the energies under consideration, only destruction processes need to be considered. Thus, Eq. (2.35) can be easily integrated as

$$\ln\left(\frac{Y_A(z_f)}{Y_A(z_i)}\right) = \int_{z_i}^{z_f} \frac{dz}{H(z)(1+z)} \frac{n_p(z)\Gamma_{pX}(z)}{\Gamma_{\gamma\mathrm{Pl}}(I,z)}\, \sigma_{\gamma+A\to P}(I)\,. \tag{2.37}$$

The explicit expressions of the photodissociation cross-sections of d and ^{7}Be can be found in Refs. [127] and [128], respectively.

It is now possible to evaluate the impact of the energy injection on the abundances of d and ^{7}Be by means of Eq. (2.37). We find that the resulting effects are negligible and do not allow us to constrain MDM. This happens because the emitted photons quickly thermalize with the baryon-photon plasma and are practically "lost" as photodissociation sources.

2.4 Antimatter Macros: proton-antiproton annihilations

In this section we discuss the second scenario considered in our analysis, i.e. dark matter in the form of macroscopic objects composed of antimatter. Following [132], we refer to this class of DM candidates as anti-Macros.

Before the recombination epoch, free protons of the cosmological fluid can be captured by anti-Macros, analogously to what happens in the case of Macros composed of ordinary matter. The annihilations between protons and antiprotons then lead to the release of high-energy photons in the baryon-photon plasma.

Differently to what happens in the case of Macros (see Eq. (2.2)), there is no inverse process available for keeping the comoving density of baryons constant at high redshifts. This implies that, as soon as anti-Macros are produced, they start absorbing protons. This also means that the constraints that we find are independent of the binding energy of anti-Macros. We leave instead the redshift at which anti-Macros are produced as a free parameter. To keep contact with the previous sections, we label again this as z_{in}.

Some regions of the parameter space of anti-Macros have already been constrained in [132], where the authors focused on the case with $V_X = 0$. Following the discussion of the previous sections, we now derive new constraints from the absorption of protons between the BBN and recombination and from spectral distortions of the CMB. Moreover, the condition that baryons and anti-Macros were not coupled at decoupling has still to be imposed. In Section 2.3.3 we have seen that the resulting constraints on the Macro parameter space are independent of the binding energy I. Since the latter fixes the redshift at which the capture of protons begins, this means that these constraints are independent of z_{in}. The same conclusion has to be true also in the case of anti-Macros, which then have to obey the same constraints as those shown in Figure 2.6.

2.4.1 Baryon density between BBN and CMB epochs

As we have done in Section 2.3.1 for Macros, we can constrain the parameter space of anti-Macros by requiring that the number of protons that have been absorbed between the BBN and CMB epochs does not exceed the experimental constraints, i.e. $\Delta \log \mathcal{N}_p \leq (\Delta \log \mathcal{N}_p)_{\mathrm{obs}}$ within the observational uncertainty.

Since the capture rate is equal to the case of Macros, these results coincide with those of Figure 2.4, with the only difference that z_{in} replaces I as a phenomenological free parameter. In particular, from Figure 2.4 we can derive the constraints on anti-Macros through the following

mapping:

$$\begin{cases} I = 0.1\,\text{MeV} \longrightarrow z_{\rm in} \simeq 1.1 \times 10^7\,, \\ I = 1\,\text{MeV} \longrightarrow z_{\rm in} \simeq 1.2 \times 10^8\,, \\ I = 3.44\,\text{MeV} \longrightarrow z_{\rm in} \simeq 4.3 \times 10^8\,. \end{cases} \tag{2.38}$$

2.4.2 CMB spectral distortions from $p\bar{p}$ annihilations

If Macros are composed of antimatter, annihilations with protons of the cosmological plasma result in the release of high-energy photons. This process has been discussed in [132], where the reduced cross-section of anti-Macros has been constrained by analyzing the effects of this energy injection on the CMB anisotropies and the BBN. The heating rate depends on which specific process takes place after the $p\bar{p}$ annihilations (like, e.g., the nature of the cascade of particles that are produced). Denoting with k the fraction of the rest energy of the proton and antiproton that is actually released in the baryon-photon plasma, we can write the heating rate as [132]

$$\dot{Q} = n_p(z)\Gamma_{pX}(z)(2km_p)\,. \tag{2.39}$$

In the following we take $k = 0.2$. This is consistent with the scenario in which $p\bar{p}$ annihilations result in the production of multi-pion states, including both neutral and charged pions. The latter (or their decay products, i.e. electrons, muons and neutrinos) are able to escape anti-Macros, while neutral pions decay after their production into four photons, each having energy $E_\gamma \sim 100$ MeV [132].

The amount of μ and y-distortions produced by anti-Macros can then be computed through Eqs. (1.140)-(1.141). The results are shown in Figure 2.8 for two different values of the initial redshift, $z_{\rm in} = 10^8$ and $z_{\rm in} = 10^7$. We also show the constraints obtained exploiting the upper bounds on spectral distortions by FIRAS, as well as the forecasted constraints obtained assuming a null detection of spectral distortions by PIXIE and SuperPIXIE. The constraints derived in [132] for $V_X = 0$ are also included and are marked with a red triangle.

Notice in particular that in this case it is possible to exclude some regions of parameter space thanks to the upper bounds on spectral distortions set by FIRAS. However, these bounds are weaker than those obtained by the capture of protons and the tight coupling condition, as we will also discuss in the next section. On the other hand, PIXIE and SuperPIXIE would allow us to improve the current constraints.

2.5 Summary of the constraints and discussion

Figure 2.9 summarizes the constraints on Macros and anti-Macros obtained from the analysis discussed in the previous sections. We show the results for both neutral and charge MDM. In the latter case, we consider two values of the surface potential of MDM, namely $V_X = -0.01$ and -10 MeV. We now comment on the main features of these results. Let us start by discussing the case of neutral MDM:

- for Macros composed of ordinary matter, the only constraints we find are derived by imposing that the amount of protons absorbed between the BBN and the CMB epochs does not exceed the observational bound (2.26). The resulting constraints are shown in the top left panel of Figure 2.9. An analytical fit to these is given by

$$\frac{\sigma_X}{M_X} \lesssim 6.8 \times 10^{-7} \left(\frac{I}{\text{MeV}}\right)^{-1.56} \text{cm}^2\,\text{g}^{-1}\,. \tag{2.40}$$

  No sizeable spectral distortions are produced, implying that future spectral distortions experiments, like PIXIE and SuperPIXIE, would not allow to improve the bound (2.40);

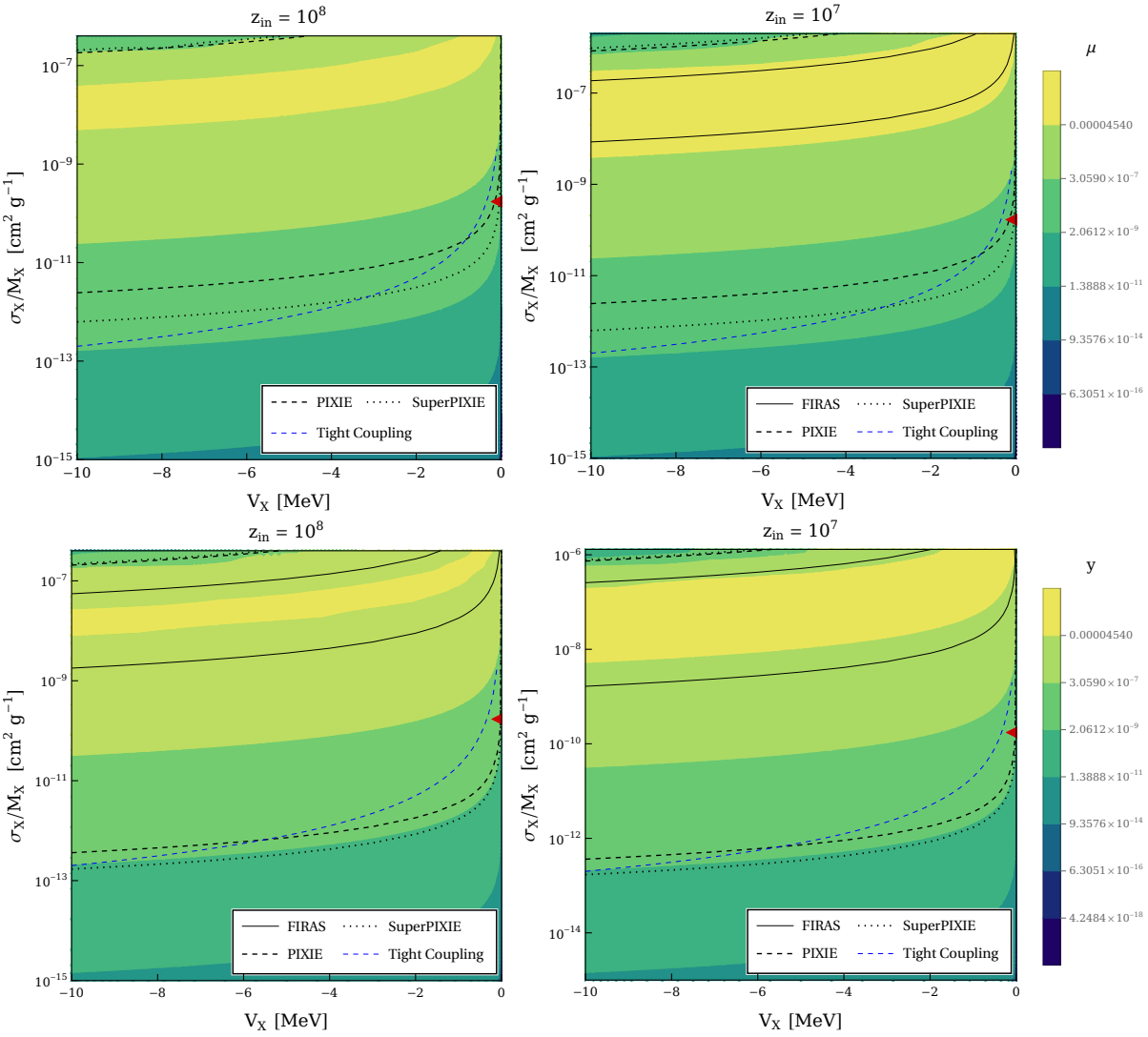

Figure 2.8: Contour plots of μ and y-distortions as a function of the reduced cross-section σ_X/M_X and the surface potential V_X of anti-Macros, for two different values of the initial redshift: 10^7 and 10^8. These are due to the emission of high energy photons as a result of $p\bar{p}$ annihilations. The region of parameter space within the black solid lines is excluded by FIRAS ($|\mu| < 9 \times 10^{-5}$, $|y| < 1.5 \times 10^{-5}$). The regions of parameter space within the black dashed and dotted lines are excluded assuming a null detection of μ-distortions from PIXIE ($|\mu| < 3 \times 10^{-8}$, $|y| < 3.4 \times 10^{-9}$) and SuperPIXIE ($|\mu| < 7.7 \times 10^{-9}$, $|y| < 1.6 \times 10^{-9}$), respectively. The dot-dashed blue curves correspond to the bounds (2.33), obtained by requiring that anti-Marcos and baryons are not coupled at decoupling. The red point denotes the constraint derived in [132], which has been obtained for $V_X = 0$.

.

- for neutral anti-Macros, the current constraints are dominated by the baryon density condition for $z_{\rm in} \gtrsim 4\times10^5$, while for $z_{\rm in} \lesssim 4\times10^5$ the FIRAS bounds on spectral distortions give the tightest constraints on the reduced cross-section. Future CMB spectral distortion experiments will probe a much larger region of the parameter space, as can be appreciated in the top right panel of Figure 2.9.

In the case of charged MDM with strong enough surface potential, the tightest constraints come from requiring that Macros and baryons are not coupled at recombination due to Coulomb scattering[8] ($\Gamma_{\rm c}/H < 1$). For small potentials (see e.g. the $V_X \simeq -0.01$ MeV case shown in the lower panels of Figure 2.9) the bounds from the baryon density can be tighter in some region of parameter space.

The tight coupling condition leads to the following conservative bound on the reduced cross-section (see also Figure 2.6)

$$\frac{\sigma_X}{M_X} \lesssim 2\times10^{-11}\left(\frac{|V_X|}{\rm MeV}\right)^{-2}{\rm cm}^2\,{\rm g}^{-1}\,, \tag{2.41}$$

where V_X denotes the Macro surface potential. An interesting point to remark is that these constraints are basically insensitive to both the Macro binding energy (or $z_{\rm in}$, in the case of anti-Macros) and the sign of the surface potential. Our interpretation for this goes as follows: first of all, the sign of the surface potential V_X determines the sign of the Macro electric charge through Eq. (2.32), but this does not affect the momentum transfer rate (2.29), which depends only on the absolute value of the charge. Secondly, both I and V_X affect the behavior of $n_p(z)$, but Γ_c does depend on the combination $n_p\mu_p + n_e\mu_e$. Since we are assuming that electrons are not absorbed by Macros, even if a non-negligible fraction of protons is absorbed, the value of the momentum transfer rate does not change too much, given that all the electrons are still available as scattering targets.

We stress that, because of this last point, the constraints from the tight coupling condition are valid also in the region of parameter where $\sigma_X/M_X \gtrsim 1{\rm cm}^2\,{\rm g}^{-1}$, contrary to constraints from the baryon density and spectral distortions (see the discussion in Sec. 2.2). Indeed, as discussed above, the constraints from the tight coupling are basically only due to the charge of Macros, which is not related to the absorption of protons, but rather remains constant at its initial value. Therefore, Coulomb scattering takes place also in the region of parameter space with $\sigma_X/M_X \gtrsim 1{\rm cm}^2\,{\rm g}^{-1}$ and the condition (2.41) has still to be satisfied.

It is then important to stress how future spectral distortions experiments would allow to improve these constraints in the case with $V_X < 0$:

- for Macros composed of ordinary matter, we find that future spectral distortions experiments would improve the bounds on the reduced cross-section for small values of $|V_X| \lesssim 0.05$ MeV. This can be seen in the lower right panel of Figure 2.9, where we report the sensitivity region for SuperPIXIE including both μ and y-type spectral distortions for the case with $V_X = -0.01$ MeV;

- for anti-Macros, we can see that the sensitivity window for SuperPIXIE roughly coincides with the region of parameter space excluded by the the tight coupling condition for $V_X = -10$ MeV, see central left panel of Figure 2.9 . For smaller values of the surface potential, SuperPIXIE would instead improve the bounds on anti-Macros. This is shown in the lower left panel of Figure 2.9 for the case with $V_X = -0.01$ MeV.

[8]Notice that in Figure 2.9 we do not report the constraints on charged anti-Macros derived from the FIRAS bounds on spectral distortions. Indeed, as can be seen in Figure 2.8, these are always below the constraints derived from the tight coupling condition.

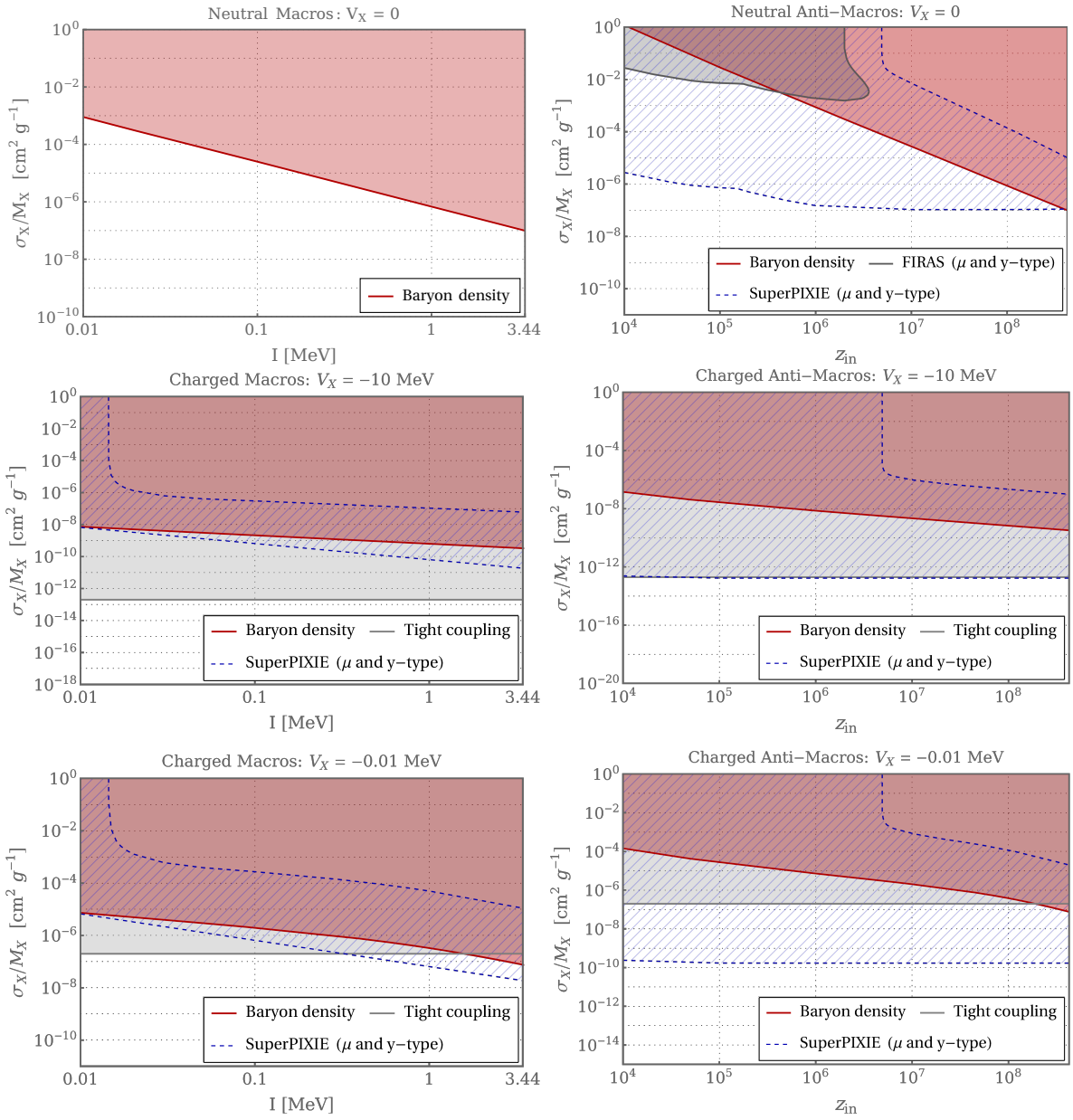

Figure 2.9: Constraints on the reduced cross-section as a function of the Macro binding energy I (or the initial redshift $z_{\rm in}$, in the case of anti-Macros), for different values of the surface potential V_X. The shaded regions are excluded by current constraints, while the hatched regions represent the sensitivity windows for SuperPIXIE. In the upper panels we show the constraints on neutral Macros (left) and neutral anti-Macros (right). In the central panels, instead, we report the constraints on charged Macros (left) and anti-Macros (right) with a surface potential $V_X = -10$ MeV. Analogous bounds are shown in the lower panels, for $V_X = -0.01$ MeV. The constraints from the baryon density and from spectral distortions are valid for $\sigma_X/M_X \lesssim 1\,{\rm cm}^2\,{\rm g}^{-1}$, since for higher values of the reduced cross-section the injected photons are not absorbed efficiently by the cosmological plasma. The bounds derived from the tight coupling condition are instead valid also for $\sigma_X/M_X > 1\,{\rm cm}^2\,{\rm g}^{-1}$.

We now want to compare our results with the cosmological constraints on Macros derived in previous literature. In particular, some constraints on σ_X/M_X as a function of V_X have been derived in Ref. [16]. However, there are some key differences with respect to our analysis that we want to outline. The constraints obtained in [16] come from the requirement that the standard BBN predictions are not altered by the interactions between Macros and baryons (both protons and neutrons). Indeed, phrased within our theoretical framework, the authors of Ref. [16] consider the case $I > I_{\rm BBN}$, since the absorption of baryons starts before BBN. This means that we are actually probing different regions of the parameter space. It is also worth mentioning that the constraints derived in [16] do not take into account the injection of photons in the primordial plasma, but are uniquely based on protons and neutrons being captured with a different rate by Macros. Since the absorption of baryons occurs earlier in their scenario, a non negligible fraction of baryons is absorbed also for $V_X > 0$, provided that $V_X \sim \mathcal{O}(\text{MeV})$. In our case, instead, the lower thermal energy of protons makes it difficult to overcome a potential barrier $V_X \gtrsim 1$ MeV. In particular, only if $I \sim I_{\rm BBN}$, i.e. if the absorption of protons starts just after the BBN, we find competitive constraints on the reduced cross-section for $V_X \sim 1$ MeV. On the other hand, the BBN constraints derived in [16] are insensitive to the case with $V_X = 0$, when protons and neutrons are absorbed with the same rate, thus not affecting primordial abundances. Baryon absorption between BBN and decoupling, instead, is also sensitive to the case with $V_X = 0$, as we have already seen.

Energy injection resulting from $p\bar{p}$ annihilations by anti-Macros has also been considered in Ref. [132]. There, the authors derived a bound on σ_X/M_X from the effects of the energy injection on CMB anisotropies and BBN, which results in $\sigma_X/M_X \lesssim 2 \times 10^{-10}\,\text{cm}^2\,\text{g}^{-1}$. Differently from our analysis, this bound has been derived only in the case with $V_X = 0$.

It is interesting to briefly comment on the implications of our findings for Macro particles with a density of the order of the one of nuclear matter, $\rho_{\rm nuc} = 3.6 \times 10^{14}\,\text{g}\,\text{cm}^{-3}$. It is straightforward to see that an upper limit on the reduced cross section $\sigma_X/M_X < \alpha$ will in this case translate to a lower limit on the mass $M_X/\text{g} > 1.4 \times 10^{-29}\alpha^{-3}$. In the case of neutral macros, this yields $M_X > 1.4 \times 10^{-8}\,\text{g}$ for a binding energy $I = 3.44\,\text{MeV}$, coming from the requirement that baryons are not absorbed in large amounts between the times of BBN and CMB decoupling. For charged macros with negative surface potential, the tight-coupling constraint in Eq. (2.41) implies $M_X > 1.7 \times 10^3\,(|V_X|/\text{MeV})^6\,\text{g}$.

Chapter 3

Axions and axion-like particles

3.1 The strong CP problem of QCD

Our description of nature at its most fundamental level relies on the Standard Model (SM) of particle physics, which describes all the elementary particles known in nature and their mutual interactions. It incorporates three of the four fundamental forces, namely the electromagnetic, weak and strong interactions. The SM is a non-abelian gauge theory whose local symmetry group is

$$SU(3)_C \times SU(2)_L \times U(1)_Y \,, \tag{3.1}$$

where:

- $SU(3)_C$ is the gauge group of quantum chromodynamics (QCD) and describes the strong interaction;
- $SU(2)_L \times U(1)_Y$ defines the electroweak (EW) sector of the SM, providing a unified description of the electromagnetic and weak interactions. It also includes the Higgs field, which gives mass to the matter fields of the SM via a spontaneous symmetry breaking (SSB).

From a modern perspective, the SM can be seen as an effective field theory (EFT) valid up to some (cut-off) energy scale, see e.g. [133]. This means that, when writing down the low-energy Lagrangian of the model, we should always include all the renormalizable operators (i.e., those having mass dimension $d \leq 4$) which respect the symmetries of the theory. In particular, QCD allows for the presence of a CP-violating θ-term in the Lagrangian, which can then be written as

$$\mathcal{L}_{\text{QCD}} = \sum_q \bar{q}\big(i\gamma^\mu D_\mu - m_q\big)q - \frac{1}{4}G^{\mu\nu}_a G^a_{\mu\nu} + \theta\frac{g_s^2}{32\pi^2}G^{\mu\nu}_a \tilde{G}^a_{\mu\nu} \,, \tag{3.2}$$

where g_s is related to the strong coupling constant α_s via $g_s = \sqrt{4\pi\alpha_s}$, $G^a_{\mu\nu}$ is the gluon field strength tensor, $\tilde{G}^a_{\mu\nu} \equiv \frac{1}{2}\epsilon_{\mu\nu\rho\sigma}G^{\rho\sigma}_a$ is its dual and the index a runs over the adjoint indices of the SU(3) group, i.e. $a = 1, ..., 8$. Besides being allowed by the symmetry of the theory, the θ-term in Eq. (3.2) arises in a natural way from the study of the QCD vacuum structure (see [134] for a review).

Another potential source of CP violation is contained in the quark masses. Indeed, when writing down a mass term for quarks in the Lagrangian as

$$\mathcal{L}_{\text{mass}} = \bar{q}_{iR}M_{ij}q_{jL} + \text{h.c.} \,, \tag{3.3}$$

the mass matrix M is in general complex. To get the physical basis, the mass matrix must be diagonalized. Since this transformation is chiral and chiral transformations change the QCD

vacuum, the net effect is to change the coefficient in front of the $G\tilde{G}$ term to [134]

$$\bar{\theta} = \theta + \arg\left(\det M\right) . \tag{3.4}$$

The most important effect of the $\bar{\theta}$-term is to generate an electric dipole moment (EDM) of the neutron d_n, which is defined in terms of the non-relativistic Hamiltonian

$$H = -d_n \mathbf{E} \cdot \hat{\mathbf{S}} . \tag{3.5}$$

The Lagrangian term responsible for the neutron EDM can be expressed in terms of a Lorentz-invariant operator as [135–137]

$$\mathcal{L} = -\frac{i}{2} d_n \bar{n} \gamma_5 \sigma_{\mu\nu} n F^{\mu\nu} . \tag{3.6}$$

Precise calculations using QCD sum-rules yield the following value of the EDM of the neutron [136]:

$$d_n = (2.4 \pm 1.0)\, \bar{\theta} \times 10^{-16}\, e\,\mathrm{cm} . \tag{3.7}$$

By comparing this prediction with the strongest experimental upper bound, given by [138]

$$|d_n| < 1.8 \times 10^{-26}\, e\,\mathrm{cm} , \tag{3.8}$$

we obtain an upper limit on the value of the $\bar{\theta}$-parameter that reads

$$|\bar{\theta}| \lesssim 10^{-10} . \tag{3.9}$$

Why nature selects such a small value of $\bar{\theta}$ represents the so-called *strong CP problem* [139–142]. Is there any dynamical mechanism able to drive $\bar{\theta}$ naturally to zero?

3.2 The Peccei-Quinn solution and the QCD axion

Among the possible solutions to the strong CP problem, the most appealing one has been proposed by Roberto Peccei and Helen Quinn in 1977 [139]. The core of the idea is to introduce a new global $U(1)_{\mathrm{PQ}}$ chiral symmetry, dubbed the *Peccei-Quinn symmetry*, which gets spontaneously broken at a given energy scale f_a. This results in the appearence of a new degree of freedom, a Nambu-Goldstone boson (NGB) which is called the *axion* [141,142]. The dynamical axion field replaces in the theory the CP-violating $\bar{\theta}$ parameter, and is dynamically driven to a CP-conserving phase as a result of the dynamics of the axion itself. This ensures the conservation of CP symmetry in the QCD sector.

The effective Lagrangian for the axion field a can be written as

$$\mathcal{L}_a = \frac{1}{2}(\partial_\mu a)(\partial^\mu a) + \xi \frac{a}{f_a} \frac{g_s^2}{32\pi^2} G_a^{\mu\nu} \tilde{G}^a_{\mu\nu} + \mathcal{L}_{\mathrm{int}}\left[\partial_\mu a / f_a, \psi\right] . \tag{3.10}$$

In addition to the canonical kinetic term, the axion Lagrangian includes all the possible model-dependent couplings with matter fields ψ, which depend on the derivative of the axion field given its NGB nature. The second term in (3.10) is present to make sure that the Noether current of the $U(1)_{\mathrm{PQ}}$ symmetry has a chiral anomaly

$$\partial_\mu J^\mu_{\mathrm{PQ}} = \xi \frac{g_s^2}{32\pi^2} G_a^{\mu\nu} \tilde{G}^a_{\mu\nu} , \tag{3.11}$$

where ξ is a model-dependent parameter. The presence of this anomalous coupling of the axion with gluons is what allows for the axion to provide a solution to the strong CP problem discussed in the previous section. Indeed, we can now write the total Lagrangian of the theory as

$$\begin{aligned}\mathcal{L} &= \mathcal{L}_{\rm SM} + \mathcal{L}_{\bar\theta} + \mathcal{L}_a \\ &= \mathcal{L}_{\rm SM} + \frac{1}{2}(\partial_\mu a)(\partial^\mu a) + \left(\bar\theta + \xi\frac{a}{f_a}\right)\frac{g_s^2}{32\pi^2}G_a^{\mu\nu}\tilde G^a_{\mu\nu} + \mathcal{L}_{\rm int}\left[\partial_\mu a/f_a, \psi\right], \end{aligned} \tag{3.12}$$

where $\mathcal{L}_{\rm SM}$ is the Lagrangian of the SM. After the SSB of the Peccei-Quinn symmetry, all the values of the vacuum expectation value (VEV) of the axion $\langle a\rangle \in [0, 2\pi]$ lying in the circle of the minima are in principle allowed. However, QCD instanton effects related to the $G\tilde G$ term generate an effective potential for the axion,[1] which is periodic in the effective vacuum angle $\bar\theta + \xi\langle a\rangle/f_a$:

$$V_{\rm eff} \sim \cos\left(\bar\theta + \frac{\xi\langle a\rangle}{f_a}\right). \tag{3.13}$$

This potential is minimized for

$$\langle a\rangle = -\frac{\bar\theta}{\xi}f_a\,. \tag{3.14}$$

Thus, as the axion field evolves towards the minimum of its potential, the CP-violating $\bar\theta$-term is removed. This provides a dynamical solution to the strong CP problem and removes the need for a fine-tuning of the value of $\bar\theta$.

The effective potential $V_{\rm eff}$ also generates a mass term for the axion, which thus becomes a pseudo Nambu-Goldstone boson (pNGB). The axion mass is given by

$$m_a^2 = \left\langle\frac{\partial^2 V_{\rm eff}}{\partial a^2}\right\rangle_{\langle a\rangle = -f_a\bar\theta/\xi} = -\frac{\xi}{f_a}\frac{g_s^2}{32\pi^2}\frac{\partial}{\partial a}\langle G_a^{\mu\nu}\tilde G^a_{\mu\nu}\rangle_{\langle a\rangle = -f_a\bar\theta/\xi}\,. \tag{3.15}$$

This can be computed using EFT techniques and reads [141, 143]

$$m_a = \frac{\sqrt{m_u m_d}}{m_u + m_d}\frac{m_\pi f_\pi}{f_a} \simeq 0.57\left(\frac{10^7\,{\rm GeV}}{f_a}\right){\rm eV}\,, \tag{3.16}$$

where $m_\pi \approx 135\,{\rm MeV}$ and $f_\pi \approx 92\,{\rm MeV}$ are the mass and the decay constant of the neutral pion, while $m_u \approx 2.16$ MeV and $m_d \approx 4.67$ MeV are the masses of the up and down quarks.

Note that both the axion mass in Eq. (3.16) and the couplings in (3.10) are proportional to $1/f_a$. This means that for large values of f_a the axion is a light and weakly-coupled particle. Models in which this condition is realized are referred to as *invisible axion models*. These will be discussed in Sec. 3.3.

3.3 A survey of QCD axion models

The first realization of the PQ mechanism was proposed by Weinberg and Wilczek in 1977 [141, 142] and is now known as the PQWW or "visible" axion model. In this model, an extra Higgs doublet is introduced to enforce the $U(1)_{\rm PQ}$ symmetry, while the SM quarks are charged under this new symmetry and generate the anomaly of the PQ current. This realization of the PQ mechanism leads to an axion decay constant f_a of order of the elctroweak scale, $v_{\rm EW} \simeq 246$ GeV. Since the axion couplings to SM fields are proportional to $1/f_a$ and f_a is not sufficiently suppressed, this model has been soon ruled out by experimental searches [144–147].

This led to the so-called "invisible" axion models, where $f_a \gg v_{\rm EW}$, so that the axion is very light and very weakly-coupled. The two prototypes of this class of models are the Kim-Shifman-Vainshtein-Zakharov (KSVZ) [148,149] and the Dine-Fischler-Srednicki-Zhitnitsky (DFSZ) [150, 151] models. These will be introduced in Secs. 3.3.1 and 3.3.2, respectively.

[1] Intuitively, we can think that the Mexican hat potential typical of the SSB gets tilted. Thus, the shift symmetry for the axion is broken, and an effective potential with minimum $\langle a\rangle \neq 0$ is generated.

3.3.1 The KSVZ axion

The KSVZ model [148, 149] is the simplest invisible axion model and extends the SM by introducing a new SM singlet complex scalar field Φ and a SM singlet heavy colored fermion $\Psi = \Psi_L + \Psi_R$. The latter is coupled to Φ via a Yukawa-like coupling and hence acquires a mass after the SSB of the PQ symmetry. The Lagrangian of the model can be written as [152]

$$\mathcal{L}_{\text{KSVZ}} = |\partial_\mu \Phi|^2 + i\bar{\Psi}\not{D}\Psi - \left(y_\Psi \bar{\Psi}_L \Phi \Psi_R + \text{h.c.}\right) - V_{\text{KSVZ}}(\Phi) \tag{3.17}$$

and features a $U(1)_{\text{PQ}}$ symmetry acting on the fields as

$$\begin{cases} \Phi \ \ \to e^{i\alpha}\Phi\,, \\ \Psi_L \to e^{i\alpha/2}\Psi_L\,, \\ \Psi_R \to e^{-i\alpha/2}\Psi_R\,. \end{cases} \tag{3.18}$$

The potential $V_{\text{KSVZ}}(\Phi)$ has the usual Mexican-hat-like shape

$$V_{\text{KSVZ}}(\Phi) = \lambda_\Phi \left(|\Phi|^2 - \frac{v_a^2}{2}\right)^2\,, \tag{3.19}$$

where v_a denotes the vacuum expectation value of the scalar field. The KSVZ axion appears as the phase of the complex scalar field Φ, which in polar coordinates can be written as

$$\Phi = \frac{1}{\sqrt{2}}\left(v_a + \rho_a\right) e^{ia/v_a}\,. \tag{3.20}$$

After the SSB of the PQ symmetry, both the radial mode ρ_a and the fermion acquire a mass, which are respectively given by

$$m_{\rho_a} = \sqrt{2\lambda_\Phi} v_a\,, \quad m_\Psi = \frac{y_\Psi v_a}{\sqrt{2}}\,. \tag{3.21}$$

If the quartic coupling $\lambda_\Phi \sim \mathcal{O}(1)$, the radial mode is very heavy, while the mass of the fermion can be smaller than the symmetry breaking scale v_a for small values of the Yukawa coupling y_Φ. Neglecting the heavy radial mode, the Lagrangian after the SSB of the PQ symmetry is

$$\mathcal{L}_{\text{KSVZ}} = \frac{1}{2}(\partial_\mu a)^2 + i\bar{\Psi}\not{D}\Psi - \left(m_\Psi \bar{\Psi}_L \Psi_R e^{ia/v_a} + \text{h.c.}\right)\,. \tag{3.22}$$

By performing a field-dependent axial transformation

$$\Psi \to e^{-i\gamma_5 \frac{a}{2v_a}}\Psi\,, \tag{3.23}$$

and then integrating out the heavy fermion Ψ, one obtains the low-energy effective Lagrangian for the axion

$$\mathcal{L}^a_{\text{KSVZ}} = \frac{1}{2}(\partial_\mu a)^2 + \frac{g_s^2}{32\pi^2}\frac{a}{v_a} G^{\mu\nu}_a \tilde{G}^a_{\mu\nu}\,, \tag{3.24}$$

where the $G\tilde{G}$ term arises due to the anomalous nature of the transformation (3.23) under QCD. With the identification $v_a = f_a$ we recover the Lagrangian (3.10) with the anomaly coefficient $\xi = 1$ and with no derivative couplings to SM fields.

In the model discussed so far, the new fermion Ψ is neutral under hypercharge, so that $E/N = 0$. If instead Ψ carries an hypercharge similar to down-type or up-type quarks, we have $E/N = 8/3$ or $E/N = 2/3$, respectively.

3.3.2 The DFSZ axion

The DFSZ model [150, 151] contains two Higgs doublets H_u and H_d like the original PQWW model plus an additional SM singlet complex scalar field Φ. The presence of this additional scalar field allows to the decouple the PQ symmetry breaking scale from the electroweak scale, making this a viable model. An important difference with respect to the KSVZ model is that the DFSZ axion couples also to SM fermions at tree-level. The Lagrangian for scalars can be written as

$$\mathcal{L}_{\rm DFSZ}^{\rm scalars} = (D^\mu H_u)^\dagger (D_\mu H_u) + (D^\mu H_d)^\dagger (D_\mu H_d) + (\partial^\mu \Phi)^\dagger (\partial_\mu \Phi) - V_{\rm DFSZ}(H_u, H_d, \Phi)\,, \tag{3.25}$$

where $V_{\rm DFSZ}(H_u, H_d, \Phi)$ is a model-dependent potential which is responsible for the SSB of both the PQ and the EW symmetries, taking place at the scales v_Φ and v, respectively. The ratio of the VEVs of the two Higgs fields is parametrized as $\tan\beta = v_u/v_d$.

Depending on which of the two Higgs doublets are involved in the Yukawa couplings to SM fermions, two variants of the model are possible, dubbed DFSZ-I and DFSZ-II:

$$\mathcal{L}_{\rm DFSZ-I}^{Y} = -Y_u \bar{q}_L u_R H_u - Y_d \bar{q}_L d_R H_d - Y_e \bar{l}_L e_R H_d + \text{h.c.}\,, \tag{3.26}$$

$$\mathcal{L}_{\rm DFSZ-II}^{Y} = -Y_u \bar{q}_L u_R H_u - Y_d \bar{q}_L d_R H_d - Y_e \bar{l}_L e_R \tilde{H}_u + \text{h.c.}\,, \tag{3.27}$$

where $\tilde{H}_u = i\sigma_2 H_u^*$. The final effective Lagrangian for the DFSZ axion is given by (see [152] for more details)

$$\begin{aligned}\mathcal{L}_{\rm DFSZ}^{a} = \frac{1}{2}(\partial_\mu a)^2 + \frac{\alpha_s}{8\pi}\frac{a}{f_a} G_a^{\mu\nu}\tilde{G}^a_{\mu\nu} + \frac{g_{a\gamma}}{4}\frac{a}{f_a} F^{\mu\nu}\tilde{F}_{\mu\nu} + \left(\frac{1}{3}\cos^2\beta\right)\frac{\partial_\mu a}{2f_a}\bar{u}\gamma^\mu\gamma_5 u \\ + \left(\frac{1}{3}\sin^2\beta\right)\frac{\partial_\mu a}{2f_a}\bar{d}\gamma^\mu\gamma_5 d + C_e\frac{\partial_\mu a}{2f_a}\bar{e}\gamma^\mu\gamma_5 e\,,\end{aligned} \tag{3.28}$$

where

$$g_{a\gamma} = \frac{\alpha_{\rm EM}}{2\pi f_a}\left(\frac{E}{N} - \frac{2}{3}\frac{4+z}{1+z}\right)\,. \tag{3.29}$$

In the above expression $z \equiv m_u/m_d \simeq 0.493(19)$ [153] is the ratio between the masses of the up and down quarks, while $E/N = 8/3$ and $2/3$ the DFSZ-I and DFSZ-II models, respectively. The coupling of the axion to the electron in Eq. (3.28) for the two variants of the model is given by $C_e^{\rm DFSZ-I} = \sin^2\beta/3$ and $C_e^{\rm DFSZ-II} = -\cos^2\beta/3$. In the DFSZ model the axion decay constant is $f_a = v_a/6$, where $v_a \simeq v_\Phi$, so that, as already anticipated, f_a is decoupled from the EW scale.

3.4 Low-energy effective Lagrangian for the axion

As we have seen in the previous section, there are many possible concrete realizations of the QCD axion and we do not know yet which is the correct UV completion of the model, if any. To study the low-energy phenomenology of the axion, it is useful to write down an effective Lagrangian valid at energies smaller than the symmetry breaking scale f_a, see e.g. [154]. At energies between the EW and the QCD scales, the effective Lagrangian is

$$\mathcal{L}_{a,\rm eff}^{>\Lambda_{\rm QCD}} = \frac{1}{2}(\partial^\mu a)(\partial_\mu a) + \frac{\alpha_s}{8\pi}\frac{a}{f_a}G^i_{\mu\nu}\tilde{G}^{\mu\nu,i} + \frac{g_{a\gamma}}{4}aF_{\mu\nu}\tilde{F}^{\mu\nu} + \frac{\partial_\mu a}{2f_a}\sum_f C_{af}\bar{\psi}_f\gamma_5\gamma^\mu\psi_f\,, \tag{3.30}$$

where the index f runs over all SM fermions. The dependencies on the specific axion model are put inside the coefficients $g_{a\gamma}$ and C_f. In particular, the axion-photon coupling $g_{a\gamma}$ can be written as in Eq. (3.29). The KSVZ and DFSZ models introduced in the previous section fit this EFT description in the following way:

- The KSVZ model is characterized by $C_f = 0$ for each SM fermion at tree level and $E/N = 0$ in its simplest realization (see the discussion at the end of Sec. 3.3.1).
- In the DFSZ model, the ratio E/N is equal to 8/3 and 2/3 for the DFSZ-I and DFSZ-II scenarios, respectively. Moreover, there are non-vanishing tree-level couplings with fermions. The couplings to electrons, up and down quarks are respectively given by [152]

$$\textbf{DFSZ}-\textbf{I}: \quad C_e = \frac{\sin^2\beta}{3}\,, \quad C_u = \frac{\sin^2\beta}{3}\,, \quad C_d = \frac{\cos^2\beta}{3}\,, \tag{3.31}$$

$$\textbf{DFSZ}-\textbf{II}: \quad C_e = -\frac{\cos^2\beta}{3}\,, \quad C_u = \frac{\sin^2\beta}{3}\,, \quad C_d = \frac{\cos^2\beta}{3}\,. \tag{3.32}$$

  We remind the reader that β is related to the ratio between the VEVs of the two Higgs doublets H_u and H_d, see Sec. 3.3.2.

At energies below $\Lambda_{\rm QCD}$ gluons and quarks confine, so the effective Lagrangian must be written in terms of the couplings to nucleons and mesons. It also includes the potential for the axion generated by instanton effects. Thus, we can write the following effective Lagrangian

$$\mathcal{L}_{a,\rm eff}^{<\Lambda_{\rm QCD}} = \frac{1}{2}(\partial^\mu a)(\partial_\mu a) - m_a^2 f_a^2\left[1-\cos\left(\frac{a}{f_a}\right)\right] + \frac{g_{a\gamma}}{4} a F_{\mu\nu}\tilde{F}^{\mu\nu} + \frac{\partial_\mu a}{2f_a}\sum_f C_{af}\bar{\psi}_f\gamma_5\gamma^\mu\psi_f + \mathcal{L}_{a\pi}\,, \tag{3.33}$$

where the index f now runs over the light SM leptons and nucleons and $\mathcal{L}_{a\pi}$ denotes the axion-pion interaction Lagrangian, which is given by

$$\mathcal{L}_{a\pi} = \frac{\partial_\mu a}{f_a}\frac{C_{a\pi}}{f_\pi}\left(\pi^0\pi^+\partial^\mu\pi^- + \pi^0\pi^-\partial^\mu\pi^+ - 2\pi^+\pi^-\partial^\mu\pi^0\right)\,. \tag{3.34}$$

The couplings of the axion to nucleons and pions are given by [143, 152]

$$C_{ap} = -0.47(3) + 0.88(3)C_u - 0.39(2)C_d\,, \tag{3.35}$$

$$C_{an} = -0.02(3) + 0.88(3)C_d - 0.39(2)C_u\,, \tag{3.36}$$

$$C_{a\pi} = 0.12(1) + \frac{1}{3}(C_d - C_u)\,, \tag{3.37}$$

where $C_u = C_d = 0$ for the KSVZ axion, while for the DFSZ axion these coefficients depend on β as in Eqs. (3.31)-(3.32).

3.5 Axion-like particles

Along with the QCD axion, other light particles with similar properties arise from various extensions of the SM, such as the spontaneous breaking of additional global symmetries [155–159], Goldstone modes from string theory compactification [160, 161], or accidental symmetries [162, 163]. In particular, models of string theory generically predict the production of axions from the decay of moduli fields, which would appear at present time as a homogeneous axion background. This axion component can lead to various electromagnetic and gravitational signals, such as the axion-photon conversion in intergalactic media or the appearance of superradiance around spinning black holes. Analogously to the QCD axion, these axion-like particles would contribute to the present dark matter budget [164, 165] and might possibly play important roles in many other cosmological scenarios, including inflation, baryogenesis and dark energy. Since these axion-like particles are not necessarily linked to the PQ mechanism, their mass m_a and couplings to SM fields g_a do not in general follow the relation $m_a \propto g_a \propto 1/f_a$ described in the previous sections for the QCD axion. This means that the parameter space available for

axion-like particles is much broader. In the following, we refer to generic axion-like particles simply as "axions".

In analogy with what discussed for the QCD axion, the effective Lagrangian for a generic axion below the energy scale f_a can be written as

$$\mathcal{L}_{\rm eff} \supset \frac{1}{2}(\partial^\mu a)(\partial_\mu a) - \frac{1}{2}m_0^2 a^2 + \frac{\alpha_s}{8\pi}\frac{C_g}{f_a}\, a G^i_{\mu\nu}\tilde{G}^{\mu\nu,i} + \frac{1}{4}g^0_{a\gamma} a F_{\mu\nu}\tilde{F}^{\mu\nu}\,, \tag{3.38}$$

where $g^0_{a\gamma}$ is the axion-photon coupling and C_g is the (dimensionless) coupling of the axion to gluons. Note the presence of an explicit mass term m_0 for the axion in the Lagrangian (3.38), leading to a soft explicit breaking of the shift symmetry.[2] Within this model, the QCD axion theory is recovered by setting $C_g = 1$ and $m_0 = 0$.

Likewise for the QCD axion, the axion-gluon coupling in (3.38) induces an irreducible electric dipole moment (EDM) of the neutron n oscillating with time t via a chiral one-loop process as $d_n = g_d a_0 \cos(m_a t)$, where a_0 is the local value of the axion field at the position of the nucleus and g_d is the axion-EDM coupling. The Lagrangian term responsible for the neutron EDM can be expressed in terms of a Lorentz invariant operator as [135,136] (see the discussion in Sec. 3.1)

$$\mathcal{L} = -\frac{i}{2} g_d a \bar{n}\gamma_5 \sigma_{\mu\nu} n F^{\mu\nu}\,, \tag{3.39}$$

with

$$g_d = \frac{C_{an\gamma}}{m_n}\frac{C_g}{f_a}\,, \tag{3.40}$$

where m_n is the mass of the neutron and $C_{an\gamma} \approx 0.0033$. Note that for the QCD axion the coupling g_d is proportional to its mass (since $C_g = 1$ and $f_a \propto 1/m_a$), while it is generally independent of the mass for an axion-like particle, for which the one-to-one correspondence between f_a and m_a in Eq. (3.16) does not hold anymore. The quantity g_d appearing in Eq. (3.40) could also receive contributions from the coupling of the axion with fermions [136]. Here, we have focused on the irreducible component that results from the coupling of the axion with the gluon field, so the relation above relies on the other contributions being suppressed.

The Lagrangian in Eq. (3.38) can be formally mapped into a chiral axion Lagrangian by a rotation of the quark fields that makes the axion-gluon term disappear [154]. Once the effects of the explicit mass breaking are taken into account, the effective axion mass squared in the chiral representation reads [154,166]

$$m_a^2 = m_0^2 + \left(\frac{C_g}{f_a}\right)^2 F_\pi^2 m_\pi^2 \frac{z}{(1+z)^2} \simeq m_0^2 + \left[5.7\left(\frac{10^{12}\,\text{GeV}}{f_a/C_g}\right)\mu\text{eV}\right]^2\,, \tag{3.41}$$

where $m_\pi \approx 135\,\text{MeV}$ and $F_\pi \approx 92\,\text{MeV}$ are the mass and the decay constant of the neutral pion, respectively, and $z \equiv m_u/m_d \simeq 0.493(19)$ [153] is the ratio between the masses of the up and down quarks. Note that by setting $m_0 = 0$ and $C_g = 1$ we recover the relation (3.16) which holds for the QCD axion. In the case of generic axions, the effective mass m_a contains two contributions from the explicit symmetry breaking term m_0 and from the effective mixing of the axion with the neutral π, η, η' mesons (see e.g. Ref. [134]). The presence of m_0 prevents the axion from solving the strong-CP problem, and for sufficiently large values of m_0 Eq. (3.41) gives $m_a \approx m_0$ so that the axion mass can be treated as an independent parameter. In the cosmological analysis discussed in Chapter 4 we consider a regime in which the value of the effective mass transitions from being dominated by the QCD effects to the value m_0. Since we restrict the analysis to the region $m_a \gtrsim 0.1\,\text{meV}$, QCD effects can be ignored for sufficiently large values of $f_a \gtrsim 10^{10}\,\text{GeV}$.

[2] While an explicit mass term is forbidden for the QCD axion in order to solve the strong CP problem, it is present for a generic axion.

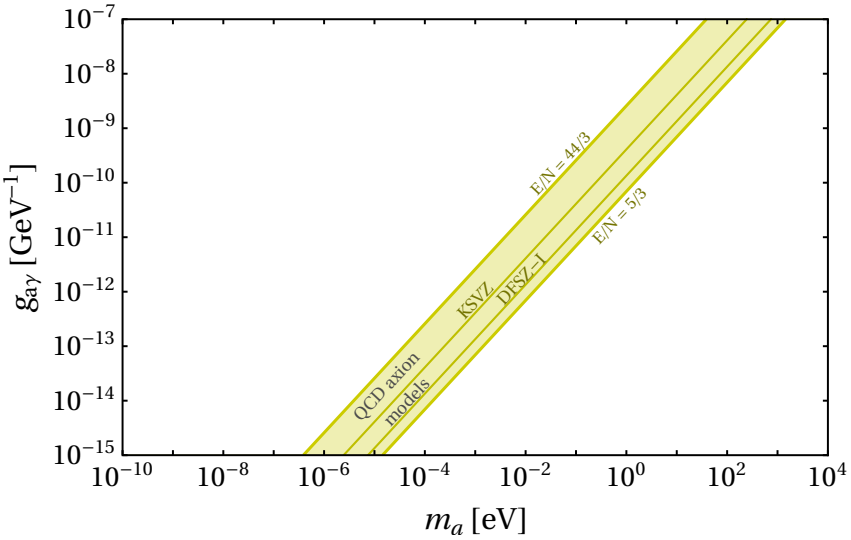

Figure 3.1: Parameter space for a generic axion. The yellow band represents the canonical QCD axion region, identified by the values $E/N = 5/3$ and $E/N = 44/3$ [167–169]. This includes the KSVZ ($E/N = 0$) and the DFSZ-I ($E/N = 8/3$) models. Note however that QCD axion solutions outside of this yellow band have also been constructed and are still viable [170–174].

In addition to the effective axion mass, the mapping onto the chiral axion Lagrangian leads to an effective coupling of the axion with the photon, with strength

$$g_{a\gamma} = g^0_{a\gamma} - \frac{\alpha_{\rm EM}}{3\pi}\frac{C_g}{f_a}\frac{4+z}{1+z} \approx g^0_{a\gamma} - 2.3\times 10^{-15}\left(\frac{10^{12}\,\text{GeV}}{f_a/C_g}\right)\text{GeV}^{-1}\,. \tag{3.42}$$

For the QCD axion $C_g = 1$ and

$$g^0_{a\gamma} = \frac{\alpha_{\rm EM}}{2\pi f_a}\frac{E}{N}\,, \tag{3.43}$$

so that we recover Eq. (3.29), which tells us that $g_{a\gamma} \propto 1/f_a \propto m_a$. For a generic axion, the coupling $g^0_{a\gamma}$ is instead a free parameter, so that the axion-photon coupling $g_{a\gamma}$ and the axion decay constant f_a can be treated as independent parameters. The same is true for $g_{a\gamma}$ and the axion mass m_a. This can be explicitly seen in Fig. 3.1, where we show the full parameter space available for a generic axion in the $g_{a\gamma} - m_a$ plane, together with the region of parameter space where canonical QCD axion models satisfying Eq. (3.43) lie.

3.6 Axion cosmology: the axion as a dark matter candidate

Axions might play an important role in many cosmological scenarios, including inflation, baryogenesis and dark energy. Most importantly, they represent a potentially good dark matter candidate. Axions can be produced in the early Universe via either thermal or non-thermal processes. Depending on the production mechanism and their mass, they can constitute a hot or a cold dark matter component. In the following we discuss the production of axions in the early Universe via both thermal and non-thermal processes, and we see which are the implication for axions as dark matter candidates.

3.6.1 Non-thermal production: the vacuum realignment mechanism

The non-thermal mechanism through which axions can be produced in the early Universe is closely connected to the PQ mechanism itself and the evolution of the axion potential. This

mechanism is usually referred to as *vacuum realignment* (VR) and leads to a population of cold axions, which thus represent a good CDM candidate (see e.g. [175–177]).

We start discussing the case of the QCD axion. As we have seen in Sec. 3.2, axions emerge as physical degrees of freedom after the SSB of the PQ symmetry. Since at this stage there is no potential for the axion, the quantity a/f_a can take any value between $-\pi$ and π. Then, at the QCD scale, instanton effects switch on a potential for the axion. When this happens, the axion field needs not to be at the minimum of this potential. This difference is parameterized by the misalignment angle, $\theta_i \equiv a_i/f_a$. If there is an initial misalignment, the axion field oscillates around the minimum of the potential. In this phase axions behave as a non-relativistic component and the energy stored in the oscillations contributes to the cold DM density.

In order to evaluate the relic abundance of cold axions produced via the VR mechanism, we need to distinguish among two scenarios:

- if the PQ symmetry is broken during inflation and then never restored (the *pre-inflation scenario*), inflation selects a single patch of the Universe with a given value of θ_i. This region is stretched to a size larger than the observable Universe, leading to a homogeneous value of the initial misalignment angle θ_i. The misalignment angle is thus a free, unpredictable parameter of the model. In this case the relic abundance of axions established via the VR mechanism is [152, 178, 179]

$$\Omega_a h^2 \simeq 0.12 \left(\frac{f_a}{9 \times 10^{11}\ \text{GeV}} \right)^{7/6} \theta_i^2 F(\theta_i)\,, \tag{3.44}$$

  where $F(\theta_i)$ is a factor that takes into account anharmonicities in the axion potential. Thus, in the pre-inflation scenario the PQ scale has to be $\lesssim 10^{12}$ GeV (or equivalently $m_a \gtrsim 6\ \mu$eV) for $\theta_i^2 F(\theta_i) \sim 1$, in order not to exceed the observed cold dark matter density, $\Omega_c h^2 \simeq 0.12$. Larger values of the PQ scale and smaller axion masses are possible if one allows for a fine-tuning of θ_i to a very small value. The first case is referred to as the "natural" axion, while the region with $f_a \gg 10^{12}$ GeV and $\theta_i \ll 1$ is the so-called "anthropic" window. In the pre-inflation scenario, topological defects produced when the SSB of the PQ symmetry takes place are inflated away. Thus, axion production from the decay of topological defects does not play any significant role;

- if instead the PQ transition happens after inflation, or the PQ symmetry is restored after inflation (the *post-inflation scenario*), the Universe remains divided in different patches, each one of them randomly sampling all possible values of θ_i with equal probability. The relic density of cold axions produced via vacuum realignment can then be computed by averaging the misalignment angle to $\langle \theta_i^2 \rangle^{1/2} = \pi/\sqrt{3} \simeq 1.81$. The axion relic abundance is thus [152, 178, 179]

$$\Omega_a h^2 \simeq 0.12 \left(\frac{f_a}{1.9 \times 10^{11}\ \text{GeV}} \right)^{7/6} . \tag{3.45}$$

  The right cold dark matter density is obtained for $f_a \simeq 2 \times 10^{11}$ GeV, or $m_a \simeq 30\ \mu$eV. Moreover, in the post-inflation scenario the decay of topological defects produced during the PQ phase transition via the Kibble mechanism [180] gives a contribution to the production of axions. This adds up to the one from the VR mechanism reported in Eq. (3.45). The contribution from the decay of cosmic axion strings is particularly relevant. This can be computed via numerical simulations and can be roughly one [181–183] or even two [184, 185] orders of magnitude higher than the one from the VR mechanism. This would increase the lower limit on the axion mass to $m_a \sim$ meV.

Analogously to the case of the QCD axion, ALPs can also be produced via the VR mechanism, thus contributing to the abundance of CDM [164, 178, 186]. For values of the axion decay

constant $f_a \leq 10^{16}$ GeV, axions can account for the entirety of the CDM abundance for an axion mass around $m_a \simeq 10^{-19}$ eV (see e.g. [178]). Given the very small values of the mass, these are commonly referred to as *ultralight axions* (ULAs). These particles arise for example from string theory compactifications [161] and have an associated de Broglie wavelength $\lambda_{\rm dB} \sim$ kpc, thus falling into the category of *fuzzy dark matter*. This results in a suppression of the structures at small scales, which might potentially solve the so-called "CDM small-scale crisis" [187, 188]. In order for ULAs to contribute to the energy density of DM, the oscillations of the axion field must start before matter-radiation equality. This sets a lower limit on the mass of ULAs to be a DM candidate given by $m_a \gtrsim 10^{-27}$ eV.

CMB observations give the constraints $m_a > 10^{-24}$ eV in order for ULAs to make up all the DM [189]. This is obtained using a combination of *Planck* temperature data, WMAP large-scale polarization data and small-scale data from the Atacama Cosmology Telescope (ACT) and the South Pole Telescope (SPT). This bound is improved to $m_a > 10^{-23}$ eV when *Planck* data are combined with those from Dark Energy Survey year 1 [190]. Even stronger bounds arise by exploiting the information encoded in the small-scale matter power spectrum. In particular, Lyman-α forest data yield the bound $m_a \gtrsim 10^{-21}$ eV [191].

3.6.2 Thermal production

Besides the non-thermal production discussed in Sec. 3.6.1, axions might also be produced thermally in the early Universe. Thermal axions are produced from scatterings involving particles belonging to the cosmological plasma at early times, see e.g. Refs. [192–200]. While axions produced from non-thermal processes are a natural cold DM candidate, thermally-produced axions can constitute either a hot, warm or cold DM component, depending on their mass. We will discuss in more details the thermal production of axions in the next chapter. In particular, we refer the reader to Sec. 4.3 for more details about the production of thermal axions resulting from processes due to the axion-photon and axion-gluon couplings.

3.7 Experimental searches for the axion

In this section we present a brief overview of the different experimental approaches aimed at detecting axions, see [179, 201–203] for more details. The state-of-the-art bounds in the axion-photon coupling-axion mass plane are summarized in Fig. 3.2, together with the projected sensitivities of some future experiments [204].

3.7.1 Axions in the lab

We start by describing the strategies to directly detect axions in laboratory experiments. These are all based on the so-called Primakoff effect, i.e. the conversion of axions and photons into each other in the presence of magnetic fields. It is common to divide these experimental approaches into three main categories:

- **Haloscopes**

  Haloscope experiments try to detect axions that constitute our local dark matter galactic halo. This means that haloscopes rely on the assumption that axions constitute the entirety of the DM. They are composed by a microwave cavity within a large superconducting magnet. This produces a strong magnetic field which triggers the conversion of axions into photons. The Axion Dark Matter eXperiment (ADMX) has reached the sensitivity to constrain axion dark matter in the μeV mass region [205], with a sensitivity to the axion-photon coupling of order of $g_{a\gamma} \sim 10^{-15}$ GeV^{-1}, see Fig. 3.2. The future MADMAX

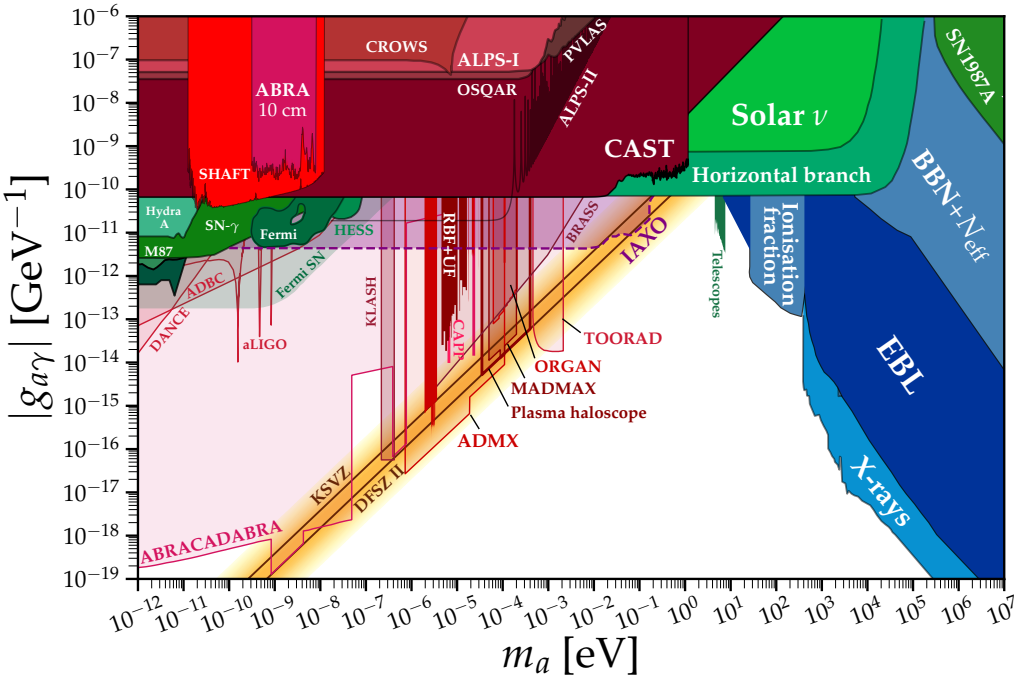

Figure 3.2: Summary of the constraints on the $g_{a\gamma} - m_a$ plane and projected sensitivities for future experiments, see the main text for details. Figure taken from [204].

experiment [206] at DESY will be able to probe axions with a coupling to photons down to $g_{a\gamma} \sim$ few $\times\, 10^{-14}$ GeV^{-1} for masses $m_a \sim 10^{-4}$ eV.

- **Helioscopes**

  Helioscope experiments try to detect axions emitted by the Sun. They consist of a magnet which aims at converting X-rays produced by the Sun into axions, when passing through a transverse magnetic field. The CAST helioscope at CERN has been able to exclude the dark red region of parameter space in Fig. 3.2. For axions with mass $m_a \lesssim 0.02$ eV, the CAST bound on the axion-photon coupling is $g_{a\gamma} < 0.66 \times 10^{-10}$ GeV^{-1} at 95% CL [207]. The successor of CAST is the International Axion Observatory (IAXO) [208], which aims at detecting solar axions with a sensitivity to the axion-photon coupling of $g_{a\gamma} \sim$ few $\times\, 10^{-12}$ GeV^{-1}. In case of no detection, the bounds on the axion-photon coupling will be improved by more than one order of magnitude with respect to the current limits from CAST. With respect to both haloscopes and LSW experiments, helioscopes are also sensitive to axion produced in the Sun via their couplings to electrons. The CAST experiment has been able to obtain constrains on the axion-electron coupling [209], but the strong astrophysical bounds on this coupling are far from the reach of lab experiments.

- **Light-shining-through-walls (LSW)**

  LSW experiments aim at producing and detecting axions in the lab. First, axions are produced by shining laser light through a strong magnetic field. These travel through a wall which blocks the laser light. A second magnetic field behind the wall will cause some of these axions to reconvert back to photons, which can then be detected. At the moment, LSW experiments have been able to set upper bounds on the axion-photon coupling of order of $10^{-6} - 10^{-7}$ GeV^{-1}, which are three order of magnitudes weaker than those from CAST. In Fig. 3.2 we can see the bounds from the ALPS experiment [210] at DESY and from the OSQAR [211] and CROWS [212] experiments at CERN. The future ALPS-II experiment [213] has the potential to increase the sensitivity on $g_{a\gamma}$ by more

than three orders of magnitude, allowing to probe axions with a coupling to photon down to $g_{a\gamma} \simeq 2 \times 10^{-11}$ GeV^{-1}. An advantage with respect to haloscopes and helioscopes is that LSW experiments do not rely on any astrophysical or cosmological assumption. On the other hand, contrary to both haloscopes and helioscopes, current and proposed LSW experiments will not be able to reach enough sensitivity to probe the region of parameter space of QCD axion models, as can be seen in Fig. 3.2.

3.7.2 Axions in astrophysics

Considerations about stellar evolution provides a very powerful way to constrain the axion couplings to photons, electrons, and nucleons, often exceeding the results achieved in laboratory experiments. Axions can be produced in the stellar interiors from the Primakoff conversion of thermal photons in the electrostatic field of electrons and nuclei. The emission of such axions provide an additional cooling mechanism for stars. In particular, the presence of this cooling process in the Sun would have an impact on its lifetime and even more on helioseismological observations and in the measured solar neutrino flux. These two considerations have been used to bound the axion-photon coupling to $g_{a\gamma} \leq 4.1 \times 10^{-10}$ GeV^{-1} [214] and $g_{a\gamma} \leq 7 \times 10^{-10}$ GeV^{-1} [215], respectively.

Even more stringent bounds are derived from horizontal-branch (HB) stars, which lead to the bound $g_{a\gamma} < 0.66 \times 10^{-10}$ GeV^{-1} at 95% CL [216], under the assumption that the axion-electron coupling is negligible.

As will be discussed in the next chapter, axions provide an additional source of energy loss from supernovae other than neutrino emission. Thus, considerations over the energy loss by supernovae represent a powerful probe to constrain the couplings of the axion to SM fields (see e.g. [217–221]).

3.7.3 Axions in cosmology

As discussed in Sec. 3.6, axions might play different roles in cosmology. Depending on how they are produced, axions can constitute either a hot or cold component, thus altering in different ways the cosmological evolution. Thus, cosmological observations, including measurements of CMB anisotropies and of the distribution of Large-Scale Structures (LSS), can play an important role in constraining the axion properties [222–232], providing complementary information to that obtained from laboratory experiments and astrophysical observations. This will be discussed at length in Chapter 4.

Chapter 4

Cosmological bounds on thermally-produced axion-like particles

In this chapter we focus on thermal axions, which are produced in the early Universe from scatterings involving particles belonging to the primordial thermal bath. In particular, we consider scattering processes that are due to the axion-gluon and axion-photon couplings in the effective Lagrangian (3.38). This thermal population of axions then decouples from the cosmological plasma at a temperature $T_d \gg m_a$ (i.e. when axions are still relativistic), with T_d being a function of the axion coupling with gluons or photons. We consider axion masses in the range between 10^{-4} and 100 eV. Depending on the value of the axion mass, axions play a different cosmological role and can behave as a hot, warm or cold DM component. Using the latest cosmological observations of the CMB by the *Planck* satellite and of BAO from galaxy surveys, we derive constraints on the axion mass and axion couplings to photons and gluons. See also Refs. [222–232] for other recent works dealing with cosmological bounds on the QCD axion and axion-like particles.

4.1 Extra radiation: the effective number of relativistic species

Any light species beyond the Standard Model (BSM) present in the early Universe contributes to the total energy density of radiation. Within the SM of particle physics, i.e. when only photons and neutrinos are accounted for, this can be written after electron-positron annihilation as

$$\rho_{\rm rad} = \rho_\gamma \left[1 + \frac{7}{8} \left(\frac{4}{11} \right)^{4/3} N_\nu \right] , \tag{4.1}$$

where $\rho_\gamma = (\pi^2/15) T^4$ is the energy density of CMB photons and N_ν is the *effective number of neutrino species*. Under the assumption that neutrinos decouple instantaneously from the cosmological plasma, thus not receiving any of the entropy that is released when electrons and positrons annihilate, the effective number of neutrino species is $N_\nu = 3$, as one naively expects. However, since neutrino decoupling is not really instantaneous, neutrinos with large momenta are partially heated during electron-positron annihilations, leading to non-thermal distortions in the neutrino distribution function. This results in a slightly higher value of N_ν. Moreover, the effects of neutrino flavour oscillations and finite-temperature QED corrections must also be taken into account. Taking into considerations all these subtleties, the effective number of neutrino species in the SM has been first computed in Ref. [233], finding that $N_\nu = 3.046$. More recently, the value $N_\nu = 3.044$ has been obtained independently in Refs. [234–237], where the

authors have updated previous calculations taking into account the effects of finite-temperature QED corrections to higher orders in the elementary electric charge and the complete expression of the collision integrals. Although $N_\nu = 3.044$ is the newly recommended value, the difference is irrelevant given the sensitivity of current experiments, hence we fix the value to $N_\nu = 3.046$ in the analysis discussed in this chapter.

The introduction of an effective number of neutrino species turns out to be convenient also to parametrize the possible presence of additional relativistic species BSM in the early Universe. In this case we speak of the *effective number of relativistic species*, $N_{\rm eff}$, which is defined as

$$N_{\rm eff} \equiv N_{\rm eff}^{\rm SM} + \Delta N_{\rm eff}\,, \tag{4.2}$$

where $\Delta N_{\rm eff}$ quantifies the deviation from the expected SM value for neutrinos, $N_{\rm eff}^{\rm SM} = N_\nu = 3.046$. For a light particle species Φ, and in the absence of entropy production after e^+e^- annihilation, $\Delta N_{\rm eff}$ does not change with time and can be simply obtained as the density of Φ (in the limit $m_\Phi \to 0$) relative to the density of a single massless neutrino species, i.e.

$$\Delta N_{\rm eff} \equiv \frac{\rho_\Phi(m_\Phi = 0)}{\rho_{\nu,\rm mless}} = \frac{\rho_\Phi(m_\Phi = 0)}{\frac{7}{8}\left(\frac{4}{11}\right)^{4/3}\rho_\gamma} = \frac{8}{7}\left(\frac{11}{4}\right)^{4/3}\left(\frac{g_\Phi}{g_\gamma}\right)\left(\frac{T_\Phi}{T_\gamma}\right)^4\,, \tag{4.3}$$

where g_Φ and $g_\gamma = 2$ are the number of internal degrees of freedom for the species Φ and for photons, respectively. In the particular case in which Φ is the axion a, $g_a = 1$. Let us assume that the species Φ decouples from the primordial plasma at a temperature T_d. After this epoch, particles of the cosmological plasma becoming non-relativistic release their entropy in the CMB photons, while the temperature of Φ is unaffected. This is analogous to what has been discussed in section 1.3.2 for cosmic neutrinos. Therefore, using entropy conservation we can write the ratio of the Φ and photon temperatures as

$$\frac{T_\Phi}{T_\gamma} = \left(\frac{g_{*s}(T_{\rm CMB})}{g_{*s}(T_d)}\right)^{1/3}\,, \tag{4.4}$$

where $g_{*s}(T_{\rm CMB}) = 2 + (7/11)N_{\rm eff}^{\rm SM} \simeq 3.94$. Inserting Eq. (4.4) into Eq. (4.3) yields

$$\Delta N_{\rm eff} \simeq 0.027 \times g_\Phi \left(\frac{g_{*s}(T_d)}{106.75}\right)^{-4/3}\,. \tag{4.5}$$

The value of $\Delta N_{\rm eff}$ as a function of the decoupling temperature T_d is shown in the top panel of Fig. 4.1 for scalar particles ($g_\Phi = 1$) like the axion, Weyl fermions ($g_\Phi = 7/4$) and massless gauge bosons ($g_\Phi = 2$). In the bottom panel of Fig. 4.1 we show instead the evolution of g_{*s} in the Standard Model as a function of the temperature, adopting the parametrization of [32].[1] Note that the higher is the temperature at which axions decouple from the cosmological plasma, the lower is the contribution to $\Delta N_{\rm eff}$. In particular, the lowest contribution to $\Delta N_{\rm eff}$ is obtained in case Φ decouples above the mass of the heaviest SM particle, the top quark ($m_t = 172.69 \pm 0.30$ [239]). In this case, all the particles of the SM annihilate when Φ is already decoupled from the cosmological plasma, so that the present temperature of Φ is maximally suppressed with respect to that of CMB photons. This minimum amount of extra radiation reads

$$\Delta N_{\rm eff} = \begin{cases} 0.027 & \text{Goldstone boson (spin-0)}\,, \\ 0.047 & \text{Weyl fermion (spin-1/2)}\,, \\ 0.054 & \text{Massless gauge boson (spin-1)}\,. \end{cases} \tag{4.6}$$

[1] See also [238] for a different parametrization and [198] for a comparison of the two approaches and results. Note in particular that the difference is negligible for decoupling temperatures $T_d \lesssim 100\,\text{MeV}$ (see Fig. 13 of [198]) corresponding to the range in reach of current experiments for light axions, see Fig. 4.7. Although a higher decoupling temperature can be probed for heavier axions of mass $m_a \gtrsim 1\,\text{eV}$, we expect that our choice for the parametrization of $g_{*s}(T)$ would not significantly impact on the final constraints.

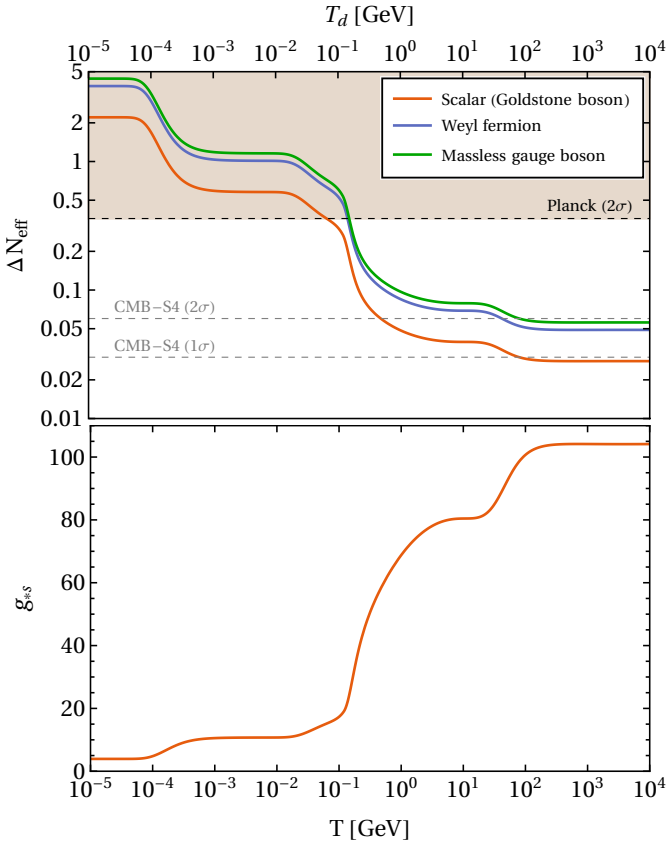

Figure 4.1: *Top panel*: $\Delta N_{\rm eff}$ as a function of the decoupling temperature T_d for different particle species. *Bottom panel*: evolution of the effective number of degrees of freedom in entropy in the Standard Model, g_{*s}, as a function of the temperature T. This is obtained following the analysis of [32].

This tells us that, if future cosmological surveys will reach the sensitivity to probe $\Delta N_{\rm eff} = 0.027$, they will be able to detect (or exclude the presence of) any particle species BSM that has ever been in thermal equilibrium with the cosmological plasma.

At the moment, the most up-to-date constraint on $N_{\rm eff}$ comes from the *Planck* collaboration, which at 68% CL obtains [6]

$$N_{\rm eff} = 2.99 \pm 0.17\,, \tag{4.7}$$

using a combination of TT,TE,EE+lowE data from the 2018 data release, plus observations from BAO. This is consistent with the SM prediction, $N_{\rm eff}^{\rm SM} = 3.046$. Future surveys, like CMB-S4, will be extremely sensitive to the deviation of $N_{\rm eff}$ from its SM value, with a forecast constraint $\Delta N_{\rm eff} \lesssim 0.06$ at 95% CL [11, 240].

4.2 Relic abundance of thermal axions

As discussed at the beginning of the chapter, we are considering a scenario in which axions are produced thermally in the early Universe and then decouple from the cosmological plasma while they are still relativistic. The present number density of axions $n_a(T_0)$, where T_0 is the temperature of cosmic photons today, is related to the photon number density n_γ due to entropy conservation as

$$n_a(T_0) = \left(\frac{g_{*s}(T_0)}{g_{*s}(T_d)}\right)\frac{n_\gamma}{2}\,. \tag{4.8}$$

Setting $g_{*s}(T_0) \simeq 3.94$ and $n_\gamma \simeq 411\,\mathrm{cm}^{-3}$ [82,83], the fractional abundance of relativistic axions at present is

$$\omega_a \equiv \Omega_a h^2 \simeq \left(\frac{m_a}{130\,\mathrm{eV}}\right)\left(\frac{g_{*s}(T_d)}{10}\right)^{-1}\,, \tag{4.9}$$

where Ω_a is the energy density of axions in units of the critical density $\rho_{\rm crit} = 3H_0^2/(8\pi G)$, H_0 is the Hubble constant, and $h = H_0/(100\ \mathrm{km\,s^{-1}\,Mpc^{-1}})$ is the reduced Hubble constant. The dependence on the decoupling temperature T_d in Eq. (4.9) can be recast into a dependence on $\Delta N_{\rm eff}$ using Eq. (4.5) with $g_\Phi = g_a = 1$. We can thus rewrite the fractional axion abundance as a function of $\Delta N_{\rm eff}$ as

$$\omega_a \simeq 0.011\left(\frac{m_a}{\mathrm{eV}}\right)\Delta N_{\rm eff}^{3/4}\,. \tag{4.10}$$

To have a better physical insight on the CMB constraints on axions, it is also useful to determine whether axions behave as a hot or a cold DM component at the epoch of CMB decoupling. This depends on both the axion mass and decoupling temperature. An estimate is obtained by computing the ratio between the thermally-averaged momentum and the axion mass at recombination, which is given by [224]

$$\frac{\langle p_{a,\rm rec}\rangle}{m_a} \approx 2.7\,\frac{T_{a,\rm rec}}{m_a} = 2.7\,\frac{T_{\rm CMB}}{m_a}\left(\frac{g_{*s}(T_{\rm CMB})}{g_{*s}(T_d)}\right)^{1/3}\,. \tag{4.11}$$

At the epoch of recombination, axions are hot DM provided $\langle p_{a,\rm rec}\rangle/m_a \gtrsim 1$. In the opposite limit $\langle p_{a,\rm rec}\rangle/m_a \ll 1$, axions behave as a CDM component. In the first case, axions are relativistic at recombination and the parameter space is bounded directly by the CMB constraints on $N_{\rm eff}$. In the second case, where axions do not contribute to $N_{\rm eff}$ and are non-relativistic at recombination, the parameter space is constrained by requiring that the relic abundance of thermal axions does not exceed that of CDM, namely $\omega_a \leq \omega_c$. In the intermediate regime, say $\langle p_{a,\rm rec}\rangle/m_a \lesssim 1$, axions act instead as warm dark matter. In this case, only a full detailed analysis can give us information about how the axion parameter space is bounded, as we discuss in more details in Sec. 4.5.2.

We conclude this section by stressing that cosmology is sensitive to two parameters related to the physics of the axion: the axion mass m_a and the axion contribution to $\Delta N_{\rm eff}$ (or, equivalently, the axion decoupling temperature T_d, since the two parameters are related via Eq. (4.5)). Since the ultimate goal of this analysis is to constrain the axion mass and the axion couplings to the photon and gluon fields, we need a relation between these couplings and T_d. This will be the subject of Sec. 4.3.

4.3 Thermal production and decoupling of axions from the cosmological plasma

As already discussed, thermal axions are produced from scattering processes between particles belonging to the primordial thermal bath. Axions then decouple from the cosmological plasma when the production rate becomes of order of the expansion rate $H(T)$. Since the production rate depends both on the axion couplings g_a and temperature, imposing the freeze-out condition yields a relation between g_a and T_d.

In more details, we first introduce the thermal axion production rate $\gamma \equiv \mathrm{d}n_a/\mathrm{d}t$, which expresses the rate of production of thermal axions from the primordial plasma times the number density of axions n_a, as derived from the imaginary part of the axion self-energy (see Refs. [193, 241–243] for more details). The evolution of the axion number density $n_a = n_a(T)$ proceeds according to a Boltzmann equation,

$$\frac{\mathrm{d}n_a}{\mathrm{d}t} + 3H(T)n_a = \gamma\left(1 - \frac{n_a}{n_a^{\rm eq}}\right)\,, \tag{4.12}$$

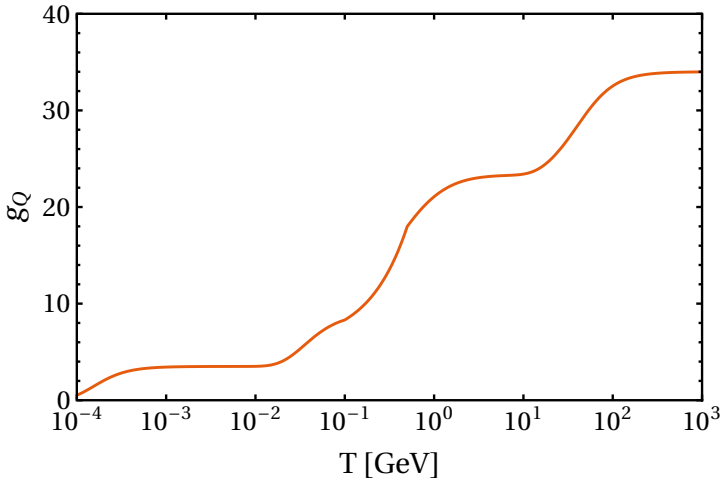

Figure 4.2: The effective number of charged relativistic degrees of freedom $g_Q(T)$ as a function of the temperature of the primordial plasma T.

where $n_a^{\rm eq}(T) = (\zeta(3)/\pi^2) g_a T^3$ is the number density at equilibrium. As discussed above, freeze-out occurs when the axion production rate ceases to keep pace with the expansion rate, at the decoupling temperature T_d such that

$$H(T_d) \simeq \Gamma(T_d, g_a) \equiv \gamma(T_d, g_a)/n_a^{\rm eq}(T_d)\,. \tag{4.13}$$

The relation between T_d and g_a is provided by the expression above, once one is able to write down the axion production rate in terms of the axion coupling under consideration. Adopting a phenomenological approach, in our analysis we assume that either axion-photon or axion-gluon processes are dominant in establishing a thermal population of axions. The two cases will be discussed separately in the following subsections.

4.3.1 Axion-photon processes

The leading mechanism contributing to the production of thermal axions due to an axion-photon coupling is the Primakoff effect, which describes the resonant conversion of photons into axions in the presence of the strong magnetic field of charged particles. Production in the primordial plasma proceeds with the rate [225, 244, 245]

$$\Gamma_{Q\gamma\to Qa} \simeq \frac{\alpha_{\rm EM}\pi^2 g_{a\gamma}^2}{36\zeta(3)} \left[\ln\left(\frac{T^2}{m_\gamma^2}\right) + 0.8194\right] n_Q\,, \tag{4.14}$$

where $m_\gamma = T/(6\alpha_{\rm EM}\sqrt{g_Q(T)})$ is the plasmon mass, $g_Q(T) = \sum_i Q_i^2 g_{*,i}(T)$ is the effective number of relativistic degrees of freedom for the i-th charged species of charge Q_i, and $n_Q = \sum_i Q_i^2 n_i \equiv (\zeta(3)/\pi^2) g_Q(T) T^3$ is the effective number density of charged particles in the cosmological plasma. In principle, to derive the evolution of $g_Q(T)$ with the temperature we would need to isolate the contribution to $g_*(T)$ from each charged particle species and weight it by the particle's charge squared. This is particularly challenging during the QCD phase transition epoch, where the total contribution to $g_*(T)$ is usually derived from lattice QCD results (see e.g. [32, 238, 246]). To overcome this issue, we first compute g_Q as described above (i.e. $g_Q = \sum_i Q_i^2 g_{*,i}$) for temperatures $T < 100\,\text{MeV}$ and $T > 500\,\text{MeV}$, with [247]

$$g_{*,i}(T) = \frac{15 g_i}{\pi^4} \int_{x_i}^{\infty} \frac{(y^2 - x_i^2)^{1/2}}{e^y \pm 1} y^2 dy\,, \tag{4.15}$$

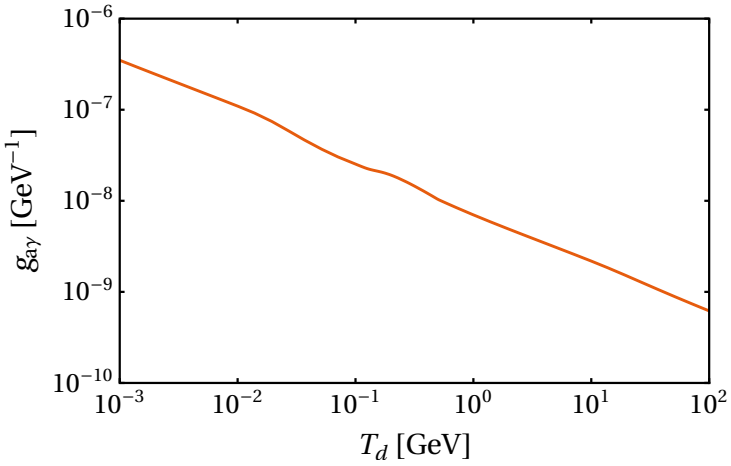

Figure 4.3: Axion-photon coupling $g_{a\gamma}$ as a function of the decoupling temperature T_d, as described in Eq. (4.16).

where the + (−) sign is for bosons (fermions) and $x_i = m_i/T$. The behavior of g_Q within the temperature range $100\,\text{MeV} < T < 500\,\text{MeV}$, where the QCD phase transition takes place, is then reconstructed by interpolating between the two regimes previously obtained. The result is shown in Fig. 4.2.

The Primakoff effect establishes a thermal population of axions that decouples from the primordial plasma at the temperature T_d, which is related to the axion-photon coupling $g_{a\gamma}$ by [245]

$$g_{a\gamma} \simeq 10^{-8} \times \frac{\sqrt{g_*}}{g_Q} \left(\frac{T_d}{\text{GeV}}\right)^{-1} \text{GeV}^{-1}\,. \tag{4.16}$$

The relation between $g_{a\gamma}$ and T_d expressed in Eq. (4.16) is shown Fig. 4.3. As one naively expects, the higher is the axion-photon coupling the longer axions stay coupled to the cosmological plasma, resulting in a lower decoupling temperature.

In addition to the thermal production via the Primakoff effect, a non-zero coupling $g_{a\gamma}$ would also induce the axion to decay into a pair of photons. The rate for the decay of axions in two photons is given by (see e.g. Refs. [245, 248, 249])

$$\Gamma_{a\to\gamma\gamma} = \frac{g_{a\gamma}^2 m_a^3}{64\pi} \simeq 4.97 \times 10^{-44} \left(\frac{g_{a\gamma}}{10^{-7}\,\text{GeV}^{-2}}\right)^2 \left(\frac{m_a}{\text{eV}}\right)^3 \text{GeV}\,. \tag{4.17}$$

The decay of axions would be accompanied by a reduction of their cosmological abundance and an injection of photons with energy $E_\gamma = m_a/2$. In our analysis we are assuming that axions are a stable relic on cosmological timescales and we are not accounting for a possible conversion of matter into radiation. This is true provided that the decay time of the axion is larger than the current age of the Universe, i.e. $\tau_D \sim \Gamma^{-1}_{a\to\gamma\gamma} \gg H_0^{-1}$. Using the expression for the decay rate in Eq. (4.17), the condition of stability of axions leads to the requirement

$$\frac{\Gamma_{a\to\gamma\gamma}}{H_0} \simeq 3.48 \times 10^{-2} \left(\frac{g_{a\gamma}}{10^{-7}\,\text{GeV}^{-1}}\right)^2 \left(\frac{m_a}{\text{eV}}\right)^3 \ll 1\,. \tag{4.18}$$

In our final results we do not consider the region of parameter space in which the condition (4.18) is not satisfied (see the red hatched areas in Fig. 4.8 and 4.9).

4.3.2 Axion-gluon processes

In case the dominant axion coupling is the one with gluons, a thermal population of axions can be established through scatterings off the quark-gluon plasma at temperatures above the

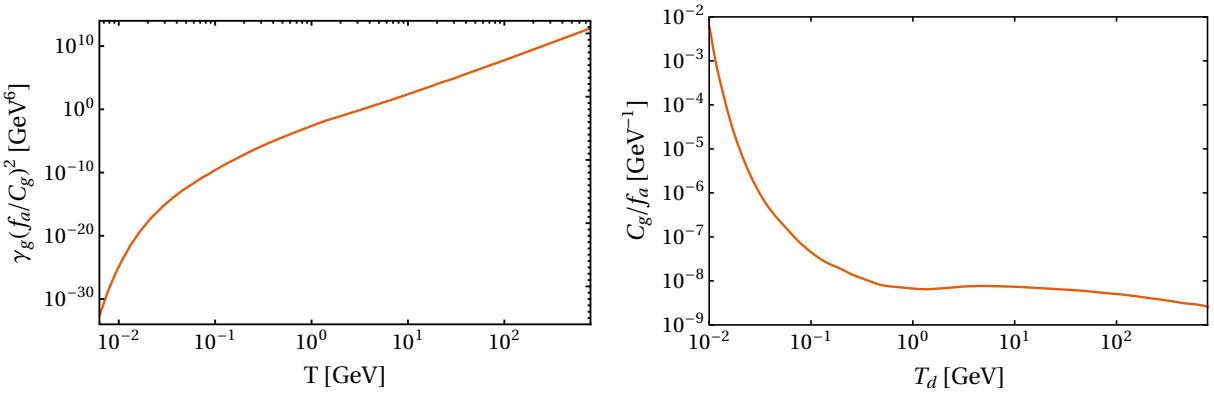

Figure 4.4: *Left panel*: Axion production rate times the inverse axion-gluon coupling squared, $\gamma_g (f_a/C_g)^2$, as a function of the temperature T of the primordial plasma. This is a reproduction of Figure 2 of Ref. [197]. *Right panel*: Axion-gluon coupling, parametrized by the inverse axion decay constant C_g/f_a, as a function of the decoupling temperature T_d. The freeze-out condition in Eq. (4.13) is imposed together with the axion production rate shown in the left panel to obtain T_d.

QCD phase transition [193–195], and through hadronic scatterings (mainly pion scatterings) at temperatures below the QCD phase transition [250–255]. In our analysis we adopt the latest result for the axion production rate obtained in Ref. [197]. As anticipated above, at a temperature $T_N \simeq 2\,\text{GeV}$ well above the QCD phase transition,[2] the axion production rate γ_g is regulated by gluon scattering processes, quark/antiquark annihilations and scatterings between quarks/antiquarks and gluons:

$$\begin{aligned} g + g &\longrightarrow g + a\,, \\ q + \bar{q} &\longrightarrow g + a\,, \\ q/\bar{q} + g &\longrightarrow q/\bar{q} + a\,. \end{aligned} \tag{4.19}$$

Instead, at temperatures below the QCD phase transition, the leading contribution is given by pion scatterings derived from the effective Lagrangian (3.34):

$$\begin{aligned} \pi^+\pi^- &\longrightarrow \pi^0 + a\,, \\ \pi^+/\pi^- + \pi^0 &\longrightarrow \pi^+/\pi^- + a\,. \end{aligned} \tag{4.20}$$

As shown in [196], the calculation for the axion-pion scattering rates using chiral perturbation theory (ChPT) is not reliable above the temperature $T_{\text{ChPT}} \simeq 62\,\text{MeV}$, since at higher temperatures perturbations can no longer be neglected and the effective field theory description breaks down. To overcome this issue, the axion production rate between the temperatures T_{ChPT} and T_N has been obtained in Refs. [197, 198] by interpolating between the two regimes. The result, reported in Figure 2 of Ref. [197], provides us with the most up-to-date description for the function $\gamma_g f_a^2$.[3] We reproduce this result in Fig. 4.4 (left panel), where we show $\gamma_g f_a^2$ as a function of the temperature of the primordial plasma.

Once we have an expression for the axion production rate, we impose the condition of thermal production at freeze-out in Eq. (4.13) to obtain a relation between the axion-gluon coupling C_g/f_a and the decoupling temperature T_d. This is shown in Fig. 4.4 (right panel).

[2] At this temperature the strong coupling constant is $\alpha_s(T_N) \simeq 0.3$, thus for $T < T_N$ a perturbative treatment of QCD processes is no longer justified.

[3] Note that in Ref. [197] the authors study the case of the QCD axion, for which we recall that $C_g = 1$. The result for the axion production rate can be adopted also for generic axions through the mapping $f_a \to f_a/C_g$.

Parameter	Prior
ω_b	$[0.005, 0.1]$
θ_s	$[0.5, 10]$
τ	$[0.01, 0.8]$
$\ln(10^{10} A_s)$	$[1.61, 3.91]$
n_s	$[0.8, 1.2]$
ω_{c+a}	$[0.001, 0.99]$
$\Delta N_{\rm eff}$	$[0, 1]$
$\log(m_a/{\rm eV})$	$[-6, 4]$

Table 4.1: Priors used for the cosmological parameters in the ΛCDM+$\Delta N_{\rm eff}$+m_a model. For the ΛCDM+$\Delta N_{\rm eff}$ the same priors are used, except for the axion mass which is fixed to a specific value.

4.4 Data sets and analysis

We now discuss the data sets composition and the software used in the analysis. We use the most recent *Planck* 2018 data of CMB temperature and polarization anisotropies [6] together with BAO data from galaxy surveys, consisting of BOSS DR12 [13], 6dFGS [14] and SDSS-MGS [15]. To compute the theoretical predictions we employ a modified version of the publicly-available Boltzmann solver code `CAMB`, which correctly includes the propagation of the axion by incorporating a Bose-Einstein distribution function.[4] This is an advance compared with the majority of previous approaches, in which cosmological constraints on bosonic thermal relics had been obtained by treating them as additional effective neutrino species (see instead Refs. [224, 256] for a few exceptions). The Markov Chain Monte Carlo sampler `CosmoMC` [257] is then used to derive constraints on the parameters of the model. We check the convergence of the chains by controlling that the Gelman-Rubin parameter $R - 1 < 0.01$, with the first 30% of total steps discarded as burn-in. The posterior distributions are then obtained and plotted using the `GetDist` package [258].

Following the discussions in the previous sections, we extend the standard cosmological model (or ΛCDM model) with two additional parameters:[5] the axion mass m_a and its contribution to the effective number of relativistic species, $\Delta N_{\rm eff}$. We refer to this as the ΛCDM+$\Delta N_{\rm eff}$+m_a model. The vector spanning the eight-dimensional parameter space is represented by

$$\Theta_{\Delta N_{\rm eff}+m_a} \equiv \{\omega_b,\, \theta_s,\, \tau,\, \ln(10^{10} A_s),\, n_s,\, \omega_{c+a},\, m_a,\, \Delta N_{\rm eff}\}\,, \tag{4.21}$$

where $\omega_b \equiv \Omega_b h^2$ is the physical density of baryons, θ_s is the angular acoustic scale at recombination, τ is the reionization optical depth, A_s is the normalization of the power spectrum, and n_s is the scalar spectral index, see Ref. [6] for additional information. In addition, $\omega_{c+a} \equiv \omega_c + \omega_a$ labels the density of CDM plus axions. The latter parametrization is useful because for certain values of m_a thermal axions behave as CDM, so that in this case ω_{c+a} quantifies the total amount of cold particles. The "non-axionic" CDM abundance can then be derived as $\omega_c = \omega_{c+a} - \omega_a$, where ω_a is computed via Eq. (4.10). Given the modification on ω_{c+a}, the first six parameters in the vector $\Theta_{\Delta N_{\rm eff}+m_a}$ describe the ΛCDM model. The priors for each component of $\Theta_{\Delta N_{\rm eff}+m_a}$ are reported in Table 4.1. In particular, we draw the values of $\Delta N_{\rm eff}$ from a flat

[4] This code has been previously used in Ref. [224] to derive the cosmological constraints on thermal QCD axions in low-reheating scenarios.

[5] We stress again that for a specific QCD axion model, the mass and decoupling temperature are related via Eq. (3.41) with $m_0 = 0$ and $C_g = 1$. Hence, in the case of the QCD axion we would have only one additional parameter with respect to ΛCDM, instead of the two parameters used here, since $g_{a\gamma} \propto m_a \propto 1/f_a$.

prior $\Delta N_{\rm eff} \in [0, 1]$, for the axion mass we set a logarithmic prior as $\log(m_a/{\rm eV}) \in [-6, 4]$, while the list of flat priors on the other cosmological parameters are chosen so that the results of ΛCDM are recovered when the axion field is removed. We assume that only one of the active neutrino species is massive, and we fix the sum of neutrino masses to the minimal value allowed by flavour oscillation experiments in the normal hierarchy scenario, $\sum m_\nu = 0.06\,{\rm eV}$. Once the `CAMB` model is run with this setup and the model has been constrained, the bounds on $\Delta N_{\rm eff}$ are then converted into constraints on the axion couplings to photons and gluons following the prescription outlined in Sec. 4.3.

We also perform a series of runs, here ΛCDM+$\Delta N_{\rm eff}$, in which the mass of the axion is fixed and we allow $\Delta N_{\rm eff}$ to vary over the range in Table 4.1, thus implementing the runs over the parameter space spanned by the vector

$$\Theta_{\Delta N_{\rm eff}} \equiv \{\omega_b,\, \theta_s,\, \tau,\, \ln(10^{10} A_s),\, n_s,\, \omega_{c+a},\, \Delta N_{\rm eff}\}\,. \tag{4.22}$$

We perform 9 different set of runs (each one with only *Planck* data and in combination with BAO) with a different value of the axion mass chosen within

$$m_a \in \{10^{-4},\, 10^{-3},\, 10^{-2},\, 0.1,\, 1,\, 3,\, 10,\, 30,\, 100\}\ {\rm eV}\,. \tag{4.23}$$

This procedure allows us to determine an upper bound on $\Delta N_{\rm eff}$, and ultimately on the axion couplings, as a function of the axion mass. These results have been used to picture the constraints on $\Delta N_{\rm eff}$ in Fig. 4.7 and then on the axion couplings to photons and gluons, see Figs. 4.8 and 4.9, respectively.

4.5 Results of the Monte Carlo analysis

In this section we discuss the results of the Monte Carlo analysis for the two models considered in this work, namely ΛCDM+$\Delta N_{\rm eff}$+m_a and ΛCDM+$\Delta N_{\rm eff}$ with fixed axion mass. Then, in Sec. 4.6 we translate the bounds on $\Delta N_{\rm eff}$ into bounds on the axion couplings to photons and gluons, which are the quantities that we want eventually to constrain.

4.5.1 ΛCDM+$\Delta N_{\rm eff}$+m_a model

We first discuss the results for the run with the full set of parameters spanned by $\Theta_{\Delta N_{\rm eff}+m_a}$. The corresponding constraints on the cosmological parameters of the ΛCDM+$\Delta N_{\rm eff}$+m_a model are reported in Table 4.2, where we also include the bounds on the axion couplings to photons and gluons (see Sec. 4.6 for details). Figure 4.5 shows the constraints obtained using *Planck* 2018 TT,TE,EE+lowE data (red) only and with the additional inclusion of BAO data (blue). Note in particular the second peak of the probability distribution of m_a and the degeneracy of $\Delta N_{\rm eff}$ with H_0 and ω_{c+a}. The shape of the 1D distribution of m_a can be understood as follows. At smaller masses, the axion is fully relativistic at the CMB epoch and the constraints mostly come from the axion contribution to $\Delta N_{\rm eff}$. For very small masses, say $m_a < 10^{-2}\,{\rm eV}$, the axion behaves as dark radiation and it is mostly constrained by its contribution to $\Delta N_{\rm eff}$. This explains why the distribution for low masses is flat. For intermediate masses, $10^{-2}\,{\rm eV} \lesssim m_a \lesssim 1\,{\rm eV}$, the axion behaves as hot dark matter. Thus, it must decouple early enough so that its contribution to the energy density budget is sufficiently diluted. This explains the sharp cutoff in the 1D distribution. At higher masses, the axion effectively behaves as a cold dark matter component. The second peak in the 1D distribution corresponds to the values of the axion mass that satisfy the cosmological constraints on the abundance of cold dark matter. The inclusion of BAO data better constrains the late-time dynamics of the Universe, thus sharpening the second peak in the 1D distribution of m_a. In more detail, BAO data exclude the high-ω_{c+a}/low-H_0 region of the parameter space (see the corresponding 2D contours in Fig. 4.5). This effect, combined

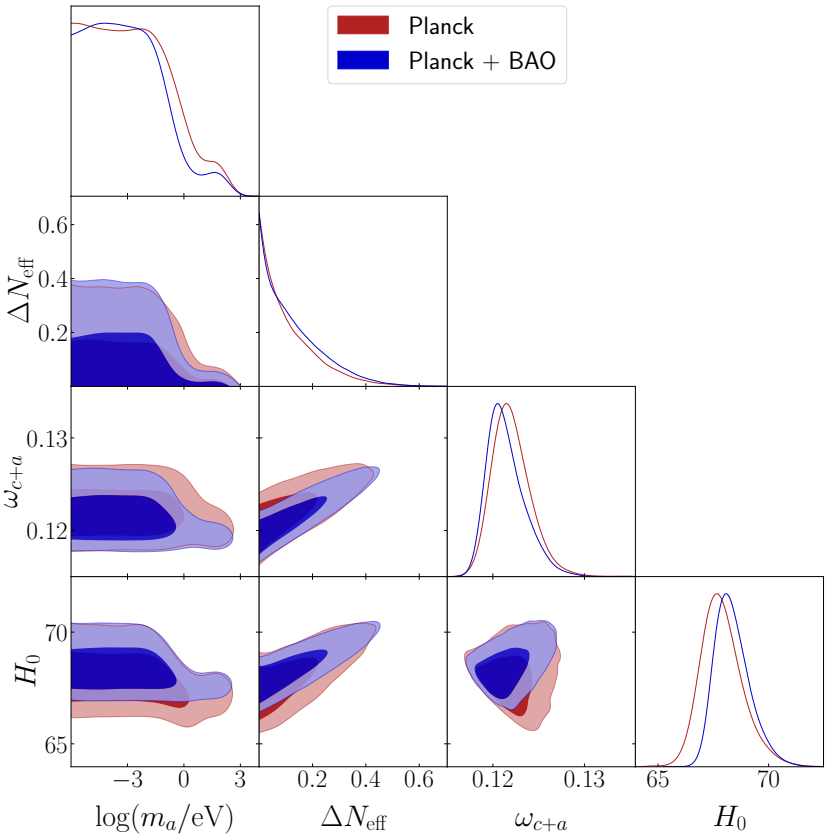

Figure 4.5: Triangle plot including 2D and 1D posteriors for different cosmological parameters in the ΛCDM+$\Delta N_{\rm eff}$+m_a model. Note in particular the shape of the 1D distribution of $\log(m_a)$ and the impact of including BAO data in the analysis. See text for details.

with the degeneracy between the Hubble constant and $\Delta N_{\rm eff}$, explains the behaviour of the 1D distribution of $\Delta N_{\rm eff}$ when BAO data are included in the analysis (for a detailed discussion, see Sec. 4.5.2). As obtained in previous literature, we note that hot axions may feebly mitigate the tension over the different Hubble constant measurements (see Ref. [259] for a recent review) although they do not erase it [260].

4.5.2 ΛCDM+$\Delta N_{\rm eff}$ model with fixed axion mass

We now turn to the discussion of the series of runs for the ΛCDM+$\Delta N_{\rm eff}$ model, with the axion mass fixed to specific values as discussed in Sec. 4.4. Each run leads to a constraint on $\Delta N_{\rm eff}$ and on the parameters of ΛCDM, as shown in Fig. 4.6 for the specific case with $m_a = 10^{-2}$ eV (left panel) and $m_a = 10$ eV (right panel).

For small values of m_a the axion is a hot DM component which greatly contributes to $\Delta N_{\rm eff}$ while not affecting ω_a. However, the increase in $\Delta N_{\rm eff}$ leads to an increased ω_c, as shown from the correlation between the two quantities in the left panel of Fig. 4.6. As CMB temperature and polarization data pin down the angular scale of sound horizon θ_s, an increase in $\Delta N_{\rm eff}$ also leads to a higher H_0. On the other hand, a massive axion would actively contribute to the CDM budget while not affecting $N_{\rm eff}$, see the right panel of Fig. 4.6. In this latter case, we obtain the bounds over ΛCDM although the total dark matter budget is given by the contribution $\omega_c + \omega_a$. This is a modification of late-time cosmology that does not alter the numerator of θ_s but it changes the angular diameter distance at the denominator, so that an increase in the CDM budget is compensated by a decrease in H_0. This explains why the correlation between

Parameter	*Planck* TT,TE,EE+lowE	*Planck* TT,TE,EE+lowE+BAO
ω_b	0.02242 ± 0.00017	0.02249 ± 0.00015
H_0	$67.90^{+0.75}_{-1.1}$ km s^{-1} Mpc^{-1}	$68.38^{+0.58}_{-0.94}$ km s^{-1} Mpc^{-1}
τ	$0.0553^{+0.0074}_{-0.0082}$	0.0563 ± 0.0079
$\ln(10^{10} A_s)$	$3.051^{+0.016}_{-0.017}$	3.051 ± 0.017
n_s	$0.9676^{+0.0050}_{-0.0061}$	$0.9700^{+0.0044}_{-0.0053}$
ω_{c+a}	$0.1221^{+0.0016}_{-0.0024}$	$0.1215^{+0.0014}_{-0.0025}$
$\Delta N_{\rm eff}$	< 0.337	< 0.358
m_a	< 11.66 eV	< 3.14 eV
$g_{a\gamma}$	$< 2.84 \times 10^{-8}$ GeV^{-1}	$< 3.16 \times 10^{-8}$ GeV^{-1}
C_g/f_a	$< 6.98 \times 10^{-8}$ GeV^{-1}	$< 1.06 \times 10^{-7}$ GeV^{-1}
g_d	$< 2.47 \times 10^{-10}$ GeV^{-2}	$< 3.77 \times 10^{-10}$ GeV^{-2}

Table 4.2: Constraints on the cosmological parameters for the ΛCDM+$\Delta N_{\rm eff}$+m_a model, obtained both from using *Planck* 2018 TT,TE,EE+lowE datasets alone and in combination with BAO. The limits on the first six parameters are reported at 68% CL, whereas the upper bounds on m_a, $\Delta N_{\rm eff}$, and the couplings are at 95% CL.

these quantities in the right panel of Fig. 4.6 is negative.

We note that the inclusion of BAO data on these two different runs acts in opposite directions with respect to constraining $\Delta N_{\rm eff}$: for lighter axions, the inclusion of BAO data leads to a broader 1D distribution of $\Delta N_{\rm eff}$, while for heavier axions the inclusion of BAO data leads to tighter constraints on all parameters, including $\Delta N_{\rm eff}$. This behaviour is ultimately due to the different role of the axion in the two regimes. Light axions are hot DM, so that their properties are mainly constrained by a measurement of $\Delta N_{\rm eff}$. Since the inclusion of BAO data pushes H_0 towards higher values (see the posterior in Fig. 4.6), the bound on $\Delta N_{\rm eff}$ relaxes. Heavier axions behave instead as CDM and the constraints are mainly due to the larger value of the axion relic abundance. Since the inclusion of BAO data improves the bound on ω_{c+a}, the constraints on $\Delta N_{\rm eff}$ are also tightened.

All these features can be well appreciated by looking at Fig. 4.7, where we collect the bounds on $\Delta N_{\rm eff}$ for the different values of the axion mass considered in our analysis. Here, the solid cyan line represents the limits that we obtain from the full analysis with *Planck*+BAO data. The region of parameter space excluded by cosmological data is the one lying below this curve. To have better physical insights about the results of the Monte Carlo analysis, we include in the plot the additional information discussed in Sec. 4.2:

- the color shades report the relic abundance of thermal axions ω_a as a function of the *effective* axion mass m_a in Eq. (3.41) (horizontal axis) and decoupling temperature T_d (vertical left axis) or, equivalently, the value of $\Delta N_{\rm eff}$ (vertical right axis). The scaling of $\Delta N_{\rm eff}$ is not logarithmic as this quantity is related to T_d by a complicated function involving the effective number of entropy degrees of freedom $g_{*s}(T)$ at temperature T. The contours range from 10^{-7} to the top left corner of the figure to 10 to the bottom right;

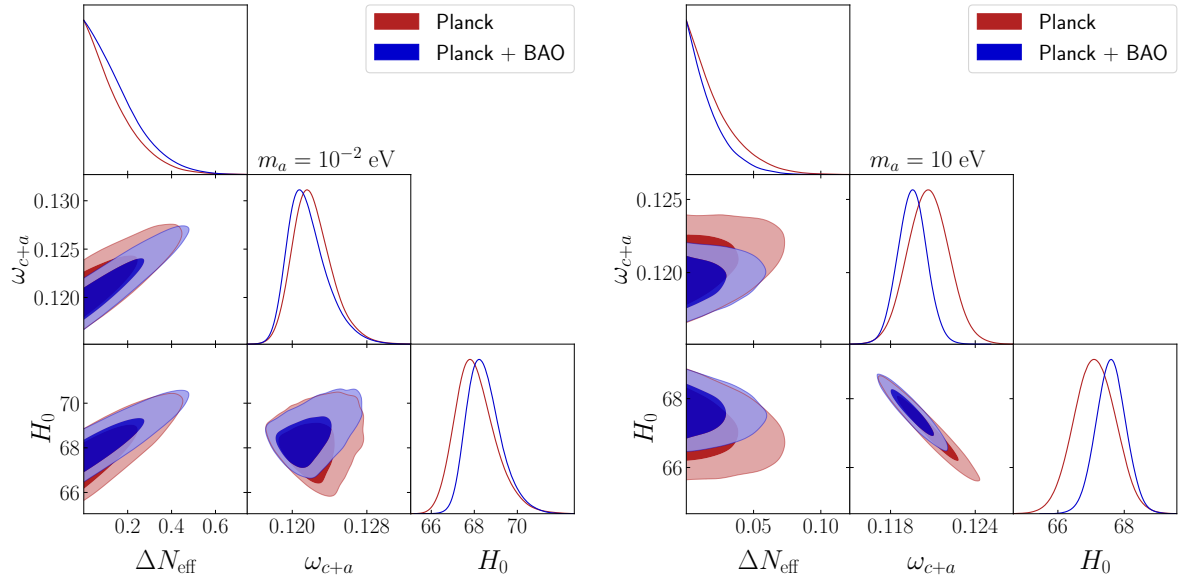

Figure 4.6: Triangle plot including 2D and 1D posteriors for different cosmological parameters in the ΛCDM+$\Delta N_{\rm eff}$ model. *Left panel:* axion mass fixed to $m_a = 10^{-2}$ eV. Note that, somehow unexpectedly, the inclusion of BAO data leads to a broader 1D distribution of $\Delta N_{\rm eff}$, see text for details. *Right panel:* axion mass fixed to $m_a = 10$ eV. The inclusion of BAO data leads to tighter constraints on all parameters, including $\Delta N_{\rm eff}$.

- the dashed white lines mark the current limits on cold dark matter (CDM), $\omega_a < \omega_c$, and hot dark matter, $\omega_a < \omega_h$. For CDM we take $\omega_c = 0.1202 \pm 0.0014$ at 68% CL from *Planck* 2018 results with TT,TE,EE+lowE data [6]. For hot DM we take instead $\omega_h \approx 2 \times 10^{-3}$.[6] Both the hot and cold DM bounds indirectly constrain the value of $\Delta N_{\rm eff}$ as a function of the effective axion mass m_a through Eq. (4.10);

- the solid red lines allow us to distinguish the regions of parameter space where the axion is relativistic or non-relativistic at recombination. Indeed, these are the curves for which the average axion momentum at recombination, see Eq. (4.11), is $\langle p_{a,\rm rec}\rangle = \{10^2, 1, 10^{-2}\}\, m_a$ from left to right. The axion is non-relativistic (ultra-relativistic) in the right (left) corner of the plot, when $\langle p_{a,\rm rec}\rangle \ll m_a$ ($\langle p_{a,\rm rec}\rangle \gg m_a$);

- finally, we show the curve of constant $\Delta N_{\rm eff} = 0.376$. This value corresponds to the 95% CL upper limit on $\Delta N_{\rm eff}$ that we obtain for an axion with mass $m_a = 10^{-4}$ eV (i.e. in the regime with $\langle p_{a,\rm rec}\rangle / m_a \gg 1$), from *Planck* 2018 TT,TE,EE+lowE data in combination with BAO measurements.

In the region in which axions are ultra-relativistic at recombination, the relevant constraints are $\Delta N_{\rm eff} \lesssim 0.376$ and $\omega_a < \omega_h \simeq 2 \times 10^{-3}$. In the region in which axions are non-relativistic at recombination, the only relevant constraint is that coming from the observed dark matter density: $\omega_a < \omega_c \simeq 0.12$. This intuition is nicely confirmed by looking at the bounds obtained by the full, more accurate analysis exactly accounting for the interplay between the axion mass and temperature. In the leftmost part of the plot ($m_a \lesssim 0.1$ eV), where axions are effectively massless and behave as dark radiation, the cyan curve reproduces the constrain on $\Delta N_{\rm eff}$. In the region $m_a \simeq 1$ eV, the axion mass starts to be relevant and axions behave as hot dark matter and the full analysis essentially yields the $\omega_a < \omega_h$ bound. Finally, in the rightmost part of

[6] The bound on hot dark matter is obtained here by translating cosmological constraints on the sum of neutrino masses Σm_ν [6] to a constraint on their energy density ω_h.

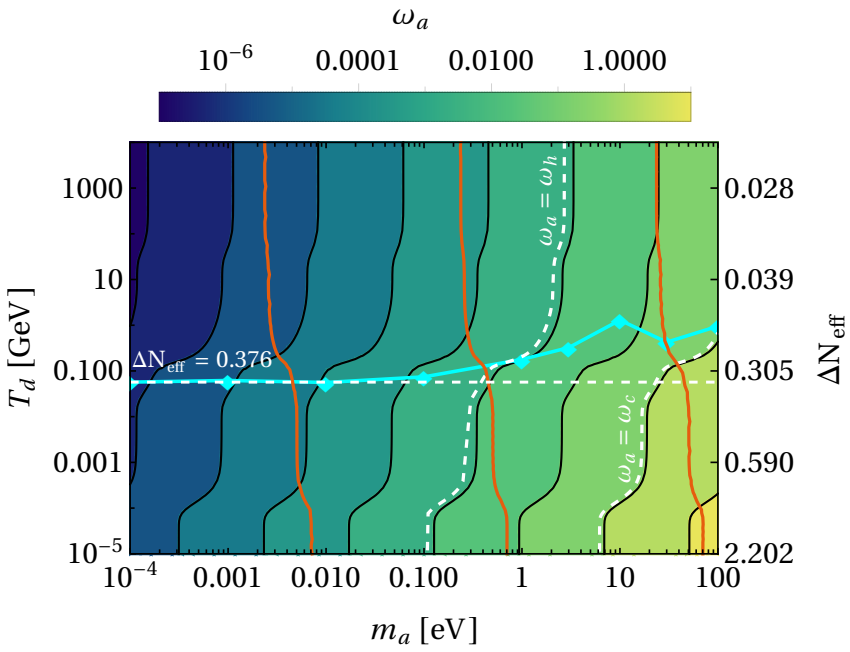

Figure 4.7: Relic abundance ω_a of thermal axions as a function of the axion mass m_a and decoupling temperature T_d (or, equivalently, $\Delta N_{\rm eff}$). The vertical dashed white lines represent the bounds on the abundance of hot and cold DM as defined in the main text. The horizontal dashed white line corresponds to $\Delta N_{\rm eff} = 0.376$ (see main text for details). Also shown are the bounds on T_d (solid cyan line) as a function of m_a. The red lines represent the pairs of axion parameters with constant values of $\langle p_{a,\rm rec}\rangle/m_a = \{10^2, 1, 10^{-2}\}$ from left to right.

the plot, $m_a \gtrsim 30$ eV axions are cold and indeed we reproduce the cold dark matter bound. In the "warm" axion region, 1 eV $\lesssim m_a \lesssim$ 30 eV, it is not possible to obtain a useful bound on T_d from a qualitative analysis. It is of course legit to expect that the actual bound will lie between the hot and cold dark matter bounds, but this is of little utility even for the purpose of getting an order-of-magnitude estimate, since as it is clear from the figure the region between the hot and cold DM curves spans many orders of magnitude in T_d. In this region, a complete analysis like the one presented in this work is the only way to obtain meaningful bounds on axion properties. The full analysis also helps to uncover features that might fail intuition. For example, the plot shows that a truly "cold" regime is only reached for relatively small values ($\lesssim 10^{-2}$) of the momentum-to-mass ratio at recombination; even for values of $\langle p_{a,\rm rec}\rangle/m_a$ of a few $\times 10^{-2}$, the constraints are (possibly much) stronger than the ones that one would naively obtain solely from the requirement $\omega_a < \omega_c$. In other words, *Planck* measurements of the CMB anisotropies are very sensitive even to a little "warmness" of axions (and other light relics in general). This was noted, in the different framework of QCD axions in low reheating scenarios, also in Ref. [224].

4.6 Bounds on the axion couplings to photons and gluons

In this section we translate the cosmological bounds on $\Delta N_{\rm eff}$ into bounds on the axion couplings to photons and gluons. We discuss both the cases of the QCD axion and a generic axion-like particle. As discussed in Sec. 4.3, the bounds on $\Delta N_{\rm eff}$ can be converted into bounds on $g_{a\gamma}$ using Eq. (4.16) when the axion is mainly produced by axion-photon scatterings, or equivalently on a bound on C_g/f_a or g_d using the relation shown in Fig. 4.4 when the axion is mainly produced from quark-gluon interactions.

We first consider the case of the ΛCDM+$\Delta N_{\rm eff}$+m_a model. In the range of axion masses spanned in this work, we obtain the following marginalized constraints at 95% CL on the axion couplings:

$$g_{a\gamma} < \begin{cases} 2.84 \times 10^{-8}\ \text{GeV}^{-1} & \textit{Planck}\ 2018 \\ 3.16 \times 10^{-8}\ \text{GeV}^{-1} & \textit{Planck}\ 2018 + \text{BAO}\,, \end{cases} \tag{4.24}$$

$$\frac{C_g}{f_a} < \begin{cases} 6.98 \times 10^{-8}\ \text{GeV}^{-1} \\ 1.06 \times 10^{-7}\ \text{GeV}^{-1} \end{cases} \quad \text{or} \quad g_d < \begin{cases} 2.47 \times 10^{-10}\ \text{GeV}^{-2} & \textit{Planck}\ 2018 \\ 3.77 \times 10^{-10}\ \text{GeV}^{-2} & \textit{Planck}\ 2018 + \text{BAO}\,. \end{cases} \tag{4.25}$$

Cosmological bounds on the coupling between ALPs and photons have been derived in Ref. [225], where the axion has been treated as an additional effective neutrino species. We note that the bound on $g_{a\gamma}$ reported in (4.24) is stronger by roughly a factor 2.

We now consider the bounds on the axion couplings in the case of the ΛCDM+$\Delta N_{\rm eff}$ model with fixed axion mass. The results for the axion-photon and axion-gluon couplings are discussed in Sections 4.6.1 and 4.6.2, respectively.

4.6.1 Axion-photon coupling

For a fixed mass, we convert the bound on $\Delta N_{\rm eff}$ into a bound on $g_{a\gamma}$ using Eq. (4.16). The resulting upper bounds at 95% CL are shown in Fig. 4.8, both from the *Planck* 2018 dataset alone (orange diamonds connected with a dashed line) and in combination with BAO data (blue diamonds connected with a dashed line).

The red hatched area (top right corner) excludes the region of the parameter space for which the decay rate of the axion into two photons is faster than the expansion rate of the Universe, so that the condition in Eq. (4.18) is not satisfied. Finally, the green region is excluded by the constraints on the axion-photon coupling derived by the CAST helioscope at CERN [207]. The allowed region of the parameter space is what is left from the combination of the constraints above, i.e., the region in the bottom right part of the figure, on the left of the green curve, below the blue diamonds and on the right of the hatched region.

The yellow band in the figure identifies the region of parameter space where QCD axion models lie. Indeed, we recall that for the QCD axion we have (see Sec. 3.4)

$$g^0_{a\gamma} = \frac{\alpha_{\rm EM}}{2\pi f_a}\frac{E}{N}\,, \tag{4.26}$$

where E/N is the ratio between the colour and the electromagnetic axion anomalies. Generally speaking, different QCD axion theories predict different values of the E/N ratio, which is expected to span from 5/3 to 44/3 [167–169]. Explicit constructions that embed the axion into the SM include the DFSZ model [150, 151] in which a new Higgs doublet is introduced, and the KSVZ model [148, 149] in which exotic heavy quarks are introduced. The line marked "KSVZ" corresponds to the choice $E/N = 0$ which is obtained if the charge of the heavy quarks vanishes, while the line marked "DFSZ" corresponds to the choice $E/N = 8/3$. Note that QCD axion solutions outside of this yellow band have also been constructed and are still viable [170–174].

Similarly to what has been discussed for the results on $\Delta N_{\rm eff}$, the trend in the constraints with heavier axion masses can be understood as follows. If we increase the value of m_a while keeping $g_{a\gamma}$ fixed, we are increasing the abundance of hot axions. This effect can be compensated by decreasing the value of $g_{a\gamma}$, which leads to an axion relic abundance that is more diluted with respect to that of cosmic photons. This is the reason why the limit on $g_{a\gamma}$ tightens up when moving to higher values of m_a. For $m_a \gtrsim 10\,\text{eV}$, axions behave as CDM at recombination and the constraints on the parameter space result from requiring that the cosmological abundance of CDM does not exceed that of thermal axions. This leads to less stringent constraints on $g_{a\gamma}$,

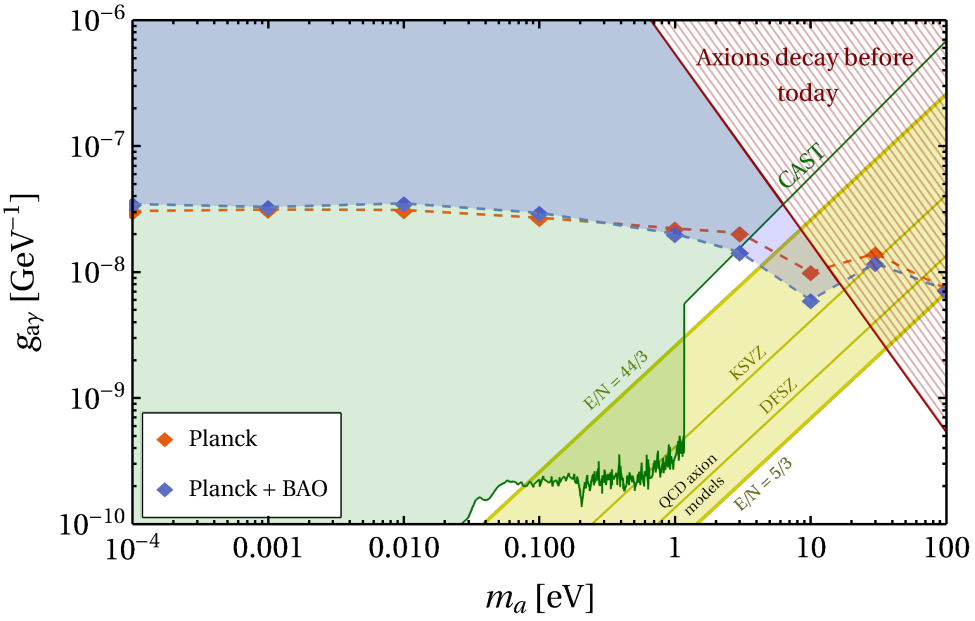

Figure 4.8: Summary of constraints in the axion-photon coupling $g_{a\gamma}$- axion mass m_a plane. Colored diamonds connected with dashed lines are 95% CL upper bounds on the axion-photon coupling $g_{a\gamma}$ as a function of the axion mass m_a, from *Planck* 2018 alone (orange) and *Planck* 2018+BAO (blue). The yellow band represents the representative QCD axion region considered (see text for details), including the KSVZ ($E/N = 0$) and the DFSZ ($E/N = 8/3$) models. The red hatched area labeled "Axions decay before today" indicates the region of parameter space where the axion lifetime before its decay into photons is smaller than the age of the Universe, see Eq. (4.18). The green shaded area represents the region excluded by the CAST helioscope [201, 207], with data taken from [204].

explaining the rise of the bound in this mass range. Finally, for $m_a \sim 100\,\text{eV}$ the constraints tightens again as the cold axion population is overproduced.

We note again that the inclusion of BAO weakens the constraints on $g_{a\gamma}$ for light axions, while heavier axions are better constrained combining *Planck* with BAO data (see the discussion in Sec. 4.5.2).

The measurements of small-scale CMB anisotropies from ACT [261, 262] provide a further opportunity to constrain the properties of additional light relics. As reported in Ref. [261], combining ACT with *Planck* data yields the bound $N_{\rm eff} = 2.74 \pm 0.17$ at 68% CL, which signals a preference for a number of relativistic species smaller than the SM value 3.046. Even though we leave a complete analysis including ACT data for future work, we anticipate how the bounds on the axion-photon coupling are improved in the region of parameter space where axions behave as dark radiation. Indeed, as we have already discussed, light axions are directly constrained by the measurement of $\Delta N_{\rm eff}$, thus we expect that they receive a higher benefit from the inclusion of ACT data with respect to heavier axions. Moreover, when dealing with heavier axions which behave as warm or cold DM, a more careful treatment of non-linearities is required. We plan to present a detailed analysis that includes ACT data for the full mass range explored in this work in a future release. In the case of an axion with mass $m_a = 10^{-4}$ eV, the bound on the axion-photon coupling from the combination of *Planck*, BAO and ACT data reads $g_{a\gamma} < 2.19 \times 10^{-8}$ GeV^{-1} at 95% CL. This represents an improvement by a factor of about 1.6 with respect to the case with only *Planck*+BAO.

Finally, let us comment on how the cosmological constraints we have derived compare with those coming from laboratory experiments.[7] Our results are tighter than the bounds placed

[7]We do not consider the constraints from the axion haloscope ADMX since they hold for axion masses of order of few μeV [205], which are smaller than those considered in this work. Moreover, haloscope experiments

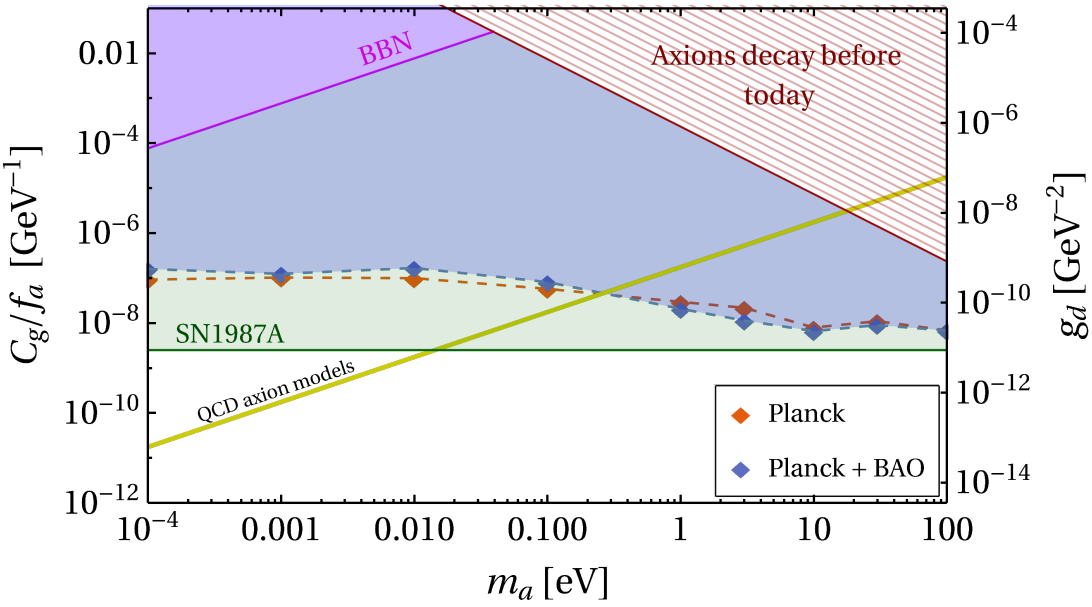

Figure 4.9: Summary of constraints in the axion-gluon coupling-axion mass plane. The vertical axis shows the axion-gluon coupling C_g/f_a (left) or the EDM coupling g_d (right) according to Eq. (3.40). Colored diamonds connected with dashed lines are 95% CL upper bounds on the axion-gluon coupling as a function of the axion mass m_a, from *Planck* alone (orange) and *Planck*+BAO (blue). The yellow band represents the QCD axion region, which is determined by the uncertainties in the computation of the axion mass in Eq. (3.41) with $m_0 = 0$ and $C_g = 1$. The green shaded area represents the region of parameter space excluded by SN1987A energy loss consideration [219], as expressed in Eq. (4.27). The red hatched area labeled "Axions decay before today" indicates the region of parameter space where the axion lifetime before its decay into photons is smaller than the age of the Universe, see Eq. (4.18). The magenta shaded area is excluded by BBN considerations [264]. Notice that the latter constraints are derived under the assumption that axions account for the entirety of the DM, whereas the other bounds do not have this restriction.

by the CAST helioscope for values of the axion mass $m_a \gtrsim 3\,\text{eV}$, according to Fig. 4.8. A conservative bound on $g_{a\gamma}$ for light axions has been derived based on the possible effect of these particles on the stellar evolution of massive stars, which translates into $g_{a\gamma} \lesssim 0.8 \times 10^{-10}\,\text{GeV}^{-1}$ [263] which is tighter than what we obtain by using cosmological data. An even stronger bound arises from the comparison of the ratio of stars in horizontal over red giant branch found in a group of globular clusters with the corresponding predictions from accurate models of stellar evolution. This leads to $g_{a\gamma} \lesssim 6.6 \times 10^{-11}\,\text{GeV}^{-1}$ at 95% CL [216]. Nevertheless, the bounds we derive are independent and complementary to laboratory searches and stellar evolution.

4.6.2 Axion-gluon coupling

We now proceed to consider the bounds obtained on the axion-gluon coupling C_g/f_a. To derive these bounds, we use the results for the set of runs ΛCDM+$\Delta N_{\rm eff}$ for fixed axion mass to then convert the bounds over $\Delta N_{\rm eff}$ into a bound over C_g/f_a using the method outlined in Sec. 4.3.2. In Fig. 4.9 we show the 95% CL upper bounds on the coupling C_g/f_a (vertical left axis) in the case where the leading interaction in establishing a thermal population of axions is the axion-gluon interaction. The yellow band in the figure represents the region of parameter space in which the representative QCD axion models lie. Similarly to what has been discussed in relation

make the assumption that axions account for all the dark matter, while the constraints derived from cosmological observations do not have this restriction.

to Fig. 4.8, the region above the blue (orange) diamonds is excluded by *Planck* alone (*Planck* in combination with BAO). These results are translated into a constraint on the coupling g_d (vertical right axis) according to Eq. (3.40).

In analogy with the results in Fig. 4.8, the red hatched area in Fig. 4.9 represents the region of parameter space where the lifetime of the axion before it decays into photons is smaller than the age of the Universe. The decay is due to the effective axion-photon coupling induced by the coupling with gluons, which is obtained by setting $g^0_{a\gamma} = 0$ in Eq. (3.42).

The magenta shaded area is excluded by BBN considerations [264]. Indeed, the presence of an oscillating axion field during BBN alters the neutron-proton mass difference, which controls the ratio between the abundances of neutrons and protons. In turns, this affects the final prediction for the abundance of ^{4}He. We stress that these bounds are derived under the assumption that axions account for the entirety of the DM, while the other constraints shown in Fig. 4.8 (including the cosmological ones) do not have this restriction.

We also compare our results with the constraints obtained from the considerations over the energy loss by supernovae. If axions exist, they provide an additional source of energy loss with respect to the standard neutrino emission from supernovae. The analysis performed in Ref. [217] (see also [218]) yields the bound

$$C_g/f_a \lesssim 2.5 \times 10^{-9}\ \text{GeV}^{-1}\,. \tag{4.27}$$

This excludes the green shaded region in Fig. 4.9 labeled "SN1987A". We note that these bounds are stronger than the cosmological ones derived in our analysis. Nevertheless, the two analysis are independent, since the physics behind the cosmological and astrophysical constraints is different and the experiments used to derive the two bounds are affected by different systematics. Thus, the cosmological bounds provide a complementary probe to exclude a region of parameter space also excluded by supernovae considerations.

Similarly to the case of the axion-photon coupling, we briefly comment on how the bounds on the axion-gluon are improved with the inclusion of ACT data. For $m_a = 10^{-4}\,\text{eV}$, we find $C_g/f_a < 2.79 \times 10^{-8}\ \text{GeV}^{-1}$ or, in terms of the EDM coupling, $g_d < 9.89 \times 10^{-11}\ \text{GeV}^{-2}$ at 95% CL, from *Planck*+ACT+BAO. This represents an improvement by a factor of about 5.7 with respect to the case with only *Planck*+BAO.

Finally, we briefly comment on the implications of our analysis for the KSVZ axion. A proper derivation of the bounds for this case would require enforcing the relation between the axion mass and coupling as a prior in the Monte Carlo run, but this is beyond the scope of the present analysis. We can anyhow estimate the constraint we would get on f_a (since $C_g = 1$ for the QCD axion) from such an analysis by looking at the intersection of our bounds with the QCD axion region in Fig. 4.9. In this way we get $f_a \gtrsim 2 \times 10^7$ GeV, which translates into an upper limit on the mass of the KSVZ axion given by $m_a \lesssim 0.3$ eV. This is in agreement with the results derived in Refs. [222–224], where cosmological bounds on the KSVZ axion have been derived.

4.7 Future prospects

Future cosmological surveys will test scenarios of exotic thermal relics with improved sensitivity with respect to what discussed in our analysis. The next-generation ground-based CMB experiment CMB-S4 has a forecast sensitivity

$$\Delta N_{\text{eff}} \lesssim 0.06 \tag{4.28}$$

at 95% CL [11, 240]. Since, as we have extensively discussed, light axions ($m_a \lesssim 10^{-2}$ eV) are mostly constrained by the bound on ΔN_{eff}, we can estimate to which extent the bounds on the axion couplings will be improved by future surveys for small axion masses. The sensitivity

of CMB-S4 reported in (4.28) will allow to probe the existence of a light (thermal) axion with coupling to photons as weak as $g_{a\gamma} \simeq 1.1 \times 10^{-8}$ GeV^{-1}, or with coupling to gluons as weak as $C_g/f_a \simeq 8.3 \times 10^{-9}$ GeV^{-1} or, equivalently, $g_d \simeq 2.9 \times 10^{-11}$ GeV^{-2}. For the axion-photon coupling this represents an improvement by roughly a factor 3. The bound on the axion-gluon coupling would instead improve our current estimates by about one order of magnitude. It will be particularly interesting to see whether the bounds on the axion-gluon coupling will be improved enought to overcome those coming from SN1987A for masses $\sim \mathcal{O}(10 - 100$ eV). A detailed analysis regarding the whole range of masses is the subject of an ongoing work.

Part III

Testing the Fundamental Symmetries of the Universe with CMB Polarization

Chapter 5

Constraints on Lorentz-violating electrodynamics from CMB polarization

Lorentz symmetry is at the foundation of our current understanding of physics at the fundamental level. Nevertheless, different theoretical considerations suggest the possibility that it might be an exact symmetry only at low energy scales. In particular, this hypothesis is deeply rooted in quantum gravity, see e.g. [265–267]. Both string theory and loop quantum gravity, two of the main contenders for a theory of quantum gravity, predict the possibility that Lorentz symmetry might not hold exactly.

A general approach to describe departures from the Lorentz symmetry is that of effective field theory. This allows us to account for Lorentz violations by extending the Lagrangian of the Standard Model with Lorentz-violating (LV) operators, which can be ordered based on their mass dimension d. This results in the so-called Standard Model Extension (SME) [17–19].

In the analysis presented in this chapter we focus on renormalizable operators of mass dimension $d \leq 4$, which defines the minimal SME, and consider in particular the photon sector of the minimal SME. The non-standard propagation of photons leads to distinctive signatures on the polarization of the CMB, such as the generation of the cosmic birefringence effect and the conversion of linear into circular polarization. We use the most recent observations of the CMB polarization from *Planck* [20, 21], BICEP/Keck [8], ACT [7], CLASS [22] and SPIDER [23] to constrain the Lorentz-violating coefficients appearing in the Lagrangian of the minimal SME.

Besides using the most recent datasets, another novelty of our analysis consists in the fact that we analyze the effects of the Lorentz-violating operators on the CMB spectra all together. Instead, previous studies focus on one single operator at a time, thus neglecting the possible interplay between them. In order to do so, we employ the formalism developed in Ref. [268], which we will briefly review in Sec. 5.2.1. This allows us to describe the effects of non-standard propagation of radiation in terms of an effective susceptibility tensor and then derive the associated modifications of the CMB spectra.

5.1 Minimal Standard Model Extension for Lorentz violation in the photon sector

As described above, Lorentz-violating effects are usually described within the framework of the SME [17–19, 67]. This is an effective field theory which is constructed as an expansion in Lorentz-violating operators of increasingly higher mass dimension d. For the photon sector and

in a general spacetime with metric $g_{\mu\nu}$, this is characterized by the action

$$S = \int d^4x\sqrt{-g}\left[-\frac{1}{4}F_{\mu\nu}F^{\mu\nu} + \frac{1}{2}\varepsilon^{\alpha\beta\mu\nu}A_\beta(\hat{k}_{AF})_\alpha F_{\mu\nu} - \frac{1}{4}(\hat{k}_F)^{\alpha\beta\mu\nu}F_{\alpha\beta}F_{\mu\nu}\right], \tag{5.1}$$

where $g = \det(g_{\mu\nu})$ and $\varepsilon^{\alpha\beta\mu\nu} = \epsilon^{\alpha\beta\mu\nu}/\sqrt{-g}$, where $\epsilon^{\alpha\beta\mu\nu}$ is the completely antisymmetric Levi-Civita symbol. Here, A_μ and $F_{\mu\nu}$ are the electromagnetic 4-potential and field-strength tensor, so that the first term in Eq. (5.1) is the standard Maxwell Lagrangian. The coefficients $(\hat{k}_{AF})_\alpha$ and $(\hat{k}_F)^{\alpha\beta\mu\nu}$ parametrize CPT-odd and CPT-even Lorentz violations, respectively. These can be written as polynomial expansions in the 4-momentum operator $p_\mu = i\partial_\mu$ as [19, 67]

$$(\hat{k}_{AF})_\alpha = \sum_{d\,\text{odd}\geq 3}(k_{AF}^{(d)})_\alpha{}^{\lambda_1\ldots\lambda_{(d-3)}}\partial_{\lambda_1}\ldots\partial_{\lambda_{(d-3)}}\,, \tag{5.2}$$

$$(\hat{k}_F)^{\alpha\beta\mu\nu} = \sum_{d\,\text{even}\geq 3}(k_F^{(d)})^{\alpha\beta\mu\nu\lambda_1\ldots\lambda_{(d-4)}}\partial_{\lambda_1}\ldots\partial_{\lambda_{(d-4)}}\,, \tag{5.3}$$

where $k_{AF}^{(d)}$ and $k_F^{(d)}$ are constant coefficients of mass dimension $4-d$.

Here, we focus on renormalizable operators of mass dimension $d \leq 4$: this defines the so-called minimal SME. In this case, the CPT-odd operator is characterized by the vector $(k_{AF})_\alpha \equiv (k_{AF}^{(3)})_\alpha$ and has dimension $d = 3$, while the CPT-even term is parametrized by the tensor $(k_F)^{\alpha\beta\mu\nu} \equiv (k_F^{(4)})^{\alpha\beta\mu\nu}$ and has dimension $d = 4$. The tensor $(k_F)^{\mu\alpha\beta\gamma}$ is thus dimensionless and respects the following symmetries

$$(k_F)^{\mu\alpha\beta\gamma} = -(k_F)^{\alpha\mu\beta\gamma} = -(k_F)^{\mu\alpha\gamma\beta}\,, \tag{5.4}$$

$$(k_F)^{\mu\alpha\beta\gamma} = (k_F)^{\beta\gamma\mu\alpha}\,, \tag{5.5}$$

$$(k_F)^{\alpha\beta}{}_{\alpha\beta} = 0\,, \tag{5.6}$$

thus implying a total of 19 independent components. The vector $(k_{AF})_\alpha$ has dimension of a mass and has 4 independent components.

Applying the Euler-Lagrange equations to the action in Eq. (5.1) in the minimal case leads to the following modified Maxwell equations:

$$\partial_\nu(\sqrt{-g}F^{\mu\nu}) + \varepsilon^{\mu\nu\rho\sigma}(k_{AF})_\nu\sqrt{-g}F_{\rho\sigma} + \partial_\nu\left[(k_F)^{\mu\nu\rho\sigma}\sqrt{-g}F_{\rho\sigma}\right] = 0\,. \tag{5.7}$$

The usual Maxwell theory is invariant under conformal transformations of the metric. Indeed, under a transformation of the kind

$$g_{\mu\nu} \to \tilde{g}_{\mu\nu} = f(x)g_{\mu\nu}\,, \qquad g^{\mu\nu} \to \tilde{g}^{\mu\nu} = f^{-1}(x)g^{\mu\nu}\,, \tag{5.8}$$

the action describing the standard electromagnetic theory,

$$S_{\text{EM}} = \int d^4x\sqrt{-g}\left(-\frac{1}{4}g^{\mu\alpha}g^{\nu\beta}F_{\mu\nu}F_{\alpha\beta}\right), \tag{5.9}$$

is left unchanged. Since the FLRW and Minkwoski spacetimes are related to each other by a conformal transformation with $f = a^2$, the conformal invariance of Maxwell's theory implies that the equations of motion in FLRW are the same as in Minkowski.

In order for this invariance to be preserved by the minimal SME action, the coefficient $(k_F)^{\alpha\beta\mu\nu}$ must transform as

$$(k_F)^{\alpha\beta\mu\nu} \to a^{-4}(k_F)^{\alpha\beta\mu\nu}\,, \tag{5.10}$$

such that the a^{-4} factor cancels out the a^4 coming from $\sqrt{-g}$. The vector $(k_{AF})_\alpha$ instead has to be left invariant by the conformal transformation, since the scaling of $\sqrt{-g}$ is canceled by that of the Levi-Civita tensor $\varepsilon^{\alpha\beta\mu\nu} \propto 1/\sqrt{-g}$.

A well-known analogy exists between Lorentz-violating electrodynamics in vacuum and the standard Maxwell electrodynamics in an anisotropic medium, see e.g. Ref. [269]. This analogy can be exploited to define an effective suceptibility tensor χ from the modified Ampère-Maxwell equation, i.e. the space component ($\nu = i$) of Eq. (5.7). We start by writing the latter in Fourier space as

$$(\nabla \times \mathbf{B})^i - \frac{1}{c^2}\frac{\partial E_i}{\partial \tau} = -2(k_{AF})_0 B^i - \frac{2}{c}(\mathbf{k_{AF}} \times \mathbf{E})^i - \frac{2}{c^2}(k_F)^{i0k0}\frac{\partial E_k}{\partial \tau} + \frac{2}{c}(k_F)^{ij0k}(\partial_j E_k) - \frac{1}{c}(k_F)^{i0jk}\epsilon_{jkr}\frac{\partial B^r}{\partial \tau} - (k_F)^{ijkl}\epsilon_{klr}(\partial_j B^r)\,. \tag{5.11}$$

Fixing the temporal gauge, $A^0 = 0$, the electric and magnetic fields can be written in terms of the vector potential as

$$E^i(\omega, \mathbf{k}) = i\omega A^i(\omega, \mathbf{k})\,, \quad B^i(\omega, \mathbf{k}) = i\left[\mathbf{k} \times \mathbf{A}(\omega, \mathbf{k})\right]^i\,. \tag{5.12}$$

This allows us to rewrite Eq. (5.11) in terms of $\mathbf{A}$ as

$$-\left[\mathbf{k} \times (\mathbf{k} \times \mathbf{A})\right]_i - \frac{\omega^2}{c^2}A_i = -2\frac{\omega^2}{c^2}(k_F)_{i0j0}\,A^j + 2\frac{\omega}{c}(k_F)_{ij0k}\,k^j A^k + \frac{\omega}{c}(k_F)_{i0jk}\,\epsilon^{jkr}(\mathbf{k} \times \mathbf{A})_r + (k_F)_{iljk}\,\epsilon^{jkr}k^l(\mathbf{k} \times \mathbf{A})_r - 2i(k_{AF})_0(\mathbf{k} \times \mathbf{A})_i - 2i\frac{\omega}{c}(\mathbf{k}_{AF} \times \mathbf{A})_i\,. \tag{5.13}$$

This equation can be compared with the standard (i.e., in the absence of LV effects) Ampère-Maxwell equation in an anisotropic medium with no external sources, which reads (see e.g. [270])

$$\frac{\omega^2}{c^2}A_i + \left[\mathbf{k} \times (\mathbf{k} \times \mathbf{A})\right]_i = -\frac{\omega^2}{c^2}\chi_{ij}A^j\,. \tag{5.14}$$

This allows us to define an effective susceptibility tensor

$$\chi_{ij} = -2(k_F)_{i0j0} - 2i\frac{c}{\omega}\epsilon_{ikj}(k_{AF})^k + 2\frac{c}{\omega}\left[-i\frac{c}{\omega}(k_{AF})_0\epsilon_{ikj} + (k_F)_{ik0j} + (k_F)_{i0kj}\right]k^k + 2\frac{c^2}{\omega^2}(k_F)_{ilkj}k^l k^k\,, \tag{5.15}$$

where ω and k are the *comoving* angular frequency and wave-number, respectively:

$$\omega = a\omega_{phys}\,, \quad k = ak_{phys}\,. \tag{5.16}$$

Note that the parity-odd operator introduces in χ_{ij} only zero- and first-order terms in the wave-vector, whereas the parity-even operator produces also a contribution that is quadratic in k. This does not come as a surprise, since it is not possible to construct a quadratic term in the wave-vector by contracting its components with those of the 3D Levi-Civita tensor and the three-vector $\mathbf{k}_{AF}$.

Now that we have the explicit expression of the susceptibility tensor χ, we can apply the formalism developed in [268] to compute the modified CMB spectra. This will be the subject of the next section.

5.2 Imprints of Lorentz violations on CMB spectra

In this section we compute the effects of the LV operators on the CMB spectra. To begin, in Sec. 5.2.1 we review the formalism adopted for the calculations, which has been developed in Ref. [268]. Then, in Secs. 5.2.2 and 5.2.3 we analyze the effects of the CPT-odd and CPT-even operators, respectively. Finally, in Sec. 5.2.4 we present the final expressions of the CMB power spectra.

5.2.1 Review of the formalism

The formalism developed in Ref. [268] allows us to map the components of the susceptibility tensor χ on three quantities, ρ_Q, ρ_U and ρ_V, which describe a general mixing between the U, V and Q Stokes parameters according to the following transport equation:

$$\frac{d}{ds}\begin{pmatrix} Q \\ U \\ V \end{pmatrix} = -\begin{pmatrix} 0 & \rho_V & -\rho_U \\ -\rho_V & 0 & \rho_Q \\ \rho_U & -\rho_Q & 0 \end{pmatrix}\begin{pmatrix} Q \\ U \\ V \end{pmatrix} . \tag{5.17}$$

Here, s is an affine parameter along the photon path and we have neglected possible emission and absorption terms. From Eq. (5.17) it is clear that ρ_V mixes Q and U polarization and gives rise to the *cosmic birefringence* effect, i.e. the rotation of the linear polarization plane of CMB photons during their propagation from the last scattering surface to us. Instead, ρ_Q and ρ_U mix the linear polarization components with V, leading to the generation of circular polarization from the conversion of the primordial linear polarization components. The ρ's coefficients are related to the components of χ by (see [268])

$$\rho_Q = 2\pi\nu\big[\left(\chi_{xx}c_\theta^2 - \chi_{yy}\right)c_\phi^2 + \left(\chi_{yy}c_\theta^2 - \chi_{xx}\right)s_\phi^2 + \chi_{zz}s_\theta^2\big] , \tag{5.18}$$

$$\rho_U = 4\pi\nu\left(\chi_{yy} - \chi_{xx}\right)c_\theta s_\phi c_\phi , \tag{5.19}$$

$$\rho_V = 4\pi\nu\big[\chi_{xy}c_\theta + (\chi_{yz}c_\phi + \chi_{xz}s_\phi)s_\theta\big] , \tag{5.20}$$

where $c_X \equiv \cos X$, $s_X \equiv \sin X$ and the angles (θ, ϕ) identify the direction of propagation of light.

Note that ρ_V is a pseudoscalar and hence has spin 0. In order to work with quantities of definite spin only, we introduce the spin-±2 fields

$$\rho_{\pm2} \equiv \frac{\rho_Q \pm i\,\rho_U}{\sqrt{2}} . \tag{5.21}$$

Then, since the effects of the LV operators on the CMB spectra are integrated along the line of sight of propagation of CMB photons, we define the quantities

$$\bar{\rho}_V(\tau) \equiv (\tau - \tau_{\rm LS})^{-1}\int_{\tau_{\rm LS}}^{\tau} \mathrm{d}\tau'\,\rho_V(\tau') , \tag{5.22}$$

$$\bar{\rho}_{\pm2}(\tau) \equiv (\tau - \tau_{\rm LS})^{-1}\int_{\tau_{\rm LS}}^{\tau} \mathrm{d}\tau'\,\rho_{\pm2}(\tau') , \tag{5.23}$$

where $\tau_{\rm LS}$ is the conformal time at the last scattering surface. We can now expand $(\tau_0 - \tau_{\rm LS})\bar{\rho}_V$ and $(\tau_0 - \tau_{\rm LS})\bar{\rho}_{\pm2}$ in spherical harmonics as

$$\bar{\rho}_V(\theta,\phi)(\tau_0 - \tau_{\rm LS}) = \sum_{\ell m} b_{V,\ell m}\,Y_{\ell m}(\theta,\phi) , \tag{5.24}$$

$$\bar{\rho}_{\pm2}(\theta,\phi)(\tau_0 - \tau_{\rm LS}) = \sum_{\ell m} b_{\pm2,\ell m}\,{}_{\pm2}Y_{\ell m}(\theta,\phi) , \tag{5.25}$$

where τ_0 denotes the conformal time today.

The coefficients $b_{V,\ell m}$ and $b_{\pm2,\ell m}$ relate the observed CMB spectra, C_ℓ^{XX}, to the ones that are expected if no LV effects are in place, $\widetilde{C}_\ell^{XX}$, in the following way [268]:

$$C_\ell^{TE} = \left(1 - \frac{\mathcal{Z}}{2}\right)\widetilde{C}_\ell^{TE} , \tag{5.26}$$

$$C_\ell^{EE} = (1 - \mathcal{Z})\,\widetilde{C}_\ell^{EE} + \sum_{\ell_1}\mathcal{K}^{11}_{\ell_1\ell}\widetilde{C}_{\ell_1}^{EE} + \sum_{\ell_1}\mathcal{K}^{22}_{\ell_1\ell}\widetilde{C}_{\ell_1}^{BB} , \tag{5.27}$$

$$C_\ell^{BB} = (1-\mathcal{Z})\,\widetilde{C}_\ell^{BB} + \sum_{\ell_1} \mathcal{K}^{11}_{\ell_1\ell}\widetilde{C}_{\ell_1}^{BB} + \sum_{\ell_1} \mathcal{K}^{22}_{\ell_1\ell}\widetilde{C}_{\ell_1}^{EE}\,, \tag{5.28}$$

$$C_\ell^{EB} = \frac{b_{V,00}}{\sqrt{4\pi}}(\widetilde{C}_\ell^{EE} - \widetilde{C}_\ell^{BB})\,, \tag{5.29}$$

$$C_\ell^{EV} = \sum_{\ell_1} \mathcal{K}^{13}_{\ell_1\ell}\tilde{C}_{\ell_1}^{EE} + \sum_{\ell_1} \mathcal{K}^{24}_{\ell_1\ell}\tilde{C}_{\ell_1}^{BB}\,, \tag{5.30}$$

$$C_\ell^{BV} = \sum_{\ell_1} \mathcal{K}^{23}_{\ell_1\ell}\tilde{C}_{\ell_1}^{EE} - \sum_{\ell_1} \mathcal{K}^{14}_{\ell_1\ell}\tilde{C}_{\ell_1}^{BB}\,, \tag{5.31}$$

$$.C_\ell^{VV} = \sum_{\ell_1} \mathcal{K}^{33}_{\ell_1\ell}\tilde{C}_{\ell_1}^{EE} + \sum_{\ell_1} \mathcal{K}^{44}_{\ell_1\ell}\tilde{C}_{\ell_1}^{BB}\,, \tag{5.32}$$

where

$$4\pi\mathcal{Z} = \sum_{\ell m}\left(|b_{V,\ell m}|^2 + |b_{2,\ell m}|^2\right)\,, \tag{5.33}$$

and the $\mathcal{K}$ kernels can be written in terms of Wigner $3j$-symbols as

$$\mathcal{K}^{11}_{\ell_1\ell} = \frac{2\ell_1+1}{4\pi}\sum_{\substack{\ell_2 m_2\\ \ell+\ell_1+\ell_2\,\text{odd}}}\left[\begin{pmatrix}\ell_1 & \ell_2 & \ell\\ -2 & 0 & 2\end{pmatrix}\right]^2 |b_{V,\ell_2 m_2}|^2\,, \tag{5.34}$$

$$\mathcal{K}^{22}_{\ell_1\ell} = \frac{2\ell_1+1}{4\pi}\sum_{\substack{\ell_2 m_2\\ \ell+\ell_1+\ell_2\,\text{even}}}\left[\begin{pmatrix}\ell_1 & \ell_2 & \ell\\ -2 & 0 & 2\end{pmatrix}\right]^2 |b_{V,\ell_2 m_2}|^2\,, \tag{5.35}$$

$$\mathcal{K}^{33}_{\ell_1\ell} = \frac{2\ell_1+1}{4\pi}\sum_{\ell_2 m_2}\left[\begin{pmatrix}\ell_1 & \ell_2 & \ell\\ -2 & 2 & 0\end{pmatrix}\right]^2 |b_{-2,\ell_2 m_2} - (-1)^{\ell+\ell_1+\ell_2} b_{2,\ell_2 m_2}|^2\,, \tag{5.36}$$

$$\mathcal{K}^{44}_{\ell_1\ell} = \frac{2\ell_1+1}{4\pi}\sum_{\ell_2 m_2}\left[\begin{pmatrix}\ell_1 & \ell_2 & \ell\\ -2 & 2 & 0\end{pmatrix}\right]^2 |b_{-2,\ell_2 m_2} + (-1)^{\ell+\ell_1+\ell_2} b_{2,\ell_2 m_2}|^2\,, \tag{5.37}$$

$$\mathcal{K}^{13}_{\ell_1\ell} = \frac{2\ell_1+1}{4\pi}\sum_{\substack{\ell_2 m_2\\ \ell_1+\ell_2+\ell\,\text{odd}}}\begin{pmatrix}\ell_1 & \ell_2 & \ell\\ -2 & 0 & 2\end{pmatrix}\begin{pmatrix}\ell_1 & \ell_2 & \ell\\ -2 & 2 & 0\end{pmatrix} b_{V,\ell_2 m_2}\left(b^*_{-2,\ell_2 m_2} + b^*_{2,\ell_2 m_2}\right)\,, \tag{5.38}$$

$$\mathcal{K}^{24}_{\ell_1\ell} = \frac{2\ell_1+1}{4\pi}\sum_{\substack{\ell_2 m_2\\ \ell_1+\ell_2+\ell\,\text{even}}}\begin{pmatrix}\ell_1 & \ell_2 & \ell\\ -2 & 0 & 2\end{pmatrix}\begin{pmatrix}\ell_1 & \ell_2 & \ell\\ -2 & 2 & 0\end{pmatrix} b_{V,\ell_2 m_2}\left(b^*_{-2,\ell_2 m_2} + b^*_{2,\ell_2 m_2}\right)\,, \tag{5.39}$$

$$\mathcal{K}^{23}_{\ell_1\ell} = -i\,\frac{2\ell_1+1}{4\pi}\sum_{\substack{\ell_2 m_2\\ \ell_1+\ell_2+\ell\,\text{even}}}\begin{pmatrix}\ell_1 & \ell_2 & \ell\\ -2 & 0 & 2\end{pmatrix}\begin{pmatrix}\ell_1 & \ell_2 & \ell\\ -2 & 2 & 0\end{pmatrix} b_{V,\ell_2 m_2}\left(b^*_{-2,\ell_2 m_2} - b^*_{2,\ell_2 m_2}\right)\,, \tag{5.40}$$

$$\mathcal{K}^{14}_{\ell_1\ell} = i\,\frac{2\ell_1+1}{4\pi}\sum_{\substack{\ell_2 m_2\\ \ell_1+\ell_2+\ell\,\text{odd}}}\begin{pmatrix}\ell_1 & \ell_2 & \ell\\ -2 & 0 & 2\end{pmatrix}\begin{pmatrix}\ell_1 & \ell_2 & \ell\\ -2 & 2 & 0\end{pmatrix} b_{V,\ell_2 m_2}\left(b^*_{-2,\ell_2 m_2} - b^*_{2,\ell_2 m_2}\right)\,. \tag{5.41}$$

Given the formalism discussed in this section, the first step we need to perform is to compute the ρ's coefficients. Then, we can derive the spherical harmonics coefficients $b_{V,\ell m}$ and $b_{\pm 2,\ell m}$ which enter Eqs. (5.26)-(5.41). We proceed in this direction in sections 5.2.2 and 5.2.3, where we analyze the effects of the CPT-odd and CPT-even operators, respectively.

5.2.2 Effects of the CPT-odd operator

We start by considering the impact of the CPT-odd operator on the CMB polarization. In this case, the explicit expressions of the $\bar{\rho}$'s coefficients read

$$\bar{\rho}_Q = 0\,, \tag{5.42}$$

$$\bar{\rho}_U = 0\,, \tag{5.43}$$
$$\bar{\rho}_V = 4c\left[(\bar{k}_{AF})^1 c_\phi s_\theta + (\bar{k}_{AF})^2 s_\phi s_\theta + (\bar{k}_{AF})^3 c_\theta + (\bar{k}_{AF})_0\right]\,, \tag{5.44}$$

where the bar once again denotes quantities averaged along the line of sight, i.e.

$$(\bar{k}_{AF})_0 \equiv \int_{\tau_{\rm LS}}^{\tau_0} (k_{AF})_0\, d\tau\,, \quad (\bar{k}_{AF})^i \equiv \int_{\tau_{\rm LS}}^{\tau_0} (k_{AF})^i d\tau\,. \tag{5.45}$$

From Eqs. (5.42)-(5.44) we understand that the CPT-odd part of the Lagrangian only leads to a mixing among the U and Q Stokes parameters, hence giving rise to cosmic birefringence, but no circular polarization is generated, since $\bar{\rho}_Q = \bar{\rho}_U = 0$.

We can then expand $\bar{\rho}_V$ in spherical harmonics as in Eq. (5.24), where the expansion coefficients $b_{V,\ell m}$ can be obtained using the orthogonality condition of spherical harmonics as

$$\begin{aligned} b_{V,\ell m} &= \int_0^\pi {\rm d}\theta \sin\theta \int_0^{2\pi} {\rm d}\phi\; \bar{\rho}_V(\theta,\phi)(\tau_0 - \tau_{\rm LS}) Y^*_{\ell m}(\theta,\phi) \\ &= (-1)^m \sqrt{\frac{2\ell+1}{4\pi}\frac{(\ell+m)!}{(\ell-m)!}} \int_0^\pi {\rm d}\theta \sin\theta \int_0^{2\pi} {\rm d}\phi\; \bar{\rho}_V(\theta,\phi)(\tau_0 - \tau_{\rm LS})\, P_\ell^{-m}(\cos\theta) e^{-im\phi}\,. \end{aligned} \tag{5.46}$$

Then, inserting Eq. (5.44) into Eq. (5.46), we find

$$b_{V,00} = 8\sqrt{\pi} c\,(\bar{k}_{AF})_0\,, \tag{5.47}$$
$$b_{V,10} = 8\sqrt{\frac{\pi}{3}} c\,(\bar{k}_{AF})^3\,, \tag{5.48}$$
$$b_{V,1-1} = 4\sqrt{\frac{2\pi}{3}} c\left[(\bar{k}_{AF})^1 + i(\bar{k}_{AF})^2\right]\,, \tag{5.49}$$
$$b_{V,11} = -4\sqrt{\frac{2\pi}{3}} c\left[(\bar{k}_{AF})^1 - i(\bar{k}_{AF})^2\right] = -b^*_{V,1-1}\,. \tag{5.50}$$

The coefficients $b_{V,\ell m}$ vanish for $\ell > 1$.

5.2.3 Effects of the CPT-even operator

Differently from the previous scenario, the presence of the CPT-even operator leads to $\bar{\rho}_V = 0$, but $\bar{\rho}_Q \neq 0$ and $\bar{\rho}_U \neq 0$, meaning that circular polarization is generated from the conversion of the primordial linear polarization components. As discussed in Sec. 5.2.1, to study this effect it is convenient to introduce the quantities $\bar{\rho}_{\pm 2}$, which under rotations transform as spin-± 2 functions. Their explicit expressions are given by

$$\begin{aligned} \bar{\rho}_{+2} = \frac{\omega}{\sqrt{2}}\Bigg\{ &\Big[4 s_\theta s_\phi \Big(c_\theta\left((\bar{k}_F)_{3020} + (\bar{k}_F)_{3121}\right) - (\bar{k}_F)_{2110} - (\bar{k}_F)_{3230}\Big) \\ &- 4 c_\theta c_{2\phi}\left((\bar{k}_F)_{3220} - (\bar{k}_F)_{3110}\right) - 4 s_\theta c_\phi \Big((\bar{k}_F)_{3130} - (\bar{k}_F)_{2120} + c_\theta\left((\bar{k}_F)_{3221} - (\bar{k}_F)_{3010}\right)\Big) \\ &- s_{2\phi}\Big((c_{2\theta}+3)\left((\bar{k}_F)_{2010} + (\bar{k}_F)_{3231}\right) - 4 c_\theta\left((\bar{k}_F)_{3120} + (\bar{k}_F)_{3210}\right)\Big)\Big] \\ &+ i\Big[c_{2\phi}\Big(\left((\bar{k}_F)_{3120} + (\bar{k}_F)_{3210}\right)(c_{2\theta}+3) - 4 c_\theta\left((\bar{k}_F)_{2010} + (\bar{k}_F)_{3231}\right)\Big) \\ &+ 4 s_\theta s_\phi \Big(c_\theta\left((\bar{k}_F)_{3130} - (\bar{k}_F)_{2120}\right) - (\bar{k}_F)_{3010} + (\bar{k}_F)_{3221}\Big) \\ &+ 4 s_\theta c_\phi \Big((\bar{k}_F)_{3020} + (\bar{k}_F)_{3121} - c_\theta\left((\bar{k}_F)_{2110} + (\bar{k}_F)_{3230}\right)\Big) \end{aligned}$$

$$- s_{2\phi}(c_{2\theta}+3)\left((\bar{k}_F)_{3110}-(\bar{k}_F)_{3220}\right)+2s_\theta^2\left(2(\bar{k}_F)_{3021}+(\bar{k}_F)_{3120}-(\bar{k}_F)_{3210}\right)\Big]\Bigg\}\,, \tag{5.51}$$

and $\bar{\rho}_{-2}=\bar{\rho}^*_{+2}$, where we have defined

$$(\bar{k}_F)_{\alpha\beta\mu\nu}\equiv\int_{\tau_{\rm LS}}^{\tau_0}\omega(k_F)_{\alpha\beta\mu\nu}\,d\tau\,. \tag{5.52}$$

Then, since spin-0 quantities are easier to handle in explicit calculations, we can use the spin-lowering and spin-raising operators (see Appendix A for their definitions and main properties) and act twice with them on $\bar{\rho}_{\pm2}$. The resulting quantities can then be expanded in spin-0 spherical harmonics. Acting twice with the spin-lowering operator $\bar{\eth}$ on $\bar{\rho}_+$ we get

$$\bar{\eth}^{\,2}\bar{\rho}_+=\bar{\eth}^{\,2}\sum_{\ell m}b_{2,\ell m}\,{}_2Y_{\ell m}(\hat{\mathbf{n}})=\sum_{\ell m}\left[\frac{(\ell+2)!}{(\ell-2)!}\right]^{1/2}b_{2,\ell m}Y_{\ell m}(\hat{\mathbf{n}})\,. \tag{5.53}$$

The coefficients $b_{2,\ell m}$ can then be obtained from Eq. (5.53) using again the orthogonality condition of spherical harmonics and read

$$b_{2,\ell m}=(-1)^m\sqrt{\frac{2\ell+1}{4\pi}\frac{(\ell+m)!}{(\ell-m)!}\frac{(\ell-2)!}{(\ell+2)!}}\int_0^\pi \mathrm{d}\theta\sin\theta\int_0^{2\pi}\mathrm{d}\phi\;\bar{\eth}^{\,2}\bar{\rho}_{+2}(\theta,\phi)\,P_\ell^{-m}(\cos\theta)e^{-im\phi}\,, \tag{5.54}$$

where we have also used the following property of spherical harmonics

$$Y^*_{\ell m}(\theta,\phi)=(-1)^mY_{\ell-m}(\theta,\phi)=(-1)^m\sqrt{\frac{2l+1}{4\pi}\frac{(\ell+m)!}{(\ell-m)!}}\,P_\ell^{-m}(\cos\theta)e^{-im\phi}\,, \tag{5.55}$$

with $P_\ell^m(\cos\theta)$ denoting the associated Legendre polynomials. Note that, since $\bar{\rho}_{-2}=\bar{\rho}^*_{+2}$, it follows that

$$b^*_{-2,\ell m}=(-1)^mb_{2,\ell-m}\,. \tag{5.56}$$

Inserting in Eq. (5.54) the explicit expression of $\bar{\rho}_{+2}$ given in Eq. (5.51), we find that the coefficients $b_{\pm2,\ell m}$ are non-vanishing only for $\ell=2$. The explicit expressions of the $b_{2,\ell m}$ are given by

$$b_{2,2-2}=4\sqrt{\frac{2\pi}{5}}\Bigg\{(\bar{k}_F)_{3110}-(\bar{k}_F)_{3220}+i\Big[(\bar{k}_F)_{3120}+(\bar{k}_F)_{3210}-(\bar{k}_F)_{2010}-(\bar{k}_F)_{3231}\Big]\Bigg\}\,, \tag{5.57}$$

$$b_{2,2-1}=4\sqrt{\frac{2\pi}{5}}\Bigg\{(\bar{k}_F)_{3130}-(\bar{k}_F)_{2120}+(\bar{k}_F)_{3221}-(\bar{k}_F)_{3010}$$
$$+i\Big[(\bar{k}_F)_{2110}+(\bar{k}_F)_{3230}-(\bar{k}_F)_{3020}-(\bar{k}_F)_{3121}\Big]\Bigg\}\,, \tag{5.58}$$

$$b_{2,20}=8i\sqrt{\frac{\pi}{15}}\Big[2(\bar{k}_F)_{3021}+(\bar{k}_F)_{3120}-(\bar{k}_F)_{3210}\Big]\,, \tag{5.59}$$

$$b_{2,21}=4\sqrt{\frac{2\pi}{5}}\Bigg\{-(\bar{k}_F)_{3130}-(\bar{k}_F)_{2120}-(\bar{k}_F)_{3221}+(\bar{k}_F)_{3010}$$
$$-i\Big[(\bar{k}_F)_{2110}+(\bar{k}_F)_{3230}+(\bar{k}_F)_{3020}+(\bar{k}_F)_{3121}\Big]\Bigg\}\,, \tag{5.60}$$

$$b_{2,22}=4\sqrt{\frac{2\pi}{5}}\Bigg\{-(\bar{k}_F)_{3110}+(\bar{k}_F)_{3220}+i\Big[(\bar{k}_F)_{3120}+(\bar{k}_F)_{3210}+(\bar{k}_F)_{2010}+(\bar{k}_F)_{3231}\Big]\Bigg\}\,. \tag{5.61}$$

The $b_{-2,\ell m}$ can be readly obtained from Eqs. (5.57)-(5.61) using the condition (5.56).

In doing these computations we have assumed that the standard dispersion relation for photons holds true, i.e. $\omega = ck$. In principle, we should take into account the corrections to the dispersion relation, which are of the kind $\omega = ck\,[1 + \mathcal{O}(k_F, k_{AF})]$. When included in Eqs. (5.57)-(5.61), these corrections lead to higher-order contributions in k_F and k_{AF}. Since LV effects are constrained to be very small [271], we can work at leading order in the LV coefficients, so that we can take $\omega \simeq ck$.

5.2.4 CMB spectra within the minimal SME

Now that we have the explicit expressions of the coefficients $b_{V,\ell m}$ (see Eqs. (5.47)-(5.50)) and $b_{\pm 2,\ell m}$ (see Eqs. (5.57)-(5.61)) we are ready to evaluate the imprints of the LV operators on the CMB spectra, according to Eqs. (5.26)-(5.41). These effects are encoded in the following 4 dimensionless phenomenological parameters related to the $b_{V,\ell m}$ and $b_{\pm 2,\ell m}$:

$$4\pi\,\beta^2_{AF,T} = b^2_{V,00}\,, \tag{5.62}$$

$$4\pi\,\beta^2_{AF,S} = \sum_m |b_{V,1m}|^2\,, \tag{5.63}$$

$$4\pi\,\beta^2_{F,E} = \sum_m |b_{-2,2m} + b_{2,2m}|^2\,, \tag{5.64}$$

$$4\pi\,\beta^2_{F,B} = \sum_m |b_{-2,2m} - b_{2,2m}|^2\,. \tag{5.65}$$

Using Eqs. (5.47)-(5.50) and (5.57)-(5.61), these can be rewritten in terms of the LV coefficients appearing in the action (5.1) as

$$\beta^2_{AF,T} = 16c^2\left[(\bar{k}_{AF})_0\right]^2\,, \tag{5.66}$$

$$\beta^2_{AF,S} = \frac{16}{3}c^2|\bar{\mathbf{k}}_{\mathbf{AF}}|^2 = \frac{16}{3}c^2\left(\left[(\bar{k}_{AF})_1\right]^2 + \left[(\bar{k}_{AF})_2\right]^2 + \left[(\bar{k}_{AF})_3\right]^2\right)\,, \tag{5.67}$$

$$\begin{aligned}\beta^2_{F,E} &= \frac{64}{5}\left[\Big((\bar{k}_F)_{3020} + (\bar{k}_F)_{3121}\Big)^2 + \Big((\bar{k}_F)_{3010} - (\bar{k}_F)_{3221}\Big)^2 + \Big((\bar{k}_F)_{2010} + (\bar{k}_F)_{3231}\Big)^2\right] \\ &\equiv \frac{64}{5}\bar{k}^2_{F,E}\,,\end{aligned} \tag{5.68}$$

$$\begin{aligned}\beta^2_{F,B} = \frac{32}{15}\Bigg\{&2\Big(2(\bar{k}_F)_{3021} + (\bar{k}_F)_{3120} - (\bar{k}_F)_{3210}\Big)^2 + 6\Big[\Big((\bar{k}_F)_{3120} + (\bar{k}_F)_{3210}\Big)^2 \\ &+ \Big((\bar{k}_F)_{3110} - (\bar{k}_F)_{3220}\Big)^2 + \Big((\bar{k}_F)_{2120} - (\bar{k}_F)_{3130}\Big)^2 \\ &+ \Big((\bar{k}_F)_{2110} + (\bar{k}_F)_{3230}\Big)^2\Big]\Bigg\} \\ \equiv \frac{32}{15}&\bar{k}^2_{F,B}\,.\end{aligned} \tag{5.69}$$

The coefficients $\beta^2_{AF,T}$ and $\beta^2_{AF,S}$ are related to the time and space components of the vector k_{AF} and thus account for CPT-odd Lorentz violations. The coefficients $\beta^2_{F,E}$ and $\beta^2_{F,B}$ are instead related to some combinations of the components of the tensor k_F and thus parametrize CPT-even Lorentz violations. The modified CMB spectra are then given by

$$C^{TE}_\ell = \left(1 - \frac{\mathcal{Z}}{2}\right)\widetilde{C}^{TE}_\ell\,, \tag{5.70}$$

$$C^{EE}_\ell = (1 - \mathcal{Z})\,\widetilde{C}^{EE}_\ell + \sum_{\ell_1}\mathcal{K}^{11}_{\ell_1\ell}\widetilde{C}^{EE}_{\ell_1} + \sum_{\ell_1}\mathcal{K}^{22}_{\ell_1\ell}\widetilde{C}^{BB}_{\ell_1}\,, \tag{5.71}$$

$$C_\ell^{BB} = (1-\mathcal{Z})\,\widetilde{C}_\ell^{BB} + \sum_{\ell_1} \mathcal{K}^{11}_{\ell_1\ell}\widetilde{C}_{\ell_1}^{BB} + \sum_{\ell_1} \mathcal{K}^{22}_{\ell_1\ell}\widetilde{C}_{\ell_1}^{EE}\,, \tag{5.72}$$

$$C_\ell^{EB} = \sqrt{\beta^2_{AF,T}}\left(\widetilde{C}_\ell^{EE} - \widetilde{C}_\ell^{BB}\right), \tag{5.73}$$

$$C_\ell^{TB} = \sqrt{\beta^2_{AF,T}}\,\widetilde{C}_\ell^{TE}\,, \tag{5.74}$$

$$C_\ell^{VV} = \sum_{\ell_1} \mathcal{K}^{33}_{\ell_1\ell}\tilde{C}_{\ell_1}^{EE} + \sum_{\ell_1} \mathcal{K}^{44}_{\ell_1\ell}\tilde{C}_{\ell_1}^{BB}\,, \tag{5.75}$$

$$C_\ell^{EV} = C_\ell^{BV} = 0\,, \tag{5.76}$$

where

$$\mathcal{Z} = \beta^2_{AF,T} + \beta^2_{AF,S} + \frac{\left(\beta^2_{F,E} + \beta^2_{F,B}\right)}{4}\,, \tag{5.77}$$

$$\sum_{\ell_1} \mathcal{K}^{11}_{\ell_1\ell}\widetilde{C}_{\ell_1}^{XX} = \beta^2_{AF,S}\,\frac{4}{\ell+\ell^2}\widetilde{C}_\ell^{XX}\,, \tag{5.78}$$

$$\sum_{\ell_1} \mathcal{K}^{22}_{\ell_1\ell}\widetilde{C}_{\ell_1}^{XX} = \beta^2_{AF,T}\,\widetilde{C}_\ell^{XX} + \beta^2_{AF,S}\left(\frac{\ell^2-4}{\ell(2\ell+1)}\widetilde{C}_{\ell-1}^{XX} + \frac{(\ell-1)(\ell+3)}{(\ell+1)(2\ell+1)}\widetilde{C}_{\ell+1}^{XX}\right), \tag{5.79}$$

$$\begin{aligned}\sum_{\ell_1} \mathcal{K}^{33(44)}_{\ell_1\ell}\widetilde{C}_{\ell_1}^{XX} = \beta^2_{F,B(E)}&\left(\frac{(\ell-2)(\ell-3)}{4(4\ell^2-1)}\tilde{C}_{\ell-2}^{XX} + \frac{3(\ell^2+\ell-2)}{2(4\ell^2+4\ell-3)}\tilde{C}_\ell^{XX}\right.\\ &\left.+\frac{(\ell+3)(\ell+4)}{4(4\ell^2+8\ell+3)}\tilde{C}_{\ell+2}^{XX}\right) + \beta^2_{F,E(B)}\left(\frac{\ell-2}{2(2\ell+1)}\tilde{C}_{\ell-1}^{XX} + \frac{3+\ell}{2(2\ell+1)}\tilde{C}_{\ell+1}^{XX}\right).\end{aligned} \tag{5.80}$$

By inspecting the expressions (5.70)-(5.80) we can identify the effects of different classes of LV operators:

- the CPT-odd operator, parametrized by $\beta^2_{AF,T}$ and $\beta^2_{AF,S}$, leads to the well-known cosmic birefringence effect. In particular, $\beta^2_{AF,T}$, related to the time component of the 4-vector k_{AF}, gives rise to isotropic birefringence [57,272–277], which produces non-vanishing EB and TB spectra and the mixing between EE and BB spectra. Anisotropic birefringence [278–283] is induced by the parameter $\beta^2_{AF,S}$, related to the space components of k_{AF}. This mixes the EE and BB spectra by introducing a coupling among different multipoles (i.e. off-diagonal correlations), such that the ℓ-th multipole is coupled to both the $(\ell-1)$-th and $(\ell+1)$-th ones;

- the VV spectrum is sourced from EE and BB spectra when the CPT-even operators are present. Similarly to what observed for anisotropic birefringence, a coupling between different multipoles is induced. In this case, it affects all the multipoles between the $(\ell-2)$-th and the $(\ell+2)$-th. Note that the VV spectrum is the only one which, if measured, could break the degeneracy between $\beta^2_{F,E}$ and $\beta^2_{F,B}$, since in the other spectra only the sum of these two parameters comes into play. In this model, no mixing is predicted between V modes and E- or B-modes;

- both the CPT-even and CPT-odd operators rescale the EE, BB and TE spectra via the parameter $\mathcal{Z}$.

The modifications to the CPT-even linear polarization spectra, Eqs. (5.70)-(5.72), and the introduction of the circular polarization spectrum, Eq. (5.75), have been implemented in a customized version of the Boltzmann code `CAMB` [284,285], hereafter `camb-cpt`.

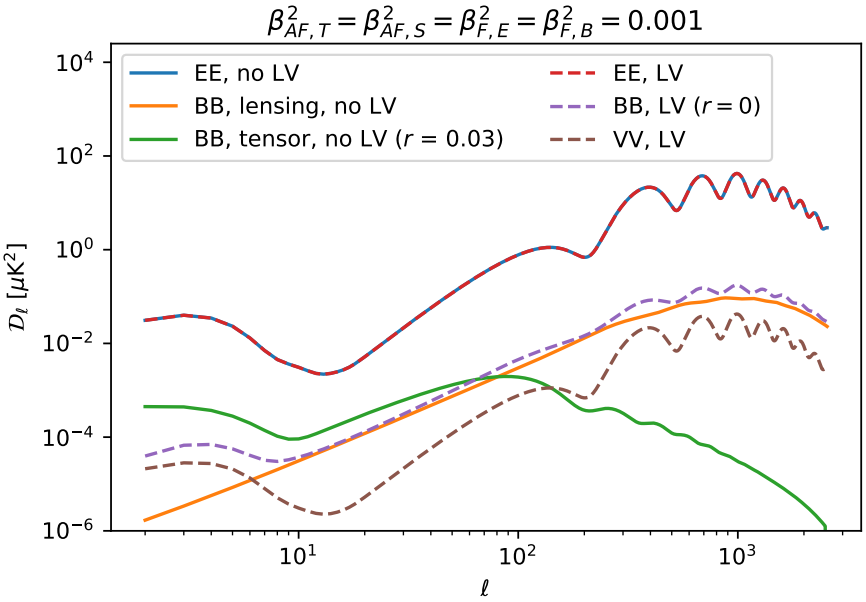

Figure 5.1: Standard CMB power spectra (no LV) in solid lines and with Lorentz violating effects (LV) in dashed lines. The LV spectra are generated according to Eqs. (5.70)-(5.75) with the choice of the parameters $\beta^2_{AF,T} = \beta^2_{AF,S} = \beta^2_{F,E} = \beta^2_{F,B} = 0.001$ using `camb-cpt`. The VV spectrum is non-vanishing only in the LV case, sourced by both the EE and BB ones. Note that the LV and standard EE spectra almost overlap and are practically indistinguishable within the scale of this plot.

Figure 5.1 shows a comparison between the standard CMB spectra (i.e. in the absence of LV effects) and those including LV effects obtained with `camb-cpt` by setting all the β^2 parameters equal to 0.001. The most relevant feature is the leakage of E- into B-modes. Another clear effect is the VV power spectrum mostly sourced by the E modes. The linear-polarization spectra are also rescaled by the $\mathcal{Z}$ factor in Eq. (5.77), which depends on all the β^2 parameters.

5.3 Data sets and analysis

We perform a Monte Carlo Markov Chain (MCMC) analysis to obtain constraints on the Lorentz-violating parameters $\beta^2_{AF,T}, \beta^2_{AF,S}, \beta^2_{F,E}, \beta^2_{F,B}$ jointly with other cosmological, foreground and nuisance parameters. To this scope, the code `camb-cpt` has been interfaced with the MCMC sampler `Cobaya` [286]. Using the Gelman-Rubin convergence statistics [287], we assume that our MCMC chains have reached convergence when $R - 1 \lesssim 0.01$.

We analyze the following data:

- *Planck* 2018: *Planck* temperature and polarization power spectra [20] and lensing reconstruction power spectrum [21], from the *Planck* 2018 legacy release;
- BICEP/Keck 2018 (BK18): combination of all the B-modes data collected by BICEP2, Keck Array and BICEP3 experiments until the 2018 season [8];
- ACT: Atacama Cosmology Telescope temperature and polarization power spectra as published in the Data Release 4 [7]. Since the ACT data are always used in combination with *Planck*, we follow the prescription of the ACT collaboration and only consider multipoles larger than 1800 in temperature. For more details see section 6.2.3 of [7];
- VV: V modes power spectra as published by CLASS [22] and SPIDER [23] experiments.

For *Planck*, BK18 and ACT we employ the official likelihood packages released by the respective collaborations. For the V-modes data, a simple custom-made likelihood has been added to the framework. The χ^2 for the V modes is computed as:

$$\chi^2_{VV} = \sum_b \frac{(D^{VV}_{b,\text{theory}} - D^{VV}_{b,\text{data}})^2}{\sigma_b^2}\,, \tag{5.81}$$

where $D^{VV}_{b,\text{data}}$ and $D^{VV}_{b,\text{theory}}$ are the data and the binned theory respectively and σ_b^2 is the error on the bandpowers. Since CLASS and SPIDER are both completely noise dominated, we can safely add together their respective χ^2 computed as in Eq. (5.81).

In our analysis we consider the following data combinations:

(i) *Planck* 2018;

(ii) *Planck* 2018+BK18;

(iii) *Planck* 2018+BK18+CLASS+SPIDER;

(iv) *Planck* 2018+BK18+ACT.

Notice that we do not consider the combination *Planck* 2018+BK18+ACT+SPIDER+CLASS since the inclusion of V-modes data does not add any constraining power, as will be discussed in Section 5.4 for more details.

The ΛCDM+r model (i.e., allowing for non-vanishing primordial gravitational waves with amplitude set by the tensor-to-scalar ratio r) provides our baseline scenario, unless otherwise stated. See Ref. [6] for details about parametrization, theoretical assumptions and priors used. For the foreground and nuisance parameters, we follow the prescriptions provided by *Planck* [6] and BICEP [8] collaborations. In addition to the baseline, we consider the β^2 parameters defined in Eqs. (5.66)-(5.69). On those parameters we impose uniform positive priors. Further model extensions are not considered in this work.

5.4 Results of the MCMC analysis

In this section we present the constraints derived on the phenomenological parameters $\beta^2_{AF,T}$, $\beta^2_{AF,S}$, $\beta^2_{F,E}$ and $\beta^2_{F,B}$ using the aforementioned datasets and parametrizations. We also discuss the possible correlations with the parameters of the standard ΛCDM model.

5.4.1 Constraints on the CPT-odd phenomenological parameters only

As a first step in our analysis, we consider only the CPT-odd term in Eq. (5.1) and fix to zero the parameters related to the CPT-even term. The effect of this term on the CMB spectra is encoded in the two parameters $\beta^2_{AF,T}$ and $\beta^2_{AF,S}$ and leads to isotropic and anisotropic birefringence effects, respectively (see the discussion at the end of Sec. 5.2.4). In Figure 5.2, we show the two-dimensional and one-dimensional posterior probability distributions of a subset of cosmological parameters, including $\beta^2_{AF,T}$ and $\beta^2_{AF,S}$, explored in the analysis with the combination of *Planck*+BK18 data. The baseline model is given by the ΛCDM+r cosmology. To better elucidate the effect of $\beta^2_{AF,T}$ and $\beta^2_{AF,S}$ on the constraints of the remaining parameters, we also vary them one at the time while fixing the other to zero. We note that varying either $\beta^2_{AF,T}$ or $\beta^2_{AF,S}$ has equivalent impact on the constraints on other cosmological parameters. This is due to the fact that both $\beta^2_{AF,T}$ and $\beta^2_{AF,S}$ lead to qualitatively equivalent modifications of the BB spectrum. Indeed, an inspection of Eq. (5.72) and Eq. (5.79) shows that the overall effect produced by non-vanishing $\beta^2_{AF,T}$ or $\beta^2_{AF,S}$ is an effective rotation of E-modes into B-modes.

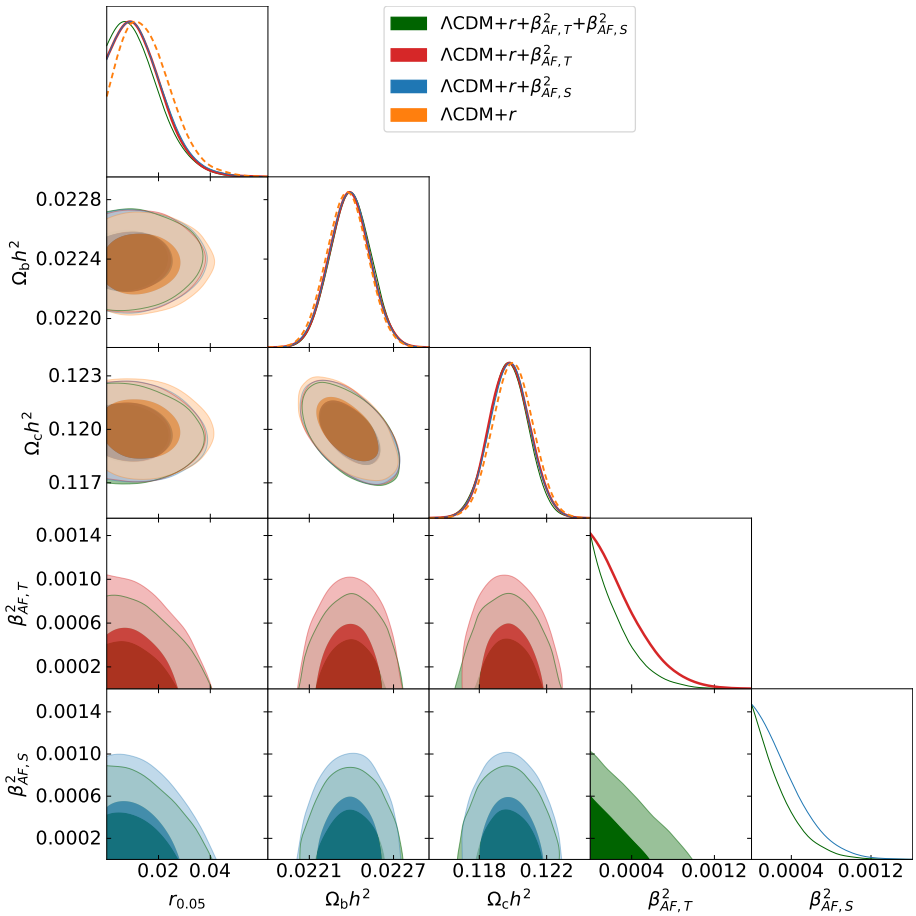

Figure 5.2: One and two-dimensional posterior probability distributions for a subset of parameters varied in the MCMC analysis. We report the constraints obtained when assuming a ΛCDM+r+$\beta^2_{AF,T}$+$\beta^2_{AF,S}$ model (in green), ΛCDM+r+$\beta^2_{AF,T}$ (in red), ΛCDM+r+$\beta^2_{AF,S}$ (in blue) and ΛCDM+r (in orange) using *Planck*+BK18 data. Note the tighter limit on r when one of the β^2_{AF} parameters is allowed to vary with respect to the case in which they are both equal to zero. Opening to both β^2_{AF} further improves the individual constraints on $\beta^2_{AF,T}$, $\beta^2_{AF,S}$ and r, see the main text for a detailed discussion.

Such rotation competes with r in increasing the power in B-modes (see Figure 5.1, where the two β^2_{AF} and r enhance the reionization and recombination bumps in the BB power spectrum). This explains why the marginalization over $\beta^2_{AF,T}$ and $\beta^2_{AF,S}$ tightens the constraints on r with respect to those obtained in the ΛCDM+r baseline analysis.

Even though in Figure 5.2 we report the results from *Planck*+BK18, the two β^2_{AF} could be also constrained with *Planck* data only, exploiting their effect on E-mode polarization. However, the resulting bounds on $\beta^2_{AF,T}$ and $\beta^2_{AF,S}$ are nearly an order-of-magnitude broader than those obtained when adding BK18 to *Planck* data. This is due to the lack of constraining power from B-modes which are more strongly affected by the two β^2_{AF}.

In Fig. 5.3 (left panel), we show the constraints on a subset of parameters and compare the results obtained with *Planck* data only in ΛCDM+β^2_{AF} and ΛCDM+r+β^2_{AF} with those obtained with the combination of *Planck*+BK18 data in ΛCDM+r+β^2_{AF}. As expected, the bounds on β^2_{AF} are tightened when r is varied jointly with the CPT-odd parameters, even if using *Planck* data only. However, the improvement is dramatic when BK18 data are added to the analysis. In the right panel of Fig. 5.3 we show a zoom-in of the lower right triangle to better appreciate the impact of BK18 data on the constraints on the β^2_{AF}. We stress again that no V-modes are sourced by the CPT-odd term of the Lagrangian.

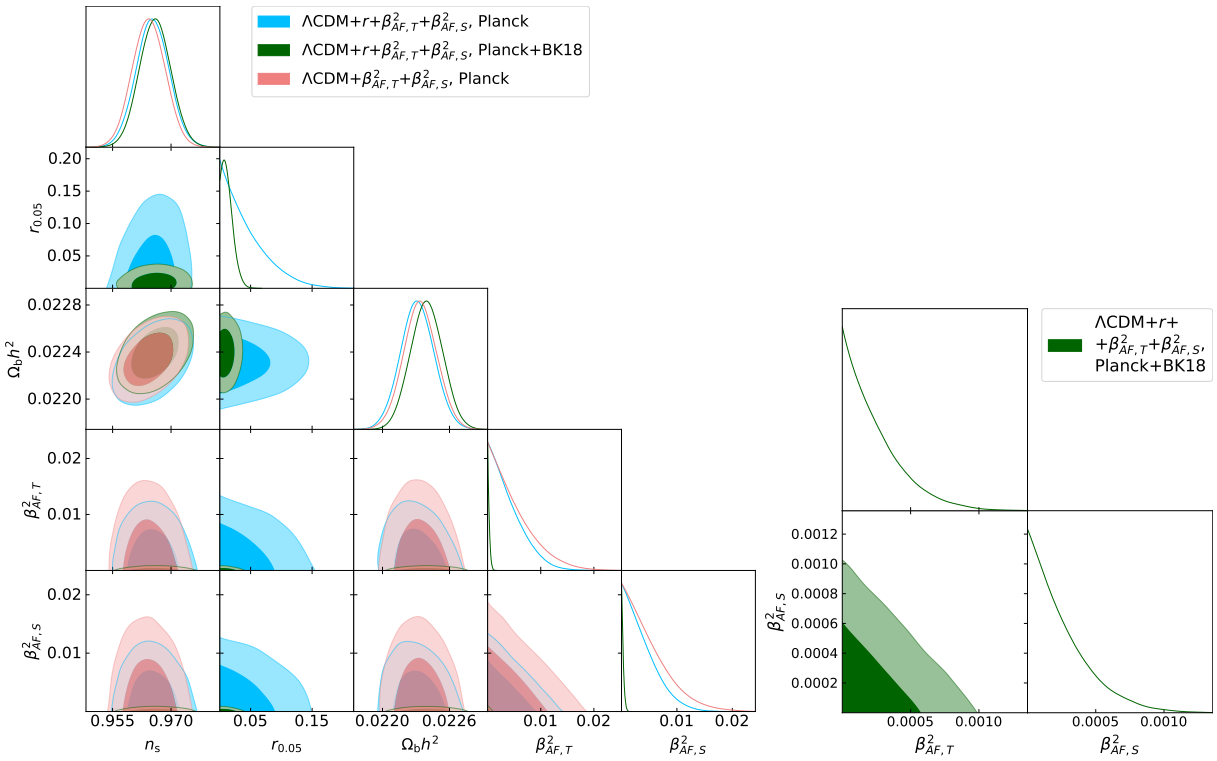

Figure 5.3: *Left panel*: one and two-dimensional posterior probability distributions for a subset of parameters varied in the MCMC analysis. We report the constraints obtained when assuming a ΛCDM+$\beta^2_{AF,T}$ + $\beta^2_{AF,S}$ (in pink) and a ΛCDM+r+$\beta^2_{AF,T}$ + $\beta^2_{AF,S}$ (in cyan and green) models. The former using only the *Planck* dataset, while the latter using both *Planck* and *Planck*+BK18. Note how much the constraints on the β^2_{AF} parameters improve when we include BK18 data. *Right panel*: zoom-in showing the constraints on $\beta^2_{AF,T}$ and $\beta^2_{AF,S}$ using *Planck*+BK18.

5.4.2 Constraints on the CPT-even phenomenological parameters only

We now focus on the CPT-even term of the action in Eq. (5.1). The effects on the CMB spectra are in this case encoded by the two parameters $\beta^2_{F,E}$ and $\beta^2_{F,B}$, which are responsible for an overall rescaling of the TE, EE and BB spectra via the parameter $\mathcal{Z}$, see Eqs. (5.70), (5.71), (5.72). If we restrict our analysis to consider only linear polarization, the impact of the two $\beta^2_{F,E/B}$ is degenerate. However, the CPT-even term sources a degree of circular polarization from a mixing of E- and B-modes appropriately rescaled by $\beta^2_{F,E}$ and $\beta^2_{F,B}$, see Eq. (5.75). The sourcing of V-modes could in principle be used to individually constrain the $\beta^2_{F,E/B}$, provided that a V-mode experiment puts statistically significant bounds on the VV signal. However, the signal-to-noise ratio in the SPIDER and CLASS data is insufficient to put significant bounds on the two parameters. This is shown in Fig. 5.4, where the posterior distributions of all the cosmological parameters, including $\beta^2_{F,E}$, with and without V-mode data are perfectly overlapping. We expect this to be exactly the same for $\beta^2_{F,B}$, since in the absence of sensitive enough V-mode data both $\beta^2_{F,E}$ and $\beta^2_{F,B}$ parameters are constrained through the rescaling of TE, EE and BB spectra within $\mathcal{Z}$. Therefore, in the following, we neglect the contribution of V modes data and we quote results for the effective parameter β^2_F, defined as

$$\beta^2_F \equiv \frac{\beta^2_{F,E} + \beta^2_{F,B}}{4} \,. \tag{5.82}$$

In Fig. 5.5, we show the 2D and 1D posterior distributions of a subset of cosmological parameters explored with the combination of *Planck*+BK18 and *Planck*+BK18+ACT data. We compare the results within the ΛCDM+r + β^2_F model and the baseline ΛCDM+r model.

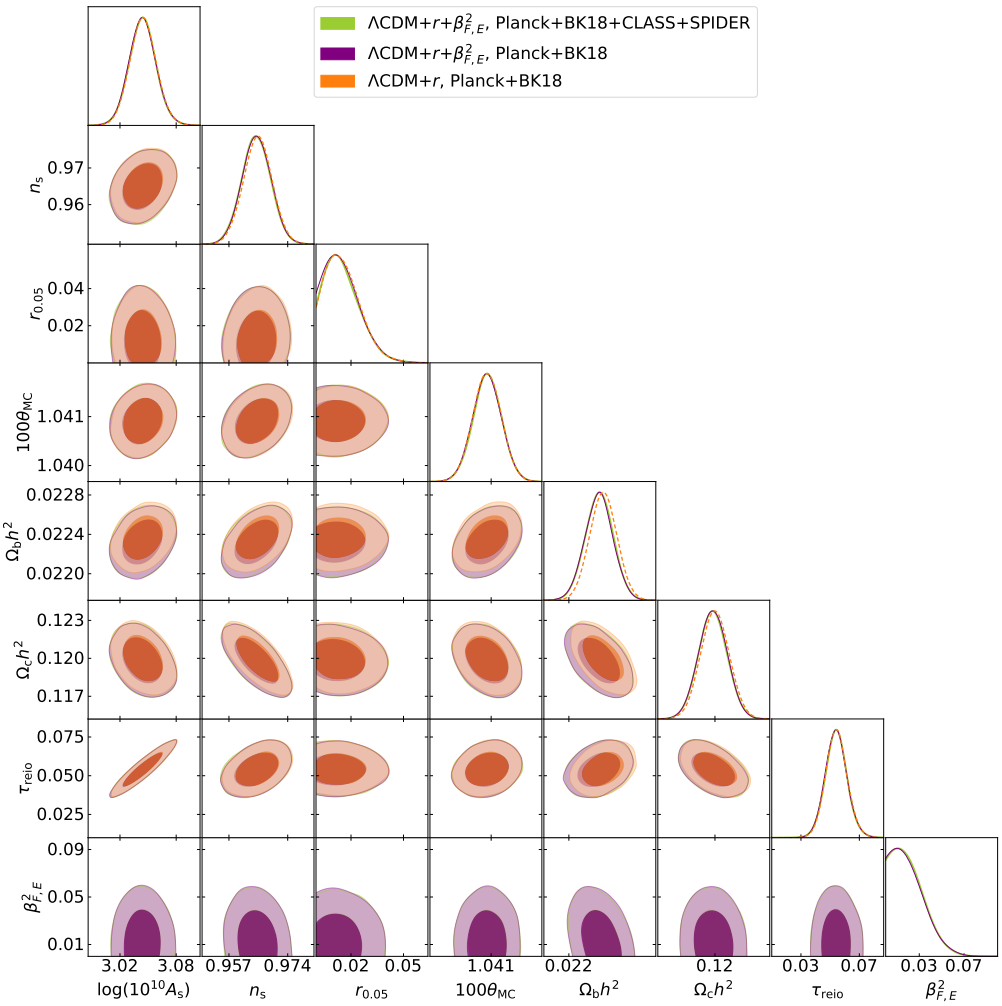

Figure 5.4: One and two-dimensional posterior probability distribution for the full set of parameters varied in the MCMC analysis. We report the constraints obtained when assuming the ΛCDM+r+$\beta^2_{F,E}$ model using the *Planck*+BK18+CLASS+SPIDER dataset (in lime) and assuming ΛCDM+r+$\beta^2_{F,E}$ (in purple) and ΛCDM+r (in orange), both using the *Planck*+BK18 dataset. The cases ΛCDM+r+$\beta^2_{F,E}$ with and without V-modes data are perfectly overlapping, showing the lack of constraining power from the current circular polarization data and justifying the choice of sampling over the combination β^2_F in Eq. (5.82).

Differently from what discussed for the CPT-odd parameters, we do not see any improvement in the bounds on r when β^2_F is varied. In this case, we expect a positive correlation between r and β^2_F, contrarily to what happens with the β^2_{AF}. Indeed, a non-vanishing β^2_F reduces the amplitude of the BB spectrum, which could be compensated by higher values of r. However, we do not appreciate such a correlation in Fig. 5.5. The reason is that most of the constraining power on β^2_F comes from TE and EE spectra, making any degeneracy with r undetectable. Indeed, the sensitivity on β^2_F from T- and E-modes only is at the same level as that on $\beta^2_{AF,T/S}$, being driven by the scaling in amplitude of EE and TE spectra. In Fig. 5.5, we also note a shift in $\Omega_b h^2$ and $\Omega_c h^2$ with respect to the constraints obtained when $\beta^2_F = 0$. The shifts can be easily explained when considering the impact of the parameters on the shape of the TE and EE spectra. The main effect of the non-vanishing β^2_F on the polarization power spectra is to rescale their overall amplitude through $\mathcal{Z}$ in Eq. (5.77). A change in $\Omega_b h^2$, instead, affects the amplitude of the TE and EE acoustic oscillations both in the photon density field (by modifying the inertia of the

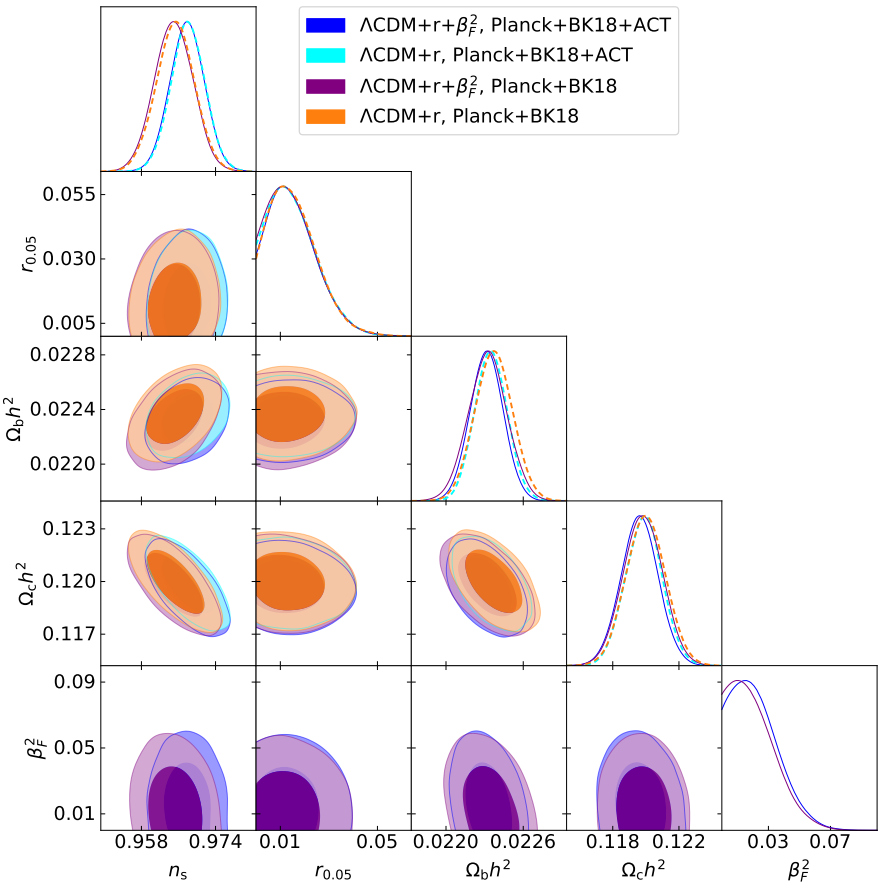

Figure 5.5: One and two-dimensional posterior probability distributions for a subset of parameters varied in the MCMC analysis. We report the constraints obtained when assuming ΛCDM+r+β_F^2 (in purple when using the *Planck*+BK18 dataset, in blue when adding ACT) and ΛCDM+r (in dashed orange and dashed cyan respectively). Since not enough constraining power comes from current V-mode data, we are note able to disentangle the effects of $\beta_{F,E}^2$ and $\beta_{F,B}^2$, and we can only set a limit on their combination $\beta_F^2 = (\beta_{F,E}^2 + \beta_{F,B}^2)/4$. Note the shifts in the posteriors of $\Omega_b h^2$ and $\Omega_c h^2$ when considering the $\Lambda\mathrm{CDM} + r + \beta_F^2$ extension, see the main text for a detailed discussion.

baryon-photon fluid, which is relevant for the temperature transfer function) and in the photon velocity field (as a result of the change in the density), which is relevant for the E-polarization transfer function. From these considerations, we can understand the correlation between β_F^2 and $\Omega_b h^2$. At sub-degree scales (high multipoles ℓ), a change in $\Omega_b h^2$ modifies the damping angular scale since a different baryon density affects the photon mean free path. As a result, the power at small scales is more or less suppressed depending on the value of $\Omega_b h^2$. This effect goes in the opposite direction of the change in the amplitude of the first peaks: a lower value of $\Omega_b h^2$ increases the amplitude of the oscillations at intermediate scales and suppresses the power at small scales. A similar effect at intermediate scales is provided by $\Omega_c h^2$. A decrease of the latter delays the onset of matter-radiation equality, thus shifting to larger scales the boosting effect due to radiation driving on the acoustic oscillations. Therefore, we expect $\Omega_c h^2$ to decrease when allowing for a non-vanishing β_F^2.

The inclusion of ACT data causes the same shift of $\Omega_b h^2$ and $\Omega_c h^2$ when sampling over β_F^2, as can be seen in Fig. 5.5. Moreover, the limit on β_F^2 is broader. This is likely driven by the known preference of ACT for larger A_s and n_s [262], which can be compensated by a larger value of β_F^2.

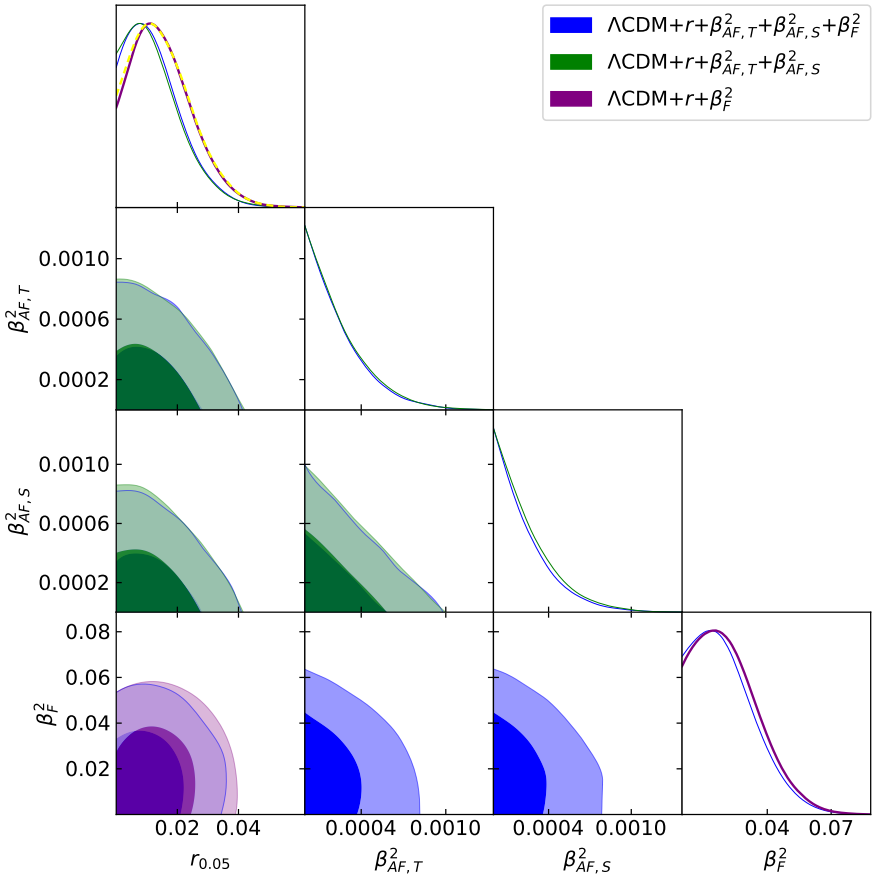

Figure 5.6: One and two-dimensional posterior probability distributions for the LV parameters β^2 varied in the MCMC analysis. We report the constraints obtained when assuming ΛCDM+r+$\beta^2_{AF,T}$+$\beta^2_{AF,S}$+β^2_F (in dark blue), ΛCDM+r+$\beta^2_{AF,T}$+$\beta^2_{AF,S}$ (in green) and ΛCDM+r+β^2_F (in purple), using the *Planck*+BK18+ACT dataset. The posterior in dashed yellow is the reference for the ΛCDM+r case using same dataset. The joint marginalization over all the β^2 parameters improves the constraints on β^2_F, while keeping unchanged those on r and the β^2_{AF} parameters.

5.4.3 Joint constraints on the CPT-odd and CPT-even phenomenological parameters

Finally, we investigate the case in which all the CPT-even and CPT-odd parameters are jointly varied. This allows us to investigate how the interplay between the effects induced by different operators affects the constraints on the LV parameters. Figure 5.6 shows the 2D and 1D posterior probabilities of a subset of cosmological parameters plus the β^2 assuming a ΛCDM+r+$\beta^2_{AF,T}$ + $\beta^2_{AF,S}$+β^2_F model. For comparison, we also include the posteriors for the ΛCDM+r+$\beta^2_{AF,T}$+$\beta^2_{AF,S}$ and ΛCDM+r+β^2_F models. On the one hand, we see that the bounds on β^2_F improve when all the β^2 are allowed to vary. In fact, in absence of V-mode data, the only effect of β^2_F is to contribute to the rescaling of the CMB spectra via $\mathcal{Z}$, in the same way as $\beta^2_{AF,T}$ and $\beta^2_{AF,S}$ do. On the other hand, the constraints on $\beta^2_{AF,T}$ and $\beta^2_{AF,S}$ do not improve significantly when the two parameters are varied jointly with β^2_F. In fact, besides rescaling the spectra, they also induce a mixing between E and B modes, which allows to disentangle them from β^2_F. Note again the improved bounds on r when $\beta^2_{AF,T}$ and $\beta^2_{AF,S}$ are varied. The inclusion of ACT mostly affects the constraint on β^2_F (see Figure 5.7), as discussed before. We have collected the 95% CL on r, $\beta^2_{AF,T}$, $\beta^2_{AF,S}$, β^2_F for the cases analyzed in Tab. 5.1.

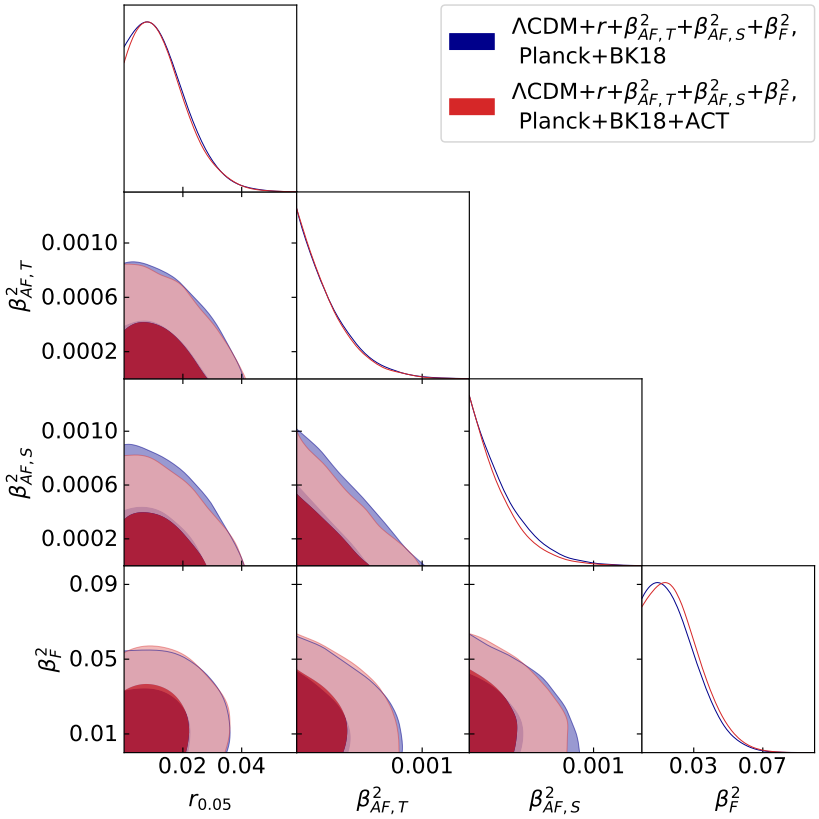

Figure 5.7: One and two-dimensional posterior probability distributions for the LV parameters β^2 varied in the MCMC analysis. We report the constraints obtained when assuming a ΛCDM+r+$\beta^2_{AF,T}$+$\beta^2_{AF,S}$+β^2_F model using *Planck*+BK18 (in dark blue) and *Planck*+BK18+ACT (in red). Including ACT data weakens the constraints mostly on β^2_F, see the main text for a detailed discussion.

5.5 Implications for the LV coefficients in the minimal SME action

In this section we translate the bounds on the phenomenological parameters $\beta^2_{AF,T}$, $\beta^2_{AF,S}$ and β^2_F introduced in Eqs. (5.66), (5.67) and (5.82) into constraints on the LV couplings k_{AF} and k_F appearing in the action in Eq. (5.1). We focus on the constraints obtained with the full dataset combination, *Planck*+BK18+ACT, in the case where the three parameters are jointly varied. The full set of constraints derived from different data and parameter combinations can be found in Table 5.2.

Focusing first on the CPT-odd effects, the constraints on the time component of k_{AF} are usually rephrased as bounds on the parameter $k^{(3)}_{(V)00} = -\sqrt{4\pi}(k_{AF})^0$ (see Refs. [271,273]). This parameter can be linked to the phenomenological parameter $\beta^2_{AF,T}$ as follows:

$$|k^{(3)}_{(V)00}| = \frac{\sqrt{\pi}}{2c(\tau_0 - \tau_{\rm LS})}\sqrt{\beta^2_{AF,T}} \simeq 6 \times 10^{-43}\sqrt{\beta^2_{AF,T}}\ {\rm GeV}\,, \tag{5.83}$$

where we have assumed that $(k_{AF})_0$ is constant along the line of sight and

$$c(\tau_0 - \tau_{\rm LS}) = \frac{c}{H_0}\int_0^{z_{\rm LS}} \frac{dz}{[\Omega_r(1+z)^4 + \Omega_m(1+z)^3 + \Omega_\Lambda]^{1/2}} \simeq 9444\,{\rm Mpc}\,. \tag{5.84}$$

Dataset	Model (ΛCDM+)	$r \times 10^{-2}$	$\beta^2_{AF,T}$ $\times 10^{-2}$	$\beta^2_{AF,S}$ $\times 10^{-2}$	β^2_F $\times 10^{-2}$
Planck	$\beta^2_{AF,T}+\beta^2_{AF,S}$	-	< 1.29	< 1.28	-
Planck	$r+\beta^2_{AF,T}+\beta^2_{AF,S}$	< 11.5	< 0.987	< 0.953	-
Planck+BK18	r	< 3.36	-	-	-
Planck+BK18	$r+\beta^2_{AF,T}$	< 3.07	< 0.0813	-	-
Planck+BK18	$r+\beta^2_{AF,S}$	< 3.13	-	< 0.0805	-
Planck+BK18	$r+\beta^2_{AF,T}+\beta^2_{AF,S}$	< 3.00	< 0.0673	< 0.0697	-
Planck+BK18	$r+\beta^2_F$	< 3.36	-	-	< 4.76
Planck+BK18	$r+\beta^2_{AF,T}+\beta^2_{AF,S}+\beta^2_F$	< 3.02	< 0.0675	< 0.0692	< 4.60
Planck+BK18+VV	$r+\beta^2_F$	< 3.36	-	-	< 4.73
Planck+BK18+ACT	$r+\beta^2_{AF,T}$	< 3.11	< 0.0765	-	-
Planck+BK18+ACT	$r+\beta^2_{AF,S}$	< 3.11	-	< 0.0765	-
Planck+BK18+ACT	$r+\beta^2_{AF,T}+\beta^2_{AF,S}$	< 3.03	< 0.0665	< 0.0668	-
Planck+BK18+ACT	$r+\beta^2_F$	< 3.35	-	-	< 4.91
Planck+BK18+ACT	$r+\beta^2_{AF,T}+\beta^2_{AF,S}+\beta^2_F$	< 3.03	< 0.0655	< 0.0645	< 4.76

Table 5.1: Bounds at 95% CL on r, $\beta^2_{AF,T}$, $\beta^2_{AF,S}$, β^2_F for the listed datasets and models. Eqs. (5.70)-(5.80) show how the β^2 parameters affect the CMB spectra. The limits have been expressed in units of 10^{-2}. The key "VV" represents the combined CLASS+SPIDER dataset for V-modes.

In order to get the estimate in Eq. (5.84), we have used the best-fit values for the cosmological parameters taken from *Planck* 2018 (TT, TE, EE + lowE constraints for ΛCDM model), namely $H_0 = 67.27$ km s^{-1} Mpc^{-1}, $z_{\rm LS} = 1089.95$, $z_{\rm eq} = 3407$, $\Omega_m = 0.3166$, $\Omega_\Lambda = 0.6834$ and $\Omega_r = \Omega_m/(1+z_{\rm eq}) \simeq 9.290 \times 10^{-5}$ [6].

Analogously, from Eq. (5.67) we find for the space components of k_{AF}

$$|\mathbf{k_{AF}}| \simeq 2.93 \times 10^{-43} \sqrt{\beta^2_{AF,S}}\ \text{GeV}\,. \tag{5.85}$$

For what concerns the CPT-even effects, recasting our constraints on β^2_F into bounds on the components of k_F is less trivial, due to the frequency dependence of Eqs. (5.68)-(5.69). From Eqs. (5.68)-(5.69) we obtain

$$k_{F,E+B} \equiv \left(2k^2_{F,E} + \frac{k^2_{F,B}}{3}\right)^{1/2} \simeq 1.29 \times 10^{-28} \left(\frac{\nu}{\text{GHz}}\right)^{-1} \sqrt{\beta^2_F}\,. \tag{5.86}$$

To account for the fact we are combining information coming from different experiments, observing the sky in different frequency channels, we can define an effective frequency ν_f following the method presented in Ref. [288]. Given the frequency dependence in Eq. (5.86), we find

$$\nu_f = \left(\frac{\sum_i \frac{1}{\sigma_i^2}\left[\ln\left(\frac{\nu^i_+}{\text{GHz}}\right) - \ln\left(\frac{\nu^i_-}{\text{GHz}}\right)\right]}{\sum_i \frac{1}{\sigma_i^2}\left(\frac{\nu^i_+}{\text{GHz}} - \frac{\nu^i_-}{\text{GHz}}\right)}\right)^{-1} \text{GHz}\,, \tag{5.87}$$

where $\left[\nu^i_-, \nu^i_+\right]$ is the frequency interval of the i-th frequency channel and σ_i is the noise level. Using Eq. (5.87), we obtain $\nu_f = 158.8\,\text{GHz}, 121.7\,\text{GHz}$ and $122.7\,\text{GHz}$ for Planck [5, 289], BK18 [8, 290] and ACT [262, 291], respectively.

We now report the 95% CL constraints on the LV coefficients using *Planck*+BK18+ACT data, in the case where the three parameters $\beta^2_{AF,T}$, $\beta^2_{AF,S}$ and β^2_F are all free to vary. For the CPT-odd terms we find

$$|k^{(3)}_{(V)00}| < 1.54 \times 10^{-44}\ \text{GeV}\,, \tag{5.88}$$

5.5. Implications for the LV coefficients in the minimal SME action

Dataset	Model (ΛCDM+)	$\lvert k^{(3)}_{(V)00}\rvert \times 10^{-44}$ (GeV)	$\lvert \mathbf{k_{AF}}\rvert \times 10^{-44}$ (GeV)	$k_{F,E+B} \times 10^{-31}$
Planck	$\beta^2_{AF,T}+\beta^2_{AF,S}$	< 6.81	< 3.31	-
Planck	$r+\beta^2_{AF,T}+\beta^2_{AF,S}$	< 5.96	< 2.86	-
Planck+BK18	$r+\beta^2_{AF,T}$	< 1.71	-	-
Planck+BK18	$r+\beta^2_{AF,S}$	-	< 0.83	-
Planck+BK18	$r+\beta^2_{AF,T}+\beta^2_{AF,S}$	< 1.56	< 0.77	-
Planck+BK18	$r+\beta^2_{F}$	-	-	< 2.31
Planck+BK18	$r+\beta^2_{AF,T}+\beta^2_{AF,S}+\beta^2_{F}$	< 1.56	< 0.77	< 2.27
Planck+BK18+ACT	$r+\beta^2_{AF,T}$	< 1.66	-	-
Planck+BK18+ACT	$r+\beta^2_{AF,S}$	-	< 0.81	-
Planck+BK18+ACT	$r+\beta^2_{AF,T}+\beta^2_{AF,S}$	< 1.55	< 0.76	-
Planck+BK18+ACT	$r+\beta^2_{F}$	-	-	< 2.35
Planck+BK18+ACT	$r+\beta^2_{AF,T}+\beta^2_{AF,S}+\beta^2_{F}$	< 1.54	< 0.74	< 2.31

Table 5.2: Bounds at 95% CL on $k^{(3)}_{(V)00}$, $|\mathbf{k_{AF}}|$ and $k_{F,E+B}$ for the listed datasets and models The constraints on $k_{F,E+B}$ are derived taking $\nu_f = 158.8$ GHz for *Planck* alone and $\nu_f = 121.7$ GHz for the combination of *Planck*, BK18 and ACT. As discussed in the main text, this choice is justified by the highest constraining power on LV coefficients given by BK18 data.

$$|\mathbf{k_{AF}}| < 0.74 \times 10^{-44}\ \text{GeV}\,, \tag{5.89}$$

whereas for the CPT-even operator we obtain

$$k_{F,E+B} < 2.31 \times 10^{-31} \left(\frac{\nu_f}{121.7\,\text{GHz}}\right)^{-1}\,. \tag{5.90}$$

Note that the bound on $k_{F,E+B}$ in Eq. (5.90) has been obtained by normalizing the effective frequency to 121.7 GHz, which is the value computed for BK18. This choice is motivated by the fact that BK18 data give the highest constraining power on the LV coefficients, see discussion in Sec. 5.4.

The bounds on the LV coefficients derived in previous literature are collected in [271], see Tables D15 and D16. For the CPT-odd case, an upper bound on the parameter $|k^{(3)}_{(V)00}|$ has been obtained in Ref. [292] using WMAP data, leading to the result $|k^{(3)}_{(V)00}| < 4.9\times10^{-43}$ GeV at 95% CL. We note that the limit derived in our analysis using *Planck*+BK18+ACT data is stronger by more than one order of magnitude, see Eq. (5.88). Analogously, a limit on the coefficient $|\mathbf{k}_{\rm AF}|$ from WMAP data has been obtained in [67, 273], yielding $|\mathbf{k}_{\rm AF}| < 2 \times 10^{-42}$ GeV at 95% CL. In this case, the bound derived in our analysis is stronger by two orders of magnitude, see Eq. (5.89). We stress that the bounds on the CPT-odd coefficients derived in this work are the strongest to date, both considering CMB and other sources. See again Ref. [271] for an exhaustive list of current bounds.

For what concerns CPT-even Lorentz violation, our bound on $k_{F,E+B}$ improves previous constraints by roughly one order of magnitude [67]. The CMB-based cosmological bounds on the CPT-even coefficients are only overcome by those obtained from optical polarimetry of extragalactic sources, see Refs. [271, 293, 294].

The bounds presented in the previous paragraphs are obtained in the most general case with all the β^2 parameters jointly varied. This represents a further novelty of our work. However, it is worth mentioning that, since all the parameters compete for the same power, the bounds obtained with a single parameter exploration are slightly weaker, as can be seen in Table 5.2.

Chapter 6

Imprints of chiral scalar-tensor theories of gravity on CMB bispectra

As we have discussed in Chapter 1, inflation is currently the most widely accepted paradigm able to solve the shortcomings of the standard cosmological model, while at the same time providing a mechanism to source the primordial density perturbations in the Universe. Standard single-field slow-roll models of inflation are based on General Relativity (GR) as the theory of gravity. However, despite the fact that GR has passed every experimental test so far, there are different reasons to expect that it does not provide the complete description of the gravitational interaction. From the point of view of fundamental physics, a quantum description of the gravitational interaction still lacks and cannot be included within the framework of GR. Furthermore, when trying to describe all the fundamental interactions in a unified framework, effective actions with non-minimal couplings with the geometry or higher-order terms involving curvature invariants usually appear. Since inflation involves extremely high energy scales, it is possible that signatures of modifications to GR are left imprinted in the statistical properties of the primordial fluctuations produced during the inflationary phase. For this reason inflation can represent a fundamental stage to test possible departures of gravity from GR.

An interesting possibility to consider is that parity symmetry is broken in the gravity sector, as predicted by several candidates of quantum gravity. A common example is represented by the gravitational Chern-Simons term, proposed for the first time in Ref. [57]. This naturally appears in the context of anomaly cancellation in string theory (via the so-called Green-Schwarz mechanism [295–301]) and in loop quantum gravity [302–306]. The Chern-Simons operator is also commonly introduced as a low energy effective field theory in an expansion in the curvature invariants [307]. Indeed, it represents the fully-covariant operator with the lowest number of derivatives that breaks parity. Another example of parity violation in the gravitational sector arises in Horava-Lifshitz gravity, see e.g. [308, 309].

In slow-roll inflation with the additional presence of these terms, the parity violation generates a different behavior in the propagation of the right (R) and left (L) handed polarization modes of primordial gravitational waves (PGWs). At linear level, the amount of parity violation is quantified by the relative difference between the super-horizon R and L-handed tensor power spectra, which in the literature is usually referred to as chirality of PGWs. Both the Horava-Lifshitz [310, 311] and the Chern-Simons [312–316] terms are predicted to give rise to a low level of chirality of PGWs.

Recently, based on the Chern-Simons term, other ghost-free parity-breaking theories of gravity have been proposed in Ref. [24]. With respect to Chern-Simons gravity, these new theories include operators with first and second derivatives of the non-minimally coupled scalar field. The level of parity violation induced by these theories in the primordial tensor power spectrum has been explored in [317]. Compared to the Chern-Simons scenario, one of the distinguishable

features of higher derivatives of the coupling scalar field is that they lead to the velocity birefringence phenomenon, i.e. they induce a difference in the propagation speed of the two circular polarizations. However, despite this distinctive feature, the final amount of chirality produced in the tensor power spectrum is still small and degenerate with the case of Chern-Simons gravity. This degeneracy manifests in the fact that the final predictions for the level of chirality is proportional to the ratio $H/M_{\rm PV}$, with H denoting the Hubble parameter during inflation and $M_{\rm PV}$ the characteristic energy scale of the parity-violating theories. In the absence of a complete theory of quantum gravity, $M_{\rm PV}$ is an unknown quantity. This makes all these models indistinguishable from the observational point of view just taking into consideration the power spectrum statistics.

This degeneracy between the different parity-violating theories can be broken by considering higher-order correlators, such as the primordial bispectra. Indeed, primordial bispectra encode information, like the shape function, that may be characteristic of the specific inflationary model (see e.g. [318–321] for general considerations), possibly removing any kind of degeneracy. In particular, various scenarios with parity-violating signatures in tensor non-Gaussianity due to modified gravity operators have already been considered in Refs. [322–332].

In the analysis discussed in this chapter we will extend these studies by analyzing the effects of the parity-violating operators introduced in [24] on the graviton bispectrum.

6.1 Chiral scalar-tensor theories with higher-order derivatives

In this section we introduce chiral scalar-tensor theories with higher-order derivatives as proposed in Ref. [24]. These consist in parity-breaking covariant terms having more derivatives with respect to both the Einstein-Hilbert and the gravitational Chern-Simons terms. The latter is the fully-covariant parity-breaking operator having the least number of derivatives (see, e.g., [307, 333]). The action of these parity-breaking theories has the following form

$$S = \int d^4x\sqrt{-g}\left[\frac{M_{Pl}^2}{2}R + \mathcal{L}_{\rm PV} + \mathcal{L}_\phi\right], \tag{6.1}$$

where $g = \det[g_{\mu\nu}]$, $M_{Pl} = (8\pi G)^{-1/2}$ is the reduced Planck mass, R is the Ricci scalar, $\mathcal{L}_{\rm PV}$ is a Lagrangian containing parity-violating operators and $\mathcal{L}_\phi$ is the Lagrangian for a scalar degree of freedom, which is assumed to be non-minimally coupled to gravity. Since we are interested in the effects of these parity-breaking theories during inflation, we will assume ϕ to play the role of the inflaton field, with $\mathcal{L}_\phi$ being the following Lagrangian

$$\mathcal{L}_\phi = -\frac{1}{2}g^{\mu\nu}\partial_\mu\phi\partial_\nu\phi - V(\phi), \tag{6.2}$$

where $V(\phi)$ denotes the (slow-roll) potential of the inflaton field. The parity-violating Lagrangian of the theory can be written as the sum of two pieces

$$\mathcal{L}_{\rm PV} = \mathcal{L}_{\rm PV1} + \mathcal{L}_{\rm PV2}, \tag{6.3}$$

where $\mathcal{L}_{\rm PV1}$ contains up to only first derivatives of the scalar field and is given by [24]

$$\mathcal{L}_{\rm PV1} = \sum_{A=1}^{4} a_A L_A, \tag{6.4}$$

where[1]

$$L_1 = \varepsilon^{\mu\nu\alpha\beta}R_{\alpha\beta\rho\sigma}R_{\mu\nu\ \lambda}^{\ \ \rho}\phi^\sigma\phi^\lambda, \qquad L_3 = \varepsilon^{\mu\nu\alpha\beta}R_{\alpha\beta\rho\sigma}R^\sigma_{\ \nu}\phi^\rho\phi_\mu,$$

[1]Here we are implicitly assuming that the higher derivative operators are suppressed by corresponding powers of the Planck mass, M_{Pl}. We will reintroduce these factors explicitly at the end of this section.

$$L_2 = \varepsilon^{\mu\nu\alpha\beta} R_{\alpha\beta\rho\sigma} R_{\mu\lambda}{}^{\rho\sigma} \phi_\nu \phi^\lambda \,, \qquad L_4 = \varepsilon^{\mu\nu\rho\sigma} R_{\rho\sigma\alpha\beta} R^{\alpha\beta}{}_{\mu\nu} \phi^\lambda \phi_\lambda \,, \tag{6.5}$$

where $\varepsilon^{\rho\sigma\alpha\beta}$ is the covariant Levi-Civita tensor defined in terms of the antisymmetric Levi-Civita symbol $\epsilon^{\rho\sigma\alpha\beta}$ as $\varepsilon^{\rho\sigma\alpha\beta} = \epsilon^{\rho\sigma\alpha\beta}/\sqrt{-g}$, $\phi^\mu \equiv \nabla^\mu \phi$ with ∇^μ denoting the covariant derivative, $R^\alpha{}_{\beta\rho\sigma}$ is the Riemann tensor and R is its trace. Notice that the couplings a_A in (6.4) are generic functions of the scalar field and its kinetic term, i.e. $a_A = a_A(\phi, \phi^\mu \phi_\mu)$. In [24] it has been shown that in the so-called unitary gauge, where the scalar field is homogeneous, these operators do not introduce the Ostrogradsky (unstable) modes[2] under the constraint

$$4a_1 + 2a_2 + a_3 + 8a_4 = 0 \,, \tag{6.6}$$

that leaves only 3 independent coefficients.

The term $\mathcal{L}_{\rm PV2}$ includes also second-order derivatives of the scalar field and reads [24]

$$\mathcal{L}_{\rm PV2} = \sum_{A=1}^{7} b_A M_A \,, \tag{6.7}$$

where

$$\begin{aligned}
M_1 &= \varepsilon^{\mu\nu\alpha\beta} R_{\alpha\beta\rho\sigma} \phi^\rho \phi_\mu \phi^\sigma_\nu \,, & M_4 &= \varepsilon^{\mu\nu\alpha\beta} R_{\alpha\beta\rho\sigma} \phi_\nu \phi^\rho_\mu \phi^\sigma_\lambda \phi^\lambda, \\
M_2 &= \varepsilon^{\mu\nu\alpha\beta} R_{\alpha\beta\rho\sigma} \phi^\rho_\mu \phi^\sigma_\nu \,, & M_5 &= \varepsilon^{\mu\nu\alpha\beta} R_{\alpha\rho\sigma\lambda} \phi^\rho \phi_\beta \phi^\sigma_\mu \phi^\lambda_\nu, \\
M_3 &= \varepsilon^{\mu\nu\alpha\beta} R_{\alpha\beta\rho\sigma} \phi^\sigma \phi^\rho_\mu \phi^\lambda_\nu \phi_\lambda \,, & M_6 &= \varepsilon^{\mu\nu\alpha\beta} R_{\beta\gamma} \phi_\alpha \phi^\gamma_\mu \phi^\lambda_\nu \phi^\lambda, \\
M_7 &= (\Box\phi) M_1 \,,
\end{aligned} \tag{6.8}$$

where in this case $\phi^\sigma_\nu \equiv \nabla^\sigma \nabla_\nu \phi$ and $b_A = b_A(\phi, \phi^\mu \phi_\mu)$. Here, in order to avoid the Ostrogradsky modes in the unitary gauge, the following conditions have to be imposed [24]

$$b_7 = 0 \,, \qquad b_6 = 2(b_4 + b_5) \,, \qquad b_2 = -\frac{A_*^2}{2}(b_3 - b_4) \,, \tag{6.9}$$

where $A_* = \dot{\phi}(t)/N$ and N is the lapse function (see Eq. (6.10) and the subsequent discussion). In this case, we are left with 4 independent coefficients.

We will adopt the Arnowitt-Deser-Misner (ADM) formalism for the perturbed Friedmann-Lemaitre-Robertson-Walker (FLRW) metric (see e.g. [44, 335, 336]), where the metric reads

$$ds^2 = -(N^2 - N_i N^i)\, dt^2 + N_i\, dx^i dt + h_{ij}\, dx^i dx^j \,, \tag{6.10}$$

where N and N_i are the lapse function and shift vector, respectively, and h_{ij} is the three-dimensional spatial metric.[3] Focusing only on transverse and traceless tensor perturbations γ_{ij}, the (non-linear) perturbed spatial metric reads [44, 338]

$$h_{ij} = a^2 \left[\exp \gamma\right]_{ij} = a^2 \left[\delta_{ij} + \gamma_{ij} + \frac{1}{2!}\gamma_{ik}\gamma^k{}_j + ...\right] \,, \tag{6.11}$$

with

$$\gamma_i{}^i = 0 \,, \quad \partial_i \gamma^{ij} = 0 \,. \tag{6.12}$$

[2] See [334] for a discussion about Ostrogradsky ghosts.

[3] In the 3+1 decomposition of spacetime, the lapse function N measures the proper time between adjacent space-like hypersurfaces, and captures the fact that the coordinate time can pass more quickly in some spacetime regions than in others; the shift vector N_i measures the change of coordinates (relative to the normal) from one hypersurface to the other, namely describes how spatial coordinates are propagated between two adjacent hypersurfaces. See e.g. [337] for more details.

It is well-known that in GR the lapse function N and the shift vector N_i are non-dynamical fields, see e.g [44]. Rather, they are Lagrange multipliers that enforce the so-called Hamiltonian and momentum constraints. This means that they can be removed in the final action after solving their algebraic Euler-Lagrange equations in terms of dynamical fields. In general, in a modified gravity setting, the equations of motion for N and N_i are changed, with the possibility to have a larger number of dynamical degrees of freedom. However, it has been shown in [24] that in the unitary gauge and under the constraints (6.6) and (6.9), N and N_i remain auxiliary fields as in GR.

Furthermore, if one is not interested in expanding the actions beyond cubic order in the perturbations, it is sufficient to find the expressions of the lapse function N and the shift vector N_i at first order (see [44, 339]). Since we are focusing only on tensor fluctuation modes and it is not possible to have first order perturbations in N and N_i including only tensor perturbations, we are left solely with their zero-th order value, namely

$$N = 1\,, \qquad N_i = 0\,. \tag{6.13}$$

Imposing the condition (6.13) together with the constraints (6.6) and (6.9), one finds the following final expressions for the Lagrangians PV1 and PV2 [24]:

$$\begin{aligned}\sqrt{-g}\,\mathcal{L}_{\rm PV1} = \frac{2\dot\phi^2}{M_{Pl}^4}\epsilon^{ijl}\Big[&2(2a_1+a_2+4a_4)\left(KK_{mi}D_lK_j^{\ m} + {}^{(3)}\!R_{mi}D_lK_j^{\ m} - K_{mi}K^{mn}D_lK_{jn}\right)\\ &-(a_2+4a_4)\left(2K_{mi}K_j^{\ n}D_nK_l^{\ m} + {}^{(3)}\!R_{jlm}{}^{n}D_nK_i^{\ m}\right)\Big]\,,\end{aligned} \tag{6.14}$$

$$\sqrt{-g}\,\mathcal{L}_{\rm PV2} = 2\frac{\dot\phi^3}{M_{Pl}^5}\epsilon^{ijl}\left[b_1K_{mi}D_lK_j^{\ m} + \frac{(b_4+b_5-b_3)}{M_{Pl}^3}\dot\phi K_{mi}K_j^{\ n}D_nK_l^{\ m}\right]\,, \tag{6.15}$$

where $K_{ij} = \dot h_{ij}/2$ is the extrinsic curvature tensor, $K = h^{ij}K_{ij}$ its trace, D_i denotes the three-dimensional covariant derivative, ${}^{(3)}\!R_{mi}$ and ${}^{(3)}\!R_{jlm}{}^{n}$ are the three-dimensional Ricci and Riemann tensors respectively. Notice that we have reintroduced the Planck mass through dimensional analysis.

In the rest of our analysis, we will assume that (6.14) and (6.15) represent the fundamental Lagrangians defining the theories that we will study. Indeed, as commented in [24], because of the presence of the Ostrogradsky modes in the original theories (6.4)-(6.7), there are two possible approaches to follow: the first is to consider these theories as low energy effective field theories valid up to the energy scale at which the Ostrogradsky modes appear; the second possibility is to restrict the theories to the unitary gauge, with the additional constraints (6.6)-(6.9), and treat them as new Lorentz-breaking (and parity-violating) theories. The latter is the approach adopted in Ref. [24], which we will also follow in our analysis. Notice that the two Lagrangians (6.14)-(6.15) do not contain any higher order time derivative of the metric, but only higher order space derivatives. Because of this fact, these theories break Lorentz invariance similarly to what happens in Horava-Lifshitz gravity [308, 309]. As we will see in the rest of this chapter, this feature will have important consequences on the phenomenology of the models under scrutiny, both in the propagation of PGWs (leading to a speed of propagation of tensor modes different from the speed of light during inflation) and in the predictions for primordial bispectra.

Before analyzing in details the effects of these parity-breaking operators on primordial tensor modes, some comments are in order regarding inflation within these modified gravity theories. The first thing to consider when introducing some modifications to gravity is how this affects the dynamics at the background level. In our specific case, it is easy to check that the new operators have no effects on the background dynamics of inflation, that is the same as in single-field slow-roll models with GR. At the perturbation level, instead, rotational invariance implies

that N-point correlation functions of scalar perturbations can have parity-odd signals only for $N \geq 4$, i.e. the trispectrum ($N = 4$) is the lowest order correlator involving only scalars that can manifest parity-breaking signatures [340]. This implies that the power spectrum of scalar perturbations has the usual expression that is obtained within GR.

6.2 Chirality in primordial tensor power spectra

In this section we review the effects of the higher order operators introduced in [24] on the dynamics of PGWs, with a particular focus on the parity-breaking signatures that arise in the primordial tensor power spectrum. This has been studied in [317] (see also [341–343] for an analysis of the propagation of gravitational waves in the late-time Universe within these parity-breaking theories). We first start by recalling the Fourier expansion of PGWs,

$$\gamma_{ij}(\mathbf{x}, t) = \int \frac{d^3k}{(2\pi)^3} \sum_{s=L,R} \gamma_s(\mathbf{k}, t) \epsilon_{ij}^{(s)}(\mathbf{k}) e^{i\mathbf{k}\cdot\mathbf{x}} \,, \tag{6.16}$$

where $\gamma_s(\mathbf{k}, t)$ are the mode function of primordial tensor modes, s is the polarization index and $\epsilon_{ij}^{(s)}(\mathbf{k})$ are the polarization tensors in the chiral basis, i.e. in the basis of L and R circular polarization states (see Appendix D for an explicit representation of the polarization tensors that will be used in the following computations). This is defined in terms of the more common $+$ and $\times$ basis as

$$\epsilon_{ij}^{R}(\mathbf{k}) = \frac{\epsilon_{ij}^{+}(\mathbf{k}) + i\epsilon_{ij}^{\times}(\mathbf{k})}{\sqrt{2}} \,, \quad \epsilon_{ij}^{L}(\mathbf{k}) = \frac{\epsilon_{ij}^{+}(\mathbf{k}) - i\epsilon_{ij}^{\times}(\mathbf{k})}{\sqrt{2}} \,, \tag{6.17}$$

and the mode functions in the two different bases are related by

$$\gamma_R(\mathbf{k}, t) = \frac{\gamma_+(\mathbf{k}, t) - i\gamma_\times(\mathbf{k}, t)}{\sqrt{2}} \,, \quad \gamma_L(\mathbf{k}, t) = \frac{\gamma_+(\mathbf{k}, t) + i\gamma_\times(\mathbf{k}, t)}{\sqrt{2}} \,. \tag{6.18}$$

This decomposition into circular polarization states is particularly useful when studying parity-violating theories. Indeed, while the $+$ and $\times$ polarization states are mixed by the parity-violating terms, the equations of motion for the L and R polarization modes are decoupled. One can prove that the following relations hold (see e.g. [312])

$$\begin{aligned}
\epsilon_{ij}^{L}(\mathbf{k})\epsilon_{L}^{ij}(\mathbf{k}) &= \epsilon_{ij}^{R}(\mathbf{k})\epsilon_{R}^{ij}(\mathbf{k}) = 0 \,, \\
\epsilon_{ij}^{L}(\mathbf{k})\epsilon_{R}^{ij}(\mathbf{k}) &= 2 \,, \\
\epsilon_{ij}^{R}(-\mathbf{k}) &= \epsilon_{ij}^{L}(\mathbf{k}) \,, \\
\epsilon_{ij}^{(s)*}(-\mathbf{k}) &= \epsilon_{ij}^{(s)}(\mathbf{k}), \\
\gamma_L(-\mathbf{k}) &= \gamma_R^*(\mathbf{k}) \,, \\
k_l \epsilon^{mlj} \epsilon_{j}^{(s)j}(\mathbf{k}) &= -i\lambda_s k \epsilon^{(s)im}(\mathbf{k}) \,,
\end{aligned} \tag{6.19}$$

where $\lambda_R = +1$ and $\lambda_L = -1$, and ϵ^{mlj} with 3 Latin indices denotes the Levi-Civita anti-symmetric symbol. We will make an extensive use of these relations throughout the following analysis.

The first step required to compute the power spectrum of PGWs is to expand the Lagrangians (6.14)-(6.15) at second order in tensor perturbations. Working at leading order in slow-roll parameters, the action derived by Lagrangian PV1 (6.14) (including the contribution from standard gravity) at quadratic order in tensor perturbations is given by

$$S_{\gamma\gamma}^{\rm PV1} = \sum_{s=L,R} \int d\tau \int \frac{d^3k}{(2\pi)^3} \left[A_{T,s}^2 |\gamma_s'(\mathbf{k}, \tau)|^2 - B_{T,s}^2 k^2 |\gamma_s(\mathbf{k}, \tau)|^2 \right] , \tag{6.20}$$

where the prime denotes a derivative with respect to the conformal time τ and we have defined

$$A_{T,s}^2 \equiv \frac{M_{Pl}^2}{2} a^2 \left(1 - \lambda_s \frac{k_{phys}}{M_{\rm PV1}}\right), \quad B_{T,s}^2 \equiv \frac{M_{Pl}^2}{2} a^2 \left[1 - \frac{4}{M_{Pl}^6} \frac{\dot{\phi}^2}{a} (\dot{f} + \dot{g}) \lambda_s k\right], \tag{6.21}$$

with

$$M_{\rm PV1} \equiv \frac{M_{Pl}^6}{8} \frac{1}{\dot{\phi}^2} \frac{1}{(f+g)H}, \tag{6.22}$$

and

$$f \equiv a_1 + \frac{a_2}{2} + 2a_4, \qquad g \equiv \frac{a_2}{2} + 2a_4, \tag{6.23}$$

where the dot denotes a derivative with respect to cosmic time. From Eq. (6.21) we realize that the right-handed graviton modes ($\lambda_R = +1$) with a physical wavenumber, $k_{phys} = k/a$, larger than $M_{\rm PV1}$ get a negative kinetic term, thus becoming unstable. At the quantum level this instability may result in severe problems, since it leads either to a violation of unitarity or to the propagation of negative energy modes forward in time. Since unitarity has to be preserved in order for the theory to make sense, we must admit the presence of particles with negative energies, which means that the energy spectrum is unbounded from below. However, in such a case, the vacuum state would be highly unstable under the decay into particles of positive and negative energies [344]. So, to avoid to deal with this kind of problem we introduce a UV cut-off $\Lambda \leq M_{\rm PV1}$ in the theory and consider only gravitons with $k_{phys} < \Lambda$ at the inset of inflation. Then, since deep inside the horizon the condition $k_{phys} \gg H$ holds, it follows that we must assume $M_{\rm PV1} \gg H$ during inflation in order for the theory to make sense.[4]

As explained in Sec. 6.1, the couplings a_i that enter in the definitions (6.23) of f and g are functions of the scalar field and its kinetic term ($= \dot{\phi}^2/2$ in the unitary gauge). This allows us to reabsorb the $\dot{\phi}^2$ terms in Eqs. (6.21)-(6.22) by defining two new couplings[5]

$$f_1 \equiv \frac{\dot{\phi}^2}{M_{Pl}^4} f, \quad g_1 \equiv \frac{\dot{\phi}^2}{M_{Pl}^4} g, \tag{6.24}$$

that are still dimensionless like f and g. If we now define the graviton speed as

$$c_{T,s}^2 \equiv \frac{B_{T,s}^2}{A_{T,s}^2}, \tag{6.25}$$

the action (6.20) can be rewritten as

$$S_{\gamma\gamma}^{\rm PV1} = \sum_{s=L,R} \int d\tau \int \frac{d^3k}{(2\pi)^3} A_{T,s}^2 \left[|\gamma_s'(\mathbf{k},\tau)|^2 - c_{T,s}^2 k^2 |\gamma_s(\mathbf{k},\tau)|^2\right]. \tag{6.26}$$

By making the field redefinition

$$\mu_s \equiv A_{T,s} \gamma_s, \tag{6.27}$$

we can then rewrite the action for the new field as

$$S_{\gamma\gamma}^{\rm PV1} = \sum_{s=L,R} \int d\tau \int \frac{d^3k}{(2\pi)^3} \left[|\mu_s'(\mathbf{k},\tau)|^2 - c_{T,s}^2 k^2 |\mu_s(\mathbf{k},\tau)|^2 + \frac{A_{T,s}''}{A_{T,s}} |\mu_s(\mathbf{k},\tau)|^2\right]. \tag{6.28}$$

[4] Notice that assuming just $M_{\rm PV1} \gtrsim H$ is not enough, as in this case a given physical mode k_{phys} encounters issues near the horizon crossing. Thus, this model can be considered well-defined only when $M_{\rm PV1} \gg H$, i.e. in the "effective field theory" limit, with $M_{\rm PV1}$ playing the role of the scale of new physics.

[5] Notice that, despite the fact that operators in (6.4) contain 6 derivatives, only some of them act on the perturbations, while the others act on the background. Thus, since these theories make sense only in unitary gauge, we are allowed to reabsorb some of the (time) derivatives through a coupling redefinition.

Varying this action yields the equations of motion for the fields μ_s, which read

$$\mu_s'' + \left(c_{T,s}^2 k^2 - \frac{A_{T,s}''}{A_{T,s}} \right) \mu_s = 0 \,, \tag{6.29}$$

where the time-dependent effective mass is

$$\frac{A_{T,s}''}{A_{T,s}} = \frac{d}{d\tau}\left(\frac{A_{T,s}'}{A_{T,s}}\right) + \left(\frac{A_{T,s}'}{A_{T,s}}\right)^2 = \frac{2+3\epsilon}{\tau^2} - \frac{\lambda_s k}{\tau}\frac{H}{M_{\rm PV1}} + \mathcal{O}\left(\epsilon^2, \frac{H^2}{M_{\rm PV1}^2}, \epsilon\frac{H}{M_{\rm PV1}}\right) , \tag{6.30}$$

and ϵ is a slow-roll parameter, defined as

$$\epsilon = \frac{M_{Pl}^2}{2}\left(\frac{V'}{V}\right)^2 \simeq \frac{1}{2}\frac{\dot{\phi}^2}{H^2 M_{Pl}^2} \,. \tag{6.31}$$

The first term in Eq. (6.30) is the usual contribution present in slow-roll models of inflation with standard gravity. The second term, instead, is a new contribution that arises similarly in inflationary models with the gravitational Chern-Simons coupling (see [312,313,316,328]), with the Chern-Simons mass replaced in our case by $M_{\rm PV1}$. Thus, the equations of motion for the fields μ_s are

$$\mu_s'' + \left(c_{T,s}^2 k^2 - \frac{\nu_T^2 - \frac{1}{4}}{\tau^2} + \lambda_s \frac{k}{\tau}\frac{H}{M_{\rm PV1}} \right) \mu_s = 0 \,, \tag{6.32}$$

with

$$\nu_T \simeq \frac{3}{2} + \epsilon \,, \tag{6.33}$$

and

$$c_{T,s}^2 \simeq 1 - \lambda_s k \frac{H}{M_{\rm PV1}}\tau \tag{6.34}$$

at leading order in slow-roll dynamics and in the ratio $H/M_{\rm PV1}$.

From Eq. (6.32) we realize that, due to the presence of the higher derivative operators, the speed of propagation of tensor modes is modified in this model, since $c_{T,s} \neq 1$; this is actually already evident from the action (6.20), since the time and space derivatives of the field are multiplied by different functions. In particular, from (6.34) we notice that the two circular polarization states propagate with a different speed during inflation, being this dependent on the polarization index s: this is the so-called velocity birefringence phenomenon and it is the main difference at quadratic level with respect to the case with Chern-Simons gravity. We also stress that the speed of tensor modes is not constant, but varies with time during inflation. This is a peculiar feature of this kind of models. Notice that in the limit where $f_1 = g_1 = 0$ ($M_{\rm PV1} = \infty$) we recover the usual result, $c_{T,s} = 1$, as expected.

There is a further important feature that arises from Eq. (6.34): during inflation one of the two polarization states of PGWs is superluminal (i.e. $c_{T,s} > 1$), while the other one is subluminal. This was already noticed e.g. in [342] and is a phenomenological manifestation of the breaking of Lorentz invariance that occurs in this model. Notice that such an invariance is recovered at the end of inflation, since $c_{T,s} \to 1$ for $k\tau \to 0$.

We can now canonically quantize the fields μ_s by expanding them in terms of the creation and annihilation operators

$$\hat{\mu}_s(\mathbf{k},\tau) = u_s(k,\tau)\hat{a}_s(\mathbf{k}) + u_s^*(k,\tau)\hat{a}_s^\dagger(-\mathbf{k}) \,. \tag{6.35}$$

The creation and annihilation operators satisfy the equal time commutation relations

$$[\hat{a}_s(\mathbf{k}), \hat{a}_{s'}^\dagger(\mathbf{k}')] = (2\pi)^3\delta^{(3)}(\mathbf{k}-\mathbf{k}')\delta_{ss'} \,, \quad [\hat{a}_s(\mathbf{k}), \hat{a}_{s'}(\mathbf{k}')] = 0 = [\hat{a}_s^\dagger(\mathbf{k}), \hat{a}_{s'}^\dagger(\mathbf{k}')] \,, \tag{6.36}$$

and act on the vacuum state as

$$\hat{a}_s|0\rangle = 0\,, \quad \langle 0|\hat{a}_s^\dagger = 0\,. \tag{6.37}$$

The equations of motion for the mode functions u_s follow straightforwardly from Eq. (6.32) and read

$$u_s'' + \left[k^2\left(1 - \lambda_s k\frac{H}{M_{\rm PV1}}\tau\right) - \frac{\nu_T^2 - \frac{1}{4}}{\tau^2} + \lambda_s\frac{k}{\tau}\frac{H}{M_{\rm PV1}}\right]u_s = 0\,. \tag{6.38}$$

This equation has the same form as Eq. (4.11) of [317] when taking $c_2 = 0$ and $c_1\epsilon_* = H/M_{\rm PV1}$. As shown in [317], equations of the kind of (6.38) admit an approximate analytical solution in terms of Airy functions [345]

$$u_s(y) = \alpha\left(\frac{\xi(y)}{g(y)}\right)^{1/4}{\rm Ai}(\xi) + \beta\left(\frac{\xi(y)}{g(y)}\right)^{1/4}{\rm Bi}(\xi)\,, \tag{6.39}$$

where α and β are two integration constants, $y = -k\tau$ and the functions $\xi(y)$ and $g(y)$ in our conventions are given by

$$g(y) = \frac{\nu_T^2}{y^2} - 1 - \lambda_s y\frac{H}{M_{\rm PV1}} + \lambda_s\frac{H}{M_{\rm PV1}}\frac{1}{y}\,, \tag{6.40}$$

and

$$\xi(y) = \begin{cases} \left(-\frac{3}{2}\int_{y_0^s}^{y}\sqrt{g(y')}\,dy'\right)^{2/3} & y \leq y_0^s\,, \\ -\left(\frac{3}{2}\int_{y_0^s}^{y}\sqrt{g(y')}\,dy'\right)^{2/3} & y \geq y_0^s\,, \end{cases} \tag{6.41}$$

with

$$y_0^s = -\frac{1 - 2^{1/3}\left[1 + 3\left(\frac{H}{M_{\rm PV1}}\right)^2\right]/Y - 2^{-1/3}Y}{3\lambda_s\frac{H}{M_{\rm PV1}}}\,, \tag{6.42}$$

where

$$Y = \left(Y_1 + \sqrt{-4\left[1 + 3\left(\frac{H}{M_{\rm PV1}}\right)^2\right]^3 + Y_1^2}\right)^{1/3}\,, \tag{6.43}$$

$$Y_1 = -2 + 27\nu_T^2\left(\frac{H}{M_{\rm PV1}}\right)^2 - 9\left(\frac{H}{M_{\rm PV1}}\right)^2\,. \tag{6.44}$$

The final solution for $u_s(y)$ is found by matching the sub-horizon limit ($y \to \infty$) of (6.39) with the following initial condition

$$\lim_{y\to+\infty} u_s(y) = \sqrt{\frac{1}{2\omega_k}}\exp\left(-i\int_{\tau_i}^{\tau}\omega_k\,d\tau'\right)\,, \tag{6.45}$$

that physically corresponds to the assumption that the Universe was initially in an adiabatic vacuum state. Here $\omega_k = k\sqrt{-g(-k\tau)}$ denotes the dispersion relation of PGWs that can be read off by Eq. (6.38). Notice that (6.45) corresponds to the usual Bunch-Davies initial vacuum state in the limit in which $\omega_k = k$. By doing this matching we find [317]

$$\alpha = \sqrt{\frac{\pi}{2k}}e^{i\pi/4}\,, \qquad \beta = i\sqrt{\frac{\pi}{2k}}e^{i\pi/4}\,, \tag{6.46}$$

that fixes our solution. In [317] it has been shown that this analytical approach is in optimal agreement with exact numerical solutions.

We can now derive the super-horizon power spectra for the two circular polarization modes of tensor perturbations, which are defined as

$$P_T^L = 2\frac{|u_L(y)_{y\ll 1}|^2}{A_{T,L}^2}\,, \qquad P_T^R = 2\frac{|u_R(y)_{y\ll 1}|^2}{A_{T,R}^2}\,. \tag{6.47}$$

At leading order in slow-roll the final result reads [317]

$$P_T^L = \frac{P_T}{2}\exp\left[\frac{\pi}{16}\frac{H}{M_{\rm PV1}}\right]\,, \qquad P_T^R = \frac{P_T}{2}\exp\left[-\frac{\pi}{16}\frac{H}{M_{\rm PV1}}\right]\,, \tag{6.48}$$

where here P_T denotes the total tensor power spectrum as predicted in general relativity.

The level of parity violation in the power spectra of primordial tensor modes can be quantified by means of the chirality parameter χ, which is defined as the relative difference between the power spectra of right and left polarization modes. The leading-order contributions to the chirality can be computed by Taylor-expanding the exponentials in Eqs. (6.48), since $H/M_{\rm PV1} \ll 1$. Thus, we find

$$\chi \equiv \frac{P_T^R - P_T^L}{P_T^R + P_T^L} = -\frac{\pi}{16}\frac{H}{M_{\rm PV1}}\,. \tag{6.49}$$

From Eq. (6.49) it is clear that, just as it happens with the gravitational Chern-Simons coupling [312, 313, 316, 328], chirality is suppressed by the requirement of dealing with an effective field theory, i.e. $H/M_{PV1} \ll 1$.

Another interesting aspect to consider is how the tensor-to-scalar ratio is modified with respect to the result obtained within standard gravity. The total dimensionless tensor power spectrum can be written as

$$\Delta_T^{\rm PV1} = \Delta_T^R + \Delta_T^L = \Delta_T\left[1 + \frac{\pi^2}{256}\left(\frac{H}{M_{\rm PV1}}\right)^2\right] = \Delta_T\left(1+\chi^2\right)\,. \tag{6.50}$$

Since, as discussed in Sec. 6.1, the scalar power spectrum does not receive any contribution from the parity-violating operators, the tensor-to-scalar ratio can be readily computed as

$$r_{\rm PV1} \equiv \frac{\Delta_T^{\rm PV1}}{\Delta_S} = r\left(1+\chi^2\right)\,, \tag{6.51}$$

where r is the tensor-to-scalar ratio obtained in slow-roll models without the parity-breaking operators. We can clearly see that, since the chirality χ is $\ll 1$ in this model, the correction to r is suppressed.

The presence of the new operators induces some corrections also to the spectral index of tensor perturbations, that quantifies how the amplitude of the fluctuations varies with the scale. This has the following expression

$$n_T \equiv \frac{d\ln\Delta_T^{\rm PV1}}{d\ln k} \simeq -2\epsilon + \frac{\pi^2}{128}\left(\frac{H}{M_{\rm PV1}}\right)\left[-2\epsilon\left(\frac{H}{M_{\rm PV1}}\right) - \frac{\dot{M}_{\rm PV1}}{M_{\rm PV1}^2}\right]\,, \tag{6.52}$$

where

$$\frac{\dot{M}_{\rm PV1}}{M_{\rm PV1}^2} \simeq \epsilon\left(\frac{H}{M_{\rm PV1}}\right) - \sqrt{2\epsilon}M_{Pl}\left(\frac{H}{M_{\rm PV1}}\right)\frac{(\partial f_1/\partial\phi) + (\partial g_1/\partial\phi)}{f_1+g_1}\,. \tag{6.53}$$

Thus, even in this case the corrections to the standard result ($n_T = -2\epsilon$) are in general small, making PGWs predicted within this model far from the reach of GW interferometers.

Now we want to make a similar analysis for the Lagrangian PV2, given by Eq. (6.15). At second order in tensor perturbations it has the following form

$$S^{\gamma\gamma}_{\rm PV2} = \sum_{s=L,R} \int d\tau \int \frac{d^3k}{(2\pi)^3} \left[\tilde{A}^2_{T,s} |\gamma_s'(\mathbf{k},\tau)|^2 - \frac{M^2_{Pl}}{2} a^2 k^2 |\gamma_s(\mathbf{k},\tau)|^2 \right] , \tag{6.54}$$

where we have defined

$$\tilde{A}^2_{T,s} \equiv \frac{M^2_{Pl}}{2} a^2 \left(1 - \lambda_s \frac{k_{phys}}{M_{\rm PV2}} \right) , \tag{6.55}$$

with

$$M_{\rm PV2} \equiv \frac{M_{Pl}}{2} \left(\tilde{b}_1 - b \frac{H}{M_{Pl}} \right)^{-1} . \tag{6.56}$$

Just like in the previous case, we have reabsorbed the powers of $\dot{\phi}^2$ by defining two new couplings $\tilde{b}_1$ and b as

$$\tilde{b}_1 \equiv \frac{\dot{\phi}^3}{M^6_{Pl}} b_1 , \quad b \equiv \frac{\dot{\phi}^4}{M^8_{Pl}} (b_4 + b_5 - b_3) , \tag{6.57}$$

where b_1, b_3, b_4 and b_5 are the independent couplings of the model. The energy scale $M_{\rm PV2}$ has been introduced for the same reason as $M_{\rm PV1}$ in the case with only first derivatives of the scalar field: it represents the energy scale at which the right-handed graviton modes acquire a negative kinetic term, thus becoming unstable. Proceeding as in the previous case, we introduce a UV cut-off $\Lambda \leq M_{\rm PV2}$ imposing that $k_{phys} < \Lambda$. By requiring also that the modes started deep inside the horizon, it follows that $H/M_{\rm PV2} \ll 1$.

By defining the new field $\mu_s \equiv \tilde{A}_{T,s} \gamma_s$ and repeating the same steps as in the previous case, we obtain the following equations of motion

$$\mu_s'' + \left(\tilde{c}^2_{T,s} k^2 - \frac{\nu_T^2 - \frac{1}{4}}{\tau^2} + \lambda_s \frac{k}{\tau} \frac{H}{M_{\rm PV2}} \right) \mu_s = 0 , \tag{6.58}$$

where also in this case

$$\nu_T \simeq \frac{3}{2} + \epsilon \tag{6.59}$$

holds at leading order in slow-roll parameters. The speed of propagation of tensor modes during inflation can be written at leading order in slow-roll and in the ratio $H/M_{\rm PV2}$ as

$$\tilde{c}^2_{T,s} \simeq 1 - \lambda_s k \frac{H}{M_{\rm PV2}} \tau . \tag{6.60}$$

If we then canonically quantize the field μ_s as

$$\hat{\mu}_s(\mathbf{k},\tau) = u_s(k,\tau) \hat{a}_s(\mathbf{k}) + u_s^*(k,\tau) \hat{a}_s^\dagger(-\mathbf{k}) , \tag{6.61}$$

we can immediately write down the equations of motion for the mode functions u_s, which read

$$u_s'' + \left[k^2 \left(1 - \lambda_s k \frac{H}{M_{\rm PV2}} \tau \right) - \frac{\nu_T^2 - \frac{1}{4}}{\tau^2} + \lambda_s \frac{k}{\tau} \frac{H}{M_{\rm PV2}} \right] u_s = 0 . \tag{6.62}$$

This is basically the same equation as Eq. (6.38), with $M_{\rm PV2}$ replacing $M_{\rm PV1}$. We can thus write the solution of Eq. (6.62) in terms of the Airy functions and the integration constants are again fixed by imposing the adiabatic initial condition (6.45). We can then compute the leading order contribution to the chirality parameter χ, which takes the following form

$$\chi = -\frac{\pi}{16} \frac{H}{M_{\rm PV2}} . \tag{6.63}$$

As in the PV1 model, the chirality of PGWs is suppressed since $H/M_{\rm PV2} \ll 1$. Analogous considerations hold for the tensor-to-scalar ratio and the spectral index of tensor perturbations, that have the same expressions as in Eqs. (6.51)-(6.52) with $M_{\rm PV2}$ replacing $M_{\rm PV1}$.

At this point, we want to make a brief comment about the observability of this signature: as emphasized in the introduction, the CMB EB and TB angular cross-correlators are able to probe parity-breaking in the primordial Universe only for models predicting maximum chirality, i.e. $\chi \simeq 1$ [346], while the models under considerations predict $\chi \ll 1$. Moreover, as we have already discussed, in general we do not expect a significant modification of the standard slow-roll models tensor tilt (see Eq. (6.52)), making in general difficult to probe these models with forthcoming interferometers.

Thus, measuring the linear effects of these parity-breaking operators seems very challenging. Another important aspect to keep in mind is the high degeneracy regarding their signatures on the primordial power spectra. In fact, the final predictions for the level of chirality (6.49) and (6.63) are equivalent apart for a redefinition of the $M_{\rm PV}$ scale, which is unknown in the absence of a more fundamental theory able to predict its value. This makes these models indistinguishable just taking into consideration the power spectrum statistics.

Therefore, it is interesting and crucial to investigate the kind of parity-breaking signatures that arise in higher-order correlators, like the graviton bispectrum. Indeed, as already discussed, higher-order correlators contain features that may be characteristic of the specific inflationary model under consideration, thus possibly removing any kind of degeneracy. For this reason, in the next section we present a detailed study of the effects of the parity-violating operators introduced in Sec. 6.1 on the primordial tensor bispectra.

6.3 Chirality in primordial tensor bispectra

Before entering into the details of the computations, let us first recall the basic definition of the bispectrum, which is the Fourier transform of the three-point correlation function. Given three perturbation fields $\delta_1(\mathbf{x},t)$, $\delta_2(\mathbf{x},t)$ and $\delta_3(\mathbf{x},t)$, the bispectrum $B(k_1,k_2,k_3)$ is defined through the relation

$$\langle \delta_1(\mathbf{k_1})\delta_2(\mathbf{k_2})\delta_3(\mathbf{k_3})\rangle = (2\pi)^3\delta^{(3)}(\mathbf{k_1}+\mathbf{k_2}+\mathbf{k_3})B(k_1,k_2,k_3)\,. \tag{6.64}$$

The Dirac delta enforces the invariance under spatial translations and implies that the wave vectors $\mathbf{k_1}$, $\mathbf{k_2}$ and $\mathbf{k_3}$ must form a closed triangle in Fourier space. Because of rotational invariance, instead, $B(k_1,k_2,k_3)$ depends only on the magnitude of the three wave vectors. The bispectrum $B(k_1,k_2,k_3)$ can further be rewritten as [319–321]

$$B(k_1,k_2,k_3) = f_{\rm NL}\frac{S(k_1,k_2,k_3)}{(k_1k_2k_3)^2}\,, \tag{6.65}$$

where $f_{\rm NL}$ is a dimensionless parameter quantifying the amplitude of the bispectrum[6] and the shape function $S(k_1,k_2,k_3)$ encodes the functional dependence of the bispectrum on the specific triangle configurations. Typically, the shape function is normalized such that $S(k,k,k)=1$ in the equilateral limit, where the three momenta are equal. Notice that, due to the fact that the momenta form a closed triangle, once we specify two of the three momenta, the third is automatically fixed. As a consequence, the shape function depends only on the ratios between

[6]The exact definition of $f_{\rm NL}$ is fixed except for a constant normalization that may vary depending on the literature and the kind of primordial bispectrum under consideration. As an example, within the Planck mission it has been chosen to normalize the $f_{\rm NL}$ coefficient of the scalar bispectrum such that [321]

$$f_{\rm NL}^{\zeta} = \frac{5}{18}\frac{B_\zeta(k,k,k)}{P_\zeta^2(k)}\,. \tag{6.66}$$

Here $B_\zeta(k_1,k_2,k_3)$ and $P_\zeta(k)$ denote respectively the scalar bispectrum and power spectrum from inflation.

two of the three momenta and the third (at least for almost scale invariant bispectra), e.g. $x_2 = k_2/k_1$ and $x_3 = k_3/k_1$.

The bispectrum of primordial tensor modes (evaluated at a given conformal time τ) can be computed by means of the in-in formalism (see, e.g., [44, 339, 347, 348]) as

$$\langle \gamma_{s_1}(\mathbf{k_1},\tau)\gamma_{s_2}(\mathbf{k_2},\tau)\gamma_{s_3}(\mathbf{k_3},\tau)\rangle = -i\int_{-\infty}^{\tau} d\tau' \langle 0|\left[\gamma_{s_1}(\mathbf{k_1},\tau)\gamma_{s_2}(\mathbf{k_2},\tau)\gamma_{s_3}(\mathbf{k_3},\tau), H_{\rm int}^{\gamma\gamma\gamma}(\tau')\right]|0\rangle\,, \tag{6.67}$$

where $H_{\rm int}^{\gamma\gamma\gamma} = -L_{\rm int}^{\gamma\gamma\gamma}$ denotes the interaction Hamiltonian at cubic order in tensor perturbations. In the computation of the in-in integrals we will adopt the usual $i\epsilon$-prescription, which amounts to deform the contour of integration by making the rotation $-\infty \to -\infty(1-i\epsilon)$ in the complex plane (see, e.g., [44]). The $i\epsilon$ contribution turns off the interactions in the far past and projects onto the vacuum state of the free theory. We are in particular interested in evaluating the primordial bispectrum on super-horizon scales, i.e. taking the limit $\tau \to 0$ of Eq. (6.67).

6.3.1 Graviton bispectra for constant coupling functions

We start with the computation of the bispectrum from the Lagrangian PV1. The explicit expressions of the operators of $\mathcal{L}_{\rm PV1}$ at cubic order in tensor perturbations, as well as the interaction Hamiltonian, can be found in Appendix B. We can then plug the interaction Hamiltonian (B.6) into the in-in formula (6.67) and use the Wick theorem, with the contractions between the fields that are given by definition by

$$\langle 0|\gamma_{s_1}(\mathbf{k_1},0)\gamma_{s_2}(\mathbf{k},\tau)\epsilon_{ij}^{(s_2)}(\mathbf{k})|0\rangle = (2\pi)^3\delta_{s_1 s_2}\delta^{(3)}(\mathbf{k_1}+\mathbf{k})u_{s_1}(\mathbf{k_1},0)u_{s_2}^*(\mathbf{k},\tau)\epsilon_{ij}^{(s_2)*}(\mathbf{k})\,, \tag{6.68}$$

$$\langle 0|\gamma_{s_1}(\mathbf{k_1},0)\gamma'_{s_2}(\mathbf{k},\tau)\epsilon_{ij}^{(s_2)}(\mathbf{k})|0\rangle = (2\pi)^3\delta_{s_1 s_2}\delta^{(3)}(\mathbf{k_1}+\mathbf{k})u_{s_1}(\mathbf{k_1},0)u_{s_2}^{*\prime}(\mathbf{k},\tau)\epsilon_{ij}^{(s_2)*}(\mathbf{k})\,. \tag{6.69}$$

The bispectrum of primordial tensor perturbations can then be written as[7]

$$\langle \gamma_{s_1}(\mathbf{k_1})\gamma_{s_2}(\mathbf{k_2})\gamma_{s_3}(\mathbf{k_3})\rangle_{\rm PV1} = (2\pi)^3\delta^{(3)}(\mathbf{k_1}+\mathbf{k_2}+\mathbf{k_3})\,4\,{\rm Im}\left(\sum_{i=1}^{9} I_i C_i^{s_1 s_2 s_3}(\mathbf{k_1},\mathbf{k_2},\mathbf{k_3})\right) + \text{perm.}\,(k_i)\,, \tag{6.70}$$

where we have defined

$$I_1 \equiv -u_{s_1}(k_1,0)u_{s_2}(k_2,0)u_{s_3}(k_3,0)\int_{-\infty}^{0}\frac{d\tau'}{\tau'}\,(f_1+g_1)\,\frac{du_{s_1}^*}{d\tau'}(k_1,\tau')\frac{du_{s_2}^*}{d\tau'}(k_2,\tau')u_{s_3}^*(k_3,\tau')\,,$$

$$I_2 \equiv -u_{s_1}(k_1,0)u_{s_2}(k_2,0)u_{s_3}(k_3,0)\int_{-\infty}^{0}d\tau'\,\frac{f_1}{2}\,\frac{du_{s_1}^*}{d\tau'}(k_1,\tau')\frac{du_{s_2}^*}{d\tau'}(k_2,\tau')\frac{du_{s_3}^*}{d\tau'}(k_3,\tau')\,,$$

$$I_3 \equiv u_{s_1}(k_1,0)u_{s_2}(k_2,0)u_{s_3}(k_3,0)\int_{-\infty}^{0}d\tau'\,\frac{(f_1+g_1)}{2}\,\frac{du_{s_1}^*}{d\tau'}(k_1,\tau')u_{s_2}^*(k_2,\tau')u_{s_3}^*(k_3,\tau')\,,$$

$$I_4 \equiv u_{s_1}(k_1,0)u_{s_2}(k_2,0)u_{s_3}(k_3,0)\int_{-\infty}^{0}d\tau'\,\frac{g_1}{2}\,u_{s_1}^*(k_1,\tau')u_{s_2}^*(k_2,\tau')\frac{du_{s_3}^*}{d\tau'}(k_3,\tau')\,,$$

$$I_5 \equiv -u_{s_1}(k_1,0)u_{s_2}(k_2,0)u_{s_3}(k_3,0)\int_{-\infty}^{0}d\tau'\,\left(f_1+\frac{g_1}{2}\right)\,\frac{du_{s_1}^*}{d\tau'}(k_1,\tau')u_{s_2}^*(k_2,\tau')u_{s_3}^*(k_3,\tau')\,,$$

$$I_6 \equiv u_{s_1}(k_1,0)u_{s_2}(k_2,0)u_{s_3}(k_3,0)\int_{-\infty}^{0}d\tau'\,\frac{f_1}{2}\,\frac{du_{s_1}^*}{d\tau'}(k_1,\tau')u_{s_2}^*(k_2,\tau')u_{s_3}^*(k_3,\tau')\,,$$

$$I_7 \equiv -u_{s_1}(k_1,0)u_{s_2}(k_2,0)u_{s_3}(k_3,0)\int_{-\infty}^{0}\frac{d\tau'}{\tau'}\,(f_1+g_1)\,u_{s_1}^*(k_1,\tau')\frac{du_{s_2}^*}{d\tau'}(k_2,\tau')\frac{du_{s_3}^*}{d\tau'}(k_3,\tau')\,,$$

[7] The delta functions in the momenta lead to terms like $\epsilon_{ij}^{(s)*}(-\mathbf{k})$, but $\epsilon_{ij}^{(s)*}(-\mathbf{k}) = \epsilon_{ij}^{(s)}(\mathbf{k})$ (6.19). The delta functions in the polarization indices instead reduce the initial nine polarizations (3+6 in the interaction Hamiltonian) down to only three.

$$I_8 \equiv u_{s_1}(k_1,0)u_{s_2}(k_2,0)u_{s_3}(k_3,0)\int_{-\infty}^{0} d\tau' \,\frac{(f_1+g_1)}{2}\, u^*_{s_1}(k_1,\tau')u^*_{s_2}(k_2,\tau')\frac{du^*_{s_3}}{d\tau'}(k_3,\tau')\,,$$
$$I_9 \equiv -u_{s_1}(k_1,0)u_{s_2}(k_2,0)u_{s_3}(k_3,0)\int_{-\infty}^{0} d\tau' \,\frac{g_1}{2}\,\frac{du^*_{s_1}}{d\tau'}(k_1,\tau')\frac{du^*_{s_2}}{d\tau'}(k_2,\tau')\frac{du^*_{s_3}}{d\tau'}(k_3,\tau')\,, \tag{6.71}$$

where the $C_i^{s_1s_2s_3}(\mathbf{k_1},\mathbf{k_2},\mathbf{k_3})$, whose full expressions can be found in Appendix C, are defined in terms of contractions between the wave vectors and the polarization tensors.

As a first approximation we assume that $a(\tau) \simeq -1/(H\tau)$, which holds at leading order in slow-roll, and take the Hubble parameter H as constant during inflation. In the same spirit, we approximate the exact graviton mode function with the mode function in a de Sitter space-time. For tensor modes, this is given by (see, e.g., [44, 348])

$$u_s(k,\tau) = \frac{iH}{M_{Pl}\sqrt{k^3}}\,(1+ik\tau)\,e^{-ik\tau}\,. \tag{6.72}$$

This is justified because the corrections to the mode function (6.72) that arise in this model are proportional to ϵ and $H/M_{\rm PV1}$, which are both very small during inflation. So, using the de Sitter mode function gives the leading order contribution to the bispectrum. For the moment we also take the coupling functions f_1 and g_1 to be constant, leaving the more general case of time dependent couplings for the next section.
We can now solve analytically the integrals in Eq. (6.71), which give

$$I_1 = (f_1+g_1)\left(\frac{H^6}{M_{Pl}^6 k_1^3k_2^3k_3^3}\right)k_1^2k_2^2\left[\frac{1}{k_T^2}+2\frac{k_3}{k_T^3}\right], \tag{6.73}$$

$$I_2 = \frac{f_1}{2}\left(\frac{H^6}{M_{Pl}^6 k_1^3k_2^3k_3^3}\right)k_1^2k_2^2k_3^2\frac{6}{k_T^4}\,, \tag{6.74}$$

$$I_3 = \frac{f_1+g_1}{2}\left(\frac{H^6}{M_{Pl}^6 k_1^3k_2^3k_3^3}\right)k_1^2\left[\frac{1}{k_T^2}+2\frac{k_2+k_3}{k_T^3}-6\frac{k_2k_3}{k_T^4}\right], \tag{6.75}$$

$$I_4 = \frac{g_1}{2}\left(\frac{H^6}{M_{Pl}^6 k_1^3k_2^3k_3^3}\right)k_3^2\left[\frac{1}{k_T^2}+2\frac{k_1+k_2}{k_T^3}-6\frac{k_1k_2}{k_T^4}\right], \tag{6.76}$$

$$I_5 = -\left(f_1+\frac{g_1}{2}\right)\left(\frac{H^6}{M_{Pl}^6 k_1^3k_2^3k_3^3}\right)k_1^2\left[\frac{1}{k_T^2}+2\frac{k_2+k_3}{k_T^3}-6\frac{k_2k_3}{k_T^4}\right], \tag{6.77}$$

$$I_6 = \frac{f_1}{2}\left(\frac{H^6}{M_{Pl}^6 k_1^3k_2^3k_3^3}\right)k_1^2\left[\frac{1}{k_T^2}+2\frac{k_2+k_3}{k_T^3}-6\frac{k_2k_3}{k_T^4}\right], \tag{6.78}$$

$$I_7 = (f_1+g_1)\left(\frac{H^6}{M_{Pl}^6 k_1^3k_2^3k_3^3}\right)k_2^2k_3^2\left[\frac{1}{k_T^2}+2\frac{k_1}{k_T^3}\right], \tag{6.79}$$

$$I_8 = \frac{f_1+g_1}{2}\left(\frac{H^6}{M_{Pl}^6 k_1^3k_2^3k_3^3}\right)k_3^2\left[\frac{1}{k_T^2}+2\frac{k_1+k_2}{k_T^3}-6\frac{k_1k_2}{k_T^4}\right], \tag{6.80}$$

$$I_9 = \frac{g_1}{2}\left(\frac{H^6}{M_{Pl}^6 k_1^3k_2^3k_3^3}\right)k_1^2k_2^2k_3^2\frac{6}{k_T^4}\,, \tag{6.81}$$

where we have defined the total momentum $k_T \equiv k_1+k_2+k_3$. Notice that all the previous integrals give real results. Since all the $C_i^{s_1s_2s_3}(\mathbf{k_1},\mathbf{k_2},\mathbf{k_3})$ terms in Eq. (6.70) are real (this is true also for the contributions proportional to $i\epsilon^{ijl}$ in Eqs. (C.3)-(C.4)-(C.6)-(C.7), as can be easily checked by direct computations), the full bispectrum vanishes:

$$\langle\gamma_{s_1}(\mathbf{k_1})\gamma_{s_2}(\mathbf{k_2})\gamma_{s_3}(\mathbf{k_3})\rangle_{\rm PV1} = 0\,. \tag{6.82}$$

Hence, no parity-violating signatures arise in the graviton bispectrum if the couplings f_1 and g_1 are taken to be constant. Notice that this is true under the approximation of using the de Sitter mode function for tensor modes. We expect that, using the exact solutions from the equation of motion of PGWs, may lead to a non-vanishing result, but with contributions that are suppressed by slow-roll parameters and the ratio $H/M_{\rm PV1}$ (see [323] for a detailed analysis of this issue in the case of slow-roll inflation with the parity-violating Weyl cubic term).

However, since there are no reasons for the coupling functions to be constant throughout all inflation, it is interesting to study the more general scenario in which the couplings are free to vary with time. In this case, using the de Sitter mode function will give the leading order non-vanishing contribution.

Before doing this, let us make a similar analysis for the Lagrangian PV2. Once again, we refer the reader to Appendix B for the full expression of the interaction Hamiltonian at third order in tensor perturbations, which is reported in Eq. (B.9). By plugging this into the in-in formula (6.67), we find

$$\begin{aligned}\langle\gamma_{s_1}(\mathbf{k_1})\gamma_{s_2}(\mathbf{k_2})\gamma_{s_3}(\mathbf{k_3})\rangle_{\rm PV2} = (2\pi)^3\delta^{(3)}(\mathbf{k_1}+\mathbf{k_2}+\mathbf{k_3})\,{\rm Im}\Bigg[\frac{\lambda_{s_1}}{2}\tilde{I}_1\,k_1\epsilon^{mi}_{(s_1)}(\mathbf{k_1})\epsilon^{(s_2)}_{mr}(\mathbf{k_2})\epsilon^{r}_{(s_3)i}(\mathbf{k_3})\\ -\frac{i}{2}(\tilde{I}_2+\tilde{I}_3)\epsilon^{ijl}k_{1r}\epsilon_l^{(s_1)m}(\mathbf{k_1})\epsilon_j^{(s_2)r}(\mathbf{k_2})\epsilon^{(s_3)}_{mi}(\mathbf{k_3})\Bigg] + \text{perm.}\,(k_i)\,,\end{aligned} \tag{6.83}$$

where we have defined

$$\begin{aligned}\tilde{I}_1 &\equiv -u_{s_1}(k_1,0)u_{s_2}(k_2,0)u_{s_3}(k_3,0)\int_{-\infty}^{0}\frac{d\tau'}{\tau'}\left[\tilde{b}_1\frac{M_{Pl}}{H}-b\right]\frac{du^*_{s_1}}{d\tau'}(k_1,\tau')\frac{du^*_{s_2}}{d\tau'}(k_2,\tau')u^*_{s_3}(k_3,\tau')\,,\\ \tilde{I}_2 &\equiv -u_{s_1}(k_1,0)u_{s_2}(k_2,0)u_{s_3}(k_3,0)\int_{-\infty}^{0}\frac{d\tau'}{\tau'}\left[\tilde{b}_1\frac{M_{Pl}}{H}-b\right]u^*_{s_1}(k_1,\tau')\frac{du^*_{s_2}}{d\tau'}(k_2,\tau')\frac{du^*_{s_3}}{d\tau'}(k_3,\tau')\,,\\ \tilde{I}_3 &\equiv u_{s_1}(k_1,0)u_{s_2}(k_2,0)u_{s_3}(k_3,0)\int_{-\infty}^{0}d\tau'\,\frac{b}{2}\,\frac{du^*_{s_1}}{d\tau'}(k_1,\tau')\frac{du^*_{s_2}}{d\tau'}(k_2,\tau')\frac{du^*_{s_3}}{d\tau'}(k_3,\tau')\,.\end{aligned} \tag{6.84}$$

Also in this case, we first work under the approximation of constant coupling functions and using the de Sitter mode functions given in Eq. (6.72) for gravitons, taking the Hubble parameter H to be constant during inflation. The integrals in (6.84) can then be easily solved and give

$$\tilde{I}_1 = \left[\tilde{b}_1\frac{M_{Pl}}{H}-b\right]\left(\frac{H^6}{M_{Pl}^6k_1^3k_2^3k_3^3}\right)k_1^2k_2^2\left[\frac{1}{k_T^2}+2\frac{k_3}{k_T^3}\right]\,, \tag{6.85}$$

$$\tilde{I}_2 = \left[\tilde{b}_1\frac{M_{Pl}}{H}-b\right]\left(\frac{H^6}{M_{Pl}^6k_1^3k_2^3k_3^3}\right)k_2^2k_3^2\left[\frac{1}{k_T^2}+2\frac{k_1}{k_T^3}\right]\,, \tag{6.86}$$

$$\tilde{I}_3 = -3b\left(\frac{H^6}{M_{Pl}^6k_1^3k_2^3k_3^3}\right)\frac{k_1^2k_2^2k_3^2}{k_T^4}\,. \tag{6.87}$$

Just like in the PV1 case, all the integrals give real contributions and thus none of the parity-breaking operators contributes to the bispectrum of primordial tensor modes:

$$\langle\gamma_{s_1}(\mathbf{k_1})\gamma_{s_2}(\mathbf{k_2})\gamma_{s_3}(\mathbf{k_3})\rangle_{\rm PV2} = 0\,. \tag{6.88}$$

Soon after our analysis was completed, Ref. [332] came out. Here, the authors have derived the most general tree-level bispectra for a massless graviton to all orders in derivatives, assuming scale invariance and adopting a boostrap approach. Interestingly, one of the results of this analysis is that a contact parity-odd correlator can only arise when $2n_{\partial_\eta}+n_{\partial_i}\leq 3$, where n_{∂_η} and n_{∂_i} are the number of time and space derivatives in the parity-odd interaction, respectively.

Looking at the explicit expressions of the interaction terms considered in our analysis (see Appendix B), we see that the previous condition is not satisfied. This explains why we find vanishing tensor bispectra in the scale-invariant limit.

6.3.2 Graviton bispectra for time dependent coupling functions

So far, we have explicitly demonstrated that the parity-breaking operators introduced in [24] give no contributions to the primordial tensor bispectrum, assuming the de Sitter mode function for gravitons and in the case of constant coupling functions. However, as already discussed, there are no theoretical reasons why the couplings should be constant during all the inflationary phase. Indeed, the couplings in Eqs. (6.24)-(6.57) depend on the scalar field and its kinetic term in full generality. Moreover, they could acquire a non-trivial time evolution because they might also depend on fields other than the inflaton field, being therefore not necessarily limited to a slow-roll evolution. Furthermore, it has been shown, e.g. in Ref. [324] for the parity-violating Weyl cubic terms, that, even if these operators do not contribute to the graviton bispectrum for constant couplings in the de Sitter limit [323], they can instead leave non-vanishing signatures if the couplings are free to vary with time.

Motivated by these reasons, we now extend the analysis of the previous section to the more general scenario where the coupling functions are allowed to evolve with time during inflation, and investigate whether parity-breaking signatures may arise in the primordial graviton bispectrum.

We start by analyzing the PV1 model (defined by the Lagrangian (6.15)). We restrict in particular to the interesting case where

$$f_1 + g_1 = 0\,, \tag{6.89}$$

such that the model is free from instabilities (see Eqs. (6.21),(6.22), (6.24), and the discussion after Eq. (6.23)). Indeed, when the condition (6.89) is realized, the cut-off scale $M_{\rm PV1} \to \infty$ and all the corrections to the quadratic action for tensor modes (6.20) disappear (this can also be seen directly from the equations of motion (6.38)). In particular, this means that we recover $c_{T,s} = 1$ and $\chi = 0$. Notice also that in such a case the theory makes sense without requiring an effective field theory treatment. If we drop (6.89), then the couplings have to obey $H/M_{PV1} \ll 1$, which will significantly limit also the amplitude of tensor bispectra.

In order to make explicit computations, we need to assume a specific form of the coupling functions. In the rest of the analysis we consider the case of a dilaton-like coupling, that naturally arises in theories with extra dimensions, like string theory. This can be written as $f_1 = e^{(\phi-\phi_*)/M}$, where M is some arbitrary energy scale. In slow-roll inflation this leads to a coupling that is simply given by some power of the conformal time[8] (see [324] for more details)

$$f_1(\tau) = \left(\frac{\tau}{\tau_*}\right)^A\,, \qquad A = \pm\sqrt{2\epsilon}\,\frac{M_{Pl}}{M}\,, \tag{6.92}$$

where ϵ is the usual slow-roll parameter, defined as in Eq. (6.31). The value of τ_* is fixed by the initial condition of Eq. (6.90). For example, we can take τ_* to be the time when the scale

[8] Indeed, in slow-roll inflation the equation of motion for the inflaton field is

$$\phi' \simeq \pm\sqrt{2\epsilon}M_{Pl}\tau^{-1}\,, \tag{6.90}$$

where the + and − signs are for $\partial V/\partial\phi > 0$ and $\partial V/\partial\phi < 0$ respectively. This can be integrated to give

$$\phi = \phi_* \pm \sqrt{2\epsilon}M_{Pl}\ln\left(\frac{\tau}{\tau_*}\right)\,. \tag{6.91}$$

Substituting this into the exponential dilaton coupling, we end up with Eq. (6.92).

corresponding to present observable Universe crosses the horizon during inflation, such that $|\tau_*| = k_*^{-1} \sim 14$ Gpc [324]. In this case, f_1 would be of order unity for the current cosmological scales.

Thanks to the constraint (6.89), the integrals I_1, I_3, I_7, I_8 in Eq. (6.71) vanish,

$$I_1 = I_3 = I_7 = I_8 = 0\,. \tag{6.93}$$

As regards the other integrals, once we have replaced the explicit expression of the mode function (6.72) for gravitons in (6.71), we end up with integrals of the kind

$$I_{(n,A)} = \tau_*^{-A} \int_{-\infty}^{0} d\tau\, \tau^{n+A} e^{ik_T\tau}\,, \tag{6.94}$$

with $n + A > -1$. These can be performed analytically (with the usual $i\epsilon$ prescription) and give

$$\begin{aligned} I_{(n,A)} &= \tau_*^{-A}(-1)^{(A+n)}\,(ik_T)^{(-1-A-n)}\,\Gamma(n+1+A) \\ &= (-1)^n\,(-i)^{(-n-1)}\,(n+A)!\,(-k_T\,\tau_*)^{-A}(-k_T)^{(-n-1)}\left[\cos\left(\frac{\pi}{2}A\right) + i\sin\left(\frac{\pi}{2}A\right)\right]\,, \end{aligned} \tag{6.95}$$

where $\Gamma(x) = (x-1)!$ is the Gamma function and in the second equality we have used the Euler's formula. Using Eq. (6.95) we find

$$I_2 = -I_9 = \frac{(3+A)!}{2}\left(\frac{H^6}{M_{Pl}^6 k_1^3 k_2^3 k_3^3}\right)\frac{k_1^2 k_2^2 k_3^2}{k_T^4}\,(-k_T\tau_*)^{-A}\left[\cos\left(\frac{\pi}{2}A\right) + i\,\sin\left(\frac{\pi}{2}A\right)\right]\,, \tag{6.96}$$

$$\begin{aligned} I_4 &= \frac{1}{2}\left(\frac{H^6}{M_{Pl}^6 k_1^3 k_2^3 k_3^3}\right)(-k_T\tau_*)^{-A}\,k_3^2\left[-\frac{(1+A)!}{k_T^2} - (2+A)!\,\frac{k_1+k_2}{k_T^3} + (3+A)!\,\frac{k_1 k_2}{k_T^4}\right] \\ &\quad\times\left[\cos\left(\frac{\pi}{2}A\right) + i\,\sin\left(\frac{\pi}{2}A\right)\right]\,, \end{aligned} \tag{6.97}$$

$$\begin{aligned} I_5 = -I_6 &= \frac{1}{2}\left(\frac{H^6}{M_{Pl}^6 k_1^3 k_2^3 k_3^3}\right)(-k_T\tau_*)^{-A}\,k_1^2\left[-\frac{(1+A)!}{k_T^2} - (2+A)!\,\frac{k_2+k_3}{k_T^3} + (3+A)!\,\frac{k_2 k_3}{k_T^4}\right] \\ &\quad\times\left[\cos\left(\frac{\pi}{2}A\right) + i\,\sin\left(\frac{\pi}{2}A\right)\right]\,. \end{aligned} \tag{6.98}$$

Notice that for $A = 0$ we recover the result of the previous section, since the imaginary parts of the integrals (6.96)-(6.98) vanish and the bispectrum receives no contributions from the PV1 operators. When instead $A \neq 0$ (i.e. for time dependent couplings), the imaginary parts of these integrals switch on parity-breaking signatures in the primordial tensor bispectrum. This can be computed by plugging Eqs. (6.96)-(6.98) into Eq. (6.70). By doing so, we find

$$\begin{aligned} \langle\gamma_{s_1}(\mathbf{k_1})\gamma_{s_2}(\mathbf{k_2})\gamma_{s_3}(\mathbf{k_3})\rangle_{\rm PV1} &= (2\pi)^3\delta^{(3)}(\mathbf{k_1}+\mathbf{k_2}+\mathbf{k_3})\left(\frac{H}{M_{Pl}}\right)^6\left(\frac{\tau_*}{\bar\tau}\right)^{-A}\sin\left(\frac{\pi}{2}A\right) \\ &\quad\times 2B^{\rm PV1}_{s_1s_2s_3}(\mathbf{k_1},\mathbf{k_2},\mathbf{k_3}) + \text{perm.}\,(k_i)\,, \end{aligned} \tag{6.99}$$

where we have defined

$$\begin{aligned} B^{\rm PV1}_{s_1s_2s_3}(\mathbf{k_1},\mathbf{k_2},\mathbf{k_3}) = \frac{1}{k_1^3k_2^3k_3^3}\Bigg\{&(3+A)!\,\frac{k_1^2k_2^2k_3^2}{k_T^4}\,T_1^{s_1s_2s_3}(\mathbf{k_1},\mathbf{k_2},\mathbf{k_3}) + k_3^2\left[-\frac{(1+A)!}{k_T^2}\right. \\ &\left.-(2+A)!\,\frac{k_1+k_2}{k_T^3} + (3+A)!\,\frac{k_1k_2}{k_T^4}\right]T_2^{s_1s_2s_3}(\mathbf{k_1},\mathbf{k_2},\mathbf{k_3}) \\ &+ k_1^2\left[-\frac{(1+A)!}{k_T^2} - (2+A)!\,\frac{k_2+k_3}{k_T^3} + (3+A)!\,\frac{k_2k_3}{k_T^4}\right] \\ &\times T_3^{s_1s_2s_3}(\mathbf{k_1},\mathbf{k_2},\mathbf{k_3})\Bigg\}\,. \end{aligned} \tag{6.100}$$

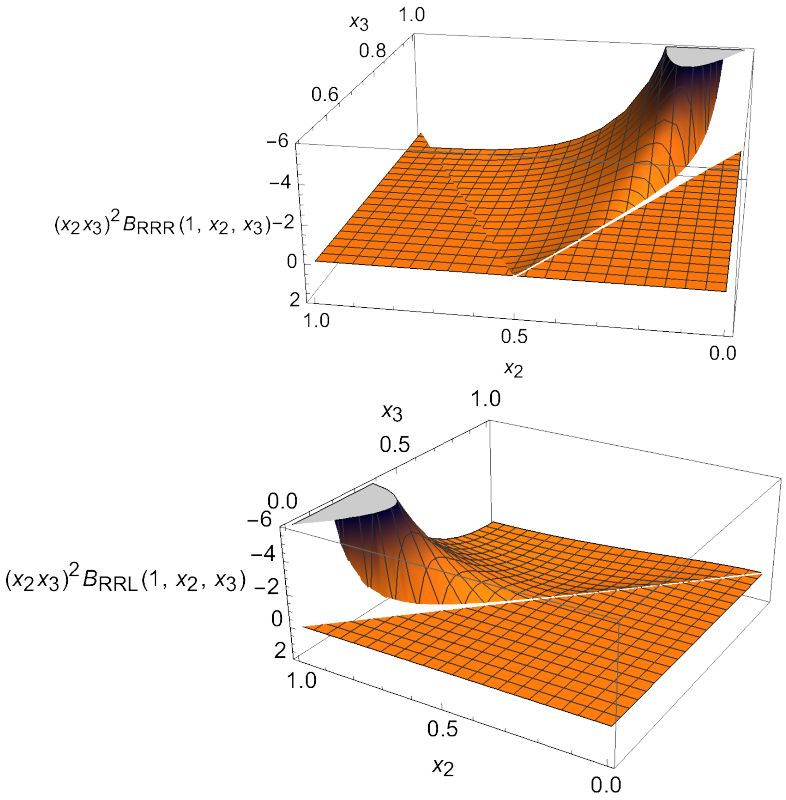

Figure 6.1: Shapes of the RRR and RRL graviton bispectra in the PV1 model, with $A = 1$. The quantities $B_{RRR}(1, x_2, x_3)x_2^2x_3^3$ and $B_{RRL}(1, x_2, x_3)x_2^2x_3^3$ are plotted as functions of $x_2 = k_2/k_1$ and $x_3 = k_3/k_1$. They are both normalized to unity in the equilateral limit, $x_2 = x_3 = 1$.

The $T_i^{s_1s_2s_3}(\mathbf{k_1}, \mathbf{k_2}, \mathbf{k_3})$ are again defined in terms of contractions between the wave vectors and the polarization tensors. Their full expressions, which can be written as linear combinations of the $C_i^{s_1s_2s_3}(\mathbf{k_1}, \mathbf{k_2}, \mathbf{k_3})$, can be found in Appendix C.

In Eq. (6.99) we have evaluated the bispectrum at the horizon-crossing time of the total momentum k_T, $\bar{\tau} = -1/k_T$. In fact, it is well known that, when performing in-in integrals, the main contributions arise around the horizon crossing of the overall momentum k_T in the case of derivative interactions, as in the models under study. Notice that, because of the term $(\tau_*/\bar{\tau})^{-A}$ arising due to the time dependence of the coupling, the amplitude of the bispectrum is scale-dependent. In particular, for values of $A < 0$ the amplitude increases going to small scales. For $A > 0$, instead, the amplitude of the graviton bispectrum increases going to large scales.

In Fig. 6.1 we plot the shape functions for two different polarization configurations, the first having $s_1 = s_2 = s_3 = R$ and the second with $s_1 = s_2 = R$ and $s_3 = L$. The other cases differ from these only by a minus sign, thus giving the same shape function. In particular, from the definition (6.65), we show the quantities $B_{RRR}(1, x_2, x_3)x_2^2x_3^3$ and $B_{RRL}(1, x_2, x_3)x_2^2x_3^3$ as functions of $x_2 = k_2/k_1$ and $x_3 = k_3/k_1$. The plots are done assuming $A = 1$, but we have checked that the qualitative behaviour of the shapes is independent from the value of A, which thus affects only the amplitude (and, in particular, its scale-dependence) of the primordial bispectra. As already remarked in the previous sections, the shape function of the bispectrum is a powerful tool to discriminate among the various inflationary models. Indeed, different models of inflation contain different interaction terms between the dynamical fields of the theory, and thus leave distinctive signatures in the shapes of the primordial bispectra [321].

To quantify how much a shape S_1 is similar to a reference shape S_2, it is common to introduce

the cosine of the two shapes

$$\cos(S_1, S_2) \equiv \frac{S_1 \cdot S_2}{(S_1 \cdot S_1)^{1/2}(S_2 \cdot S_2)^{1/2}}\,, \tag{6.101}$$

where the scalar product is defined as (see, e.g., [319, 324, 349])

$$S_1 \cdot S_2 \equiv \sum_{k_i} \frac{S_1(k_1, k_2, k_3) S_2(k_1, k_2, k_3)}{P(k_1)P(k_2)P(k_3)}\,. \tag{6.102}$$

Here, the summation runs over all the wave vectors that form a triangle in the momentum space and $P(k)$ denotes the (tensor) power spectrum. By definition, the cosine is equal to 1 when $S_1 = S_2$. Apart for an overall coefficient (that eventually cancels out when computing (6.101)), the quantity (6.102) can be expressed as an integral over x_2 and x_3 as[9]

$$S_1 \cdot S_2 \propto \int_{\frac{k_{\rm min}}{k_{\rm max}}}^{1-\frac{k_{\rm min}}{k_{\rm max}}} dx_2 \int_{1-x_2}^{1-\frac{k_{\rm min}}{k_{\rm max}}} dx_3\, x_2^4 x_3^4\, S_1(1, x_2, x_3)\, S_2(1, x_2, x_3)\,. \tag{6.103}$$

As far as CMB experiments are concerned, in the following we evaluate the cosine between the shapes by summing over all the corresponding configurations in multipole space (using, as a first approximation, that $\ell \propto k$) for multipoles ℓ ranging, in an ideal case, from $\ell_{\rm min} = 2$ up to $\ell_{\rm max} = 1000$.[10] In the case of the shapes plotted in Fig. 6.1, we find

$$\cos\left(B^{\rm PV1}_{RRR}, B_S\right) \simeq \begin{cases} 0.006\,, & S = \text{equilateral} \\ 0.795\,, & S = \text{local} \\ 0.328\,, & S = \text{orthogonal} \end{cases} \tag{6.104}$$

for the RRR case, while for the RRL polarizations we have

$$\cos\left(B^{\rm PV1}_{RRL}, B_S\right) \simeq \begin{cases} 0.046\,, & S = \text{equilateral} \\ 0.546\,, & S = \text{local} \\ 0.299\,, & S = \text{orthogonal}\,. \end{cases} \tag{6.105}$$

From these results and Fig. 6.1, we realize that the maximum contributions come mainly from the squeezed configuration (corresponding to, e.g., $k_3 \ll k_1 \simeq k_2$).

We now compute the bispectrum from the PV2 Lagrangian (6.15), assuming time dependent couplings. Analogously to what we have done for the PV1 model, we restrict to the case with

$$\tilde{b}_1 \frac{M_{Pl}}{H} - b = 0\,, \tag{6.106}$$

such that the model is free from instabilities. As a time dependent dilaton-like coupling we choose

$$b(\tau) = \left(\frac{\tau}{\tau_*}\right)^A\,, \qquad A = \pm\sqrt{2\epsilon}\,\frac{M_{Pl}}{M}\,. \tag{6.107}$$

[9] Notice that the ratio between two scales that enter in a given bispectrum can never be exactly 0 or 1, as in both cases we would deal with unphysical infinite-wavelength modes. This motivates the presence of the ratios $k_{\rm min}/k_{\rm max}$ in the extremes of integration in (6.103), so that the cosine between shapes depends on the ratio between the minimum and maximum scales that a given experiment can probe.

[10] In such a case, the choice of $\ell_{\rm max} = 1000$ is just indicative. Notice that this choice is rather optimistic if one considers bispectra involving the B-mode polarization field of the CMB (see [350, 351]). However, we have explicitly checked that the cosines between the shapes are only weakly dependent on $\ell_{\rm max}$ for $\ell_{\rm max} \gtrsim 100$.

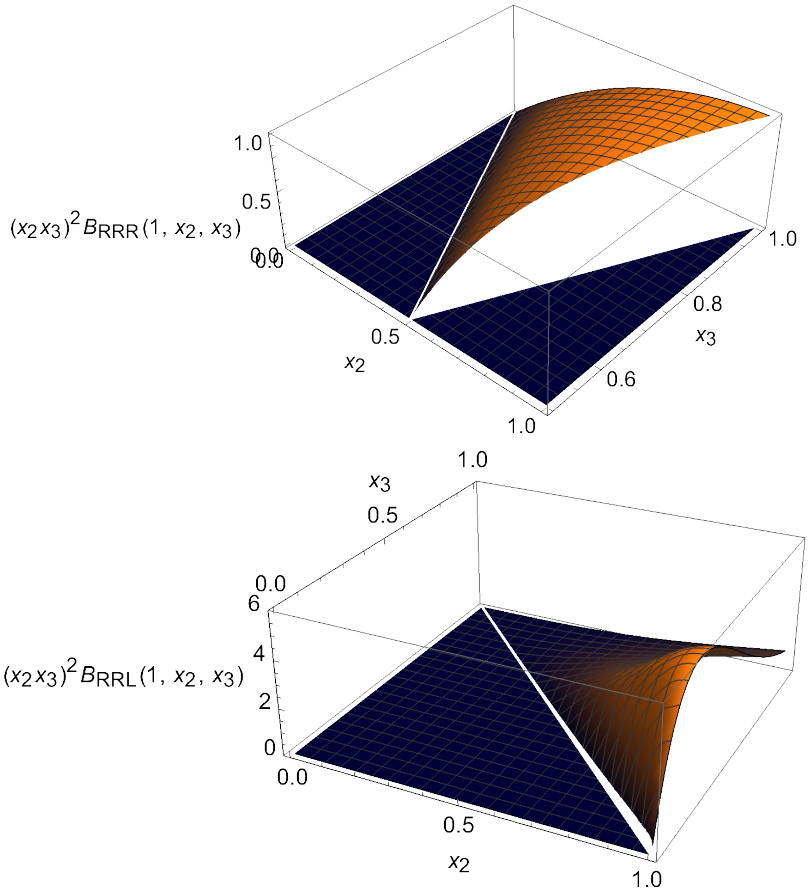

Figure 6.2: Shapes of the RRR and RRL graviton bispectra in the PV2 model, with $A = 1$. The quantities $B_{RRR}(1, x_2, x_3)x_2^2x_3^3$ and $B_{RRL}(1, x_2, x_3)x_2^2x_3^3$ are plotted as functions of $x_2 = k_2/k_1$ and $x_3 = k_3/k_1$. They are both normalized to unity in the equilateral limit, $x_2 = x_3 = 1$.

The integrals $\tilde{I}_1$ and $\tilde{I}_2$ in Eq. (6.84) vanish, while for $\tilde{I}_3$ we find

$$\tilde{I}_3 = -(3+A)! \left(\frac{H^6}{M_{Pl}^6 k_1^3 k_2^3 k_3^3}\right) \frac{k_1^2 k_2^2 k_3^2}{k_T^4} (-k_T\tau_*)^{-A} \left[\cos\left(\frac{\pi}{2}A\right) + i\sin\left(\frac{\pi}{2}A\right)\right] . \tag{6.108}$$

The bispectrum in Eq. (6.83) can thus be rewritten as

$$\begin{aligned}\langle\gamma_{s_1}(\mathbf{k_1})\gamma_{s_2}(\mathbf{k_2})\gamma_{s_3}(\mathbf{k_3})\rangle_{\rm PV2} = (2\pi)^3\delta^{(3)}(\mathbf{k_1}+\mathbf{k_2}+\mathbf{k_3})\,\frac{(3+A)!}{2}\left(\frac{H}{M_{Pl}}\right)^6\left(\frac{\tau_*}{\bar{\tau}}\right)^{-A}\sin\left(\frac{\pi}{2}A\right)\\ \times B^{\rm PV2}_{s_1s_2s_3}(\mathbf{k_1},\mathbf{k_2},\mathbf{k_3}) + \text{perm.}\,(k_i)\,,\end{aligned} \tag{6.109}$$

where we have defined

$$B^{\rm PV2}_{s_1s_2s_3}(\mathbf{k_1},\mathbf{k_2},\mathbf{k_3}) = \frac{1}{k_1^3k_2^3k_3^3}\left\{\frac{k_1^2k_2^2k_3^2}{k_T^4}\left[i\epsilon^{ijl}k_{1r}\,\epsilon_l^{(s_1)m}(\mathbf{k_1})\epsilon_j^{(s_2)r}(\mathbf{k_2})\epsilon_{mi}^{(s_3)}(\mathbf{k_3})\right]\right\}. \tag{6.110}$$

Thus, also the PV2 operators give a non-vanishing contribution to the three graviton bispectrum in the case of time-dependent couplings. Notice that in the limit where $A = 0$ we recover the result of the previous section and the parity-breaking signatures are not present anymore.

In Fig. 6.2 we plot the shape functions for the polarization configurations RRR and RRL. As in the previous case, we can compute the cosine of the shape functions. For $\ell_{\rm max} = 1000$, we

find

$$\cos\left(B^{\rm PV2}_{RRR}, B_S\right) \simeq \begin{cases} 0.999\,, & S = \text{equilateral} \\ 0.421\,, & S = \text{local} \\ 0.205\,, & S = \text{orthogonal} \end{cases} \tag{6.111}$$

for the RRR case, and

$$\cos\left(B^{\rm PV2}_{RRL}, B_S\right) \simeq \begin{cases} 0.700\,, & S = \text{equilateral} \\ 0.429\,, & S = \text{local} \\ 0.095\,, & S = \text{orthogonal} \end{cases} \tag{6.112}$$

for the RRL polarizations. The RRR shape peaks in the equilateral configuration (corresponding to $k_1 \simeq k_2 \simeq k_3$), as can also be seen directly from Fig. 6.2. The RRL shape receives instead a non-negligible contribution also in the squeezed configuration.

6.3.3 Comments on the consistency relation

An interesting feature of the bispectra just derived is that they potentially lead to the breaking of the single field slow-roll consistency relation for tensor bispectra [44, 352–354].[11] These relations allow to predict the strict squeezed limit behaviour of the primordial bispectra in terms of the primordial power spectra [44, 352–358, 360–363]. According to these and neglecting the small scale dependence of the power spectra, the squeezed limit expression of the 3-graviton bispectrum is predicted to be

$$\langle \gamma_{s_1}(\mathbf{k_1})\gamma_{s_2}(\mathbf{k_2})\gamma_{s_3}(\mathbf{k_3})\rangle\big|_{k_1\to 0} = (2\pi)^3\delta^{(3)}(\mathbf{k_1}+\mathbf{k_2}+\mathbf{k_3})\,\frac{3}{2}\,P_T^{s_1}(k_1)P_T^{s_2}(k_2)\,\epsilon_{ij}^{(s_1)}\,\frac{k_2^i k_2^j}{k_2^2}\,\delta_{s_2 s_3}\,. \tag{6.113}$$

In the literature we already find some examples of models breaking the tensor consistency relation, such as scenarios where we have either additional particle content [354, 364, 365], violation of the adiabatic evolution of tensor perturbations [366–368], or violation of spatial diffeomorphisms [369, 370].

In our case, we have found that both RRR (LLL) and RRL (LLR) tensor bispectra originated by the new PV1 parity-breaking operators give a nonzero contribution in the squeezed limit (see Fig. 6.1), which is proportional to the couplings f_1 and g_1. On the contrary, primordial tensor power spectra, being the same of general relativity due to the constraint (6.89), do not depend by either f_1 or g_1. The result is that this squeezed signal is not predicted by Eq. (6.113), leading to the violation of the 3-graviton consistency relation. A similar pattern is also shared by the RRL (LLR) bispectrum originated by the PV2 parity-breaking operators.[12] Notice that a similar pattern has been found previously in [325, 326] in the context of studies of primordial

[11] It has been argued (see, e.g., [355–358]) that in the context of single field slow-roll models of inflation primordial bispectra in the squeezed limit (when one of the k_i modes is much smaller than the others) correspond to a gauge artifact: in such a case one can perform a residual gauge transformation, passing from global coordinates to Conformal Fermi Coordinates (CFC), the latter being the coordinate frame of an observer that follows inflation in the background perturbed by this long-wavelength mode k_L. After performing this coordinate transformation, the squeezed limit bispectrum vanishes at leading order in the k_L/k_S ratio, with corrections that, by the virtue of the equivalence principle, must be quadratic in k_L/k_S. However, recently in [359] it has been shown that at least for the case of the scalar bispectrum this gauge artifact is valid only in the unphysical exactly infinite-wavelength limit where the long mode $k_L = 0$, while for physical modes $k_L \neq 0$ we lose this residual gauge freedom so that the consistency relations are indeed physical and measurable.

[12] The reason why the RRR (LLL) bispectrum originated by PV2 operators does not follow this behavior seems to be that, in the case where one correlates the same polarizations states, the squeezed contributions arise from the operators with more spatial derivatives, e.g. those in Eq. (6.14) which contain the Riemann or Ricci tensors

non-Gaussianities in Horava-Lifshitz gravity: in such a case we get squeezed parity-violating tensor bispectra that violate the tensor consistency relation, as they get a nonzero contribution in the exact squeezed limit that is not completely predicted by how primordial tensor power spectra in the right-hand side of (6.113) are modified by Horava-Lifshitz gravity.

We argue that this analogy is not accidental, but related to the fact that both the theories introduce parity-violating operators that violate also the Lorentz symmetry. In this regards, notice that this signature can be found only in particular late-time observables sensitive to the parity violation. In fact, for instance the modification introduced to the overall tensor bispectra (when summing over all the tensor polarizations) is equal to zero, due to the fact that the graviton bispectra under consideration have odd parity, i.e. they obey

$$\langle\gamma_R(\mathbf{k_1})\gamma_R(\mathbf{k_2})\gamma_R(\mathbf{k_3})\rangle = -\langle\gamma_L(-\mathbf{k_1})\gamma_L(-\mathbf{k_2})\gamma_L(-\mathbf{k_3})\rangle\,, \tag{6.114}$$

and analogously for RRL bispectrum versus LLR.

6.4 Imprints of parity violation during inflation on CMB bispectra

In this section we want to briefly discuss the observational prospects for detecting these parity-breaking signatures in the primordial bispectra through CMB experiments. In order to find out CMB bispectra sensitive to our parity-breaking signature, we follow the same reasoning as in [324, 330, 371, 372]. The starting point is the expression of the following spherical harmonic coefficients of the temperature ($X = T$) and E/B-mode polarization ($X = E/B$) anisotropies from the two circular polarization states of tensor perturbations [373, 374]

$$a_{\ell m}^{(t)X} = 4\pi(-i)^\ell \int \frac{d^3k}{(2\pi)^3} T^X_{\ell(t)}(k) \sum_{s=\pm2} \left(\frac{s}{2}\right)^x \gamma_s(\mathbf{k})\, {}_{-s}Y^*_{\ell m}(\hat{k})\,, \tag{6.115}$$

where for convenience of the subsequent notation we have defined $\gamma_{\pm2}(\mathbf{k}) \equiv \gamma_{R/L}(\mathbf{k})$. Here, ${}_sY_{\ell m}(\hat{k})$ denotes a spin-weighted spherical harmonic, $T^X_{\ell(t)}(k)$ is the tensor transfer function, and $x \equiv 0\,(1)$ for $X = T, E\,(B)$. The explicit expressions of the tensor transfer functions can be found in Ref. [373]. Using Eq. (6.115), the CMB bispectra sourced by the primordial graviton bispectra can be written as

$$\begin{aligned}\left\langle a^{(t)X_1}_{\ell_1 m_1} a^{(t)X_2}_{\ell_2 m_2} a^{(t)X_3}_{\ell_3 m_3}\right\rangle = \prod_{n=1}^{3} 4\pi(-i)^{\ell_n} \int \frac{d^3k_n}{(2\pi)^3} T^{X_n}_{\ell_n(t)}(k_n) \sum_{s_n=\pm2} \left(\frac{s_n}{2}\right)^{x_n} {}_{-s_n}Y^*_{\ell_n m_n}(\hat{k}_n) \\ \times \langle\gamma_{s_1}(\mathbf{k_1})\gamma_{s_2}(\mathbf{k_2})\gamma_{s_3}(\mathbf{k_3})\rangle\,.\end{aligned} \tag{6.116}$$

Using the following well-known property of the weighted spherical harmonics

$${}_{-s}Y_{\ell m}(-\hat{k}) = (-1)^\ell\, {}_sY_{\ell m}(\hat{k})\,, \tag{6.117}$$

in the PV1 case. However, in the PV2 model these operators do not give any contribution to tensor perturbations (see Appendix B), as they also contain the derivative of the lapse function, which vanishes since $N = 1$. Because of this, in the PV2 model we find a signal that peaks in the equilateral shape when the three polarizations are equal, but peaks in between the equilateral and squeezed limits for bispectra involving mixed polarization states. A similar feature has been found in the bispectra of PGWs in Horava-Lifshitz gravity for some of the operators, as noticed in [325]. We expect however that squeezed contributions may be present in the PV2 model in mixed correlators between scalar and tensor perturbations, since in this case also the operators with more spatial derivatives contribute to the final result.

we can rewrite Eq. (6.116) as

$$\left\langle a^{(t)X_1}_{\ell_1 m_1} a^{(t)X_2}_{\ell_2 m_2} a^{(t)X_3}_{\ell_3 m_3} \right\rangle = \prod_{n=1}^{3} 4\pi(-i)^{\ell_n} \int \frac{d^3\vec{k}_n}{(2\pi)^3} T^{X_n}_{\ell_n(t)}(k_n) \sum_{s_n=\pm 2} \left(\frac{s_n}{2}\right)^{x_n} {}_{-s_n}Y^*_{\ell_n m_n}(\hat{k}_n) \\ \times (-1)^{x_1+x_2+x_3+\ell_1+\ell_2+\ell_3} \langle \gamma_{-s_1}(-\mathbf{k_1}) \gamma_{-s_2}(-\mathbf{k_2}) \gamma_{-s_3}(-\mathbf{k_3}) \rangle \,. \tag{6.118}$$

Now, matching Eq. (6.116) with (6.118) under the parity-odd condition (6.114), we find that

$$\left\langle a^{(t)X_1}_{\ell_1 m_1} a^{(t)X_2}_{\ell_2 m_2} a^{(t)X_3}_{\ell_3 m_3} \right\rangle \left[1 + (-1)^{x_1+x_2+x_3+\ell_1+\ell_2+\ell_3}\right] = 0 \tag{6.119}$$

must always hold, independently from the kind of CMB modes that we are cross-correlating. Thus, a non-vanishing contribution to the CMB angular bispectrum is confined to the following multipole configurations

$$x_1 + x_2 + x_3 + \ell_1 + \ell_2 + \ell_3 = \text{odd} \,. \tag{6.120}$$

It is worth stressing that these combinations are not realized by the usual parity-conserving theories like Einstein gravity, for which the sum defined in (6.120) has to be even. For this reason they can be robust indicators of parity-breaking models with odd tensor bispectra if they are detected.

According to the latest forecasts and previsions (see, e.g., [350, 351, 372, 375]), forthcoming CMB experiments focusing on the polarization field (like, e.g., the LiteBIRD mission) will be able to probe order 1 amplitudes of tensor squeezed non-Gaussianities through the measurement of the CMB angular bispectra involving the B-modes. This would justify a more detailed analysis of the detection prospects of these models in CMB angular bispectra in view of next experiments focusing on the search for the B-mode polarization field of the CMB.

Part IV

Overview and conclusions

Over the past decades, our understanding of the Universe has been revolutionized. In the era of precision cosmology, a wealth of cosmological observations has allowed to establish the concordance ΛCDM model, which describes the evolution of our Universe from its early stages until today in terms of just six parameters. At the same time, the Standard Model (SM) of particle physics, which describes our Universe at subnuclear level, has been tested with impressive precision in a number of laboratory and collider experiments. Nevertheless, there are still plenty of open issues that are yet to be understood, such as the nature of dark matter (DM) and dark energy or the physics underlying inflation. Moreover, the stunning level of accuracy that cosmological observations have reached allows us to test with increasing precision possible departures from the standard models of cosmology and particle physics. This is the topic of this Thesis, where we have used the latest measurements of the Cosmic Microwave Background (CMB) and the Large-Scale Structure (LSS) of the Universe to constrain fundamental physics scenarios that go beyond the two aforementioned standard models.

First of all, in chapter 1 we have reviewed the foundations of the standard cosmological model, its shortcomings and we have introduced the inflationary paradigm as a possible solution to them. Inflation also provides a compelling mechanism to produce the primordial perturbations in the Universe.

Then, in chapter 2 we have analyzed the possibility that the DM is composed of macroscopic-size objects, dubbed Macro Dark Matter (MDM) [16]. By keeping a phenomenological approach, we have focused on a particular process that might be associated to MDM, namely the capture of baryons of the cosmological plasma by Macros. This results in the injection of high-energy photons in the baryon-photon plasma. We have considered two broad classes of MDM: in the first one, Macros are composed of ordinary matter and the amount of energy released is set by the binding energy I of Macros, which we have treated as a free parameter; in the second scenario, Macros are composed of antibaryons and proton capture results in proton-antiproton annihilations. We have derived constraints on the Macro parameter space from three cosmological processes: the change in the baryon density between the end of the Big Bang Nucleosynthesis (BBN) and the CMB decoupling, the production of spectral distortions in the CMB and the kinetic coupling between charged MDM and baryons at the time of recombination. In the case of neutral Macros we have found that the tightest constraints are set by the baryon density condition in most of the parameter space. For Macros composed of ordinary matter and with binding energy I, this has led to the following bound on the reduced cross-section: $\sigma_X/M_X \lesssim 6.8 \times 10^{-7}\,(I/\mathrm{MeV})^{-1.56}\ \mathrm{cm}^2\,\mathrm{g}^{-1}$. Charged Macros with surface potential V_X, instead, are mainly constrained by the tight coupling with baryons, resulting in $\sigma_X/M_X \lesssim 2 \times 10^{-11}\,(|V_X|/\mathrm{MeV})^{-2}\,\mathrm{cm}^2\,\mathrm{g}^{-1}$. Finally, we have shown that future CMB spectral distortions experiments, like PIXIE and SuperPIXIE, would have the sensitivity to probe larger regions of the parameter space.

Then, we have focused on axions. In chapter 3 we have introduced the QCD axion as a possible solution to the strong CP problem of QCD. We have discussed the main QCD axion models, namely the KSVZ and the DFSZ axions, and we have seen how the parameter space can be expanded to consider more general axion-like particles (hereafter simply axions).

In chapter 4 we have considered thermal axions in the mass range $10^{-4} \leq m_a \leq 100$ eV. These are produced from scattering processes between particles belonging to the primordial cosmological plasma. Depending on their mass, thermally-produced axions play a different cosmological role and can behave either as dark radiation or as a hot, warm or cold DM component. Our analysis naturally accounts for all these possibilities. Under the assumption that axions are predominantly produced from either axion-photon or axion-gluon processes, we have constrained the axion couplings to photons and gluons using data of the CMB temperature and polarization anisotropies and baryon acoustic oscillations (BAO). The bounds on the axion-photon coupling are stronger than those obtained from the CAST collaboration for masses $m_a \gtrsim 3$ eV. The bounds on the axion-gluon coupling are only overcome by those coming from SN1987A energy loss considerations. Nevertheless, the cosmological limits derived in our analysis are independent and complementary to the astrophysical ones. For the KSVZ (QCD) axion, our results translate into a lower limit on the axion decay constant given by $f_a \gtrsim 2 \times 10^7$ GeV. This implies an upper limit on the mass of the KSVZ axion given by $m_a \lesssim 0.3$ eV.

Future CMB surveys will be able to probe the presence of thermal relics with improved sensitivity. Considering the forecast sensitivity of CMB Stage-4 (CMB-S4) to extra relativistic species, the bound on the axion-photon coupling will be improved by roughly a factor 3 in the case of light axions behaving as dark radiation ($m_a \lesssim 10^{-2}$ eV). The bound on the axion-gluon coupling would instead improve our current estimates by about one order of magnitude. As regards heavier axions behaving as warm or cold DM, including the measurements of small-scale CMB anisotropies calls for a more careful treatment of non-linearities in the CMB lensing. This is still an open issue which must be taken into account when dealing with data from both ACT and future surveys like CMB-S4 and SO.

In chapter 5 we have derived new bounds on Lorentz-violating (LV) electrodynamics exploiting the most recent measurements of the CMB polarization. In the framework of the minimal Standard Model Extension (SME) [17–19], we have considered the effects generated by renormalizable operators of mass dimension $d \leq 4$. These consist of a CPT-odd ($d = 3$) and a CPT-even ($d = 4$) operator. Such operators are responsible, respectively, for cosmic birefringence, i.e. the rotation of the linear polarization plane of CMB photons, and for the generation of circular polarization. Our analysis relies on the formalism developed in Ref. [268]. We have provided the first concrete application of this formalism, which allows to describe the effects of non-standard propagation of radiation in terms of an effective susceptibility tensor and then derive the associated modifications to the CMB spectra. In our specific case, the effects of the minimal LV operators on the CMB spectra are encoded in four phenomenological parameters, defined in Eqs. (5.66)-(5.69). The parameters characterizing the CPT-odd term are $\beta^2_{AF,T}$ and $\beta^2_{AF,S}$ and are related to the time and space components of the vector k_{AF} in the action in Eq. (5.1). The CPT-even term is parameterized by $\beta^2_{F,E}$ and $\beta^2_{F,B}$, which depend on the components of the tensor k_F. We have shown that, given the sensitivity of current V-modes experiments, we are able to constrain only the combination of the CPT-even coefficients defined in Eq. (5.86), which we have labeled $k_{F,E+B}$. This parameter has been constrained to $k_{F,E+B} < 2.31 \times 10^{-31}$ at 95% CL. This improves the previous bound derived using CMB data by roughly one order of magnitude. This is only overcome by the bound coming from optical polarimetry of extragalactic sources. The limits we have obtained on the CPT-odd coefficients, i.e. $|k^{(3)}_{(V)00}| < 1.54 \times 10^{-44}$ GeV and $|\mathbf{k_{AF}}| < 0.74 \times 10^{-44}$ GeV at 95% CL, are respectively one and two orders of magnitude stronger than previous CMB-based limits. These are the strongest constraints to date, even looking beyond CMB analyses.

The method adopted in our analysis paves the way for many possible extensions and generalizations of our work. On one hand, a detailed forecast analysis will shed light on the sensitivity of future CMB surveys to Lorentz violations. Indeed, CMB polarization is the main target of next-generation CMB surveys. Likely, future experiments which will improve the current measurements of V-modes will allow to disentangle the effects of the two CPT-even parameters, potentially setting individual bounds on these two coefficients. At the same time, our study could be extended to consider possible generalizations of the theoretical model, both in the context of current and future CMB data. As an example, it would be interesting to analyze the effects of the non-renormalizable ($d > 4$) operators of the SME action on the CMB. These might carry more direct information about the high-energy physics underlying the effective Lagrangian of the SME.

Finally, in chapter 6 we have studied inflation within chiral scalar-tensor theories of gravity, that extend Chern-Simons gravity by including parity-violating operators containing first and second derivatives of the non-minimally coupled inflaton field [24]. The parity violation induces a different behaviour in the propagation of the two circular polarization states of primordial gravitational waves (PGWs). At linear level, this effect is quantified by the relative difference between the left-handed and right-handed tensor power spectra, the so-called chirality of PGWs. We have shown that the amount of chirality in the power spectrum of PGWs is suppressed and it is degenerate with the prediction of other parity-violating theories of gravity. Motivated by these considerations, we have made a detailed analysis of the parity-breaking signatures on the bispectrum of primordial tensor modes. We have shown that the new contributions to the graviton bispectra are vanishing if the couplings in the new operators are constant in a pure de Sitter phase. An explanation based on symmetry arguments has been proposed in [332]. If instead the coupling functions are time-dependent during inflation, the tensor bispectra acquire non-vanishing contributions from the parity-breaking operators even in the exact de Sitter limit, with maximal signal in the squeezed and equilateral configurations. We have discussed the impact of these parity-violating signatures on the CMB bispectra and the prospects for detecting them with forthcoming CMB experiments. Indeed, it is widely known that primordial non-Gaussianities (PNG) are a powerful observable, given their direct connection to the high-energy physics underlying the inflationary dynamics. The increased sensitivity of future CMB experiments to PNG might open a unique window to probe fundamental physics at energies far beyond the ones accessible with both laboratory experiments and astrophysical observations.

With the huge amount of available data, cosmological observations have marked a revolution in our understanding of the Universe. Even though many questions are still left without an answer, the increasing precision of future cosmological surveys will give us an unprecedented opportunity to shed light on some of these open issues, bringing to important advances in our comprehension of the fundamental laws of Nature.

Appendix A

Spin-weighted functions and spin operators

Here, we briefly review the definitions and the main properties of the spin-raising and spin-lowering operators. For more details we refer to reader to [376]. Given a spin-s function ${}_sf(\theta,\phi)$ defined on the 2D sphere, the spin-raising ($\eth$) and spin-lowering ($\bar{\eth}$) operators act on ${}_sf(\theta,\phi)$ as

$$\eth\, {}_sf(\theta,\phi) = -(\sin\theta)^s \left[\frac{\partial}{\partial\theta} + i\csc\theta\frac{\partial}{\partial\phi}\right](\sin\theta)^{-s}\, {}_sf(\theta,\phi)\,, \tag{A.1}$$

$$\bar{\eth}\, {}_sf(\theta,\phi) = -(\sin\theta)^{-s} \left[\frac{\partial}{\partial\theta} - i\csc\theta\frac{\partial}{\partial\phi}\right](\sin\theta)^{s}\, {}_sf(\theta,\phi)\,. \tag{A.2}$$

The new functions $\eth\, {}_sf(\theta,\phi)$ and $\bar{\eth}\, {}_sf(\theta,\phi)$ have spin $s+1$ and $s-1$, respectively. In the context of CMB polarization, we usually have to deal with spin-2 quantities, ${}_{\pm2}f(\theta,\phi)$. Since spin-0 quantities are easier to be handled, we can act twice on ${}_{\pm2}f$ with the spin-raising and lowering operators, so that we get

$$\eth^{\,2}\, {}_{-2}f(\mu,\phi) = \left(-\partial_\mu - \frac{m}{1-\mu^2}\right)^2 \left[(1-\mu^2)\, {}_{-2}f(\mu,\phi)\right]\,, \tag{A.3}$$

$$\bar{\eth}^{\,2}\, {}_{+2}f(\mu,\phi) = \left(-\partial_\mu + \frac{m}{1-\mu^2}\right)^2 \left[(1-\mu^2)\, {}_{2}f(\mu,\phi)\right]\,, \tag{A.4}$$

with $\mu \equiv \cos\theta$ and m is defined by the condition $\partial_\phi\, {}_sf(\mu,\phi) = im\, {}_sf(\mu,\phi)$.

As a scalar field can be expanded on the sphere in a basis of spherical harmonics $Y_{\ell m}(\theta,\phi)$, spin-weighted functions with spin $s \neq 0$ can be expanded on the sphere in terms of the spin-s spherical harmonics, ${}_sY_{\ell m}(\theta,\phi)$. These satisfy the following orthogonality and completeness relations:

$$\int_0^{2\pi} d\phi \int_{-1}^{1} d\cos\theta\, {}_sY^*_{\ell' m'}(\theta,\phi)\, {}_sY_{\ell m}(\theta,\phi) = \delta_{\ell\ell'}\delta_{mm'}\,, \tag{A.5}$$

$$\sum_{\ell m} {}_sY^*_{\ell m}(\theta,\phi)\, {}_sY_{\ell m}(\theta',\phi') = \delta(\phi-\phi')\delta(\cos\theta - \cos\theta')\,. \tag{A.6}$$

Using Eqs. (A.1)-(A.2), we can express the spin-weighted spherical harmonics ${}_sY_{\ell m}(\theta,\phi)$ in terms of the common spin-0 spherical harmonics $Y_{\ell m}(\theta,\phi)$ as

$${}_sY_{\ell m}(\theta,\phi) = \left[\frac{(\ell+s)!}{(\ell-s)!}\right]^{-1/2} \eth^{\,s} Y_{\ell m}(\theta,\phi) \qquad (0 \leq s \leq \ell)\,, \tag{A.7}$$

$$ {}_sY_{\ell m}(\theta,\phi) = \left[\frac{(\ell+s)!}{(\ell-s)!}\right]^{1/2} (-1)^s \bar{\partial}^{\,-s} Y_{\ell m}(\theta,\phi) \quad (-\ell \leq s \leq) \,. \tag{A.8} $$

Finally, it is possible that spin-weighted spherical harmonics satisfy the following relations:

$$ {}_sY^*_{\ell m}(\theta,\phi) = (-1)^s \, {}_{-s}Y_{\ell -m}(\theta,\phi) \,, \tag{A.9} $$

$$ \eth \, {}_sY_{\ell m}(\theta,\phi) = \left[(\ell-s)(\ell+s+1)\right]^{1/2} {}_{s+1}Y_{\ell m}(\theta,\phi) \,, \tag{A.10} $$

$$ \bar{\eth} \, {}_sY_{\ell m}(\theta,\phi) = -\left[(\ell+s)(\ell-s+1)\right]^{1/2} {}_{s-1}Y_{\ell m}(\theta,\phi) \,, \tag{A.11} $$

$$ \bar{\eth}\eth \, {}_sY^*_{\ell m}(\theta,\phi) = -(\ell-s)(\ell+s+1) {}_sY^*_{\ell m}(\theta,\phi) \,. \tag{A.12} $$

Appendix B

Interaction Hamiltonians of chiral scalar-tensor theories at cubic order in tensor perturbations

B.1 PV1 interaction Hamiltonian

By expanding γ_{ij} up to third order, the operators present in (6.14) at cubic order in tensor perturbations take the following forms

$$\epsilon^{ijl} K K_{mi} D_l K_j{}^m = \frac{3}{4}\dot{a}a\,\epsilon^{ijl}\left[(\partial_l\dot{\gamma}_j{}^m)\dot{\gamma}_{mr}\gamma^r{}_i + (\partial_r\gamma_l{}^m)\dot{\gamma}_j{}^r\dot{\gamma}_{mi}\right], \tag{B.1}$$

$$\begin{aligned}\epsilon^{ijl}\,{}^{(3)}R_{mi} D_l K_j{}^m = \frac{1}{4}\epsilon^{ijl}\Bigg[&-\frac{1}{2}(\partial_r\partial^r\gamma_{mi})(\partial_l\gamma_{jk})\dot{\gamma}^{km} - \frac{1}{2}(\partial_r\partial^r\gamma_{mi})\gamma_{jk}(\partial_l\dot{\gamma}^{km})\\ &-\frac{1}{2}(\partial_r\partial^r\gamma_{mi})(\partial_k\gamma_l{}^m)\dot{\gamma}_j{}^k + \frac{1}{2}(\partial_r\partial^r\gamma_{mi})(\partial^m\gamma_{lk})\dot{\gamma}_j{}^k\\ &+(\partial_l\dot{\gamma}_j{}^m)\gamma^{kr}(\partial_k\partial_r\gamma_{mi}) + (\partial_l\dot{\gamma}_j{}^m)(\partial_m\gamma^{kr})(\partial_k\gamma_{ir})\\ &-(\partial_l\dot{\gamma}_j{}^m)\gamma^{kr}(\partial_k\partial_i\gamma_{mr}) - \frac{1}{2}(\partial_l\dot{\gamma}_j{}^m)\gamma^r{}_i(\partial_k\partial^k\gamma_{mr})\\ &-\frac{1}{2}(\partial_l\dot{\gamma}_j{}^m)(\partial_i\gamma_r{}^k)(\partial_m\gamma_k{}^r) - (\partial_l\dot{\gamma}_j{}^m)(\partial^k\gamma_{ri})(\partial^r\gamma_{km})\Bigg],\end{aligned} \tag{B.2}$$

$$\epsilon^{ijl} K_{mi} K^{mn} D_l K_{jn} = \epsilon^{ijl}\left[-\frac{1}{2}\dot{a}a\,(\partial_r\gamma_l{}^m)\dot{\gamma}_{jm}\dot{\gamma}_i{}^r + \frac{1}{2}\dot{a}a(\partial_l\dot{\gamma}_{jr})\gamma_{mi}\dot{\gamma}^{mr} + \frac{1}{8}a^2(\partial_l\dot{\gamma}_{jr})\dot{\gamma}_{mi}\dot{\gamma}^{mr}\right], \tag{B.3}$$

$$\epsilon^{ijl} K_{mi} K_j{}^n D_n K_l{}^m = \frac{1}{4}\epsilon^{ijl}\left[\dot{a}a\,(\partial_j\dot{\gamma}_l{}^m)\dot{\gamma}_{mr}\gamma^r{}_i + \dot{a}a\,(\partial_r\gamma_j{}^m)\dot{\gamma}_l{}^r\dot{\gamma}_{mi} + \frac{1}{2}a^2(\partial_r\dot{\gamma}_l{}^m)\dot{\gamma}_j{}^r\dot{\gamma}_{mi}\right], \tag{B.4}$$

$$\begin{aligned}\epsilon^{ijl}\,{}^{(3)}R_{jlm}{}^n D_n K_i{}^m = \frac{1}{4}\epsilon^{ijl}\Bigg[&-\gamma_{lr}(\partial_m\partial_j\gamma^{rn})(\partial_n\dot{\gamma}_i{}^m) + \gamma_{lr}(\partial^n\partial_j\gamma^r{}_m)(\partial_n\dot{\gamma}_i{}^m)\\ &-2\gamma^{pn}(\partial_m\partial_l\gamma_{pj})(\partial_n\dot{\gamma}_i{}^m) - 2\gamma^{pn}(\partial_p\partial_j\gamma_{lm})(\partial_n\dot{\gamma}_i{}^m)\\ &+(\partial_m\gamma_j{}^r)(\partial_r\gamma_l{}^n)(\partial_n\dot{\gamma}_i{}^m) - (\partial_m\gamma_j{}^r)(\partial^n\gamma_{lr})(\partial_n\dot{\gamma}_i{}^m)\\ &-(\partial^n\gamma_j{}^r)(\partial_r\gamma_{lm})(\partial_n\dot{\gamma}_i{}^m) - (\partial^n\gamma_{mr})(\partial_l\gamma^r{}_j)(\partial_n\dot{\gamma}_i{}^m)\\ &+(\partial_r\gamma_{mj})(\partial_l\gamma^{nr})(\partial_n\dot{\gamma}_i{}^m) - (\partial_r\gamma_{mj})(\partial^r\gamma_l{}^n)(\partial_n\dot{\gamma}_i{}^m)\\ &-(\partial_j\gamma_{rm})(\partial_l\gamma^{nr})(\partial_n\dot{\gamma}_i{}^m) + (\partial_j\gamma_{rm})(\partial^r\gamma_l{}^n)(\partial_n\dot{\gamma}_i{}^m)\\ &+2(\partial_m\partial_l\gamma^n{}_j)\dot{\gamma}_{ik}(\partial_n\gamma^{km}) + (\partial_m\partial_l\gamma^n{}_j)\gamma_{ik}(\partial_n\dot{\gamma}^{km})\\ &+(\partial^n\partial_j\gamma_{lm})\gamma_{ik}(\partial_n\dot{\gamma}^{km}) - (\partial_m\partial_l\gamma^n{}_j)(\partial_i\gamma_n{}^k)\dot{\gamma}_k{}^m\end{aligned}$$

$$
\begin{aligned}
&- (\partial^n\partial_j\gamma_{lm})(\partial_i\gamma_n{}^k)\dot{\gamma}_k{}^m + (\partial_m\partial_l\gamma^n{}_j)(\partial^k\gamma_{ni})\dot{\gamma}_k{}^m \\
&+ (\partial^n\partial_j\gamma_{lm})(\partial^k\gamma_{ni})\dot{\gamma}_k{}^m - (\partial_m\partial_l\gamma^n{}_j)(\partial^m\gamma_{nk})\dot{\gamma}_i{}^k\Big].
\end{aligned} \tag{B.5}
$$

From these, we can then compute the interaction Hamiltonian. In Fourier space, this reads

$$
\begin{aligned}
H^{\rm PV1}_{\gamma\gamma\gamma}(\tau) = \sum_{s_1,s_2,s_3}\int d^3k\int d^3p\int d^3q\ \frac{\delta^{(3)}(\mathbf{k}+\mathbf{p}+\mathbf{q})}{(2\pi)^6}2\Big\{&\lambda_{s_1}(f_1+g_1)aHk\gamma'^{s_1}_{\mathbf{k}}\gamma'^{s_2}_{\mathbf{p}}\gamma^{s_3}_{\mathbf{q}} \\
&\times\epsilon^{mi}_{(s_1)}(\mathbf{k})\epsilon^{mr}_{(s_2)}(\mathbf{p})\epsilon^{r}_{(s_3)i}(\mathbf{q}) + \lambda_{s_2}\frac{(f_1+g_1)}{2}k^2p\gamma'^{s_1}_{\mathbf{k}}\gamma^{s_2}_{\mathbf{p}}\gamma^{s_3}_{\mathbf{q}}\epsilon^{(s_1)}_{mi}(\mathbf{k})\epsilon^{(s_2)i}_{k}(\mathbf{p})\epsilon^{km}_{(s_3)}(\mathbf{q}) \\
&+\lambda_{s_3}(f_1+g_1)qk_kq_r\gamma'^{s_1}_{\mathbf{k}}\gamma^{s_2}_{\mathbf{p}}\gamma^{s_3}_{\mathbf{q}}\epsilon^{(s_1)m}_{j}(\mathbf{k})\epsilon^{kr}_{(s_2)}(\mathbf{p})\epsilon^{(s_3)j}_{m}(\mathbf{q}) - \lambda_{s_1}\left(f_1+\frac{g_1}{2}\right)kp_mq_k \\
&\times\gamma'^{s_1}_{\mathbf{k}}\gamma^{s_2}_{\mathbf{p}}\gamma^{s_3}_{\mathbf{q}}\epsilon^{mi}_{(s_1)}(\mathbf{k})\epsilon^{kr}_{(s_2)}(\mathbf{p})\epsilon^{s_3}_{ir}(\mathbf{q}) + \lambda_{s_1}\frac{f_1}{2}kq^2\gamma'^{s_1}_{\mathbf{k}}\gamma^{s_2}_{\mathbf{p}}\gamma^{s_3}_{\mathbf{q}}\epsilon^{mi}_{(s_1)}(\mathbf{k})\epsilon^{r}_{(s_2)i}(\mathbf{p})\epsilon^{(s_3)}_{mr}(\mathbf{q}) \\
&+\lambda_{s_1}\frac{f_1}{2}kp_iq_m\gamma'^{s_1}_{\mathbf{k}}\gamma^{s_2}_{\mathbf{p}}\gamma^{s_3}_{\mathbf{q}}\epsilon^{mi}_{(s_1)}(\mathbf{k})\epsilon^{(s_2)k}_{r}(\mathbf{p})\epsilon^{(s_3)r}_{k}(\mathbf{q}) + \lambda_{s_2}(f_1+g_1)pp^kq^r\gamma'^{s_1}_{\mathbf{k}}\gamma^{s_2}_{\mathbf{p}}\gamma^{s_3}_{\mathbf{q}} \\
&\times\epsilon^{mi}_{(s_1)}(\mathbf{k})\epsilon^{(s_2)j}_{r}(\mathbf{p})\epsilon^{(s_3)}_{km}(\mathbf{q}) - \lambda_{s_1}\frac{f_1}{2}k\gamma'^{s_1}_{\mathbf{k}}\gamma'^{s_2}_{\mathbf{p}}\gamma'^{s_3}_{\mathbf{q}}\epsilon^{(s_1)i}_{r}(\mathbf{k})\epsilon^{(s_2)}_{mi}(\mathbf{p})\epsilon^{mr}_{(s_3)}(\mathbf{q}) \\
&+\lambda_{s_1}\frac{g_1}{2}kk_np_m\gamma^{s_1}_{\mathbf{k}}\gamma^{s_2}_{\mathbf{p}}\gamma'^{s_3}_{\mathbf{q}}\epsilon^{(s_1)i}_{r}(\mathbf{k})\epsilon^{rn}_{(s_2)}(\mathbf{p})\epsilon^{(s_3)m}_{i}(\mathbf{q}) + \lambda_{s_2}\frac{g_1}{2}k^2p\gamma^{s_1}_{\mathbf{k}}\gamma^{s_2}_{\mathbf{p}}\gamma'^{s_3}_{\mathbf{q}} \\
&\times\epsilon^{(s_1)}_{mr}(\mathbf{k})\epsilon^{ri}_{(s_2)}(\mathbf{p})\epsilon^{(s_3)m}_{i}(\mathbf{q}) + \lambda_{s_1}\frac{g_1}{2}kk_mq_n\gamma^{s_1}_{\mathbf{k}}\gamma^{s_2}_{\mathbf{p}}\gamma'^{s_3}_{\mathbf{q}}\epsilon^{ni}_{(s_1)}(\mathbf{k})\epsilon^{(s_2)}_{ik}(\mathbf{p})\epsilon^{km}_{(s_3)}(\mathbf{q}) \\
&+\lambda_{s_1}\frac{g_1}{2}k(\mathbf{k}\cdot\mathbf{p})\gamma^{s_1}_{\mathbf{k}}\gamma^{s_2}_{\mathbf{p}}\gamma'^{s_3}_{\mathbf{q}}\epsilon^{(s_1)i}_{m}(\mathbf{k})\epsilon^{(s_2)}_{ik}(\mathbf{p})\epsilon^{km}_{(s_3)})(\mathbf{q}) - \lambda_{s_1}\frac{g_1}{2}kk_mp_i\gamma^{s_1}_{\mathbf{k}}\gamma^{s_2}_{\mathbf{p}}\gamma'^{s_3}_{\mathbf{q}} \\
&\times\epsilon^{ni}_{(s_1)}(\mathbf{k})\epsilon^{(s_2)k}_{n}(\mathbf{p})\epsilon^{(s_3)m}_{k}(\mathbf{q}) + \lambda_{s_1}\frac{g_1}{2}kk^np_i\gamma^{s_1}_{\mathbf{k}}\gamma^{s_2}_{\mathbf{p}}\gamma'^{s_3}_{\mathbf{q}}\epsilon^{(s_1)i}_{m}(\mathbf{k})\epsilon^{(s_2)k}_{n}(\mathbf{p})\epsilon^{(s_3)m}_{k}(\mathbf{q}) \\
&+\lambda_{s_1}\frac{g_1}{2}kk_mp^k\gamma^{s_1}_{\mathbf{k}}\gamma^{s_2}_{\mathbf{p}}\gamma'^{s_3}_{\mathbf{q}}\epsilon^{ni}_{(s_1)}(\mathbf{k})\epsilon^{(s_2)}_{ni}(\mathbf{p})\epsilon^{(s_3)m}_{k}(\mathbf{q}) - \lambda_{s_1}\frac{g_1}{2}kk^np^k\gamma^{s_1}_{\mathbf{k}}\gamma^{s_2}_{\mathbf{p}}\gamma'^{s_3}_{\mathbf{q}} \\
&\times\epsilon^{(s_1)i}_{m}(\mathbf{k})\epsilon^{(s_2)}_{ni}(\mathbf{p})\epsilon^{(s_3)m}_{k}(\mathbf{q}) + \epsilon^{ijl}\Big[-i(f_1+g_1)aHk_r\gamma^{s_1}_{\mathbf{k}}\gamma'^{s_2}_{\mathbf{p}}\gamma'^{s_3}_{\mathbf{q}} \\
&\times\epsilon^{(s_1)m}_{l}(\mathbf{k})\epsilon^{(s_2)r}_{j}(\mathbf{p})\epsilon^{(s_3)}_{mi}(\mathbf{q}) - i\frac{(f_1+g_1)}{2}k^2q_l\gamma^{s_1}_{\mathbf{k}}\gamma^{s_2}_{\mathbf{p}}\gamma'^{s_3}_{\mathbf{q}}\epsilon^{(s_1)}_{mi}(\mathbf{k})\epsilon^{(s_2)}_{jk}(\mathbf{p})\epsilon^{km}_{(s_3)}(\mathbf{q}) \\
&-i\frac{(f_1+g_1)}{2}k^2p_k\gamma^{s_1}_{\mathbf{k}}\gamma^{s_2}_{\mathbf{p}}\gamma'^{s_3}_{\mathbf{q}}\epsilon^{(s_1)}_{mi}(\mathbf{k})\epsilon^{(s_2)m}_{l}(\mathbf{p})\epsilon^{(s_3)k}_{j}(\mathbf{q}) + i\frac{(f_1+g_1)}{2}k^2p^m\gamma^{s_1}_{\mathbf{k}}\gamma^{s_2}_{\mathbf{p}}\gamma'^{s_3}_{\mathbf{q}} \\
&\times\epsilon^{(s_1)}_{mi}(\mathbf{k})\epsilon^{(s_2)}_{lk}(\mathbf{p})\epsilon^{(s_3)k}_{j}(\mathbf{q}) + i\left(f_1+\frac{g_1}{2}\right)k_kp_lq_r\gamma'^{s_1}_{\mathbf{k}}\gamma^{s_2}_{\mathbf{p}}\gamma^{s_3}_{\mathbf{q}}\epsilon^{(s_1)m}_{j}(\mathbf{k})\epsilon^{kr}_{(s_2)}(\mathbf{p})\epsilon^{(s_3)}_{mi}(\mathbf{q}) \\
&-i\left(f_1+\frac{g_1}{2}\right)k_np_lq_i\gamma'^{s_1}_{\mathbf{k}}\gamma^{s_2}_{\mathbf{p}}\gamma^{s_3}_{\mathbf{q}}\epsilon^{(s_1)m}_{j}(\mathbf{k})\epsilon^{nr}_{(s_2)}(\mathbf{p})\epsilon^{(s_3)}_{mr}(\mathbf{q}) + i\left(f_1+\frac{g_1}{2}\right)p^kq_lq^r. \\
&\times\gamma'^{s_1}_{\mathbf{k}}\gamma^{s_2}_{\mathbf{p}}\gamma^{s_3}_{\mathbf{q}}\epsilon^{(s_1)m}_{j}(\mathbf{k})\epsilon^{(s_2)}_{ri}(\mathbf{p})\epsilon^{(s_3)}_{km}(\mathbf{q}) + i\frac{g_1}{2}k_r\gamma'^{s_1}_{\mathbf{k}}\gamma'^{s_2}_{\mathbf{p}}\gamma'^{s_3}_{\mathbf{q}}\epsilon^{(s_1)m}_{l}(\mathbf{k})\epsilon^{(s_2)r}_{j}(\mathbf{p})\epsilon^{(s_3)}_{mi}(\mathbf{q}) \\
&-i\frac{g_1}{2}(\mathbf{p}\cdot\mathbf{q})p_j\gamma^{s_1}_{\mathbf{k}}\gamma^{s_2}_{\mathbf{p}}\gamma'^{s_3}_{\mathbf{q}}\epsilon^{(s_1)}_{lr}(\mathbf{k})\epsilon^{r}_{(s_2)m}(\mathbf{p})\epsilon^{(s_3)m}_{i}(\mathbf{q}) - i\frac{g_1}{2}k_mp_rq_n\gamma^{s_1}_{\mathbf{k}}\gamma^{s_2}_{\mathbf{p}}\gamma'^{s_3}_{\mathbf{q}} \\
&\times\epsilon^{(s_1)r}_{j}(\mathbf{k})\epsilon^{(s_2)n}_{l}(\mathbf{p})\epsilon^{(s_3)m}_{i}(\mathbf{q}) - i\frac{g_1}{2}(\mathbf{k}\cdot\mathbf{p})k_m\gamma^{s_1}_{\mathbf{k}}\gamma^{s_2}_{\mathbf{p}}\gamma'^{s_3}_{\mathbf{q}}\epsilon^{(s_1)r}_{j}(\mathbf{k})\epsilon^{(s_2)}_{lr}(\mathbf{p})\epsilon^{(s_3)m}_{i}(\mathbf{q})\Big]\Big\},
\end{aligned} \tag{B.6}
$$

where the prime denotes a derivative with respect to conformal time.

B.2 PV2 interaction Hamiltonian

At cubic order in tensor perturbations, the operators in the Lagrangian (6.15) read

$$
\epsilon^{ijl}K_{mi}D_lK_j{}^m = \frac{1}{4}a^2\,\epsilon^{ijl}\left[(\partial_l\dot{\gamma}_j{}^m)\dot{\gamma}_{mr}\gamma^r{}_i + (\partial_r\gamma_l{}^m)\dot{\gamma}_j{}^r\dot{\gamma}_{mi}\right], \tag{B.7}
$$

$$\epsilon^{ijl}K_{mi}K_j^{\ n}D_nK_l^{\ m}=\frac{1}{4}\epsilon^{ijl}\left[\dot{a}a\left(\partial_j\dot{\gamma}_l^{\ m}\right)\dot{\gamma}_{mr}\gamma^r_{\ i}+\dot{a}a\left(\partial_r\gamma_j^{\ m}\right)\dot{\gamma}_l^{\ r}\dot{\gamma}_{mi}+\frac{1}{2}a^2(\partial_r\dot{\gamma}_l^{\ m})\dot{\gamma}_j^{\ r}\dot{\gamma}_{mi}\right]. \tag{B.8}$$

The interaction Hamiltonian in Fourier space is thus given by

$$\begin{aligned}H^{\rm PV2}_{\gamma\gamma\gamma}=\sum_{s_1,s_2,s_3}\int d^3k\int d^3p\int d^3q\ \frac{\delta^{(3)}(\mathbf{k}+\mathbf{p}+\mathbf{q})}{(2\pi)^6}\left\{\frac{1}{2}\left[\tilde{b}_1M_{Pl}-bH\right]\left[\lambda_{s_1}ak\gamma'^{s_1}_{\mathbf{k}}\gamma'^{s_2}_{\mathbf{p}}\gamma^{s_3}_{\mathbf{q}}\right.\right.\\ \left.\times\epsilon^{mi}_{(s_1)}(\mathbf{k})\epsilon^{(s_2)}_{mr}(\mathbf{p})\epsilon^r_{(s_3)i}(\mathbf{q})+i\epsilon^{ijl}ak_r\gamma^{s_1}_{\mathbf{k}}\gamma'^{s_2}_{\mathbf{p}}\gamma'^{s_3}_{\mathbf{q}}\epsilon_l^{(s_1)m}(\mathbf{k})\epsilon_j^{(s_2)r}(\mathbf{p})\epsilon^{(s_3)}_{mi}(\mathbf{q})\right]\\ \left.+i\frac{b}{4}\epsilon^{ijl}k_r\gamma'^{s_1}_{\mathbf{k}}\gamma'^{s_2}_{\mathbf{p}}\gamma'^{s_3}_{\mathbf{q}}\epsilon_l^{(s_1)m}(\mathbf{k})\epsilon_j^{(s_2)r}(\mathbf{p})\epsilon^{(s_3)}_{mi}(\mathbf{q})\right\}.\end{aligned} \tag{B.9}$$

Appendix C

Explicit expressions of $C_i^{s_1 s_2 s_3}(\mathbf{k_1}, \mathbf{k_2}, \mathbf{k_3})$ and $T_i^{s_1 s_2 s_3}(\mathbf{k_1}, \mathbf{k_2}, \mathbf{k_3})$

We report here the complete expressions of the contributions that appear in the PV1 bispectrum (6.70):

$$C_1^{s_1 s_2 s_3}(\mathbf{k_1}, \mathbf{k_2}, \mathbf{k_3}) = C_2^{s_1 s_2 s_3}(\mathbf{k_1}, \mathbf{k_2}, \mathbf{k_3}) = \lambda_{s_1} k_1 \epsilon^{mi}_{(s_1)}(\mathbf{k_1}) \epsilon^{(s_2)}_{mr}(\mathbf{k_2}) \epsilon^{r}_{(s_3)i}(\mathbf{k_3}) \,, \tag{C.1}$$

$$\begin{aligned} C_3^{s_1 s_2 s_3}(\mathbf{k_1}, \mathbf{k_2}, \mathbf{k_3}) = {} & \lambda_{s_2} k_2 \left[k_1^2 \epsilon^{(s_1)}_{mi}(\mathbf{k_1}) \epsilon^{(s_2)i}_{k}(\mathbf{k_2}) \epsilon^{km}_{(s_3)}(\mathbf{k_3}) + 2 k_2^k k_3^r \, \epsilon_j^{(s_1)m}(\mathbf{k_1}) \epsilon_r^{(s_2)j}(\mathbf{k_2}) \epsilon^{(s_3)}_{km}(\mathbf{k_3}) \right] \\ & + 2 \lambda_{s_3} k_3 k_{1k} k_{3r} \, \epsilon_j^{(s_1)m}(\mathbf{k_1}) \epsilon^{kr}_{(s_2)}(\mathbf{k_2}) \epsilon_m^{(s_3)j}(\mathbf{k_3}) \,, \end{aligned} \tag{C.2}$$

$$\begin{aligned} C_4^{s_1 s_2 s_3}(\mathbf{k_1}, \mathbf{k_2}, \mathbf{k_3}) = {} & \left[\lambda_{s_2} k_1^2 k_2 + \lambda_{s_1} (\mathbf{k_1} \cdot \mathbf{k_2}) k_1 \right] \epsilon^{(s_1)}_{ri}(\mathbf{k_1}) \epsilon^{im}_{(s_2)}(\mathbf{k_2}) \epsilon_m^{(s_3)r}(\mathbf{k_3}) \\ & + \lambda_{s_1} k_1 k_{1n} k_{2m} \Big[\epsilon_r^{(s_1)i}(\mathbf{k_1}) \epsilon^{rn}_{(s_2)}(\mathbf{k_2}) \epsilon_i^{(s_3)m}(\mathbf{k_3}) - \epsilon^{rm}_{(s_1)}(\mathbf{k_1}) \epsilon_r^{(s_2)i}(\mathbf{k_2}) \epsilon_i^{(s_3)n}(\mathbf{k_3}) \\ & \qquad + \epsilon_r^{(s_1)m}(\mathbf{k_1}) \epsilon^{ni}_{(s_2)}(\mathbf{k_2}) \epsilon_i^{(s_3)r}(\mathbf{k_3}) + \epsilon^{ri}_{(s_1)}(\mathbf{k_1}) \epsilon^{(s_2)}_{ri}(\mathbf{k_2}) \epsilon^{mn}_{(s_3)}(\mathbf{k_3}) \\ & \qquad - \epsilon_r^{(s_1)i}(\mathbf{k_1}) \epsilon^{n}_{(s_2)i}(\mathbf{k_2}) \epsilon^{mr}_{(s_3)}(\mathbf{k_3}) \Big] \\ & + \lambda_{s_1} k_1 k_{1n} k_{3m} \, \epsilon^{mi}_{(s_1)}(\mathbf{k_1}) \epsilon^{(s_2)}_{ir}(\mathbf{k_2}) \epsilon^{rn}_{(s_3)}(\mathbf{k_3}) \\ & + i \epsilon^{ijl} \Big[(\mathbf{k_2} \cdot \mathbf{k_3}) k_{2j} \, \epsilon^{(s_1)}_{lr}(\mathbf{k_1}) \epsilon^{r}_{(s_2)m}(\mathbf{k_2}) \epsilon_i^{(s_3)m}(\mathbf{k_3}) \\ & \qquad + k_{1m} k_{2r} k_{3n} \, \epsilon_j^{(s_1)r}(\mathbf{k_1}) \epsilon_l^{(s_2)n}(\mathbf{k_2}) \epsilon_i^{(s_3)m}(\mathbf{k_3}) \\ & \qquad + (\mathbf{k_1} \cdot \mathbf{k_2}) k_{1m} \, \epsilon_j^{(s_1)r}(\mathbf{k_1}) \epsilon^{(s_2)}_{lr}(\mathbf{k_2}) \epsilon_i^{(s_3)m}(\mathbf{k_3}) \Big] \,, \end{aligned} \tag{C.3}$$

$$\begin{aligned} C_5^{s_1 s_2 s_3}(\mathbf{k_1}, \mathbf{k_2}, \mathbf{k_3}) = {} & \lambda_{s_1} k_1 k_{2m} k_{3k} \, \epsilon^{mi}_{(s_1)}(\mathbf{k_1}) \epsilon^{kr}_{(s_2)}(\mathbf{k_2}) \epsilon^{(s_3)}_{ir}(\mathbf{k_3}) \\ & + i \epsilon^{ijl} \Big[k_{1k} k_{2l} k_{3r} \, \epsilon_j^{(s_1)m}(\mathbf{k_1}) \epsilon^{kr}_{(s_2)}(\mathbf{k_2}) \epsilon^{(s_3)}_{mi}(\mathbf{k_3}) \\ & \qquad - k_{1k} k_{2l} k_{3i} \epsilon_j^{(s_1)m}(\mathbf{k_1}) \epsilon^{kr}_{(s_2)}(\mathbf{k_2}) \epsilon^{(s_3)}_{mr}(\mathbf{k_3}) \\ & \qquad + k_2^k k_{3l} k_3^r \, \epsilon_j^{(s_1)m}(\mathbf{k_1}) \epsilon^{(s_2)}_{ri}(\mathbf{k_2}) \epsilon^{(s_3)}_{km}(\mathbf{k_3}) \Big] \,, \end{aligned} \tag{C.4}$$

$$C_6^{s_1 s_2 s_3}(\mathbf{k_1}, \mathbf{k_2}, \mathbf{k_3}) = \lambda_{s_1} k_1 \left[k_{2i} k_{3m} \, \epsilon^{mi}_{(s_1)}(\mathbf{k_1}) \epsilon_r^{(s_2)k}(\mathbf{k_2}) \epsilon_k^{(s_3)r}(\mathbf{k_3}) + k_3^2 \epsilon^{mi}_{(s_1)}(\mathbf{k_1}) \epsilon^{r}_{(s_2)i}(\mathbf{k_2}) \epsilon^{(s_3)}_{mr}(\mathbf{k_3}) \right] \,, \tag{C.5}$$

$$C_7^{s_1 s_2 s_3}(\mathbf{k_1}, \mathbf{k_2}, \mathbf{k_3}) = C_9^{s_1 s_2 s_3}(\mathbf{k_1}, \mathbf{k_2}, \mathbf{k_3}) = i \epsilon^{ijl} k_{1r} \, \epsilon_l^{(s_1)m}(\mathbf{k_1}) \epsilon_j^{(s_2)r}(\mathbf{k_2}) \epsilon^{(s_3)}_{mi}(\mathbf{k_3}) \,, \tag{C.6}$$

$$C_8^{s_1s_2s_3}(\mathbf{k_1},\mathbf{k_2},\mathbf{k_3}) = ik_1^2\epsilon^{ijl}\Big[k_{3l}\,\epsilon_{mi}^{(s_1)}(\mathbf{k_1})\epsilon_{jk}^{(s_2)}(\mathbf{k_2})\epsilon_{(s_3)}^{km}(\mathbf{k_3}) + k_{2k}\,\epsilon_{mi}^{(s_1)}(\mathbf{k_1})\epsilon_{l}^{(s_2)m}(\mathbf{k_2})\epsilon_{j}^{(s_3)k}(\mathbf{k_3}) - k_2^m\epsilon_{mi}^{(s_1)}(\mathbf{k_1})\epsilon_{lk}^{(s_2)}(\mathbf{k_2})\epsilon_{j}^{(s_3)k}(\mathbf{k_3})\Big]\,. \tag{C.7}$$

The $T_i^{s_1s_2s_3}(\mathbf{k_1},\mathbf{k_2},\mathbf{k_3})$ that enter in the final expression of the PV1 bispectrum (6.99) with time-dependent couplings can be written in terms of the $C_i^{s_1s_2s_3}(\mathbf{k_1},\mathbf{k_2},\mathbf{k_3})$ as

$$T_1^{s_1s_2s_3}(\mathbf{k_1},\mathbf{k_2},\mathbf{k_3}) = C_2^{s_1s_2s_3}(\mathbf{k_1},\mathbf{k_2},\mathbf{k_3}) - C_7^{s_1s_2s_3}(\mathbf{k_1},\mathbf{k_2},\mathbf{k_3})\,, \tag{C.8}$$

$$T_2^{s_1s_2s_3}(\mathbf{k_1},\mathbf{k_2},\mathbf{k_3}) = C_4^{s_1s_2s_3}(\mathbf{k_1},\mathbf{k_2},\mathbf{k_3})\,, \tag{C.9}$$

$$T_3^{s_1s_2s_3}(\mathbf{k_1},\mathbf{k_2},\mathbf{k_3}) = C_5^{s_1s_2s_3}(\mathbf{k_1},\mathbf{k_2},\mathbf{k_3}) - C_6^{s_1s_2s_3}(\mathbf{k_1},\mathbf{k_2},\mathbf{k_3})\,. \tag{C.10}$$

Appendix D

Polarization tensors

In this section we set our conventions for the polarization tensors of PGWs by fixing an explicit representation for them. We can first use the momentum conservation, $\mathbf{k_1} + \mathbf{k_1} + \mathbf{k_3} = 0$, and the invariance under rotations to make the three wave vectors lying on the same plane, that we choose to be the (x, y) plane:

$$\mathbf{k_1} = k_1(1, 0, 0)\,, \quad \mathbf{k_2} = k_2(\cos\theta, \sin\theta, 0)\,, \quad \mathbf{k_3} = k_3(\cos\varphi, \sin\varphi, 0)\,, \tag{D.1}$$

where θ and φ are the angles that $\mathbf{k_1}$ forms with $\mathbf{k_2}$ and $\mathbf{k_3}$ respectively. Without loss of generality, we can choose $0 \leq \theta \leq \pi$ and $\pi \leq \varphi \leq 2\pi$, such that

$$\cos\theta = \frac{k_3^2 - k_1^2 - k_2^2}{2k_1k_2}\,, \quad \sin\theta = \frac{\lambda}{2k_1k_2}\,, \quad \cos\varphi = \frac{k_2^2 - k_3^2 - k_1^2}{2k_3k_1}\,, \quad \sin\varphi = -\frac{\lambda}{2k_3k_1}\,, \tag{D.2}$$

with

$$\lambda = \sqrt{2k_1^2k_2^2 + 2k_2^2k_3^2 + 2k_3^2k_1^2 - k_1^4 - k_2^4 - k_3^4}\,. \tag{D.3}$$

With this representation of the wave vectors we can then write explicitly the polarization tensors as [323, 377]

$$\epsilon^{(s)}(\mathbf{k_1}) = \frac{1}{\sqrt{2}}\begin{pmatrix} 0 & 0 & 0 \\ 0 & 1 & i\lambda_s \\ 0 & i\lambda_s & -1 \end{pmatrix}, \tag{D.4}$$

$$\epsilon^{(s)}(\mathbf{k_2}) = \frac{1}{\sqrt{2}}\begin{pmatrix} \sin^2\theta & -\sin\theta\cos\theta & -i\lambda_s\sin\theta \\ -\sin\theta\cos\theta & \cos^2\theta & i\lambda_s\cos\theta \\ -i\lambda_s\sin\theta & i\lambda_s\cos\theta & -1 \end{pmatrix}, \tag{D.5}$$

$$\epsilon^{(s)}(\mathbf{k_3}) = \frac{1}{\sqrt{2}}\begin{pmatrix} \sin^2\varphi & -\sin\varphi\cos\varphi & -i\lambda_s\sin\varphi \\ -\sin\varphi\cos\varphi & \cos^2\varphi & i\lambda_s\cos\varphi \\ -i\lambda_s\sin\varphi & i\lambda_s\cos\varphi & -1 \end{pmatrix}, \tag{D.6}$$

where $\lambda_s = \pm 1$ for $s = R$ and $s = L$, respectively.

Ringraziamenti

Vorrei cominciare ringraziando i miei supervisori, Max e Martina. La vostra guida e il vostro sostegno nel corso di questi tre anni sono stati preziosi. Grazie in particolare per i consigli e per il supporto in quest'ultimo periodo di costante indecisione.

Grazie a Luca, perché le chiacchierate di prima mattina davanti ad un caffè, così come le serate pizza post-ufficio, sono state una parte importante di questi anni. Grazie per tutti i suggerimenti e i consigli, specialmente in questi ultimi mesi.

Vorrei poi ringraziare tutto il gruppo CosmoFe. Sono profondamente convinto che non possa esistere un ambiente migliore in cui lavorare e trascorrere il proprio tempo. Mi ritengo incredibilmente fortunato ad aver avuto la possibilità di passare questi tre anni insieme a tutti voi. Grazie dunque a Paolo, per aver dato vita a questo gruppo fantastico e per tutto il lavoro svolto quotidianamente per continuare ad alimentarlo ed espanderlo.

Desidero inoltre ringraziare le persone con cui ho avuto la possibilità di collaborare in questi anni: Nicola Bartolo, Giulia Gubitosi, Giorgio Orlando, Angelo Ricciardone e Luca Visinelli.

Giunto alla fine del mio percorso universitario mi è venuto naturale guardarmi indietro e ripensare al viaggio che mi ha portato a raggiungere questo traguardo. Vorrei dunque ringraziare tutti i miei compagni di avventure negli anni bolognesi e padovani, che hanno contribuito a rendere questo percorso così speciale e memorabile, anche nelle sue difficoltà. Tra questi, un ringraziamento speciale va senza dubbio a Davide, Fede, Nicole e Sergio.

Un grazie infinito a tutti i miei compagni di questi tre anni di dottorato, a paritre da quelli con cui ho condiviso i miei primi momenti qui a Ferrara fino a quelli che sono arrivati più di recente. Ognuno di voi, a suo modo, ha contribuito a rendere questi anni ferraresi indimenticabili. Perché per quanto certe esperienze possano essere incredibili già di per sé, acquisiscono un valore ben più grande quando sono condivise con persone speciali. Tra lanci con il paracadute, vacanze in montagna e al mare, trasferte all'Oktoberfest da cui sono tornato con una caviglia in meno e serate ferraresi finite droppando Negroni (sì, anch'io di tanto in tanto uso degli inglesismi!), non avrei potuto sperare in compagni di avventure migliori di voi. Quindi grazie ad Andrea, Anna, Basz, Bianca, Cate, Dani, Giorgia, Marco, Marghe, Nicola, Nicolò, Pari, Salvatore, Sere, Shaz e Ste.

Un grazie particolare a Dani, compagno di mille avventure e improbabili serate ferraresi, e Marghe, per tutte le chiacchierate e i consigli che sei sempre in grado di darmi al momento giusto. Con voi, più di tutti, ho condiviso questo percorso, anche nei suoi momenti più difficili. Senza di voi sarebbe stato tutto sicuramente più complicato e meno divertente.

Grazie ad Eugi e Gio, con i quali ho avuto la fortuna di convivere il primo anno qui a Ferrara. Tra cene pazzesche, calcetti e serate tv, sicuramente non avrei potuto trovare persone migliori con cui iniziare questo percorso.

Un ringraziamento speciale va poi senza dubbio al mio amico Ale. La nostra capacità di passare ore al telefono a parlare del nulla assoluto (ma anche di cose interessanti e importanti, eh!) è qualcosa che non finirà mai di stupirmi e che non darò mai per scontato. Anche nelle giornate più complicate riesci sempre a strapparmi una (anzi, più di una) risata e per questo non potrò mai ringraziarti abbastanza.

Infine, il più grande grazie va a tutta la mia famiglia, in particolare ai miei genitori e a mio fratello Lorenzo. Grazie per il vostro sostegno incondizionato di fronte a tutte le scelte che mi si sono poste davanti e per avermi sempre spronato a seguire le mie passioni.

Bibliography

[1] N. Bartolo, L. Caloni, G. Orlando and A. Ricciardone, *Tensor non-Gaussianity in chiral scalar-tensor theories of gravity*, *JCAP* **03** (2021) 073, [2008.01715].

[2] L. Caloni, M. Gerbino and M. Lattanzi, *Updated cosmological constraints on Macroscopic Dark Matter*, *JCAP* **07** (2021) 027, [2105.13932].

[3] L. Caloni, M. Gerbino, M. Lattanzi and L. Visinelli, *Novel cosmological bounds on thermally-produced axion-like particles*, *JCAP* **09** (2022) 021, [2205.01637].

[4] L. Caloni, S. Giardiello, M. Lembo, M. Gerbino, G. Gubitosi, M. Lattanzi et al., *Probing Lorentz-violating electrodynamics with CMB polarization*, 2212.04867.

[5] Planck collaboration, N. Aghanim et al., *Planck 2018 results. I. Overview and the cosmological legacy of Planck*, *Astron. Astrophys.* **641** (2020) A1, [1807.06205].

[6] Planck collaboration, N. Aghanim et al., *Planck 2018 results. VI. Cosmological parameters*, *Astron. Astrophys.* **641** (2020) A6, [1807.06209].

[7] S. Aiola, E. Calabrese, L. Maurin, S. Naess, B. L. Schmitt, M. H. Abitbol et al., *The atacama cosmology telescope: Dr4 maps and cosmological parameters*, *Journal of Cosmology and Astroparticle Physics* **2020** (Dec, 2020) 047–047.

[8] BICEP, Keck collaboration, P. A. R. Ade et al., *Improved Constraints on Primordial Gravitational Waves using Planck, WMAP, and BICEP/Keck Observations through the 2018 Observing Season*, *Phys. Rev. Lett.* **127** (2021) 151301, [2110.00483].

[9] M. Hazumi et al., *LiteBIRD: A Satellite for the Studies of B-Mode Polarization and Inflation from Cosmic Background Radiation Detection*, *J. Low Temp. Phys.* **194** (2019) 443–452.

[10] Simons Observatory collaboration, P. Ade et al., *The Simons Observatory: Science goals and forecasts*, *JCAP* **02** (2019) 056, [1808.07445].

[11] CMB-S4 collaboration, K. N. Abazajian et al., *CMB-S4 Science Book, First Edition*, 1610.02743.

[12] P. D. Meerburg et al., *Primordial Non-Gaussianity*, 1903.04409.

[13] BOSS collaboration, S. Alam et al., *The clustering of galaxies in the completed SDSS-III Baryon Oscillation Spectroscopic Survey: cosmological analysis of the DR12 galaxy sample*, *Mon. Not. Roy. Astron. Soc.* **470** (2017) 2617–2652, [1607.03155].

[14] F. Beutler, C. Blake, M. Colless, D. H. Jones, L. Staveley-Smith, L. Campbell et al., *The 6dF Galaxy Survey: Baryon Acoustic Oscillations and the Local Hubble Constant*, *Mon. Not. Roy. Astron. Soc.* **416** (2011) 3017–3032, [1106.3366].

[15] A. J. Ross, L. Samushia, C. Howlett, W. J. Percival, A. Burden and M. Manera, *The clustering of the SDSS DR7 main Galaxy sample – I. A 4 per cent distance measure at $z = 0.15$*, *Mon. Not. Roy. Astron. Soc.* **449** (2015) 835–847, [1409.3242].

[16] D. M. Jacobs, G. D. Starkman and B. W. Lynn, *Macro Dark Matter*, *Mon. Not. Roy. Astron. Soc.* **450** (2015) 3418–3430, [1410.2236].

[17] D. Colladay and V. A. Kostelecky, *Lorentz violating extension of the standard model*, *Phys. Rev. D* **58** (1998) 116002, [hep-ph/9809521].

[18] V. A. Kostelecky, *Gravity, Lorentz violation, and the standard model*, *Phys. Rev. D* **69** (2004) 105009, [hep-th/0312310].

[19] V. A. Kostelecky and M. Mewes, *Electrodynamics with Lorentz-violating operators of arbitrary dimension*, *Phys. Rev. D* **80** (2009) 015020, [0905.0031].

[20] Planck collaboration, N. Aghanim et al., *Planck 2018 results. V. CMB power spectra and likelihoods*, *Astron. Astrophys.* **641** (2020) A5, [1907.12875].

[21] Planck collaboration, N. Aghanim et al., *Planck 2018 results. VIII. Gravitational lensing*, *Astron. Astrophys.* **641** (2020) A8, [1807.06210].

[22] I. L. Padilla et al., *Two-year Cosmology Large Angular Scale Surveyor (CLASS) Observations: A Measurement of Circular Polarization at 40 GHz*, 1911.00391.

[23] SPIDER collaboration, J. M. Nagy et al., *A New Limit on CMB Circular Polarization from SPIDER*, *Astrophys. J.* **844** (2017) 151, [1704.00215].

[24] M. Crisostomi, K. Noui, C. Charmousis and D. Langlois, *Beyond Lovelock gravity: Higher derivative metric theories*, *Phys. Rev. D* **97** (2018) 044034, [1710.04531].

[25] E. Hubble, *A relation between distance and radial velocity among extra-galactic nebulae*, *Proc. Nat. Acad. Sci.* **15** (1929) 168–173.

[26] R. A. Alpher, H. Bethe and G. Gamow, *The origin of chemical elements*, *Phys. Rev.* **73** (1948) 803–804.

[27] A. A. Penzias and R. W. Wilson, *A Measurement of excess antenna temperature at 4080-Mc/s*, *Astrophys. J.* **142** (1965) 419–421.

[28] Planck collaboration, P. A. R. Ade et al., *Planck 2015 results. XVI. Isotropy and statistics of the CMB*, *Astron. Astrophys.* **594** (2016) A16, [1506.07135].

[29] BOSS collaboration, K. S. Dawson et al., *The Baryon Oscillation Spectroscopic Survey of SDSS-III*, *Astron. J.* **145** (2013) 10, [1208.0022].

[30] D. Baumann, *Cosmology: Part III Mathematical Tripos*, .

[31] *https://supernova.eso.org/exhibition/images/Universe-Geometry_v2-cc/*, .

[32] K. Saikawa and S. Shirai, *Primordial gravitational waves, precisely: The role of thermodynamics in the Standard Model*, *JCAP* **05** (2018) 035, [1803.01038].

[33] S. Dodelson, *Modern Cosmology*. Academic Press, Amsterdam, 2003.

[34] R. J. Cooke, M. Pettini and C. C. Steidel, *One Percent Determination of the Primordial Deuterium Abundance*, *Astrophys. J.* **855** (2018) 102, [1710.11129].

[35] E. Aver, K. A. Olive and E. D. Skillman, *The effects of He I λ10830 on helium abundance determinations*, *JCAP* **07** (2015) 011, [1503.08146].

[36] R. Consiglio, P. F. de Salas, G. Mangano, G. Miele, S. Pastor and O. Pisanti, *PArthENoPE reloaded*, *Comput. Phys. Commun.* **233** (2018) 237–242, [1712.04378].

[37] S. Gariazzo, P. F. de Salas, O. Pisanti and R. Consiglio, *PArthENoPE Revolutions*, 2103.05027.

[38] B. D. Fields, K. A. Olive, T.-H. Yeh and C. Young, *Big-Bang Nucleosynthesis after Planck*, *JCAP* **03** (2020) 010, [1912.01132].

[39] M. Lattanzi and M. Gerbino, *Status of neutrino properties and future prospects - Cosmological and astrophysical constraints*, *Front. in Phys.* **5** (2018) 70, [1712.07109].

[40] S. S. Gershtein and Y. B. Zel'dovich, *Rest Mass of Muonic Neutrino and Cosmology*, *ZhETF Pisma Redaktsiiu* **4** (Sept., 1966) 174.

[41] E. W. Kolb and M. S. Turner, *The Early Universe*, vol. 69. 1990. 10.1201/9780429492860.

[42] P. J. E. Peebles, *Recombination of the Primeval Plasma*, *Astrophys. J.* **153** (1968) 1.

[43] *https://sci.esa.int/web/planck/-/51560-the-history-of-structure-formation-in-the-universe*, .

[44] J. M. Maldacena, *Non-Gaussian features of primordial fluctuations in single field inflationary models*, *JHEP* **05** (2003) 013, [astro-ph/0210603].

[45] Planck collaboration, Y. Akrami et al., *Planck 2018 results. X. Constraints on inflation*, *Astron. Astrophys.* **641** (2020) A10, [1807.06211].

[46] D. J. Fixsen, *The Temperature of the Cosmic Microwave Background*, *Astrophys. J.* **707** (2009) 916–920, [0911.1955].

[47] M. Zaldarriaga and U. Seljak, *An all sky analysis of polarization in the microwave background*, *Phys. Rev. D* **55** (1997) 1830–1840, [astro-ph/9609170].

[48] R. K. Sachs and A. M. Wolfe, *Perturbations of a cosmological model and angular variations of the microwave background*, *Astrophys. J.* **147** (1967) 73–90.

[49] M. Zaldarriaga and D. D. Harari, *Analytic approach to the polarization of the cosmic microwave background in flat and open universes*, *Phys. Rev. D* **52** (1995) 3276–3287, [astro-ph/9504085].

[50] J. Silk, *Cosmic black body radiation and galaxy formation*, *Astrophys. J.* **151** (1968) 459–471.

[51] S. Dodelson and J. M. Jubas, *Reionization and its imprint on the cosmic microwave background*, *Astrophys. J.* **439** (1995) 503–516, [astro-ph/9308019].

[52] W. Hu, D. Scott and J. Silk, *Reionization and cosmic microwave background distortions: A Complete treatment of second order Compton scattering*, *Phys. Rev. D* **49** (1994) 648–670, [astro-ph/9305038].

[53] N. Sugiyama, J. Silk and N. Vittorio, *Reionization and cosmic microwave anisotropies*, *Astrophys. J. Lett.* **419** (1993) L1, [astro-ph/9310051].

[54] Z. Hou, R. Keisler, L. Knox, M. Millea and C. Reichardt, *How Massless Neutrinos Affect the Cosmic Microwave Background Damping Tail*, *Phys. Rev. D* **87** (2013) 083008, [1104.2333].

[55] M. Kamionkowski, A. Kosowsky and A. Stebbins, *Statistics of cosmic microwave background polarization*, *Phys. Rev. D* **55** (1997) 7368–7388, [astro-ph/9611125].

[56] A. Kosowsky, *Cosmic microwave background polarization*, *Annals Phys.* **246** (1996) 49–85, [astro-ph/9501045].

[57] A. Lue, L.-M. Wang and M. Kamionkowski, *Cosmological signature of new parity violating interactions*, *Phys. Rev. Lett.* **83** (1999) 1506–1509, [astro-ph/9812088].

[58] M. Li and X. Zhang, *Cosmological CPT violating effect on CMB polarization*, *Phys. Rev. D* **78** (2008) 103516, [0810.0403].

[59] M. Pospelov, A. Ritz, C. Skordis, A. Ritz and C. Skordis, *Pseudoscalar perturbations and polarization of the cosmic microwave background*, *Phys. Rev. Lett.* **103** (2009) 051302, [0808.0673].

[60] A. Kosowsky and A. Loeb, *Faraday rotation of microwave background polarization by a primordial magnetic field*, *Astrophys. J.* **469** (1996) 1–6, [astro-ph/9601055].

[61] A. Cooray, A. Melchiorri and J. Silk, *Is the cosmic microwave background circularly polarized?*, *Phys. Lett. B* **554** (2003) 1–6, [astro-ph/0205214].

[62] M. Giovannini, *The V-mode polarization of the Cosmic Microwave Background*, *Phys. Rev. D* **80** (2009) 123013, [0909.3629].

[63] S. De and H. Tashiro, *Circular Polarization of the CMB: A probe of the First stars*, *Phys. Rev. D* **92** (2015) 123506, [1401.1371].

[64] P. Montero-Camacho and C. M. Hirata, *Exploring circular polarization in the CMB due to conventional sources of cosmic birefringence*, *JCAP* **08** (2018) 040, [1803.04505].

[65] N. Lemarchand, J. Grain, G. Hurier, F. Lacasa and A. Ferté, *Secondary CMB anisotropies from magnetized haloes - I. Power spectra of the Faraday rotation angle and conversion rate*, *Astron. Astrophys.* **630** (2019) A149, [1810.09221].

[66] D. Ejlli, *On the CMB circular polarization: I. The Cotton–Mouton effect*, *Eur. Phys. J. C* **79** (2019) 231, [1810.04947].

[67] V. A. Kostelecky and M. Mewes, *Lorentz-violating electrodynamics and the cosmic microwave background*, *Phys. Rev. Lett.* **99** (2007) 011601, [astro-ph/0702379].

[68] S. Alexander, J. Ochoa and A. Kosowsky, *Generation of Circular Polarization of the Cosmic Microwave Background*, *Phys. Rev. D* **79** (2009) 063524, [0810.2355].

[69] D. Ejlli, *Magneto-optic effects of the cosmic microwave background*, *Nucl. Phys. B* **935** (2018) 83–128, [1607.02094].

[70] D. Ejlli, *Millicharged fermion vacuum polarization in a cosmic magnetic field and generation of CMB elliptic polarization*, *Phys. Rev. D* **96** (2017) 023540, [1704.01894].

[71] K. Inomata and M. Kamionkowski, *Circular polarization of the cosmic microwave background from vector and tensor perturbations*, *Phys. Rev. D* **99** (2019) 043501, [1811.04957].

[72] N. Bartolo, A. Hoseinpour, S. Matarrese, G. Orlando and M. Zarei, *CMB Circular and B-mode Polarization from New Interactions*, *Phys. Rev. D* **100** (2019) 043516, [1903.04578].

[73] A. Hoseinpour, M. Zarei, G. Orlando, N. Bartolo and S. Matarrese, *CMB V modes from photon-photon forward scattering revisited*, *Phys. Rev. D* **102** (2020) 063501, [2006.14418].

[74] A. Kogut, M. H. Abitbol, J. Chluba, J. Delabrouille, D. Fixsen, J. C. Hill et al., *CMB Spectral Distortions: Status and Prospects*, 1907.13195.

[75] J. Chluba et al., *New Horizons in Cosmology with Spectral Distortions of the Cosmic Microwave Background*, 1909.01593.

[76] J. Chluba et al., *Spectral Distortions of the CMB as a Probe of Inflation, Recombination, Structure Formation and Particle Physics: Astro2020 Science White Paper*, *Bull. Am. Astron. Soc.* **51** (2019) 184, [1903.04218].

[77] L. Danese and G. De Zotti, *Double compton process and the spectrum of the microwave background*, *Astronomy and Astrophysics* **107** (1982) 39–42.

[78] W. Hu and J. Silk, *Thermalization and spectral distortions of the cosmic background radiation*, *Phys. Rev. D* **48** (1993) 485–502.

[79] J. Chluba and R. A. Sunyaev, *The evolution of CMB spectral distortions in the early Universe*, *Mon. Not. Roy. Astron. Soc.* **419** (2012) 1294–1314, [1109.6552].

[80] J. Chluba, *Green's function of the cosmological thermalization problem*, *Mon. Not. Roy. Astron. Soc.* **434** (2013) 352, [1304.6120].

[81] J. Chluba, *Which spectral distortions does ΛCDM actually predict?*, *Mon. Not. Roy. Astron. Soc.* **460** (2016) 227–239, [1603.02496].

[82] J. C. Mather et al., *Measurement of the Cosmic Microwave Background spectrum by the COBE FIRAS instrument*, *Astrophys. J.* **420** (1994) 439–444.

[83] D. J. Fixsen, E. S. Cheng, J. M. Gales, J. C. Mather, R. A. Shafer and E. L. Wright, *The Cosmic Microwave Background spectrum from the full COBE FIRAS data set*, *Astrophys. J.* **473** (1996) 576, [astro-ph/9605054].

[84] A. Kogut et al., *The Primordial Inflation Explorer (PIXIE): A Nulling Polarimeter for Cosmic Microwave Background Observations*, *JCAP* **07** (2011) 025, [1105.2044].

[85] B. A. Bassett and R. Hlozek, *Baryon Acoustic Oscillations*, 0910.5224.

[86] D. J. Eisenstein, H.-j. Seo and M. J. White, *On the Robustness of the Acoustic Scale in the Low-Redshift Clustering of Matter*, *Astrophys. J.* **664** (2007) 660–674, [astro-ph/0604361].

[87] G. Bertone, D. Hooper and J. Silk, *Particle dark matter: Evidence, candidates and constraints*, *Phys. Rept.* **405** (2005) 279–390, [hep-ph/0404175].

[88] K. Garrett and G. Duda, *Dark Matter: A Primer*, *Adv. Astron.* **2011** (2011) 968283, [1006.2483].

[89] J. L. Feng, *Dark Matter Candidates from Particle Physics and Methods of Detection*, *Ann. Rev. Astron. Astrophys.* **48** (2010) 495–545, [1003.0904].

[90] S. Profumo, L. Giani and O. F. Piattella, *An Introduction to Particle Dark Matter*, *Universe* **5** (2019) 213, [1910.05610].

[91] E. Witten, *Cosmic Separation of Phases*, *Phys. Rev. D* **30** (1984) 272–285.

[92] C. Alcock and E. Farhi, *The Evaporation of Strange Matter in the Early Universe*, *Phys. Rev. D* **32** (1985) 1273.

[93] C. Alcock, E. Farhi and A. Olinto, *Strange stars*, *Astrophys. J.* **310** (1986) 261–272.

[94] E. Farhi and R. L. Jaffe, *Strange Matter*, *Phys. Rev. D* **30** (1984) 2379.

[95] B. W. Lynn, A. E. Nelson and N. Tetradis, *Strange baryon matter*, *Nuclear Physics B* **345** (1990) 186–209.

[96] S. R. Coleman, *Q Balls*, *Nucl. Phys. B* **262** (1985) 263.

[97] T. D. Lee and Y. Pang, *Nontopological solitons*, *Phys. Rept.* **221** (1992) 251–350.

[98] A. Kusenko and M. E. Shaposhnikov, *Supersymmetric Q balls as dark matter*, *Phys. Lett. B* **418** (1998) 46–54, [hep-ph/9709492].

[99] A. Kusenko, L. Loveridge and M. Shaposhnikov, *Supersymmetric dark matter Q-balls and their interactions in matter*, *Phys. Rev. D* **72** (2005) 025015, [hep-ph/0405044].

[100] A. Kusenko, V. Kuzmin, M. E. Shaposhnikov and P. G. Tinyakov, *Experimental signatures of supersymmetric dark matter Q balls*, *Phys. Rev. Lett.* **80** (1998) 3185–3188, [hep-ph/9712212].

[101] A. Zhitnitsky, *Cold dark matter as compact composite objects*, *Phys. Rev. D* **74** (2006) 043515, [astro-ph/0603064].

[102] A. Zhitnitsky, *The Width of the 511-KeV Line from the Bulge of the Galaxy*, *Phys. Rev. D* **76** (2007) 103518, [astro-ph/0607361].

[103] D. T. Cumberbatch, J. Silk and G. D. Starkman, *Difficulties for Compact Composite Object Dark Matter*, *Phys. Rev. D* **77** (2008) 063522, [astro-ph/0606429].

[104] Y. Bai, A. J. Long and S. Lu, *Tests of Dark MACHOs: Lensing, Accretion, and Glow*, *JCAP* **09** (2020) 044, [2003.13182].

[105] J. M. Cline, Z. Liu, G. Moore and W. Xue, *Composite strongly interacting dark matter*, *Phys. Rev. D* **90** (2014) 015023, [1312.3325].

[106] B. Carr, F. Kuhnel and M. Sandstad, *Primordial Black Holes as Dark Matter*, *Phys. Rev. D* **94** (2016) 083504, [1607.06077].

[107] B. Carr and F. Kühnel, *Primordial black holes as dark matter: Recent developments*, *Annual Review of Nuclear and Particle Science* **70** (2020) 355–394.

[108] LIGO Scientific, Virgo collaboration, R. Abbott et al., *GW190814: Gravitational Waves from the Coalescence of a 23 Solar Mass Black Hole with a 2.6 Solar Mass Compact Object*, *Astrophys. J. Lett.* **896** (2020) L44, [2006.12611].

[109] I. Bombaci, A. Drago, D. Logoteta, G. Pagliara and I. Vidaña, *Was GW190814 a black hole – strange quark star system?*, *Phys. Rev. Lett.* **126** (2021) 162702, [2010.01509].

[110] A. R. Zhitnitsky, *Dark matter as dense color superconductor*, *Nucl. Phys. B Proc. Suppl.* **124** (2003) 99–102, [astro-ph/0204218].

[111] A. Zhitnitsky, *'Nonbaryonic' dark matter as baryonic colour superconductor*, *J. Phys. G* **30** (2004) S513–S517.

[112] X. Liang and A. Zhitnitsky, *Axion field and the quark nugget's formation at the QCD phase transition*, *Phys. Rev. D* **94** (2016) 083502, [1606.00435].

[113] Y. Bai, A. J. Long and S. Lu, *Dark Quark Nuggets*, *Phys. Rev. D* **99** (2019) 055047, [1810.04360].

[114] Y. Bai and A. J. Long, *Six Flavor Quark Matter*, *JHEP* **06** (2018) 072, [1804.10249].

[115] J.-M. Richard, *Antiproton physics*, *Front. in Phys.* **8** (2020) 6, [1912.07385].

[116] A. Zdziarski and R. Svensson, *Absorption of x-rays and gamma rays at cosmological distances*, *The Astrophysical Journal* **344** (1989) 551–566.

[117] M. Kawasaki and T. Moroi, *Electromagnetic cascade in the early universe and its application to the big bang nucleosynthesis*, *Astrophys. J.* **452** (1995) 506, [astro-ph/9412055].

[118] Planck collaboration, N. Aghanim et al., *Planck 2018 results. VI. Cosmological parameters*, 1807.06209.

[119] J. Singh Sidhu, *Charge Constraints of Macroscopic Dark Matter*, *Phys. Rev. D* **101** (2020) 043526, [1912.04732].

[120] S. D. McDermott, H.-B. Yu and K. M. Zurek, *Turning off the Lights: How Dark is Dark Matter?*, *Phys. Rev. D* **83** (2011) 063509, [1011.2907].

[121] S. L. Dubovsky, D. S. Gorbunov and G. I. Rubtsov, *Narrowing the window for millicharged particles by CMB anisotropy*, *JETP Lett.* **79** (2004) 1–5, [hep-ph/0311189].

[122] A. D. Dolgov, S. L. Dubovsky, G. I. Rubtsov and I. I. Tkachev, *Constraints on millicharged particles from Planck data*, *Phys. Rev. D* **88** (2013) 117701, [1310.2376].

[123] S. L. Dubovsky and D. S. Gorbunov, *Small second acoustic peak from interacting cold dark matter?*, *Phys. Rev. D* **64** (2001) 123503, [astro-ph/0103122].

[124] A. Melchiorri, A. Polosa and A. Strumia, *New bounds on millicharged particles from cosmology*, *Phys. Lett. B* **650** (2007) 416–420, [hep-ph/0703144].

[125] C. Dvorkin, K. Blum and M. Kamionkowski, *Constraining Dark Matter-Baryon Scattering with Linear Cosmology*, *Phys. Rev. D* **89** (2014) 023519, [1311.2937].

[126] D. Tseliakhovich and C. Hirata, *Relative velocity of dark matter and baryonic fluids and the formation of the first structures*, *Phys. Rev. D* **82** (2010) 083520, [1005.2416].

[127] R. H. Cyburt, J. R. Ellis, B. D. Fields and K. A. Olive, *Updated nucleosynthesis constraints on unstable relic particles*, *Phys. Rev. D* **67** (2003) 103521, [astro-ph/0211258].

[128] H. Ishida, M. Kusakabe and H. Okada, *Effects of long-lived 10 MeV-scale sterile neutrinos on primordial elemental abundances and the effective neutrino number*, *Phys. Rev. D* **90** (2014) 083519, [1403.5995].

[129] V. Poulin and P. D. Serpico, *Loophole to the Universal Photon Spectrum in Electromagnetic Cascades and Application to the Cosmological Lithium Problem*, *Phys. Rev. Lett.* **114** (2015) 091101, [1502.01250].

[130] V. Poulin and P. D. Serpico, *Nonuniversal BBN bounds on electromagnetically decaying particles*, *Phys. Rev. D* **91** (2015) 103007, [1503.04852].

[131] L. Salvati, L. Pagano, M. Lattanzi, M. Gerbino and A. Melchiorri, *Breaking Be: a sterile neutrino solution to the cosmological lithium problem*, *JCAP* **08** (2016) 022, [1606.06968].

[132] J. Singh Sidhu, R. J. Scherrer and G. Starkman, *Antimatter as Macroscopic Dark Matter*, *Phys. Lett. B* **807** (2020) 135574, [2006.01200].

[133] I. Brivio and M. Trott, *The Standard Model as an Effective Field Theory*, *Phys. Rept.* **793** (2019) 1–98, [1706.08945].

[134] R. D. Peccei, *The Strong CP problem and axions*, *Lect. Notes Phys.* **741** (2008) 3–17, [hep-ph/0607268].

[135] R. J. Crewther, P. Di Vecchia, G. Veneziano and E. Witten, *Chiral Estimate of the Electric Dipole Moment of the Neutron in Quantum Chromodynamics*, *Phys. Lett. B* **88** (1979) 123.

[136] M. Pospelov and A. Ritz, *Theta induced electric dipole moment of the neutron via QCD sum rules*, *Phys. Rev. Lett.* **83** (1999) 2526–2529, [hep-ph/9904483].

[137] P. W. Graham and S. Rajendran, *New Observables for Direct Detection of Axion Dark Matter*, *Phys. Rev. D* **88** (2013) 035023, [1306.6088].

[138] C. Abel et al., *Measurement of the Permanent Electric Dipole Moment of the Neutron*, *Phys. Rev. Lett.* **124** (2020) 081803, [2001.11966].

[139] R. D. Peccei and H. R. Quinn, *CP Conservation in the Presence of Instantons*, *Phys. Rev. Lett.* **38** (1977) 1440–1443.

[140] R. D. Peccei and H. R. Quinn, *Constraints Imposed by CP Conservation in the Presence of Instantons*, *Phys. Rev. D* **16** (1977) 1791–1797.

[141] S. Weinberg, *A New Light Boson?*, *Phys. Rev. Lett.* **40** (1978) 223–226.

[142] F. Wilczek, *Problem of Strong P and T Invariance in the Presence of Instantons*, *Phys. Rev. Lett.* **40** (1978) 279–282.

[143] G. Grilli di Cortona, E. Hardy, J. Pardo Vega and G. Villadoro, *The QCD axion, precisely*, *JHEP* **01** (2016) 034, [1511.02867].

[144] T. W. Donnelly, S. J. Freedman, R. S. Lytel, R. D. Peccei and M. Schwartz, *Do Axions Exist?*, *Phys. Rev. D* **18** (1978) 1607.

[145] L. J. Hall and M. B. Wise, *FLAVOR CHANGING HIGGS - BOSON COUPLINGS*, *Nucl. Phys. B* **187** (1981) 397–408.

[146] F. Wilczek, *Decays of Heavy Vector Mesons Into Higgs Particles*, *Phys. Rev. Lett.* **39** (1977) 1304.

[147] A. Zehnder, *Axion Search in a Monochromatic γ Transition: A New Lower Limit for the Axion Mass*, *Phys. Lett. B* **104** (1981) 494–498.

[148] J. E. Kim, *Weak Interaction Singlet and Strong CP Invariance*, *Phys. Rev. Lett.* **43** (1979) 103.

[149] M. A. Shifman, A. I. Vainshtein and V. I. Zakharov, *Can Confinement Ensure Natural CP Invariance of Strong Interactions?*, *Nucl. Phys. B* **166** (1980) 493–506.

[150] M. Dine, W. Fischler and M. Srednicki, *A Simple Solution to the Strong CP Problem with a Harmless Axion*, *Phys. Lett. B* **104** (1981) 199–202.

[151] A. R. Zhitnitsky, *On Possible Suppression of the Axion Hadron Interactions. (In Russian)*, *Sov. J. Nucl. Phys.* **31** (1980) 260.

[152] L. Di Luzio, M. Giannotti, E. Nardi and L. Visinelli, *The landscape of QCD axion models*, *Phys. Rept.* **870** (2020) 1–117, [2003.01100].

[153] Particle Data Group collaboration, P. A. Zyla et al., *Review of Particle Physics*, *Progress of Theoretical and Experimental Physics* **2020** (08, 2020) , [https://academic.oup.com/ptep/article-pdf/2020/8/083C01/34673722/ptaa104.pdf].

[154] H. Georgi, D. B. Kaplan and L. Randall, *Manifesting the Invisible Axion at Low-energies*, *Phys. Lett. B* **169** (1986) 73–78.

[155] J. McDonald, *Gauge singlet scalars as cold dark matter*, *Phys. Rev. D* **50** (1994) 3637–3649, [hep-ph/0702143].

[156] C. P. Burgess, M. Pospelov and T. ter Veldhuis, *The Minimal model of nonbaryonic dark matter: A Singlet scalar*, *Nucl. Phys. B* **619** (2001) 709–728, [hep-ph/0011335].

[157] X.-G. He, T. Li, X.-Q. Li, J. Tandean and H.-C. Tsai, *The Simplest Dark-Matter Model, CDMS II Results, and Higgs Detection at LHC*, *Phys. Lett. B* **688** (2010) 332–336, [0912.4722].

[158] G. Cacciapaglia, G. Ferretti, T. Flacke and H. Serôdio, *Light scalars in composite Higgs models*, *Front. in Phys.* **7** (2019) 22, [1902.06890].

[159] W. Lin, L. Visinelli, D. Xu and T. T. Yanagida, *Neutrino astronomy as a probe of physics beyond the Standard Model: decay of sub-MeV B-L gauge boson dark matter*, 2202.04496.

[160] P. Svrcek and E. Witten, *Axions In String Theory*, *JHEP* **06** (2006) 051, [hep-th/0605206].

[161] A. Arvanitaki, S. Dimopoulos, S. Dubovsky, N. Kaloper and J. March-Russell, *String Axiverse*, *Phys. Rev. D* **81** (2010) 123530, [0905.4720].

[162] K. Harigaya, M. Ibe, K. Schmitz and T. T. Yanagida, *Peccei-Quinn symmetry from a gauged discrete R symmetry*, *Phys. Rev. D* **88** (2013) 075022, [1308.1227].

[163] L. Di Luzio, E. Nardi and L. Ubaldi, *Accidental Peccei-Quinn symmetry protected to arbitrary order*, *Phys. Rev. Lett.* **119** (2017) 011801, [1704.01122].

[164] P. Arias, D. Cadamuro, M. Goodsell, J. Jaeckel, J. Redondo and A. Ringwald, *WISPy Cold Dark Matter*, *JCAP* **06** (2012) 013, [1201.5902].

[165] L. Visinelli, *Light axion-like dark matter must be present during inflation*, *Phys. Rev. D* **96** (2017) 023013, [1703.08798].

[166] D. Aloni, Y. Soreq and M. Williams, *Coupling QCD-Scale Axionlike Particles to Gluons*, *Phys. Rev. Lett.* **123** (2019) 031803, [1811.03474].

[167] J. E. Kim, *Constraints on very light axions from cavity experiments*, *Phys. Rev. D* **58** (1998) 055006, [hep-ph/9802220].

[168] L. Di Luzio, F. Mescia and E. Nardi, *Redefining the Axion Window*, *Phys. Rev. Lett.* **118** (2017) 031801, [1610.07593].

[169] L. Di Luzio, F. Mescia and E. Nardi, *Window for preferred axion models*, *Phys. Rev. D* **96** (2017) 075003, [1705.05370].

[170] M. Farina, D. Pappadopulo, F. Rompineve and A. Tesi, *The photo-philic QCD axion*, *JHEP* **01** (2017) 095, [1611.09855].

[171] P. Agrawal, J. Fan, M. Reece and L.-T. Wang, *Experimental Targets for Photon Couplings of the QCD Axion*, *JHEP* **02** (2018) 006, [1709.06085].

[172] A. Hook, *Solving the Hierarchy Problem Discretely*, *Phys. Rev. Lett.* **120** (2018) 261802, [1802.10093].

[173] L. Di Luzio, B. Gavela, P. Quilez and A. Ringwald, *An even lighter QCD axion*, *JHEP* **05** (2021) 184, [2102.00012].

[174] A. V. Sokolov and A. Ringwald, *Photophilic hadronic axion from heavy magnetic monopoles*, *JHEP* **06** (2021) 123, [2104.02574].

[175] L. F. Abbott and P. Sikivie, *A Cosmological Bound on the Invisible Axion*, *Phys. Lett. B* **120** (1983) 133–136.

[176] J. Preskill, M. B. Wise and F. Wilczek, *Cosmology of the Invisible Axion*, *Phys. Lett. B* **120** (1983) 127–132.

[177] M. Dine and W. Fischler, *The Not So Harmless Axion*, *Phys. Lett. B* **120** (1983) 137–141.

[178] D. J. E. Marsh, *Axion Cosmology*, *Phys. Rept.* **643** (2016) 1–79, [1510.07633].

[179] I. G. Irastorza, *An introduction to axions and their detection*, *SciPost Phys. Lect. Notes* **45** (2022) 1, [2109.07376].

[180] T. W. B. Kibble, *Some Implications of a Cosmological Phase Transition*, *Phys. Rept.* **67** (1980) 183.

[181] T. Hiramatsu, M. Kawasaki, K. Saikawa and T. Sekiguchi, *Production of dark matter axions from collapse of string-wall systems*, *Phys. Rev. D* **85** (2012) 105020, [1202.5851].

[182] M. Kawasaki, K. Saikawa and T. Sekiguchi, *Axion dark matter from topological defects*, *Phys. Rev. D* **91** (2015) 065014, [1412.0789].

[183] M. Buschmann, J. W. Foster, A. Hook, A. Peterson, D. E. Willcox, W. Zhang et al., *Dark matter from axion strings with adaptive mesh refinement*, *Nature Commun.* **13** (2022) 1049, [2108.05368].

[184] M. Gorghetto and G. Villadoro, *Topological Susceptibility and QCD Axion Mass: QED and NNLO corrections*, *JHEP* **03** (2019) 033, [1812.01008].

[185] M. Gorghetto, E. Hardy and G. Villadoro, *More axions from strings*, *SciPost Phys.* **10** (2021) 050, [2007.04990].

[186] L. Hui, J. P. Ostriker, S. Tremaine and E. Witten, *Ultralight scalars as cosmological dark matter*, *Phys. Rev. D* **95** (2017) 043541, [1610.08297].

[187] W. H. Press, B. S. Ryden and D. N. Spergel, *Single Mechanism for Generating Large Scale Structure and Providing Dark Missing Matter*, *Phys. Rev. Lett.* **64** (1990) 1084.

[188] W. Hu, R. Barkana and A. Gruzinov, *Cold and fuzzy dark matter*, *Phys. Rev. Lett.* **85** (2000) 1158–1161, [astro-ph/0003365].

[189] R. Hlozek, D. Grin, D. J. E. Marsh and P. G. Ferreira, *A search for ultralight axions using precision cosmological data*, *Phys. Rev. D* **91** (2015) 103512, [1410.2896].

[190] M. Dentler, D. J. E. Marsh, R. Hložek, A. Laguë, K. K. Rogers and D. Grin, *Fuzzy dark matter and the Dark Energy Survey Year 1 data*, *Mon. Not. Roy. Astron. Soc.* **515** (2022) 5646–5664, [2111.01199].

[191] V. Iršič, M. Viel, M. G. Haehnelt, J. S. Bolton and G. D. Becker, *First constraints on fuzzy dark matter from Lyman-α forest data and hydrodynamical simulations*, *Phys. Rev. Lett.* **119** (2017) 031302, [1703.04683].

[192] M. S. Turner, *Thermal Production of Not SO Invisible Axions in the Early Universe*, *Phys. Rev. Lett.* **59** (1987) 2489.

[193] E. Masso, F. Rota and G. Zsembinszki, *On axion thermalization in the early universe*, *Phys. Rev. D* **66** (2002) 023004, [hep-ph/0203221].

[194] P. Graf and F. D. Steffen, *Thermal axion production in the primordial quark-gluon plasma*, *Phys. Rev. D* **83** (2011) 075011, [1008.4528].

[195] A. Salvio, A. Strumia and W. Xue, *Thermal axion production*, *JCAP* **01** (2014) 011, [1310.6982].

[196] L. Di Luzio, G. Martinelli and G. Piazza, *Breakdown of chiral perturbation theory for the axion hot dark matter bound*, *Phys. Rev. Lett.* **126** (2021) 241801, [2101.10330].

[197] F. D'Eramo, F. Hajkarim and S. Yun, *Thermal Axion Production at Low Temperatures: A Smooth Treatment of the QCD Phase Transition*, *Phys. Rev. Lett.* **128** (2022) 152001, [2108.04259].

[198] F. D'Eramo, F. Hajkarim and S. Yun, *Thermal QCD Axions across Thresholds*, *JHEP* **10** (2021) 224, [2108.05371].

[199] A. Notari, F. Rompineve and G. Villadoro, *Improved hot dark matter bound on the QCD axion*, 2211.03799.

[200] L. Di Luzio, J. Martin Camalich, G. Martinelli, J. A. Oller and G. Piazza, *Axion-pion thermalization rate in unitarized NLO chiral perturbation theory*, 2211.05073.

[201] I. G. Irastorza and J. Redondo, *New experimental approaches in the search for axion-like particles*, *Prog. Part. Nucl. Phys.* **102** (2018) 89–159, [1801.08127].

[202] P. W. Graham, I. G. Irastorza, S. K. Lamoreaux, A. Lindner and K. A. van Bibber, *Experimental Searches for the Axion and Axion-Like Particles*, *Ann. Rev. Nucl. Part. Sci.* **65** (2015) 485–514, [1602.00039].

[203] P. Di Vecchia, M. Giannotti, M. Lattanzi and A. Lindner, *Round Table on Axions and Axion-like Particles*, *PoS* **Confinement2018** (2019) 034, [1902.06567].

[204] C. O'Hare, *cajohare/axionlimits: Axionlimits*, July, 2020. 10.5281/zenodo.3932430.

[205] ADMX collaboration, C. Bartram et al., *Search for Invisible Axion Dark Matter in the 3.3–4.2 μeV Mass Range*, *Phys. Rev. Lett.* **127** (2021) 261803, [2110.06096].

[206] MADMAX collaboration, P. Brun et al., *A new experimental approach to probe QCD axion dark matter in the mass range above 40 μeV*, *Eur. Phys. J. C* **79** (2019) 186, [1901.07401].

[207] CAST collaboration, V. Anastassopoulos et al., *New CAST Limit on the Axion-Photon Interaction*, *Nature Phys.* **13** (2017) 584–590, [1705.02290].

[208] E. Armengaud et al., *Conceptual Design of the International Axion Observatory (IAXO)*, *JINST* **9** (2014) T05002, [1401.3233].

[209] K. Barth et al., *CAST constraints on the axion-electron coupling*, *JCAP* **05** (2013) 010, [1302.6283].

[210] K. Ehret et al., *New ALPS Results on Hidden-Sector Lightweights*, *Phys. Lett. B* **689** (2010) 149–155, [1004.1313].

[211] OSQAR collaboration, R. Ballou et al., *New exclusion limits on scalar and pseudoscalar axionlike particles from light shining through a wall*, *Phys. Rev. D* **92** (2015) 092002, [1506.08082].

[212] M. Betz, F. Caspers, M. Gasior, M. Thumm and S. W. Rieger, *First results of the CERN Resonant Weakly Interacting sub-eV Particle Search (CROWS)*, *Phys. Rev. D* **88** (2013) 075014, [1310.8098].

[213] R. Bähre et al., *Any light particle search II —Technical Design Report*, *JINST* **8** (2013) T09001, [1302.5647].

[214] N. Vinyoles, A. Serenelli, F. L. Villante, S. Basu, J. Redondo and J. Isern, *New axion and hidden photon constraints from a solar data global fit*, *JCAP* **10** (2015) 015, [1501.01639].

[215] P. Gondolo and G. G. Raffelt, *Solar neutrino limit on axions and keV-mass bosons*, *Phys. Rev. D* **79** (2009) 107301, [0807.2926].

[216] A. Ayala, I. Domínguez, M. Giannotti, A. Mirizzi and O. Straniero, *Revisiting the bound on axion-photon coupling from Globular Clusters*, *Phys. Rev. Lett.* **113** (2014) 191302, [1406.6053].

[217] G. G. Raffelt, *Astrophysical axion bounds*, *Lect. Notes Phys.* **741** (2008) 51–71, [hep-ph/0611350].

[218] P. Carenza, T. Fischer, M. Giannotti, G. Guo, G. Martínez-Pinedo and A. Mirizzi, *Improved axion emissivity from a supernova via nucleon-nucleon bremsstrahlung*, *JCAP* **10** (2019) 016, [1906.11844].

[219] G. Lucente, L. Mastrototaro, P. Carenza, L. Di Luzio, M. Giannotti and A. Mirizzi, *Axion signatures from supernova explosions through the nucleon electric-dipole portal*, *Phys. Rev. D* **105** (2022) 123020, [2203.15812].

[220] F. Calore, P. Carenza, M. Giannotti, J. Jaeckel and A. Mirizzi, *Bounds on axionlike particles from the diffuse supernova flux*, *Phys. Rev. D* **102** (2020) 123005, [2008.11741].

[221] F. Calore, P. Carenza, M. Giannotti, J. Jaeckel, G. Lucente and A. Mirizzi, *Supernova bounds on axionlike particles coupled with nucleons and electrons*, *Phys. Rev. D* **104** (2021) 043016, [2107.02186].

[222] F. D'Eramo, E. Di Valentino, W. Giarè, F. Hajkarim, A. Melchiorri, O. Mena et al., *Cosmological Bound on the QCD Axion Mass, Redux*, 2205.07849.

[223] W. Giarè, E. Di Valentino, A. Melchiorri and O. Mena, *New cosmological bounds on hot relics: axions and neutrinos*, *Mon. Not. Roy. Astron. Soc.* **505** (2021) 2703–2711, [2011.14704].

[224] P. Carenza, M. Lattanzi, A. Mirizzi and F. Forastieri, *Thermal axions with multi-eV masses are possible in low-reheating scenarios*, *JCAP* **07** (2021) 031, [2104.03982].

[225] M. Millea, *New cosmological bounds on axions in the XENON1T window*, 2007.05659.

[226] S. Hannestad, A. Mirizzi, G. G. Raffelt and Y. Y. Y. Wong, *Cosmological constraints on neutrino plus axion hot dark matter*, *JCAP* **08** (2007) 015, [0706.4198].

[227] A. Melchiorri, O. Mena and A. Slosar, *An improved cosmological bound on the thermal axion mass*, *Phys. Rev. D* **76** (2007) 041303, [0705.2695].

[228] M. Archidiacono, S. Hannestad, A. Mirizzi, G. Raffelt and Y. Y. Y. Wong, *Axion hot dark matter bounds after Planck*, *JCAP* **10** (2013) 020, [1307.0615].

[229] E. Giusarma, E. Di Valentino, M. Lattanzi, A. Melchiorri and O. Mena, *Relic Neutrinos, thermal axions and cosmology in early 2014*, *Phys. Rev. D* **90** (2014) 043507, [1403.4852].

[230] E. Di Valentino, E. Giusarma, M. Lattanzi, A. Melchiorri and O. Mena, *Axion cold dark matter: status after Planck and BICEP2*, *Phys. Rev. D* **90** (2014) 043534, [1405.1860].

[231] E. Di Valentino, E. Giusarma, M. Lattanzi, O. Mena, A. Melchiorri and J. Silk, *Cosmological Axion and neutrino mass constraints from Planck 2015 temperature and polarization data*, *Phys. Lett. B* **752** (2016) 182–185, [1507.08665].

[232] V. Poulin, T. L. Smith, D. Grin, T. Karwal and M. Kamionkowski, *Cosmological implications of ultralight axionlike fields*, *Phys. Rev. D* **98** (2018) 083525, [1806.10608].

[233] G. Mangano, G. Miele, S. Pastor and M. Peloso, *A Precision calculation of the effective number of cosmological neutrinos*, *Phys. Lett. B* **534** (2002) 8–16, [astro-ph/0111408].

[234] J. J. Bennett, G. Buldgen, M. Drewes and Y. Y. Y. Wong, *Towards a precision calculation of the effective number of neutrinos $N_{\rm eff}$ in the Standard Model I: the QED equation of state*, *JCAP* **03** (2020) 003, [1911.04504].

[235] J. J. Bennett, G. Buldgen, P. F. De Salas, M. Drewes, S. Gariazzo, S. Pastor et al., *Towards a precision calculation of $N_{\rm eff}$ in the Standard Model II: Neutrino decoupling in the presence of flavour oscillations and finite-temperature QED*, *JCAP* **04** (2021) 073, [2012.02726].

[236] K. Akita and M. Yamaguchi, *A precision calculation of relic neutrino decoupling*, *JCAP* **08** (2020) 012, [2005.07047].

[237] J. Froustey, C. Pitrou and M. C. Volpe, *Neutrino decoupling including flavour oscillations and primordial nucleosynthesis*, *JCAP* **12** (2020) 015, [2008.01074].

[238] M. Drees, F. Hajkarim and E. R. Schmitz, *The Effects of QCD Equation of State on the Relic Density of WIMP Dark Matter*, *JCAP* **06** (2015) 025, [1503.03513].

[239] Particle Data Group collaboration, R. L. Workman, *Review of Particle Physics*, *PTEP* **2022** (2022) 083C01.

[240] K. Abazajian et al., *CMB-S4 Science Case, Reference Design, and Project Plan*, 1907.04473.

[241] H. A. Weldon, *Reformulation of finite temperature dilepton production*, *Phys. Rev. D* **42** (1990) 2384–2387.

[242] C. Gale and J. I. Kapusta, *Vector dominance model at finite temperature*, *Nucl. Phys. B* **357** (1991) 65–89.

[243] G. G. Raffelt, *Stars as laboratories for fundamental physics: The astrophysics of neutrinos, axions, and other weakly interacting particles*. University of Chicago Press, 5, 1996.

[244] M. Bolz, A. Brandenburg and W. Buchmuller, *Thermal production of gravitinos*, *Nucl. Phys. B* **606** (2001) 518–544, [hep-ph/0012052].

[245] D. Cadamuro and J. Redondo, *Cosmological bounds on pseudo Nambu-Goldstone bosons*, *JCAP* **02** (2012) 032, [1110.2895].

[246] HotQCD collaboration, A. Bazavov et al., *Equation of state in (2+1)-flavor QCD*, *Phys. Rev. D* **90** (2014) 094503, [1407.6387].

[247] Y. Watanabe and E. Komatsu, *Improved Calculation of the Primordial Gravitational Wave Spectrum in the Standard Model*, *Phys. Rev. D* **73** (2006) 123515, [astro-ph/0604176].

[248] D. Cadamuro, S. Hannestad, G. Raffelt and J. Redondo, *Cosmological bounds on sub-MeV mass axions*, *JCAP* **02** (2011) 003, [1011.3694].

[249] J. P. Conlon and M. C. D. Marsh, *The Cosmophenomenology of Axionic Dark Radiation*, *JHEP* **10** (2013) 214, [1304.1804].

[250] Z. G. Berezhiani, A. S. Sakharov and M. Y. Khlopov, *Primordial background of cosmological axions*, *Sov. J. Nucl. Phys.* **55** (1992) 1063–1071.

[251] S. Chang and K. Choi, *Hadronic axion window and the big bang nucleosynthesis*, *Phys. Lett. B* **316** (1993) 51–56, [hep-ph/9306216].

[252] S. Hannestad, A. Mirizzi and G. Raffelt, *New cosmological mass limit on thermal relic axions*, *JCAP* **07** (2005) 002, [hep-ph/0504059].

[253] F. D'Eramo, L. J. Hall and D. Pappadopulo, *Multiverse Dark Matter: SUSY or Axions*, *JHEP* **11** (2014) 108, [1409.5123].

[254] M. Kawasaki, M. Yamada and T. T. Yanagida, *Observable dark radiation from a cosmologically safe QCD axion*, *Phys. Rev. D* **91** (2015) 125018, [1504.04126].

[255] R. Z. Ferreira, A. Notari and F. Rompineve, *Dine-Fischler-Srednicki-Zhitnitsky axion in the CMB*, *Phys. Rev. D* **103** (2021) 063524, [2012.06566].

[256] M. Archidiacono, D. C. Hooper, R. Murgia, S. Bohr, J. Lesgourgues and M. Viel, *Constraining Dark Matter-Dark Radiation interactions with CMB, BAO, and Lyman-α*, *JCAP* **10** (2019) 055, [1907.01496].

[257] A. Lewis and S. Bridle, *Cosmological parameters from CMB and other data: A Monte Carlo approach*, *Phys. Rev. D* **66** (2002) 103511, [astro-ph/0205436].

[258] A. Lewis, *GetDist: a Python package for analysing Monte Carlo samples*, 1910.13970.

[259] E. Di Valentino, O. Mena, S. Pan, L. Visinelli, W. Yang, A. Melchiorri et al., *In the realm of the Hubble tension—a review of solutions*, *Class. Quant. Grav.* **38** (2021) 153001, [2103.01183].

[260] F. D'Eramo, R. Z. Ferreira, A. Notari and J. L. Bernal, *Hot Axions and the H_0 tension*, *JCAP* **11** (2018) 014, [1808.07430].

[261] ACT collaboration, S. K. Choi et al., *The Atacama Cosmology Telescope: a measurement of the Cosmic Microwave Background power spectra at 98 and 150 GHz*, *JCAP* **12** (2020) 045, [2007.07289].

[262] ACT collaboration, S. Aiola et al., *The Atacama Cosmology Telescope: DR4 Maps and Cosmological Parameters*, *JCAP* **12** (2020) 047, [2007.07288].

[263] A. Friedland, M. Giannotti and M. Wise, *Constraining the Axion-Photon Coupling with Massive Stars*, *Phys. Rev. Lett.* **110** (2013) 061101, [1210.1271].

[264] K. Blum, R. T. D'Agnolo, M. Lisanti and B. R. Safdi, *Constraining Axion Dark Matter with Big Bang Nucleosynthesis*, *Phys. Lett. B* **737** (2014) 30–33, [1401.6460].

[265] D. Mattingly, *Modern tests of Lorentz invariance*, *Living Rev. Rel.* **8** (2005) 5, [gr-qc/0502097].

[266] G. Amelino-Camelia, *Quantum-Spacetime Phenomenology*, *Living Rev. Rel.* **16** (2013) 5, [0806.0339].

[267] A. Addazi et al., *Quantum gravity phenomenology at the dawn of the multi-messenger era—A review*, *Prog. Part. Nucl. Phys.* **125** (2022) 103948, [2111.05659].

[268] M. Lembo, M. Lattanzi, L. Pagano, A. Gruppuso, P. Natoli and F. Forastieri, *Cosmic Microwave Background Polarization as a Tool to Constrain the Optical Properties of the Universe*, *Phys. Rev. Lett.* **127** (2021) 011301, [2007.08486].

[269] V. A. Kostelecky and M. Mewes, *Signals for Lorentz violation in electrodynamics*, *Phys. Rev. D* **66** (2002) 056005, [hep-ph/0205211].

[270] D. B. Melrose and R. C. McPhedran, *Electromagnetic Processes in Dispersive Media*. Cambridge University Press, 1991. 10.1017/CBO9780511600036.

[271] V. A. Kostelecky and N. Russell, *Data Tables for Lorentz and CPT Violation*, 0801.0287.

[272] B. Feng, M. Li, J.-Q. Xia, X. Chen and X. Zhang, *Searching for CPT Violation with Cosmic Microwave Background Data from WMAP and BOOMERANG*, *Phys. Rev. Lett.* **96** (2006) 221302, [astro-ph/0601095].

[273] V. A. Kostelecky and M. Mewes, *Astrophysical Tests of Lorentz and CPT Violation with Photons*, *Astrophys. J. Lett.* **689** (2008) L1–L4, [0809.2846].

[274] G. Gubitosi, L. Pagano, G. Amelino-Camelia, A. Melchiorri and A. Cooray, *A Constraint on Planck-scale Modifications to Electrodynamics with CMB polarization data*, *JCAP* **08** (2009) 021, [0904.3201].

[275] L. Pagano, P. de Bernardis, G. De Troia, G. Gubitosi, S. Masi, A. Melchiorri et al., *CMB Polarization Systematics, Cosmological Birefringence and the Gravitational Waves Background*, *Phys. Rev. D* **80** (2009) 043522, [0905.1651].

[276] A. Gruppuso, M. Gerbino, P. Natoli, L. Pagano, N. Mandolesi, A. Melchiorri et al., *Constraints on cosmological birefringence from Planck and Bicep2/Keck data*, *JCAP* **06** (2016) 001, [1509.04157].

[277] Y. Minami and E. Komatsu, *New Extraction of the Cosmic Birefringence from the Planck 2018 Polarization Data*, *Phys. Rev. Lett.* **125** (2020) 221301, [2011.11254].

[278] V. Gluscevic, D. Hanson, M. Kamionkowski and C. M. Hirata, *First CMB Constraints on Direction-Dependent Cosmological Birefringence from WMAP-7*, *Phys. Rev. D* **86** (2012) 103529, [1206.5546].

[279] G. Gubitosi, M. Migliaccio, L. Pagano, G. Amelino-Camelia, A. Melchiorri, P. Natoli et al., *Using CMB data to constrain non-isotropic Planck-scale modifications to Electrodynamics*, *JCAP* **11** (2011) 003, [1106.6049].

[280] D. Contreras, P. Boubel and D. Scott, *Constraints on direction-dependent cosmic birefringence from Planck polarization data*, *JCAP* **12** (2017) 046, [1705.06387].

[281] SPT collaboration, F. Bianchini et al., *Searching for Anisotropic Cosmic Birefringence with Polarization Data from SPTpol*, *Phys. Rev. D* **102** (2020) 083504, [2006.08061].

[282] A. Gruppuso, D. Molinari, P. Natoli and L. Pagano, *Planck 2018 constraints on anisotropic birefringence and its cross-correlation with CMB anisotropy*, *JCAP* **11** (2020) 066, [2008.10334].

[283] M. Bortolami, M. Billi, A. Gruppuso, P. Natoli and L. Pagano, *Planck constraints on cross-correlations between anisotropic cosmic birefringence and CMB polarization*, *JCAP* **09** (2022) 075, [2206.01635].

[284] A. Lewis, A. Challinor and A. Lasenby, *Efficient computation of CMB anisotropies in closed FRW models*, **538** (2000) 473–476, [astro-ph/9911177].

[285] C. Howlett, A. Lewis, A. Hall and A. Challinor, *CMB power spectrum parameter degeneracies in the era of precision cosmology*, *JCAP* **04** (2012) 027, [1201.3654].

[286] J. Torrado and A. Lewis, *Cobaya: Code for Bayesian Analysis of hierarchical physical models*, *JCAP* **05** (2021) 057, [2005.05290].

[287] A. Gelman and D. B. Rubin, *Inference from Iterative Simulation Using Multiple Sequences*, *Statist. Sci.* **7** (1992) 457–472.

[288] G. Gubitosi and F. Paci, *Constraints on cosmological birefringence energy dependence from CMB polarization data*, *JCAP* **02** (2013) 020, [1211.3321].

[289] Planck collaboration, N. Aghanim et al., *Planck 2018 results. III. High Frequency Instrument data processing and frequency maps*, *Astron. Astrophys.* **641** (2020) A3, [1807.06207].

[290] BICEP/Keck collaboration, T. St Germaine et al., *Optical characterization of the Keck Array and BICEP3 CMB Polarimeters from 2016 to 2019*, *J. Low Temp. Phys.* **199** (2020) 824–832, [2002.05197].

[291] R. J. Thornton et al., *The Atacama Cosmology Telescope: The polarization-sensitive ACTPol instrument*, *Astrophys. J. Suppl.* **227** (2016) 21, [1605.06569].

[292] T. Kahniashvili, R. Durrer and Y. Maravin, *Testing Lorentz Invariance Violation with WMAP Five Year Data*, *Phys. Rev. D* **78** (2008) 123009, [0807.2593].

[293] A. S. Friedman, R. Gerasimov, D. Leon, W. Stevens, D. Tytler, B. G. Keating et al., *Improved constraints on anisotropic birefringent Lorentz invariance and CPT violation from broadband optical polarimetry of high redshift galaxies*, *Phys. Rev. D* **102** (2020) 043008, [2003.00647].

[294] R. Gerasimov, P. Bhoj and F. Kislat, *New Constraints on Lorentz Invariance Violation from Combined Linear and Circular Optical Polarimetry of Extragalactic Sources*, *Symmetry* **13** (2021) 880, [2104.00238].

[295] M. B. Green and J. H. Schwarz, *Anomaly Cancellation in Supersymmetric D=10 Gauge Theory and Superstring Theory*, *Phys. Lett. B* **149** (1984) 117–122.

[296] J. Polchinski, *String theory. Vol. 2: Superstring theory and beyond.* Cambridge Monographs on Mathematical Physics. Cambridge University Press, 2007. 10.1017/CBO9780511618123.

[297] K. Choi, J.-c. Hwang and K. W. Hwang, *String theoretic axion coupling and the evolution of cosmic structures*, *Phys. Rev. D* **61** (2000) 084026, [hep-ph/9907244].

[298] S. H.-S. Alexander, M. E. Peskin and M. M. Sheikh-Jabbari, *Leptogenesis from gravity waves in models of inflation*, *Phys. Rev. Lett.* **96** (2006) 081301, [hep-th/0403069].

[299] D. H. Lyth, C. Quimbay and Y. Rodriguez, *Leptogenesis and tensor polarisation from a gravitational Chern-Simons term*, *JHEP* **03** (2005) 016, [hep-th/0501153].

[300] S. Alexander and N. Yunes, *Chern-Simons Modified General Relativity*, *Phys. Rept.* **480** (2009) 1–55, [0907.2562].

[301] K. Kamada, J. Kume and Y. Yamada, *Renormalization in gravitational leptogenesis with pseudo-scalar-tensor coupling*, 2007.08029.

[302] A. Ashtekar, A. P. Balachandran and S. Jo, *The CP Problem in Quantum Gravity*, *International Journal of Modern Physics A* **4** (Jan., 1989) 1493–1514.

[303] V. Taveras and N. Yunes, *The Barbero-Immirzi Parameter as a Scalar Field: K-Inflation from Loop Quantum Gravity?*, *Phys. Rev. D* **78** (2008) 064070, [0807.2652].

[304] G. Calcagni and S. Mercuri, *The Barbero-Immirzi field in canonical formalism of pure gravity*, *Phys. Rev. D* **79** (2009) 084004, [0902.0957].

[305] J. Gates, S.James, S. V. Ketov and N. Yunes, *Seeking the Loop Quantum Gravity Barbero-Immirzi Parameter and Field in 4D, N = 1 Supergravity*, *Phys. Rev. D* **80** (2009) 065003, [0906.4978].

[306] S. Mercuri and V. Taveras, *Interaction of the Barbero-Immirzi Field with Matter and Pseudo-Scalar Perturbations*, *Phys. Rev. D* **80** (2009) 104007, [0903.4407].

[307] S. Weinberg, *Effective Field Theory for Inflation*, *Phys. Rev. D* **77** (2008) 123541, [0804.4291].

[308] P. Horava, *Quantum Gravity at a Lifshitz Point*, *Phys. Rev. D* **79** (2009) 084008, [0901.3775].

[309] A. Wang, *Horava gravity at a Lifshitz point: A progress report*, *Int. J. Mod. Phys. D* **26** (2017) 1730014, [1701.06087].

[310] T. Takahashi and J. Soda, *Chiral Primordial Gravitational Waves from a Lifshitz Point*, *Phys. Rev. Lett.* **102** (2009) 231301, [0904.0554].

[311] A. Wang, Q. Wu, W. Zhao and T. Zhu, *Polarizing primordial gravitational waves by parity violation*, *Phys. Rev. D* **87** (2013) 103512, [1208.5490].

[312] S. Alexander and J. Martin, *Birefringent gravitational waves and the consistency check of inflation*, *Phys. Rev. D* **71** (2005) 063526, [hep-th/0410230].

[313] M. Satoh, *Slow-roll Inflation with the Gauss-Bonnet and Chern-Simons Corrections*, *JCAP* **11** (2010) 024, [1008.2724].

[314] Y. S. Myung and T. Moon, *Primordial massive gravitational waves from Einstein-Chern-Simons-Weyl gravity*, *JCAP* **08** (2014) 061, [1406.4367].

[315] S. H. S. Alexander, *Inflationary Birefringence and Baryogenesis*, *Int. J. Mod. Phys. D* **25** (2016) 1640013, [1604.00703].

[316] M. Mylova, *Chiral primordial gravitational waves in extended theories of Scalar-Tensor gravity*, 1912.00800.

[317] J. Qiao, T. Zhu, W. Zhao and A. Wang, *Polarized primordial gravitational waves in the ghost-free parity-violating gravity*, *Phys. Rev. D* **101** (2020) 043528, [1911.01580].

[318] N. Bartolo, E. Komatsu, S. Matarrese and A. Riotto, *Non-Gaussianity from inflation: Theory and observations*, *Phys. Rept.* **402** (2004) 103–266, [astro-ph/0406398].

[319] D. Babich, P. Creminelli and M. Zaldarriaga, *The Shape of non-Gaussianities*, *JCAP* **0408** (2004) 009, [astro-ph/0405356].

[320] J. Fergusson and E. Shellard, *The shape of primordial non-Gaussianity and the CMB bispectrum*, *Phys. Rev. D* **80** (2009) 043510, [0812.3413].

[321] Planck collaboration, Y. Akrami et al., *Planck 2018 results. IX. Constraints on primordial non-Gaussianity*, 1905.05697.

[322] J. M. Maldacena and G. L. Pimentel, *On graviton non-Gaussianities during inflation*, *JHEP* **09** (2011) 045, [1104.2846].

[323] J. Soda, H. Kodama and M. Nozawa, *Parity Violation in Graviton Non-gaussianity*, *JHEP* **08** (2011) 067, [1106.3228].

[324] M. Shiraishi, D. Nitta and S. Yokoyama, *Parity Violation of Gravitons in the CMB Bispectrum*, *Prog. Theor. Phys.* **126** (2011) 937–959, [1108.0175].

[325] Y. Huang, A. Wang, R. Yousefi and T. Zhu, *Primordial non-Gaussianity of gravitational waves in Horava-Lifshitz gravity*, *Phys. Rev. D* **88** (2013) 023523, [1304.1556].

[326] T. Zhu, W. Zhao, Y. Huang, A. Wang and Q. Wu, *Effects of parity violation on non-gaussianity of primordial gravitational waves in Horava-Lifshitz gravity*, *Phys. Rev. D* **88** (2013) 063508, [1305.0600].

[327] L. Bordin, G. Cabass, P. Creminelli and F. Vernizzi, *Simplifying the EFT of Inflation: generalized disformal transformations and redundant couplings*, *JCAP* **09** (2017) 043, [1706.03758].

[328] N. Bartolo and G. Orlando, *Parity breaking signatures from a Chern-Simons coupling during inflation: the case of non-Gaussian gravitational waves*, *JCAP* **1707** (2017) 034, [1706.04627].

[329] C. Cordova, J. Maldacena and G. J. Turiaci, *Bounds on OPE Coefficients from Interference Effects in the Conformal Collider*, *JHEP* **11** (2017) 032, [1710.03199].

[330] N. Bartolo, G. Orlando and M. Shiraishi, *Measuring chiral gravitational waves in Chern-Simons gravity with CMB bispectra*, *JCAP* **01** (2019) 050, [1809.11170].

[331] L. Bordin and G. Cabass, *Graviton non-Gaussianities and Parity Violation in the EFT of Inflation*, 2004.00619.

[332] G. Cabass, E. Pajer, D. Stefanyszyn and J. Supeł, *Bootstrapping large graviton non-Gaussianities*, *JHEP* **05** (2022) 077, [2109.10189].

[333] R. Jackiw and S. Pi, *Chern-Simons modification of general relativity*, *Phys. Rev. D* **68** (2003) 104012, [gr-qc/0308071].

[334] R. P. Woodard, *Avoiding dark energy with 1/r modifications of gravity*, *Lect. Notes Phys.* **720** (2007) 403–433, [astro-ph/0601672].

[335] R. L. Arnowitt, S. Deser and C. W. Misner, *The Dynamics of general relativity*, *Gen. Rel. Grav.* **40** (2008) 1997–2027, [gr-qc/0405109].

[336] J. M. Bardeen, *Gauge Invariant Cosmological Perturbations*, *Phys. Rev. D* **22** (1980) 1882–1905.

[337] E. Gourgoulhon, *3+1 formalism and bases of numerical relativity*, 2007. 10.48550/ARXIV.GR-QC/0703035.

[338] D. S. Salopek and J. R. Bond, *Nonlinear evolution of long wavelength metric fluctuations in inflationary models*, *Phys. Rev.* **D42** (1990) 3936–3962.

[339] X. Chen, M.-x. Huang, S. Kachru and G. Shiu, *Observational signatures and non-Gaussianities of general single field inflation*, *JCAP* **0701** (2007) 002, [hep-th/0605045].

[340] M. Shiraishi, *Parity violation in the CMB trispectrum from the scalar sector*, *Phys. Rev. D* **94** (2016) 083503, [1608.00368].

[341] J. Qiao, T. Zhu, W. Zhao and A. Wang, *Waveform of gravitational waves in the ghost-free parity-violating gravities*, *Phys. Rev. D* **100** (2019) 124058, [1909.03815].

[342] A. Nishizawa and T. Kobayashi, *Parity-violating gravity and GW170817*, *Phys. Rev. D* **98** (2018) 124018, [1809.00815].

[343] X. Gao and X.-Y. Hong, *Propagation of gravitational waves in a cosmological background*, *Phys. Rev. D* **101** (2020) 064057, [1906.07131].

[344] S. Dyda, E. E. Flanagan and M. Kamionkowski, *Vacuum Instability in Chern-Simons Gravity*, *Phys. Rev. D* **86** (2012) 124031, [1208.4871].

[345] "*NIST Digital Library of Mathematical Functions*." http://dlmf.nist.gov/, Release 1.0.27 of 2020-06-15.

[346] M. Gerbino, A. Gruppuso, P. Natoli, M. Shiraishi and A. Melchiorri, *Testing chirality of primordial gravitational waves with Planck and future CMB data: no hope from angular power spectra*, *JCAP* **1607** (2016) 044, [1605.09357].

[347] S. Weinberg, *Quantum contributions to cosmological correlations*, *Phys. Rev.* **D72** (2005) 043514, [hep-th/0506236].

[348] X. Chen, *Primordial Non-Gaussianities from Inflation Models*, *Adv. Astron.* **2010** (2010) 638979, [1002.1416].

[349] E. Komatsu and D. N. Spergel, *Acoustic signatures in the primary microwave background bispectrum*, *Phys. Rev.* **D63** (2001) 063002, [astro-ph/0005036].

[350] P. D. Meerburg, J. Meyers, A. van Engelen and Y. Ali-Haïmoud, *CMB B -mode non-Gaussianity*, *Phys. Rev. D* **93** (2016) 123511, [1603.02243].

[351] A. J. Duivenvoorden, P. D. Meerburg and K. Freese, *CMB B-mode non-Gaussianity: optimal bispectrum estimator and Fisher forecasts*, 1911.11349.

[352] K. Hinterbichler, L. Hui and J. Khoury, *An Infinite Set of Ward Identities for Adiabatic Modes in Cosmology*, *JCAP* **1401** (2014) 039, [1304.5527].

[353] M. Mirbabayi and M. Zaldarriaga, *Double Soft Limits of Cosmological Correlations*, *JCAP* **03** (2015) 025, [1409.6317].

[354] L. Bordin, P. Creminelli, M. Mirbabayi and J. Noreña, *Tensor Squeezed Limits and the Higuchi Bound*, *JCAP* **1609** (2016) 041, [1605.08424].

[355] T. Tanaka and Y. Urakawa, *Dominance of gauge artifact in the consistency relation for the primordial bispectrum*, *JCAP* **1105** (2011) 014, [1103.1251].

[356] E. Pajer, F. Schmidt and M. Zaldarriaga, *The Observed Squeezed Limit of Cosmological Three-Point Functions*, *Phys. Rev.* **D88** (2013) 083502, [1305.0824].

[357] P. Creminelli, A. Perko, L. Senatore, M. Simonović and G. Trevisan, *The Physical Squeezed Limit: Consistency Relations at Order q^2*, *JCAP* **1311** (2013) 015, [1307.0503].

[358] G. Cabass, E. Pajer and F. Schmidt, *How Gaussian can our Universe be?*, *JCAP* **01** (2017) 003, [1612.00033].

[359] S. Matarrese, L. Pilo and R. Rollo, *Resilience of long modes in cosmological observables*, 2007.08877.

[360] P. Creminelli and M. Zaldarriaga, *Single field consistency relation for the 3-point function*, *JCAP* **0410** (2004) 006, [astro-ph/0407059].

[361] P. Creminelli, G. D'Amico, M. Musso and J. Noreña, *The (not so) squeezed limit of the primordial 3-point function*, *JCAP* **1111** (2011) 038, [1106.1462].

[362] L. Dai, D. Jeong and M. Kamionkowski, *Anisotropic imprint of long-wavelength tensor perturbations on cosmic structure*, *Phys. Rev.* **D88** (2013) 043507, [1306.3985].

[363] P. Creminelli, J. Noreña, M. Simonović and F. Vernizzi, *Single-Field Consistency Relations of Large Scale Structure*, *JCAP* **12** (2013) 025, [1309.3557].

[364] E. Dimastrogiovanni, M. Fasiello and M. Kamionkowski, *Imprints of Massive Primordial Fields on Large-Scale Structure*, *JCAP* **02** (2016) 017, [1504.05993].

[365] L. Iacconi, M. Fasiello, H. Assadullahi and D. Wands, *Small-scale Tests of Inflation*, 2008.00452.

[366] S. Kundu, *Non-Gaussianity Consistency Relations, Initial States and Back-reaction*, *JCAP* **04** (2014) 016, [1311.1575].

[367] N. Bartolo, S. Matarrese, M. Peloso and A. Ricciardone, *Anisotropy in solid inflation*, *JCAP* **08** (2013) 022, [1306.4160].

[368] O. Ozsoy, M. Mylova, S. Parameswaran, C. Powell, G. Tasinato and I. Zavala, *Squeezed tensor non-Gaussianity in non-attractor inflation*, *JCAP* **09** (2019) 036, [1902.04976].

[369] N. Bartolo, D. Cannone, A. Ricciardone and G. Tasinato, *Distinctive signatures of space-time diffeomorphism breaking in EFT of inflation*, *JCAP* **03** (2016) 044, [1511.07414].

[370] A. Ricciardone and G. Tasinato, *Primordial gravitational waves in supersolid inflation*, *Phys. Rev. D* **96** (2017) 023508, [1611.04516].

[371] M. Shiraishi, M. Liguori and J. R. Fergusson, *Observed parity-odd CMB temperature bispectrum*, *JCAP* **01** (2015) 007, [1409.0265].

[372] M. Shiraishi, *Tensor Non-Gaussianity Search: Current Status and Future Prospects*, *Front. Astron. Space Sci.* **6** (2019) 49, [1905.12485].

[373] M. Shiraishi, S. Yokoyama, K. Ichiki and K. Takahashi, *Analytic formulae of the CMB bispectra generated from non-Gaussianity in the tensor and vector perturbations*, *Phys. Rev. D* **82** (2010) 103505, [1003.2096].

[374] M. Shiraishi, D. Nitta, S. Yokoyama, K. Ichiki and K. Takahashi, *CMB Bispectrum from Primordial Scalar, Vector and Tensor non-Gaussianities*, *Prog. Theor. Phys.* **125** (2011) 795–813, [1012.1079].

[375] V. De Luca, G. Franciolini, A. Kehagias, A. Riotto and M. Shiraishi, *Constraining graviton non-Gaussianity through the CMB bispectra*, *Phys. Rev. D* **100** (2019) 063535, [1908.00366].

[376] J. N. Goldberg, A. J. MacFarlane, E. T. Newman, F. Rohrlich and E. C. G. Sudarshan, *Spin s spherical harmonics and edth*, *J. Math. Phys.* **8** (1967) 2155.

[377] P. McFadden and K. Skenderis, *Cosmological 3-point correlators from holography*, *JCAP* **06** (2011) 030, [1104.3894].